UNIVERSIDADE ESTADUAL DE CAMPINAS

Faculdade de Engenharia Mecânica

HANDEL ANDRES MARTINEZ SARACHE

Experimental assessment of fixed-bed combustion of sugarcane processing by-products

Avaliação experimental da combustão em leito fixo de resíduos da indústria sucroalcooleira

Campinas

2023

HANDEL ANDRES MARTINEZ SARACHE

Experimental assessment of fixed-bed combustion of sugarcane processing by-products

Avaliação experimental da combustão em leito fixo de resíduos da indústria sucroalcooleira

Tese de Doutorado apresentada à Faculdade de Engenharia Mecânica da Universidade Estadual de Campinas como parte dos requisitos exigidos para a obtenção do título de Doutor em Engenharia Mecânica, na Área de Térmica e Fluidos.

Thesis presented to the Faculty of Mechanical Engineering of the University of Campinas in partial fulfillment of the requirements for the degree of Doctor in Mechanical Engineering, in the area of Thermal and Fluids.

Orientador: Prof. Dr. Waldir Antônio Bizzo

ESTE TRABALHO CORRESPONDE À VERSÃO FINAL DA TESE DE DOUTORADO DEFENDIDA PELO ALUNO HANDEL ANDRES MARTINEZ SARACHE, E ORIENTADA PELO PROF. DR. WALDIR ANTÔNIO BIZZO.

Campinas

2023

Ficha catalográfica
Universidade Estadual de Campinas
Biblioteca da Área de Engenharia e Arquitetura
Rose Meire da Silva - CRB 8/5974

M366e

Martinez Sarache, Handel Andres, 1986-
Experimental assessment of fixed-bed combustion of sugarcane processing by-products / Handel Andres Martinez Sarache. – Campinas, SP : [s.n.], 2023.

Orientador: Waldir Antônio Bizzo.
Tese (doutorado) – Universidade Estadual de Campinas, Faculdade de Engenharia Mecânica.

1. Combustão. 2. Biomassa. 3. Cana-de-açúcar. I. Bizzo, Waldir Antônio, 1955-. II. Universidade Estadual de Campinas. Faculdade de Engenharia Mecânica. III. Título.

Informações Complementares

Título em outro idioma: Avaliação experimental da combustão em leito fixo de resíduos da indústria sucroalcooleira
Palavras-chave em inglês:
Combustion
Biomass
Sugarcane
Área de concentração: Térmica e Fluídos
Titulação: Doutor em Engenharia Mecânica
Banca examinadora:
Waldir Antônio Bizzo [Orientador]
Marcio Luiz de Souza Santos
Erick de Moraes Franklin
João Andrade de Carvalho Junior
Yesid Javier Rueda Ordoñez
Data de defesa: 20-09-2023
Programa de Pós-Graduação: Engenharia Mecânica

Identificação e informações acadêmicas do(a) aluno(a)
- ORCID do autor: https://orcid.org/0000-0002-2879-4899
- Currículo Lattes do autor: http://lattes.cnpq.br/0367636311901129

UNIVERSIDADE ESTADUAL DE CAMPINAS
FACULDADE DE ENGENHARIA MECÂNICA

TESE DE DOUTORADO ACADÊMICO

Experimental assessment of fixed-bed combustion of sugarcane processing by-products

Avaliação experimental da combustão em leito fixo de resíduos da indústria sucroalcooleira

Autor: Handel Andres Martinez Sarache

Orientador: Prof. Dr. Waldir Antônio Bizzo

A Banca Examinadora composta pelos membros abaixo aprovou esta Tese de Doutorado:

Prof. Dr. Waldir Antonio Bizzo
Faculdade de Engenharia Mecânica/UNICAMP

Prof. Dr. Marcio Luiz de Souza Santos
Faculdade de Engenharia Mecânica/UNICAMP

Prof Dr. Erick de Moraes Franklin
Faculdade de Engenharia Mecânica/UNICAMP

Prof. Dr. Yesid Javier Rueda Ordoñez
Escuela de Ingeniería Mecánica/UIS (Colômbia)

Dr. João Andrade de Carvalho Junior
Faculdade de Engenharia/UNESP

A Ata de Defesa com as respectivas assinaturas dos membros encontra-se no SIGA/Sistema de Fluxo de Dissertação/Tese e na Secretaria do Programa da Unidade.

Campinas, 20 de setembro de 2023

DEDICATÓRIA

Este trabajo es la cristalización del sueño de un adolescente y está dedicado a todas aquellas personas que de una u otra forma me acompañaron durante todos estos años, principalmente a lo largo de los momentos más oscuros donde fueron luz e inspiración para continuar. Siempre los tendré en mi corazón.

Madre, lo logramos.

ACKNOWLEDGEMENTS

O desenvolvimento deste trabalho não teria sido possível sem o apoio dos meus estimados colegas Vitor Simões, João Altoé e André Martelli. Sempre estarei agradecido com vocês.

Agradeço ao professor Waldir Bizzo. Durante esses anos, mais que orientador, ele tornou-se um grande amigo de quem sempre recebi apoio, conselho e comprenssão.

Agradeço a minha mãe por ser o suporte esencial e incondicional em esses anos de esforço.

O presente trabalho foi realizado com apoio da Coordenação de Aperfeiçoamento de Pessoal de Nível Superior – Brasil (CAPES) – Código de Financiamento 001, e a Fundação de Amparo à Pesquisa do Estado de São Paulo (FAPESP) - processo No. 2019/07764-2.

RESUMO

No Brasil, as usinas de produção de açúcar utilizam principalmente o bagaço de cana como fonte de combustível nas caldeiras de cogeração. Essas usinas são caracterizadas principalmente por serem de leito fixo com uma grelha através da qual o ar primário é alimentado. Embora haja um interesse crescente na integração das folhas da planta no processo de cogeração, é obrigatório conhecer as implicações da adição de um novo combustível no comportamento da combustão para uma implementação adequada. O objetivo deste trabalho foi avaliar experimentalmente o desempenho da combustão dos resíduos do processamento da cana-de-açúcar em reatores de leito fixo operados em contracorrente . Para simular as condições presentes no interior de um queimador industrial, foi utilizado um queimador de leito fixo a escala de laboratoro preparado para monitorar continuamente as propriedades da biomassa durante a sua combustão. Com base em um delineamento experimental fatorial, foi realizada uma campanha experimental para avaliar o efeito combinado do fluxo de ar primário e da composição da mistura das biomassas no desempenho de sua combustão. Uma contribuição importante deste trabalho surgiu a partir de uma análise da evolução da diferença de pressão ao longo do leito em diferentes pontos. Com essa análise, estabeleceu-se um critério para a estimativa da posição do nível do leito durante a sua combustão. Esse resultado permitiu determinar parâmetros associados à propagação da zona de reação . Por outro lado, os resultados experimentais revelaram um comportamento sinérgico entre ambas as biomassas durante a sua combustão quando foram utilizadas misturas compostas por proporções equivalentes de folhas de cana-de-açúcar e bagaço. Essa melhoria, em comparação com a combustão do bagaço, está relacionada ao efeito catalítico dos álcalis nas fases de pirólise e combustão do char devido à contribuição das folhas. Com uma adequada extrapolação, espera-se que os resultados relatados neste estudo forneçam diretrizes para uma melhor utilização energética da ampla disponibilidade de resíduos gerados durante o processamento da cana-de-açúcar em reatores industriais de leito fixo.

Palavras–chave: Combustão, leito-fixo, biomassa, cana-de-açúcar

ABSTRACT

In Brazil, sugar mills primarily use sugarcane bagasse as a fuel source in cogeneration boilers. These plants are mainly characterized as fixed-bed plants with a grate through which primary air is supplied. Although there is a growing interest in integrating plant leaves into the cogeneration process, it is essential to understand the implications of adding a new fuel on combustion behavior for proper implementation. The objective of this study was to experimentally investigate evaluate the combustion performance of sugarcane straw and bagasse in counterflow operated fixed-bed reactors. To simulate the conditions inside an industrial combustor, a laboratory-scale fixed-bed burner was used, which was equipped for continuous monitoring of biomass properties during combustion. Based on a factorial design, an experimental campaign was conducted to evaluate the combined effect of primary air flow and biomass mixture composition on combustion performance. An important contribution of this work emerged from an analysis of the pressure drop evolution along the bed at different points. This analysis established a criterion for estimating the bed level position during combustion, allowing the determination of parameters associated with the reaction zone propagation. On the other hand, the experimental results revealed a synergistic behavior between both biomass types during combustion when mixtures composed of equivalent proportions of sugarcane leaves and bagasse were used. This improvement, compared to bagasse combustion, is related to the catalytic effect of alkalis due to the contribution of sugarcane leaves on the pyrolysis and char combustion phases. With proper extrapolation, it is expected that the results reported in this study will provide guidelines for a better energy utilization of the abundant availability of residues generated during sugarcane processing in industrial fixed-bed reactors.

Keywords: Combustion, fixed-bed, biomass, sugarcane residues

LIST OF FIGURES

LIST OF TABLES

LIST OF SYMBOLS

A_{bed}	Cross-section surface of the combustion chamber.
b_0	Constant regression coefficient
$b_{\dot{m}a}$	Airflow rate related regression coefficient
$b_{\dot{m}a2}$	Second-order airflow rate related regression coefficient
$b_{\dot{m}aYp}$	Airflow rate-Sugarcane leaves proportion related regression coefficient
b_{Yp}	Sugarcane proportion related regression coefficient
b_{Yp2}	Second-order sugarcane leaves proportion related regression coefficient
Bi	Biot's numer
C_p	Specific heat
d_p	Particle's diameter
d_{sv}	Surface-volume diameter
dm/dt	Mass loss rate
$(dT/dt)_{ig}$	Mean heating rate during ignition phase
H/C	Hidrogen–Carbon ratio
HHV	High heating value
H_i	Height over grate of temperature port i
$m_{r,SP}$	Residual mass after steady-state phase
$\dot{m}''_a$	Air flow rate
$\dot{m}''_{a,cr}$	Critical air flow rate
$\dot{m}''_{bur}$	Burning rate or mass loss rate
$\dot{m}''_{char}$	Char mass burning rate

$\dot{m}''_{ig}$	Ignition rate
O/C	Oxygen–Carbon ratio
$t(T^{ref})$	Time when T^{ref} is measured
t_{SP}	Steady-state duration
t_{tot}	Total experimental time
T_i	Measured temperature at position i
$T_{ig,max}$	Maximum ignition phase temperature
T_{max}	Maximum bed combustion temperature
T^{ref}	Reference temperature for ignition front velocity estimation
U_a	Superficial velocity
v_{ig}	Ignition front velocity
V_p	Particle's volume
X	Average concentration of a gas specie X
Y_p	Sugarcane leaves mass fraction in sample mixtures
δ	Reaction zone thickness
ΔP	Pressure drop
λ	Stoichiometric ratio
ρ_b	Bulk density
ρ_p	Particle's density
ϕ	Bed porosity
ω	Fuel moisture content

CONTENTS

1 INTRODUCTION

Due to the negative impact of fossil fuels' massive usage on the planet's climate, several nations have committed to increasing the use of environmentally friendly and sustainable energy sources. In the face of this scenario, biomass became a strategic raw material for energy purposes given its environmental, social, and economic advantages and geographic availability (Koppejan; Loo, 2012). Those characteristics make biomass an ideal candidate for partial substitution of traditional fossil fuels, allowing for prolonged and gradual strategies that have minimal impact on the current processes and operations. The benefits of biomass as an energy source have stimulated governments to implement policies for increasing biomass participation in their national energy mix. These policies promote the exploration of new biomasses, mainly from agro-industrial activities. In 2019, 9.37% of the primary energy supplied on the planet came from biomass sources (IEA – International Energy Agency, 2021).

In Brazil, just in 2020, 6.0% of the electricity supplied came from sugarcane processing plants (Ministerio de Minas e Energia, 2021), which traditionally used bagasse to power steam generators. Another sugarcane residues are the leaves which acquired relevance since the rising mechanical collecting popularity because of banning the field burning practice before manual harvesting (Bizzo et al., 2014). The subsequent increment in biomass availability attracts interest in sugarcane leaves for their potential employment with bagasse on cogeneration thermal cycle (Carvalho, 2017). Indeed, some sugarcane mills are already burning cane along with leaves (SUCRE, 2019).

High alkali metals, chloride, and sulfur content are the primary causes of the main issues associated with agricultural residues combustion. These elements are well-known for deposits and corrosion formation on heat transfer surfaces in boilers (Niu et al., 2016). For instance, results obtained from measurements at five sugarcane operating mills revealed that the co-combustion of bagasse and leaves exhibited unstable behaviour and increased incrustation and corrosion-related problems (SUCRE, 2019). Such challenges highlight the need for criteria to effectively harness the energetic potential of sugarcane residues as fuels for direct combustion.

Among the available solid fuel combustion technologies, fixed-bed reactors offer greater flexibility to burn solid fuels with diverse granulometries and lower operational and in-

stallation investment (Rayaprolu, 2009; Vakkilainen, 2016). Although fixed-bed systems dominated coal-burning technologies during the first part of the XX century, today it is thought obsolete its implementation in large-scale plants (> 150 MW$_{th}$) for power generation (Rayaprolu, 2009; Woodruff et al., 2017). However, many units are still operating worldwide, mainly consuming biomass . For example, most boilers in Brazil burning sugarcane residues use grate furnaces (CTC, 2009).

Ideally, the best operational conditions result from direct measurements in the burner after exposing the fuel to variations in the operative parameters. Nevertheless, measurements at industrial installations show technical and economic limitations. On the other hand, although computational modelling offers a detailed insight into the fuel's thermochemical conversion phenomena, the consistency and precision of the results depend on data and assumed hypotheses from experimental measurements (Yin et al., 2008; Khodaei et al., 2015; Dernbecher et al., 2019). Among the myriad of experimental techniques for studying solid fuel combustion laboratory-scale fixed-bed reactors have attributes that motivate their application in the characterization of the combustion of different fuels (Lans et al., 2000; Liang et al., 2008; Mitchell et al., 2016). Fixed-bed reactors stand-out for their sample size and the conditions emulated during combustion test, which are close to the observed in industrial installations. Furthermore, such experimental setups allow direct monitoring of the relevant bed combustion parameters as ignition and burning rates.

This work evaluated the co-combustion behaviour of sugarcane residues in fixed-bed burners under conditions experimentally simulated at laboratory-scale fixed-bed reactor. For this purpose, an experimental campaign exposed samples of mixtures with different proportions of sugarcane bagasse and leaves to variations in the primary air supply. Additionally, a discussion concerning the reaction zone propagation phenomena has been conducted on an extensive literature review about experimental packed bed combustion.

1.1 Research objectives

This thesis aimed to experimentally evaluate the performance of sugarcane residues co-combustion in a laboratory-scale fixed-bed reactor.

1.1.1 Specific objectives

- Through a systematic literature review of experimental studies about counter-current fixed-bed combustion, synthesize and consolidate the knowledge generated from a phenomenological perspective of the flame propagation process through a solid fuel fixed bed.

- Define the main operative parameters for describing the sample's combustion performance during the experiments.

- Based on statistical analysis, identify effects on reaction zone propagation caused by interactions between fixed-bed operative factors variation.

- Determine if the sugarcane residues co-combustion have characteristics that might improve or worsen their individual harnessing in fixed-bed burners.

2 FIXED-BED COMBUSTION LITERATURE REVIEW

2.1 Introduction

Due to the negative impact of fossil fuels' massive usage on the planet's climate, several nations have committed to increasing the use of environmentally friendly and sustainable energy sources. In the face of this scenario, biomass becomes a strategic raw material for energy purposes given its environmental, social, and economic advantages and geographic availability (Koppejan; Loo, 2012). Those characteristics make biomass an ideal candidate for partial substitution of traditional fossil fuels, allowing for prolonged and gradual strategies that have minimal impact on the current processes and operations. Historically, biomass is the oldest primary energy source known by humanity. The benefits of biomass as an energy source have stimulated governments to implement policies for increasing biomass participation in their national energy mix. These policies promote the exploration of new biomasses mainly from agro-industrial activities.

Just in 2019, 9.37% of the primary energy supplied on the planet came from biomass sources (IEA – International Energy Agency, 2021). However, this renewable resource is currently underutilized through modern applications to produce energy at a grand scale. Among the available solid fuel combustion technologies, fixed-bed reactors present higher flexibility to burn different granulometries and lower operational and installation costs (Rayaprolu, 2009; Vakkilainen, 2016). Although fixed-bed systems dominated coal-burning technologies during the first part of the XX century, today it is thought obsolete its implementation in grand scale plants (< 150 MW$_{th}$) for heat generation (Rayaprolu, 2009; Woodruff et al., 2017). However, there are still many operating units around the world, mainly for biomass combustion.

Inside a burner, the combustion process must ensure the best performance which include high combustion efficiency and low emissions of pollutants and particulate matter. In order to achieve this objective, the burner operative parameters – airflow rate, primary-secondary air distribution, and fuel residence time – must be controlled and optimized. Ideally, the best operational conditions are obtained from direct measurements in the burner after exposing the fuel to variations of operational parameters. Nevertheless, there are several technical and economic limitations for such measurements at industrial installations. On the other hand, although computational modelling offers a detailed insight into the fuel's thermochemical conversion

phenomena, the consistency and precision of the results depend on data and assumed hypotheses from experimental measurements (Yin et al., 2008; Khodaei et al., 2015; Dernbecher et al., 2019)

Yet there are several experimental techniques for solid fuel combustion studying; laboratory-scale fixed-bed reactors have attributes that motivate their application in the characterization of different fuels combustion (Lans et al., 2000; Liang et al., 2008; Mitchell et al., 2016). Fixed-bed reactors stand-out for their sample size and the conditions emulated during combustion test, which are close to the observed in industrial installations. Such experimental setups allow direct monitoring of the relevant bed combustion parameters as ignition and burning rates.

Many publications in the literature report observations from experimental combustion tests of biomass in laboratory-scale fixed-bed reactors. These works evaluated the fuel combustion behaviour under different combinations of the operational parameters. The obtained results from these works support the current knowledge about: (i) ignition front propagation; (ii) pollutants emission; and (iii) particulate matter formation. Additionally, the acquired data gave the basis to validate numerical models. However, the abundant scientific evidence generated over the years is yet dispersed in the specialized literature. Such an absence of organization hinders a critical approach to the state-of-the-art to identify gaps for future research.

Even though the lack of review about biomass combustion in fixed-bed burners, some papers synthesized technical and numerical aspects of this phenomenon in thermal installations. Yin et al. (2008) reviewed biomass combustion in industrial fixed-bed reactors. That paper presents aspects of relevant topics such as equipment description, secondary air supply distribution, ash-related depositions formation, and computational models. Nevertheless, the work lacks a more detailed description of the process inside the bed. Recman e Hájek (2009) revised the main characteristics of laboratory-scale fixed-bed reactors from different installations around the world. In that review, the authors only focused on technical characteristics. Khodaei et al. (2015) presented a summary of the different modelling approaches to fixed-bed biomass combustion at a laboratory scale. That work stands out because it defines relevant properties of bed combustion such as consumption rate, ignition front velocity, peak temperature, and reaction zone thickness. Dernbecher et al. (2019) consolidate a review of the numerical methodologies applied in biomass fixed-bed combustion modelling at different scales. The work distinguishes each subprocess involved in biomass combustion and classifies the ap-

proaches adopted to simulate the combustion in the bed zone at different complexity degrees.

This chapter presents a systematic review of the available literature about experimental studies of fixed-bed combustion of biomass in laboratory-scale reactors. Since most of the current fixed-bed burners for biomass combustion operate in a counter-current regime, the present chapter limited the scope of to such a technique. Initially, a search strategy has been employed to collect the pertinent literature from the Scopus and WOS databases. Thereafter, the publications that compose the bibliographic references of this paper have been selected to include only those related to the following topics: biomass combustion, experimental studies in laboratory-scale fixed-bed reactors at counter-current regime, and numerical studies accompanied with experimental validation carried out by the same authors. In this review the knowledge generated from a phenomenological perspective of the flame propagation process in a biomass fixed bed has been summarized and consolidated.

2.2 Solid fuel particles combustion

Many works in the literature aimed to follow in real-time the evolution of fuel particles during their combustion. Various experimental techniques as thermogravimetry (El-Sayed et al., 2019; Barzegar et al., 2020; Rico et al., 2022), optic pyrometry (Saastamoinen et al., 1993; Levendis et al., 2011), and high speed cinematography (Mason et al., 2015; Mock et al., 2016; Panahi et al., 2017; Riaza et al., 2017; Shan et al., 2018) have been used for this purpose. The results obtained demonstrate that every solid fuel particle goes through sequential phases during its combustion regardless of the fuel burned. However, the evolution and duration of each stage will depend on the origin and physicochemical characteristics of the fuel used.

Figure 2.1 illustrates the combustion of a fuel particle inside a high-temperature environment with similar conditions to the observed in industrial furnaces. Initially, the particle internal energy increases at a high rate, and its temperature suddenly increases until it overpasses the boiling point of the moisture in the particle, drying it. The moisture only takes a part of the heat transferred to the fuel particle as latent enthalpy. The excess of internal energy increases the particle's temperature to initiate the expulsion of the volatile material in the fuel. This process is defined as pyrolysis. During pyrolysis, a cloud composed of combustible gases, soot, and tar surrounds the solid matrix and isolates its contact with the oxygen (Levendis et al., 2011; Saastamoinen et al., 1993). The released gases mix with oxygen by diffusion and convection. Due to the gradual temperature increase, the gaseous mixture attains its ignition

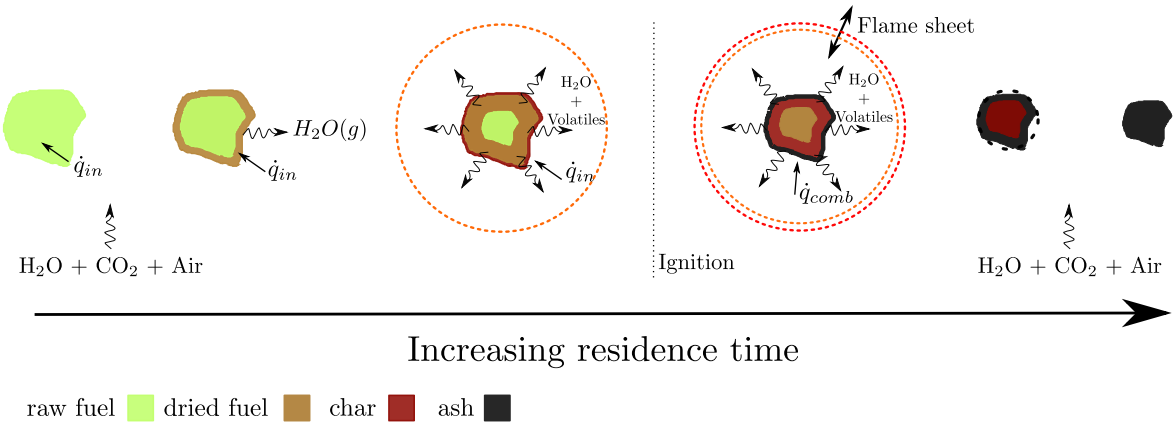

Figure 2.1 – Solid particle combustion process.

point, and a homogeneous flame forms around the particle. Depending on the flow of oxidant present, the flame varies in both size and intensity (Williams, 2018; Turns, 2011). The energy released by the flame promotes the pyrolysis phase in the particle. As each layer in the particle exhaust its volatiles content, a carbonaceous material – named char – and ashes remains in the solid matrix. Since the release of volatiles prevents oxygen access to the carbonaceous matrix, the char is initially prevented from reacting with oxygen. However, carbon dioxide and water vapor produced during combustion reach the char surface, starting its gasification. In some conditions, depending on temperature, oxygen concentration, particle size, and particle motion relative to the volatiles cloud, simultaneous combustion of the char particle and volatiles may occur (Saastamoinen et al., 1993). When all volatile content depletes, the gas cloud size reduces, and eventually, the oxygen comes into contact with the char starting its oxidation. This process lasts until the combustible material contained in the particle is consumed.

As the temperature of the particle increases, a conversion front appears inside it that propagates from the outermost layers (Figure 2.1). This front leads each layer through the drying, pyrolysis, and char oxidation stages. The propagation speed of such a front depends on the particle size and the external conditions, related by the dimensionless parameter Biot's number (Bi). Bi establishes a criterion for solid particle combustion modelling (Yang et al., 2005; Yin et al., 2008; Biswas; Umeki, 2015; Mehrabian et al., 2012). When $Bi < 0.1$ the internal temperature and concentration gradients may be neglected, simplifying the problem by a thermally thin particle approach. On the other hand, if $Bi \geq 0.1$, it is necessary to include the heat diffusion inside the particle. This approach is named thermally thick particle. The particle thermal behaviour influences the time necessary for its complete combustion inside the burner

and offers a basis for selecting the most suitable burning technology.

Due to the nature and composition of biomass particles, their combustion presents considerable differences compared to the behaviour observed in coal or other solid fuels:

- In general, biomass has a higher volatile content (60-80%) than coal (20-30%); consequently, biomass particles combustion presents a more extended pyrolysis stage that starts at lower temperatures than coal particles (Levendis et al., 2011; Zhou et al., 2014; Magdziarz; Wilk, 2013; Saeed et al., 2016; Rico et al., 2022). During this phase, the biomass particle releases the most part of its energy content (Williams et al., 2012). Since biomass expels less amount of soot and tar than coal, the flame of volatiles from a biomass particle is dim (Levendis et al., 2011; Khatami et al., 2012). The high volatile material content in biomass is because of its high molar H/C and O/C ratios. Likewise, the presence of alkali impacts on particle's volatiles production, and its reactivity and the production of tar (Nowakowski et al., 2007; Guo et al., 2020; Jones et al., 2007; Saddawi et al., 2012). These elements participate as catalysts in pyrolysis reactions, reducing the temperatures at which this phase starts and increasing the volatiles release rates (Fahmi et al., 2007).

- Although the elevated amount of oxygen bonded to biomass structure covers part of the one needed for the particle combustion (Koppejan; Loo, 2012), its high-level impacts on the HHV of biomass. The biomass HHV is lower in comparison with other fuels. However, the resulting char after the pyrolysis phase tends to be more reactive than the char obtained during the combustion of coal (Williams et al., 2012). In addition, the alkalis in the biomass also have a catalytic effect on the production of the char left after pyrolysis (Nowakowski et al., 2007; Guo et al., 2020; Saddawi et al., 2012).

- Biomass has high moisture content compared to other solid fuels. This excess moisture delays the pyrolysis and the ignition of the volatiles because of the energy required dry the particle. On the other hand, excess moisture dilutes the content of alkali compounds in the biomass, inhibiting its catalytic effects. Nevertheless, the reduction in alkali content reduces the problems related to deposit formation on the surfaces of the furnace (Mason et al., 2015). During its growth, a plant absorbs K and Na from the soil. These elements are either in the form of ions bound to the organic matrix or as salts precipitated (Jones et al., 2007; Saddawi et al., 2012). Amid combustion, alkali compounds are released in

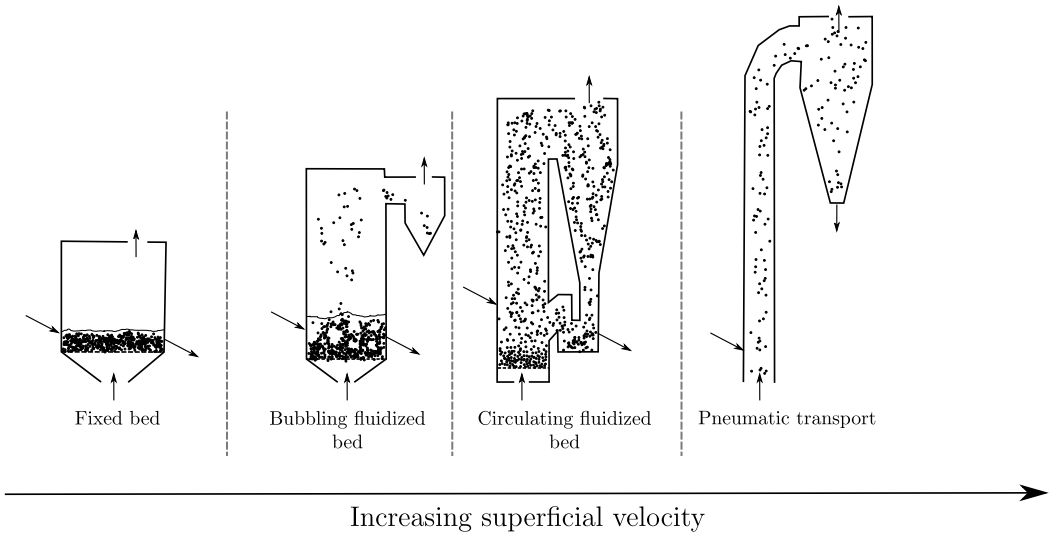

Figure 2.2 – Particles system fluid-dynamic states. Based on Hobbs et al. (1993).

two stages that coincide with the pyrolysis and char combustion phases (Saddawi et al., 2012). These minerals are soluble in water and other solutions such as HCl that partially "wash down" them out from the biomass particle.

In the case of coal, since it has lower volatile content, its combustion may present or not a pyrolysis stage followed by the oxidation-gasification of the char. All this depending on the range of coal (Woodruff et al., 2017; Khatami et al., 2012). However, given coal's low O/C molar ratio, its heating value is higher than biomass. Another important characteristic of coal combustion is its lower reactivity, so its ignition starts at higher temperatures than in biomass. In addition, the volatile flame presents an intense luminosity due to the high formation of soot and tar (Levendis et al., 2011).

2.3 Solid fuel combustion systems

The behaviour of solid fuel and its evolution throughout the combustion sequential phases depend on the particle's geometry and its physicochemical properties. When selecting the more suitable combustion technology for a given solid fuel, the previous properties lead to technical challenges. The contemplated approaches are different for each considered fuel (Hupa et al., 2017).

There are diverse burning techniques for solid fuels that work under a respective fluid-dynamic regime of the fuel particles. Hence, the technologies for solid fuel combustion

are classified into fixed-bed, fluidized bed, and pneumatic transport systems (see the Figure 2.3).

In a fixed-bed reactor, the superficial gas velocity that crosses the bed in an upward direction is insufficient to generate relative movement between solid particles. If the gas velocity surpasses the minimal fluidization velocity, the fuel particles enter a state of partial suspension that enables every particle to move randomly in the bed. Under this condition, the fluidized bed systems operate. Likewise, the fluidization state divides in regimes that depend on the intensity of the gas flow: from bubbling fluidization to circulating fluidization. At high gas flows, exceeding the terminal velocity of all the particles in the bed, the particles reach the state of pneumatic transport (suspension). Each particle is dragged by the gas or remains suspended inside the reactor in this regime.

2.3.1 Fixed-bed combustion technology

Fixed-bed combustion is the oldest and most common conversion method for the energy use of solid fuels (Hobbs et al., 1993; Vakkilainen, 2016). In these systems, particles stacked on the grate form a porous medium through the combustion air circulates, promoting thermochemical reactions in the solid phase. Both the fuel gases released during the pyrolysis and gasification stages and the entrained fine particles burn in suspension through secondary air injection. There are different classifications for fixed-bed burners defined by: (1) the way the fuel particles feed the reactor – underfeed-, overfeed, and spread-stokers; (2) the mechanism used to move the bed inside the burner – traveling-, moving-, vibrating-, and chain-grate; and (3) the direction in which the flame front propagates relative the airflow direction – co-current and counter-current. However, in terms of the physics phenomena presented during the bed combustion, the later classification is usually employed.

The reaction zone is the region inside the bed where fuel particles undergoes the combustion phases. In a counter-current setup, since both flame front and oxidant current flow in oppose directions the reaction zone is narrower than similar situation at co-current setup. Additionally, because of the dissipative convective effect from oxidant flow, radiative heat transfer is the main mechanism responsible for the combustion energy reaching unreacted particles inside the bed (Saastamoinen et al., 2001). Consequently, the flame front propagates slowly along the bed. In contrast, in a co-current setup, as oxidant flow and flame front move in the same direction, radiation and convection contribute together for the energy, released by combustion, to reach a wider region of unreacted particles. Therefore, in a co-current regime, the reac-

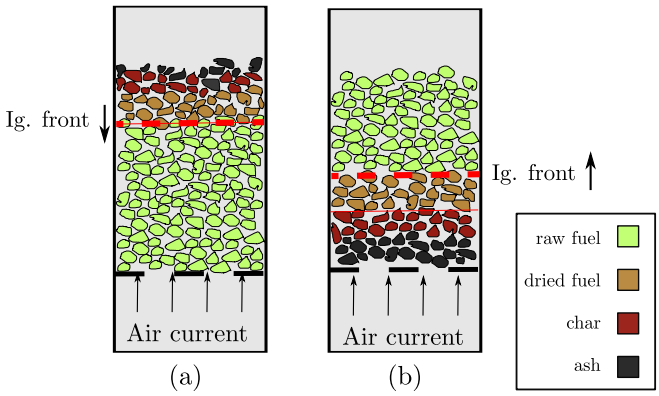

Figure 2.3 – Fixed bed combustion setups in function of the relative direction between the flame front propagation and oxidant flow. (a) Counter-current, (b) Co-current.

tion zone is thicker and propagates faster than in the counter-current mechanism. Despite their disadvantage compared with co-current setup, counter-current mechanism is extensively used in grate-combustion installations. On the other side, co-current technology is more applied in gasification processes.

Fixed-bed reactors have high flexibility to burn a wide variety of fuels whose granulometry and physicochemical characteristics difficult their application with other technologies. For this reason, they are currently widely used in biomass cogeneration plants and municipal solid waste incineration (Rönnbäck et al., 2008; Vakkilainen, 2016) in order to reduce the large volumes of waste generated and, at the same time, producing thermal energy (Niu et al., 2016; Williams et al., 2012; Oman et al., 1999). Also residential and domestic appliances extensively use this technology to burn biomass, as wood logs, for heating purposes (Price-Allison et al., 2019; Maxwell et al., 2020). However, many medium and large-scale fixed-bed combustion units for burning biofuels are too old. These plants were initially derived from projects for coals using (Williams et al., 2012). Therefore, its application with biomass has required adaptations to guarantee a regular performance of the equipment during operation. Although some problems remain during the operation of fixed-bed burners, such as unburned carbon losses, particulate matter emissions, and combustion instabilities, these installations manage to fulfill their primary function. The occurrence of these problems are associated with the lack of knowledge of the most appropriate operating conditions to burn the growing supply of biomass with energy potential (Milijković, 2015).

2.4 Description of laboratory-scale fixed-bed reactors

Establishing operating criteria for the efficient performance of combustion devices requires knowing the transformations that fuel undergoes during its combustion. Ideally, such transformations should be monitored under the burner's operating conditions. However, this task demands technical and economic challenges because of the equipment's structural configuration (Zhou et al., 2005; Porteiro et al., 2010; Mehrabian et al., 2014). There are limitations to accessing industrial burners with measurement instruments, especially in grate combustion systems, where the main combustion reactions occur within the bed (Zhou et al., 2005; Porteiro et al., 2010; Markovic et al., 2014). On the contrary, experimental setups comprise simplistic geometries and total control over operative parameters allowing the continuous monitoring of a fuel sample during its combustion. These setups facilitate to understand the physical basic phenomena behind the macroscopic behaviour around solid fuel combustion.

Among the different experimental techniques to study solid fuels combustion, laboratory-scale fixed-bed reactors stand out because the conditions emulated during their operation are very close to the observed in industrial equipment (Saastamoinen et al., 2000; Gehrmann et al., 2010). These systems are a robust tool for observing bed combustion behaviour in function of controlled variations in operational parameters (Lenis et al., 2013).

Figure 2.4 shows a schematic representation of a laboratory-scale fixed-bed reactor setup as well as the basic systems that composed it. These systems comprise:

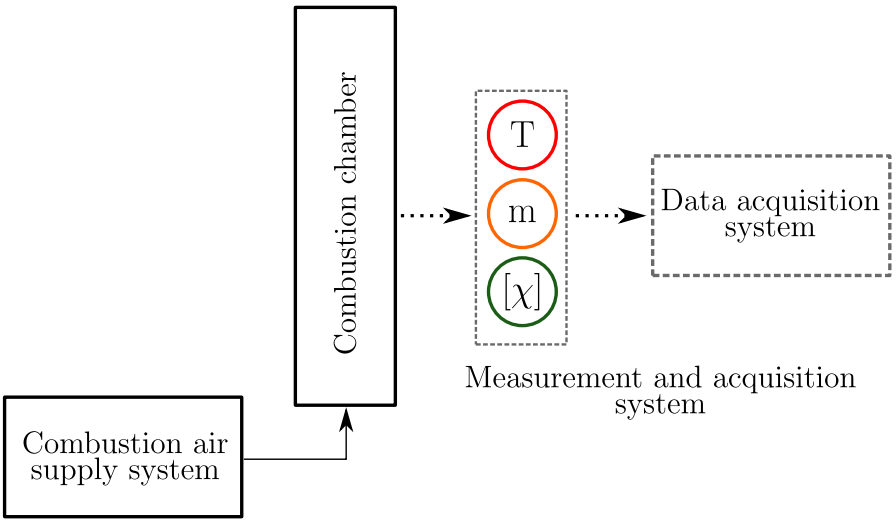

Figure 2.4 – Generic laboratory-scale fixed-bed reactor setup.

Combustion chamber Consists of a circular or rectangular container inside which the sample

is placed. At the chamber's bottom, the sample rest on a grate through the oxidant gas enters. Though initially bricks were used to build the combustion chambers (Eapen et al., 1977), in general, stainless steel is the material employed because of its high temperature tolerance and corrosion strength (Olanders; Gunners, 1994; Kuo et al., 1997; Oman et al., 1999; Wiinikka; Gebart, 2004; Houshfar et al., 2011; Mantananont; Patumsawad, 2016; Khodaei et al., 2017; Trudel et al., 2018). However, normally the combustion chamber is thermally isolated in order to increase the results replicability, thus enabling comparisons with other works. Along combustion chamber, there are orifices to allow measuring and gas sampling. Some works have adapted a section for direct observation of sample combustion, using glass with high thermal resistance (Ryan; Hallett, 2002; Febrero et al., 2015; Rashidian et al., 2016; Polesek-Karczewska et al., 2018). Further, some installations included additional systems on the freeboard to study some processes present in real burners as heat exchangers or heat deflectors (Rashidian et al., 2016).

Combustions air supply system Usually, a fan is the main component of this system. It takes the air from the atmosphere and injects it into the plenum under the grate through a duct. The grate distributes the air entering the combustion chamber through its orifices and supports the fuel bed. Generally, the grate's open area coincides with those employed in industrial furnaces (Castro, 2018). The fan's motor rotatory speed is controlled to obtain the desired air flux. Some setups incorporate air staging and a continuous fuel feeding system. Other systems add electric heaters for studying the effect of air pre-heating over bed combustion.

Measurement and data-acquisition system Because of the large samples in experiments, it is possible to continuously measure local properties inside the bed during its combustion. Among the properties monitored during each experiment there are:

- Thermocouples inserted in the bed through uniformly spaced orifices measure the temperature along the combustion chamber. The combustion chamber region is filled with bed particles. Since particles in the bed surround each inserted thermocouple, the radiative effect on temperature is negligible. However, this simplification does not precisely represents the combustion chamber over the bed – freeboard (Rashidian et al., 2017).

- Different instruments have been used to measure flue gases concentration, both continuously and non-continuously. However, the presence of tar and particles in condensed phases, as well as high temperatures difficult *in situ* measurement. Therefore, most experimental setups integrate a flue gas conditioner system before gases injection into the composition detector instrument. This solution has limited the complete picture of the evolution of the gaseous species from its liberation from fuel particles.
- The variation in sample mass content during its combustion is registered with electronic balances. There are two ways of arranging the weight of the reactor on the scale: suspended or on top.

Despite the simplicity of these setups, researchers have drawn operation criteria over the most important parameters in fixed-bed combustion – airflow rate, fuel feeding rate, and ignition time. Further, the results obtained offer data to validate numerical models. Nevertheless, some discrepancies arise because the samples consist of a batch of particles. In an experimental test, each fuel particle keeps its position relative to the others. On the other hand, some grate types induce movements on the bed to improve the combustion in industrial burners. The absence of movement in the sample is the main error source at the moment for implement the experimental results in burners with those grate types (Saastamoinen et al., 2000; Thunman; Leckner, 2001; Kessel et al., 2004; Gehrmann et al., 2010). Nevertheless, the data obtained are very accurate for traveling grate burners (Stubington; Fenton, 1984; Saastamoinen et al., 2000; 'Aliman; Pasek, 2018).

In addition to the above discrepancies, fuel particles are ideally packed in a laboratory-scale fixed-bed reactor with uniform size distribution. Otherwise, there exists the odd of high porosity spots formation inside the bed that may induce bed channelling (Yang et al., 2003). Channelling is an effect caused by interconnected void spaces in the matrix formed by the packed bed, generates preferential passages for the air or gas flow to traverse. These preferential routes cause the ignition front to propagate much faster along the inner surfaces of the passage than over other surfaces of the bed, causing chaotic burning patterns and great fluctuations and peaks of temperature (Yang et al., 2003; Ryu et al., 2006; Khor et al., 2007; Ryu et al., 2007b).

2.5 Fuel particles fixed-bed combustion

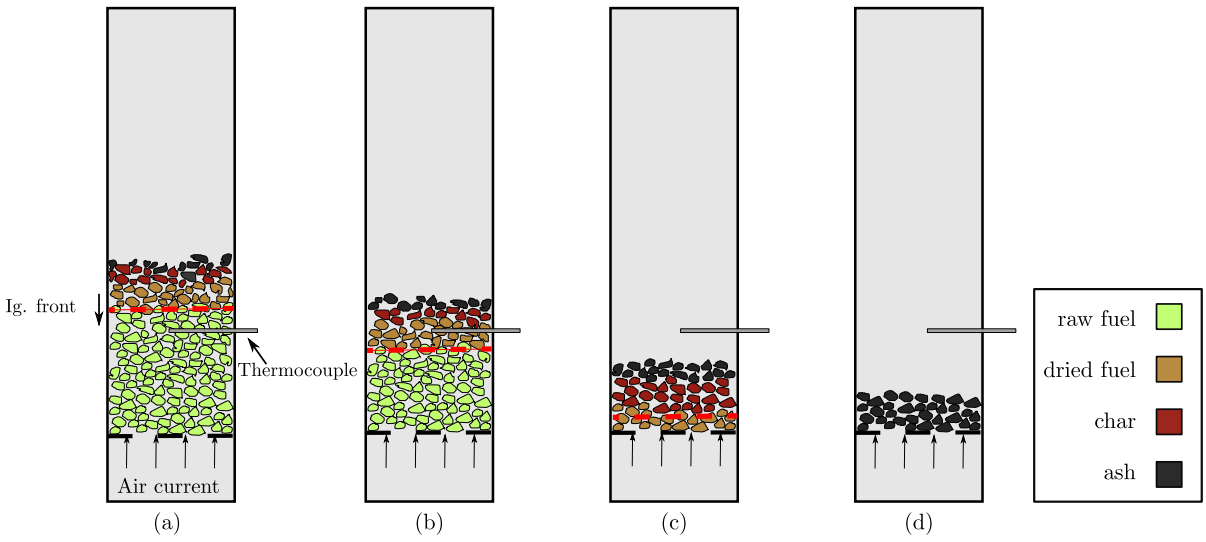

Figure 2.5 – Description of combustion process in a fixed bed.

The Figure 2.5 illustrates the fixed bed combustion process in a laboratory-scale reactor with a batch counter-current configuration. Following ignition on the bed surface, an ignition front forms and propagates downwards across the bed in the opposite direction of the air current. This wave is flat and normal to its path because of the uniform temperature distribution along the cross-section (Eapen et al., 1977). When the ignition front reaches unreacted fuel particles, their temperature soars, causing such particles to go through drying and pyrolysis phases. Pyrolysis gases enter combustion, consuming the oxygen from the air current. Char particles compose the layers left behind the ignition front, and they are exposed to oxygen, combustion gases, and volatiles. Under these environment, combustion and gasification reactions deplete char particles (Varunkumar et al., 2011; Tanui et al., 2018; Mahapatra; Dasappa, 2014), and consequently bed volume progressively shrinks. When the ignition front reaches the region near the grate, almost all volatile content in fuel particles runs out. Therefore, the oxygen in the air is available to react with residual char particles layers and a new reaction front forms. This new front travels co-current with the airflow, leaving ashes in its way.

The ignition front establishes a thermochemical boundary between fresh particles and those under combustion. This region is defined as the reaction zone. Therefore, the ignition front serves as a reaction zone mobile border.

There are three graphs obtained from measurements during the experiment, which

describe the combustion behaviour of a fuel bed sample: history of temperatures, mass variation, and flue gas composition. Despite the stochastic nature of these profiles, they conserve their tendencies independent of the fuel tested (Friberg; Blasiak, 2002; Saastamoinen et al., 2000). Indeed, Lenis et al. (2013) evaluated repeatability of fixed bed combustion experiments in a laboratory-scale burner. By analysis of variance, they determined, with 95% of reliability, that fixed-bed combustion parameters – ignition front propagation velocity, burning rate, and stoichiometric ratio – are repeatable.

At following, we describe each of these three characteristic plots. The Figures 2.6 to 2.8 show the results obtained in eucalyptus residues combustion experiments in the laboratory-scale fixed bed reactor of the University of Campinas (Simões, 2022).

2.5.1 History of bed temperature

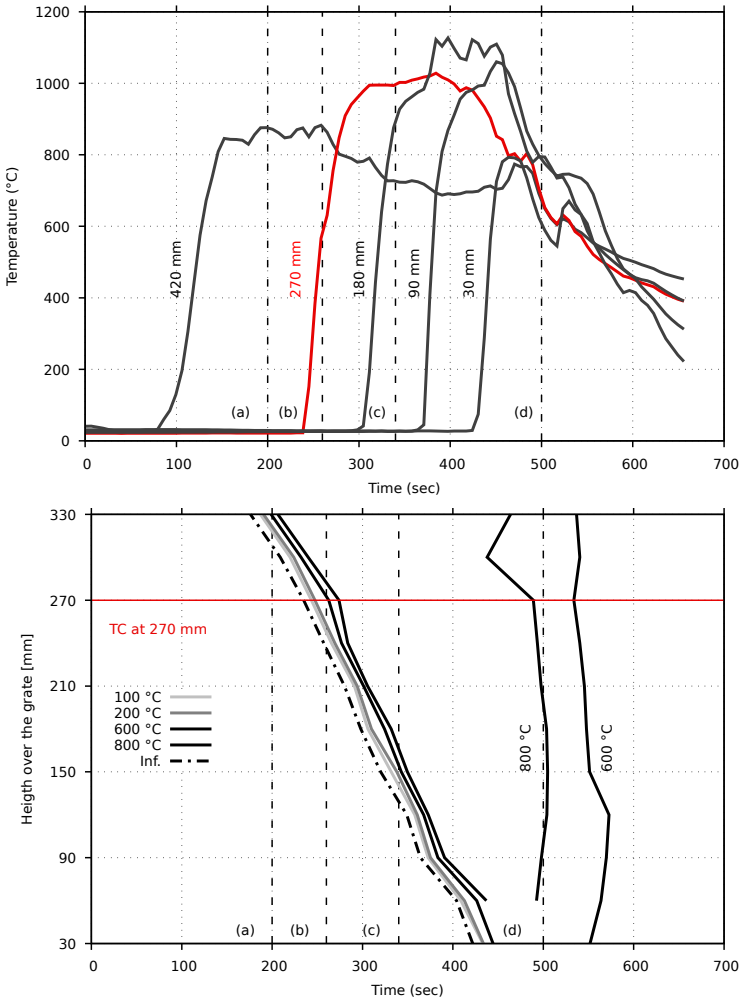

Figure 2.6 – History of bed temperature profile and isothermal field in the function of thermocouple position and time. Adapted from data obtained by Simões (2022).

Usually, the ignition front arises on the fuel bed top and travels downward to the grate. The thermocouples at different heights along the bed register the temperature variation in a fixed location as ignition front moves. This graph is defined as history of bed temperature. Figure 2.6 illustrates the history of bed temperature from sugar cane bagasse experimental data measured in our laboratory (Simões, 2022). Additionally, Figure 2.6 presents the isothermal field in function of time and position. In the graph, four phases, defined as (a), (b), (c), and (d) divide the curves with vertical lines. These indexes coincide with the show in the Figure 2.5 and they point out four states of local combustion temperature at 180 mm over the grate.

When the particles in a bed layer enter the reaction zone, their temperature increases abruptly from room conditions (state (a)). Rapidly, the particles go through drying and pyrolysis phases. The volatiles released from fuel particles reach their flammability point and ignite, boosting the local temperature (state (b)). During this period, particles under combustion reactions surround the thermocouple. The isothermal lines in this phase have similar slope at the height vs. time diagram, which indicates the ignition front propagates through the bed at constant velocity (Figure 2.6). When the bed surface reaches the thermocouple, the local temperature achieves a peak value. At this moment, the thermocouple is exposed to the reactor walls that, along with the oxidant current, dissipates part of energy released from the combustion of char particles and volatiles (Liang et al., 2008; Fatehi; Kaviany, 1994; Olanders; Gunners, 1994; Rogaume et al., 2002; Yang et al., 2003). Because the heat transfer dissipative effect, that also leads to gasification reactions of char particles in contact with CO_2 and steam (Zhou et al., 1995; Kuo et al., 1997; Lans et al., 2000; Varunkumar et al., 2011), local temperature drops. However, the reactions of fuel particles in the middle of the ignition front path make local temperature variation more stable (state (c)). When the ignition front reaches the grate, the thermocouple reads another temperature increase. This effect is the consequence of the high oxygen availability to consume residual char particles left after all volatile material depletes (Kuo et al., 1997; Sun et al., 2016a; Sakthivadivel; Iniyan, 2017). The temperature plummets when combustible material in the bed is too small to keep the high temperature (state (d)). At this moment, the dissipative effects prevail, cooling the reactor. As the height vs time plot points out (Figure 2.6), the isothermal lines in this last phase are almost vertical because the temperature is the same in all positions of the combustion chamber.

From the history of temperature, it is possible to estimate the ignition front propagation velocity as follows:

1. For each thermocouple inserted along the combustion chamber, it is necessary to define any reference temperature (T_{ref}) during the ignition phase (as (b) in Figure 2.6). There are two approaches for selecting T_{ref}: (i) by choosing any temperature inside the ignition phase; and (ii) by estimating the temperature inflection point, which is present at the sharp change in temperature profile from room conditions.

2. To calculate the ratio of the distance between adjacent thermocouples ($H_{i+1} - H_i$) and the time when each thermocouple registers T^{ref} is measured ($t(T^{ref})_{i+1} - t(T_{ref})_i$).

3. Finally, the ignition front velocity is obtained by the average of the ratios estimated in the previous step.

$$v_{ig} = \frac{1}{N_T} \sum_{i=1}^{N_T - 1} \frac{H_{i+1} - H_i}{t(T_{ref})_{i+1} - t(T_{ref})_i} \tag{2.1}$$

The ignition front velocity varies along each bed section (Zhou et al., 1995) because a nonuniform bed porosity, that affects airflow distribution (Lenis et al., 2013). However, by taking the slope of the regression line formed by isothermal points in a position vs. time diagram, as shown in 2.6, it is possible to reduce the deviation in v_{ig}.

An additional approach for v_{ig} estimation uses visuals techniques (Polesek-Karczewska et al., 2018; Kluska et al., 2018). By utilizing a photographic camera, Polesek-Karczewska et al. (2018) took the combustion process pictures of a fixed bed composed of poultry residues. Then, the authors decomposed each photograph pixel color in its RGB constituents with an image processing software. After that, they found the position of the ignition front in the bed because, during combustion, there is an intensity peak related to red color inside the reaction zone. With the position of the ignition front during bed combustion, it was possible to estimate v_{ig}. The velocities obtained by this method and to the ones estimated from thermocouple measurements were convergent (Polesek-Karczewska et al., 2018).

With v_{ig} ignition rate, $\dot{m}''_{ig}$, is determined. Ignition rate defines the mass swept by ignition front during its propagation along the bed, per units of time and surface (Ryu et al., 2006). $\dot{m}''_{ig}$ is directly related to the bed's releasing rate of volatile gases, also called pyrolysis rate (Saastamoinen et al., 2001). Ignition rate is the result of the product between ignition front propagation velocity (v_{ig}) and raw bed bulk density (ρ_b).

$$\dot{m}''_{ig} = \rho_{bulk} v_{ig} \tag{2.2}$$

2.5.2 Bed mass variation

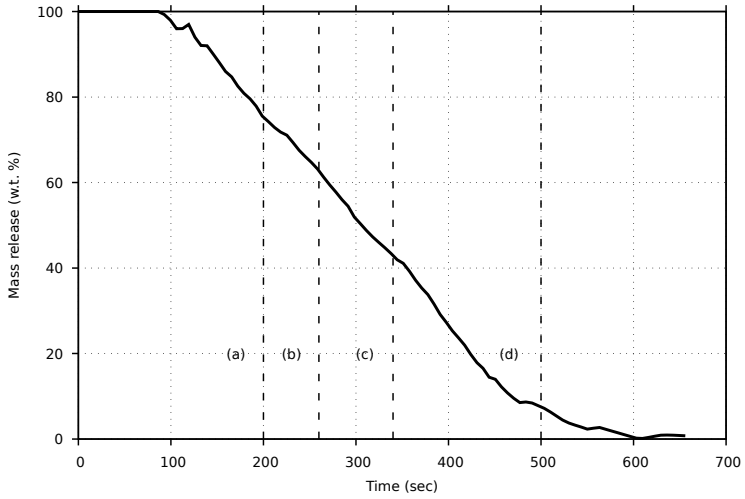

Figure 2.7 – Fuel particles bed mass variation. The letters (a), (b), (c), and (d) represent the moments in Figure 2.5. Adapted from data obtained by Simões (2022).

Figure 2.7 illustrates a typical mass variation profile during a combustion test. After bed ignition, there is a period in which bed mass loss velocity (slope of bed mass variation profile) progressively increments as combustion reactions reach their stability state (Zhou et al., 1995; Porteiro et al., 2012). After transitory effects, the bed mass reduces linearly, evidencing that the reaction zone moves at constant velocity. From this moment, the experimental conditions are established, and the relevant measurements can be taken. Finally, when all combustible material runs out, the slope of the curve slowly decreases as the combustion extinguishes.

The burning rate, $\dot{m}''_{bur}$, is a parameter that represents the mass flux released as a result of fuel combustion-gasification reactions. It measures the instant mass deficit inside the bed. Therefore, $\dot{m}''_{bur}$ includes the loss of mass caused by moisture vaporization, volatile release, char consumption, and fine particles entrainment. The burning rate is estimated by the product of the ratio between the slope of the bed mass variation graph when the reaction zone stably propagates (Figure 2.7), and the cross-section of the fixed bed:

$$\dot{m}''_{bur} = \frac{1}{A_{bed}} \frac{dm}{dt} \tag{2.3}$$

2.5.3 Flue gas composition

The plotted data in 2.8 correspond to measurements of combustion gases composition taken in a fixed position over the bed in our laboratory-scale bed combustion reactor.

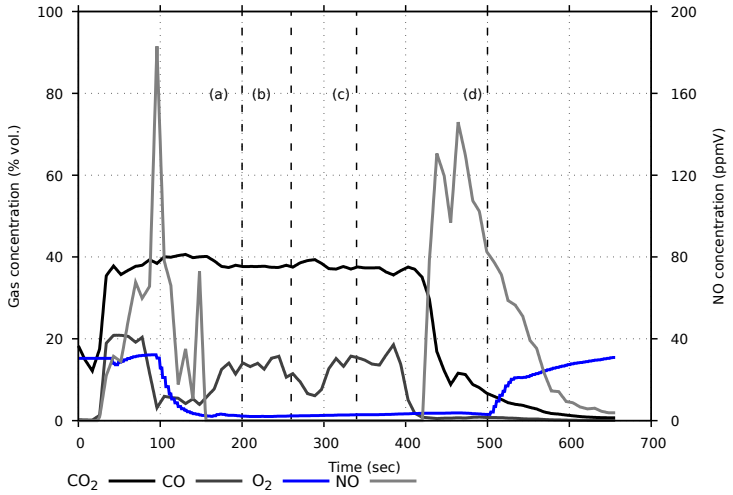

Figure 2.8 – Evolution of flue gases level during experimental tests of a sugarcane bagasse fixed bed. Adapted from data obtained by Simões (2022).

However, the profiles of gaseous species compositions against time at that position have similar tendencies as those obtained in a position inside the bed (Li et al., 2008; Liang et al., 2008; Meng et al., 2018a) After bed ignition or when the ignition front passes through the gas sampling port, the O_2 level plummets to a minimum value. In contrast, CO and CO_2 concentrations increase to reach a peak. These transitory events indicate that the fuel layers enter go through combustion. During the stable stage of bed combustion, CO and CO_2 levels remain relatively uniform until the ignition front reaches the grate. At this moment, CO concentration increases, and CO_2 reduces due to char gasification reactions. When volatile gases released from fuel particles, at the end of ignition front propagation, the O_2 availability for char combustion increases. Therefore, CO level drops to near zero, and CO_2 concentration increases until reaching a maximum as residual combustible material burns. In this paragraph we just are describing the gas emission profile. The reaction zone thickness and its role in the fixed bed combustion process is discussed in next section.

In the case of NO_x level, represented by NO variation in Figure 2.8, its graph has three representative features:

1. Just after bed ignition, NO level spikes. This effect corresponds to the gases evolving from the pyrolysis of the nearest particles to ignition front. Those gases enter a rich ambient where NO_x-precursors – HCN and NH_3 – oxidize to form NO, following the

reactions (Nussbaumer, 1997):

$$NO + NH_2 \rightarrow N_2 + H_2O \tag{2.4}$$

$$NO + CO \rightarrow CO_2 + \frac{1}{2}N_2 \tag{2.5}$$

$$NO + CH_4 \rightarrow CO + 2H_2 + \frac{1}{2}N_2 \tag{2.6}$$

$$NO + H_2 \rightarrow H_2O + \frac{1}{2}N_2 \tag{2.7}$$

$$NO + C \rightarrow CO + \frac{1}{2}N_2 \tag{2.8}$$

When O_2 concentration reduces, due to pyrolysis gases combustion (see textbfFigure 2.8), the rate of NO formation reduced, and its concentration drops.

2. Subsequently, after the sampling orifice immerses inside the reaction zone, NO concentration stabilizes well as HCN, and NH_3 concentrations (Stubenberger et al., 2008; Anca-Couce et al., 2018); and

3. when ignition front arrives at the grate, the reduction of volatile rate releasing leads to an increase in O_2 availability for char oxidation. This events promotes NO production and its concentration reaches a maximum (Anca-Couce et al., 2018), as Figure 2.8 shows. Finally, NO formation stops along with reactive-to-oxygen compounds in char.

The average concentration of a gas specie X, [X], is obtained by calculating the area under its temporal-variation graph (Figure 2.8) over the total experiment time:

$$[X] = \frac{1}{t_{tot}} \int_0^{t_{tot}} [x]dt \tag{2.9}$$

The combustion gas composition allows to recognize which reactions need to be intensified for reducing non-burned fuel gases or the concentration of pollutants (Yang et al., 2003).

The properties defined above – ignition rate, burning rate, and average concentration of specie X – describe reaction zone behaviour during its displacement along the bed and characterize the reactor performance. However, other essential characteristics allow a more profound insight into the fixed bed combustion phenomenon to set reference conditions for evaluating numerical models. Figure 2.9 shows some of these parameters together with the previously discussed. These properties are defined as reaction zone thickness, δ; maximum bed

combustion temperature, T_{max}; particulate matter emission rate; particle size, and bed packing characteristics.

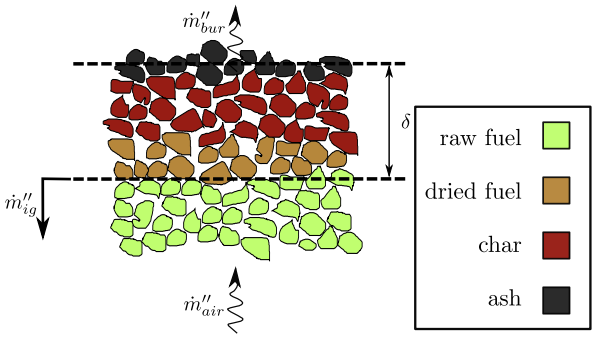

Figure 2.9 – Main parameters in fixed bed combustion.

2.5.3.0.1 Reaction zone thickness

Reaction zone is the region where those reactions that support ignition front propagation along the bed occur (Fatehi; Kaviany, 1994; Shin; Choi, 2000). The ignition front and the surface with non-reacting particles, close to the bed's top, limit the reaction zone (Figure 2.9). The bed stoichiometry is determined inside the reaction zone. This region is a consequence of the difference between ignition and burning rates (Khor et al., 2007; Meng et al., 2018b) which begins since bed ignition. Initially, fuel particles increase their energy due to the ignition source. Depending on factors like the rate of heat exchange with the ignition source, bed packing level, and airflow rate, the energy transferred reaches a certain depth inside the bed. The temperature inside the bed is lower and even lower in the farthest particle layers from the ignition source. Those particles directly exposed to the ignition source increase their temperature and go through drying and pyrolysis stages. In some locations in the middle of the ignition source influence zone, the mixture of combustible gases with air reaches its flammability point, issuing the combustion. The formed char starts to burn as well. Through heat exchange by radiation and conduction, energy is transferred downwards to fresh fuel particles, out of the ignition source influence zone (Thunman; Leckner, 2001). Henceforth, the ignition front forms and propagates, as explained in the above sections. Since the char consumption rate is lower than the ignition rate, those particles left behind the ignition front continue the combustion process, and the reaction zone establishes. The reaction zone thickness depends mainly on oxidant flow rate and combustion reaction kinetics.

A generally accepted assumption in numerical studies of solid fuel combustion establishes that fuel particles reduce their size during the char consumption phase (Dernbecher et al., 2019). On the contrary, during the drying and devolatilization stages, the size of a solid particle remains relatively constant as it loses mass. In the fixed-bed combustion context, the volume occupied by a column of packed particles keeps uniform while the particles lose their volatile material. Since moisture and volatile material content are an essential portion of the particle mass, drying and devolatilization directly affect particle density and bulk density. In contrast, when the carbonaceous part of the solid matrix is exposed to the oxidant, the fuel particle size reduces or shrinks as heterogeneous gasification and combustion reactions progress. Therefore, in a bed of packed fuel particles under combustion, the bed height reduces by the action of char consumption as the reaction zone advances. In this way, it is possible to directly relate the bed top surface displacement velocity with the char consumption rate. Therefore, from the evolution of reaction zone thickness, it is possible to draw strategies to improve airflow distribution across the grate and reduce unburned-particles inefficiencies (Porteiro et al., 2012).

There are challenges associated with measuring δ caused by difficulties in following the bed top surface position without affecting the combustion process. Nevertheless, some authors have successfully estimated this position experimentally (Stubington; Fenton, 1984; Yang et al., 2003; Porteiro et al., 2012). Stubington e Fenton (1984) by employing a graduated rod to directly measure the bed top surface position during fixed-bed combustion experiments of sugar cane residues. Yang et al. (2003) estimated δ from temperature history profile and ignition front velocity. They defined δ as the physical distance in the bed to go from room to peak temperature. Porteiro et al. (2012) used an articulated auxiliary structure to monitor the bed's height during experiments with wood pellet samples.

2.5.3.0.2 Maximum bed combustion temperature

The literature shows the maximum combustion temperatures reported are lower than 1300 °C. However, some biomass combustion effects, which are carried out below this value, have technical and environmental interest. For instance, ashes produced during biomass combustion have low melting temperatures due to the presence of relatively elevated concentration of alkalis compounds and chlorine. These compounds partially melt or even vaporize at relatively low temperatures – around 873 K (Niu et al., 2016)– deposit and accumulate on the

burner and on the boiler tube surfaces. It is possible to control the occurrence of ashes-related problems by previous knowledge of the composition of the inorganic compounds in the fuel and the maximum temperature reached during its combustion (Sommersacher et al., 2012). Additionally, since maximum combustion temperature is associated with the energy released during combustion, it is also used as a parameter to evaluate the burner performance.

2.5.3.0.3 Particulate matter

One disadvantage of using fixed bed burners rests in the high emission of fine particles released from the fuel bed. Particles released during solid fuel combustion are mainly composed by ashes, soot and char. The impacts that particulate matter causes on the integrity of the equipment, health, and the environment is a topic of high discussion in literature (Niu et al., 2016). Similar to the estimation of reaction zone thickness, diverse methodologies are used to quantify the particulate matter emitted during a fixed-bed combustion test. Nevertheless, the potential impact of a fuel bed to release particulate matter is expressed in terms of emission rate. This parameter states the mass of particles emitted in flue gases over either the initial mass of fuel or the net energy liberated along the test (Mantananont; Patumsawad, 2016).

There are few experimental studies aimed at researching particulate emissions formation during biomass combustion in fixed-bed burners. Among these works, the contributions of Wiinikka and collaborators stand out (Wiinikka; Gebart, 2005; Wiinikka; Gebart, 2004; Wiinikka et al., 2006; Wiinikka et al., 2007). They investigated the evolution of the particulate matter released during the combustion of different wood samples in an experimental fixed-bed reactor with staged air supply. They discovered the important role of fuel composition and burner's operational conditions in forming the fine particles mode – with a size smaller than 2.5 μm. Contrary to entrained particles, fine particles are of primary concern because their small size prevents their separation from flue gases by conventional systems (Wiinikka; Gebart, 2004). Their formation depends on the type of fuel used in the bed as also pointed out by Mantananont e Patumsawad (2016) and Sommersacher et al. (2015). On the other hand, reducing char temperature at bed level and increasing the mixture rate in the secondary combustion zone reduced the quantity of particulate matter during wood samples combustion test (Wiinikka; Gebart, 2004). However, in fixed-bed combustion tests of wood carried out by Pettersson et al. (2010) in an experimental reactor without a staged air supply, the particulate matter emissions were unaffected by bed temperature.

2.5.3.0.4 Particle size and bed packing characteristics

The phases a solid particle goes through during its combustion are surface phenomena. A fuel particle's size, shape, and density affect its consumption time. However, packing properties – size distribution, bulk density, and porosity – also influence the combustion of a fixed bed of particles. Since individual and group physical characteristics of the particles are closely related, it is impossible to study in isolation the effect of one parameter without affecting the others (Horttanainen et al., 2002). Additionally, since fuel particles are of nonuniform shape and size, it is necessary to describe the bed particles population by a particle size distribution and an estimator of that distribution (Rhodes, 2008).

The size of a particle depends on its shape. Therefore, a characteristic dimension is defined. For instance, the length depicts slender and cylindrical particles; in the case of flattened particles, a particle diameter (d_p) is the best choice. Regarding d_p, there are different definitions available that include hydraulic diameter, surface diameter, sieve diameter, and surface-volume diameter or Sauter diameter (d_{sv}). Hallett et al. (2013) simulated fixed-bed combustion of commercial hardwood charcoal by using different definitions of particle diameter to describe the bed. Compared with experimental data, the numerical results showed d_{sv} is the most suitable parameter to represent particle diameter in models of processes that include surface chemical reactions.

The following equation serves to calculate Sauter diameter:

$$d_{sv} = \frac{d_v^3}{d_s^2} \tag{2.10}$$

where, d_v is the particle volume diameter – diameter of a sphere with similar volume to the particle –, and d_s is the surface diameter – diameter of a sphere with the same surface area as the particle.

At the bed scale, the nature of the phenomena carried out between solid particles and the gases flowing around are related by porosity (ϕ), which represents the ratio between the volume of the voids in the bed and the total bed volume and is expressed in terms of particle density (ρ_p) and bulk density (ρ_b):

$$\phi = 1 - \frac{\rho_b}{\rho_p} \tag{2.11}$$

In the next section, we discuss the effect of variation in the dominant operational in fixed bed combustion.

2.6 Effects of most influencing operational factors on fixed-bed combustion

2.6.1 Effect of oxidant medium

The mass flow rate of oxidant medium – such as air ($\dot{m}''_a$) – is the most influential parameter over bed combustion. Its variation impacts the stability and propagation of the bed's reaction zone and pollutant compound formation (for instance NO_x). Those effects on bed combustion behaviour depend on the oxidant medium composition and the dynamics of its flow through the bed. For a given oxidant medium, oxygen availability affects the released energy during the combustion of volatile and char particles. The mass flow rate of the oxidant controls such availability. However, this parameter induces a convective effect that dissipates the released energy from combustion. Thus, the reaction front propagation results from the net energy transferred to fuel particles in layers near the reaction zone.

Various studies report the influence of thermodynamic state (temperature and composition) and flow dynamic (superficial velocity) of oxidant medium over fixed bed combustion. Their results show that the reaction zone may present different behaviours depending on the combination of these parameters. The following sections expose most discussed effects of oxidant medium over fixed bed combustion:

1. We present the effect of the mass flow rate of oxidant for a given composition and temperature – air specifically.

2. The effects of oxidant medium temperature are pointed out.

3. The influence of the oxidant medium composition is discussed.

2.6.1.1 Combustion regimes

Regardless of the fuel used in the bed, ignition and burning rates show similar trends with variations in the oxidant medium flow rate. Figure 2.10 illustrates this behaviour. Also, this behaviour has been observed under oxidizing media other than air, such as mixtures of CO_2 with O_2 (Tanui et al., 2018) and mixtures of N_2 with different concentrations of O_2 (Meng et al., 2012). The similarity observed in each fuel allows identifying that the combustion process

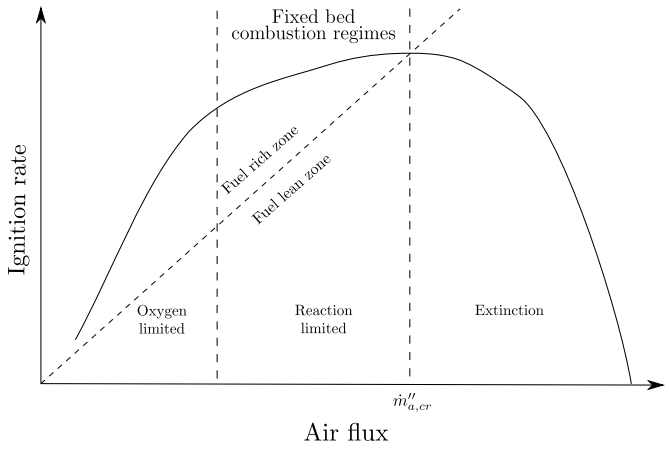

Figure 2.10 – Variation in ignition rate with air flow rate. The dashed line represents stoichiometric conditions. Based in (Shin; Choi, 2000).

takes place in different regimes depending on the magnitude of the oxidant medium flow rate supplied. These regimes also set boundaries inside which the bed combustion occur. Each of these regimes and their main characteristics is discussed below.

2.6.1.1.1 Oxygen-limited regime

The first regime arises for very low air flow rates, but with enough oxygen available to sustain a flammable mixture with volatile gases (Fatehi; Kaviany, 1994; Saastamoinen et al., 2001). At these conditions, the volatiles released stay close the fuel particles and keep a cloud around of them. In those particle bed layers located near the ignition front, the gases ignite. The slow reaction kinetics and the insufficient mixture between pyrolysis gases and oxygen induce a combustion at very fuel-rich conditions (Varunkumar et al., 2013); therefore, great part of the oxygen leaves the bed without reacting (Rönnbäck et al., 2008; Shin; Choi, 2000; Rogaume et al., 2002). The reactions concentrate the released energy near the ignition front, supporting its propagation along the bed, but under transitory conditions. Ahead the ignition front, a layer of unburned particles builds-up (Fatehi; Kaviany, 1994; Stubington; Fenton, 1984), but only a fraction receives energy from the ignition front. These particles continue reacting at very slow rates, mainly at gasification conditions (Rogaume et al., 2002; Rönnbäck et al., 2008; Varunkumar et al., 2013). Since $\dot{m}''_{bur}$ in this particles layer is much lower than v_{ig} (Figure 2.11), the reaction zone thickness continually increases until ignition front reaches the bottom of the bed (Stubington; Fenton, 1984; Razuan et al., 2010). Some authors define this transitory phase as gasification with incomplete consumption of oxygen (Rönnbäck et al., 2008; Varunkumar et al.,

2013; Shin; Choi, 2000; Saastamoinen et al., 2001). Pérez et al. (2012) designate this combustion as a smouldering process since heterogeneous reactions rule and sustain the combustion of the bed.

By increasing the airflow rate, the oxygen availability increases with the reaction and energy release rates (Shin; Choi, 2000; Tao et al., 2010). Additionally, combustion temperature, ignition rate, and burning rate are higher. Hence, reaction zone thickness growth reduces. A new transition to another combustion arises when the reaction rate exceeds the oxygen supply rate. Under these conditions, all oxygen that gets into the reaction zone is completely consumed in the bed. This transition was defined by Rönnbäck et al. (2008) as gasification with complete consumption of oxygen.

In the two transitions described above, the reaction rate increases with oxygen availability.

2.6.1.1.2 Reaction-limited regime

At a higher airflow rate, both oxygen availability within the reaction zone and the convective dissipation rate of the air current increase (Tao et al., 2010). Depending on fuel properties and bed characteristics, two situations might occur:

- In the first case, the oxidation reaction rate reaches a maximum, which exceeds the rate of energy dissipation by the increase in airflow velocity. In this situation, $\dot{m}''_{ig}$ and $\dot{m}''_{bur}$ are approximately similar; therefore, the reaction zone uniformly travels along the bed holding its thickness (Figure 2.11) (Porteiro et al., 2010). This situation is characterized by the absence of the char burning stage after the ignition front reaches the bed bottom (Ryu et al., 2007c; Yang et al., 2004; Čepić; Nakomčić-Smarahdakis, 2017). As its velocity increases, the reaction zone becomes narrower and narrower at higher airflow velocities. However, the increase of $\dot{m}''_{ig}$ and $\dot{m}''_{bur}$ with airflow rate increment is lower than the observed in the limited by oxygen regime. This trend continues until the ignition and burning rates reach their maximum. At this moment, the reaction zone thickness is minimized (Nicholls, 1934). Figure 2.11 shows this behaviour.

- The second situation manifests when the convective dissipation rate attains the reaction rate before the latter get its maximum. In this case, despite $\dot{m}''_{ig}$ and $\dot{m}''_{bur}$ increase with the airflow rate, the reaction zone unstably propagates through the bed. Like the first

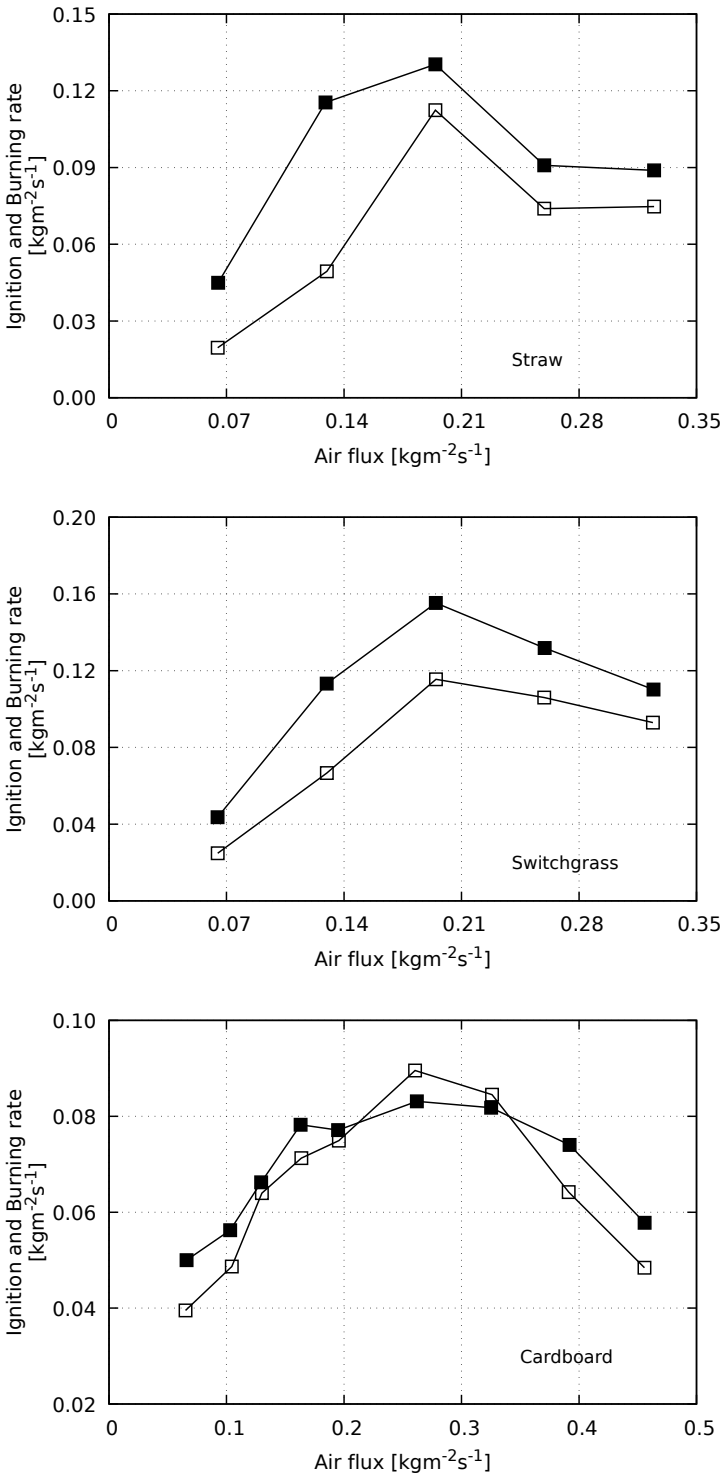

Figure 2.11 – Effect of airflow rate variation over ignition and combuston rate for some biomass: Straw (Khor et al., 2007), switchgrass (Khor et al., 2007), cardboard (Ryu et al., 2007a). □ Burning rate, ■ Ignition rate.

case, increasing the reaction zone propagation rates requires an even higher airflow rate, but as $\dot{m}''_{ig}$ and $\dot{m}''_{bur}$ are different, the reaction zone thickness continues increasing and accumulating material before ignition front reach the grate. Khor et al. (2007) observed this behaviour during the combustion of straw and switchgrass samples in an experimental fixed-bed reactor (Figure 2.11).

In both above situations, fixed bed combustion is limited by both the maximum reaction rate and the convective dissipation rate (Shin; Choi, 2000). Various authors define this state as reaction-limited regime. This regime is present until the ignition and burning rates reach their maximum values. Henceforth, the release of heat and convective dissipation rates are balanced (Yang et al., 2004).

2.6.1.1.3 Extinction regime

The critical air flow rate ($\dot{m}''_{a,cr}$) is a parameter that limits fixed bed combustion efficiency. It is defined as the airflow rate at which ignition and burning rates reach their maximum.

At higher airflow rates than $\dot{m}''_{a,cr}$ the intensity of releasing energy is lower than the convective dissipation rate. Therefore, the aircurrent cools down the char particles and drags the volatile flame away from the bed (Pérez et al., 2012). At particular airflow rates, the temperature of the reaction zone is very low, and the combustion extinguishes. This regime is known as extinction regime (Porteiro et al., 2010; Saastamoinen et al., 2000).

The combustion regimes profile for a fixed bed as Figure 2.11 depends on fuel properties, such as particle geometry, thermal degradation kinetics, and bed characteristics. (Saastamoinen et al., 2001; Horttanainen et al., 2002; Yang et al., 2003; Granada et al., 2012; Pérez et al., 2012). In this graphic it is possible to point out that both the height – defined by the maximum ignition rate – and the graph width are different from one fuel to another.

Figure 2.12 shows the variation of ignition rate with air flow rate for some experimental results found in literature. In order to facilitate the plot reading and regarding the curve shape is roughly the same as $\dot{m}''_{ig}$, the burning rate variation is excluded of Figure 2.12. This figure also presents the change in bed stoichiometry with the air flow rate. The stoichiometric ratio (λ) in Figure 2.12 was estimated by the ratio between stoichiometric ignition rate and the

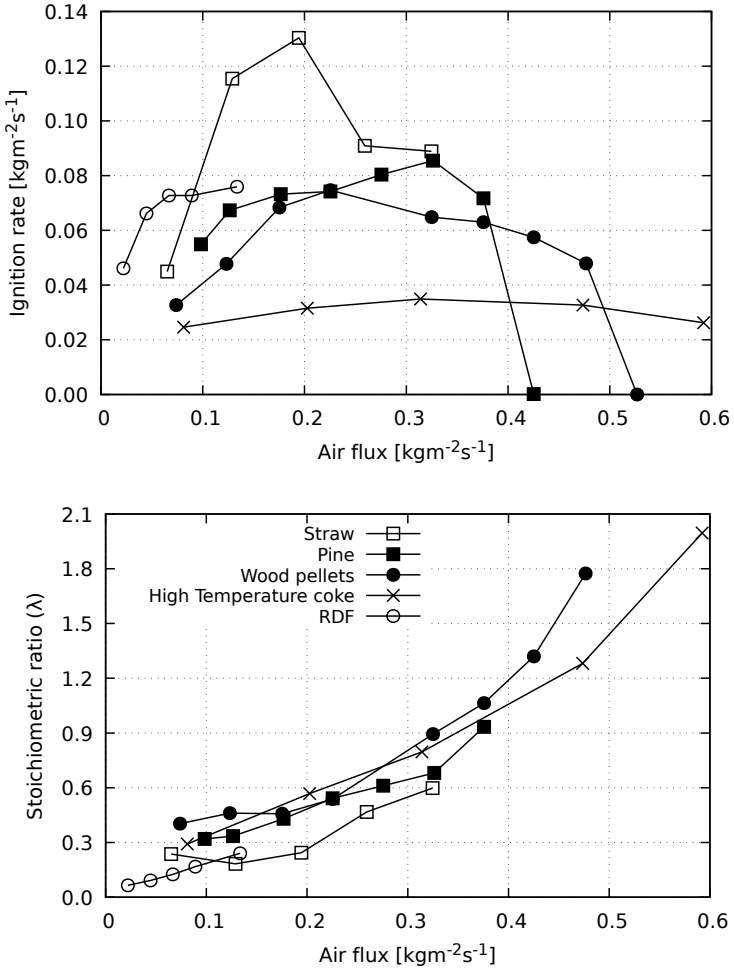

Figure 2.12 – Effect of air flow rate over ignition rate for some fixed bed of fuels: Straw (Khor et al., 2007); pine and wood pellets (Porteiro et al., 2010); high temperature coke (Nicholls, 1934); and RDF (Tripathi; Rao, 2022). The data shown are a version corrected to dry basis from the originally collected from literature.

one experimentally measured:

$$\lambda = \frac{\dot{m}''_{ig,sto}}{\dot{m}''_{ig}} \tag{2.12}$$

where, $\dot{m}''_{ig,sto}$ was calculated by the expression:

$$\dot{m}''_{ig,sto} = \frac{\dot{m}''_{a}}{[A/F]_{sto}} \tag{2.13}$$

As can be seen in Figure 2.12, at low air flow rates, in the region where $\dot{m}''_{ig}$ proportionally increases with air flow rate, the bed stoichiometry keeps almost uniform. However, in the reaction limited regime, even though $\dot{m}''_{ig}$ continues increasing, the bed combustion evolves under increasing lean conditions. Experimental results have shown that reaction zone thickness

controls bed stoichiometry, which is similarly governed by char consumption rate (Porteiro et al., 2010). In the oxygen limited regime, the rise in $\dot{m}''_{ig}$, specially in $\dot{m}''_{bur}$, regulates the bed stoichiometry keeping it roughly uniform at very rich conditions. As the air flow rate increases, the char consumption rate grows affecting the reaction zone thickness which becomes thinner (Regueiro et al., 2016). Since, char inside the reaction zone reduces, more oxygen escapes away from the bed without reacting and consequently the combustion is carried out at super stoichiometric conditions. This effect is stronger in the reaction limited regime and rises quickly in the extinction regime.

Figure 2.12 also shows that the fuels develop their maximum ignition rates at sub-stoichiometric conditions in the reaction-controlled regime. Beyond this point, the bed reaction zone stoichiometry increases rapidly while the bed combustion enters the extinction regime (see Figure 2.13). During the two initial combustion regimes, the level of CO is high. This level progressively drops as the airflow rate injected to the bed increases (Yang et al., 2004; Čepić; Nakomčić-Smarahdakis, 2017; Tao et al., 2011; Razuan et al., 2010; Zhou et al., 2005); in contrast, the average CO_2 concentration in flue gases increases until reach a stable value (Olanders; Gunners, 1994), what indicates most of combustible material in the bed is burned. Finally, before the airflow reaches the extinction point, which stops the fixed bed combustion, the CO_2 levels drop quickly by the reaction zone quenching.

The variation in fixed-bed combustion stoichiometry with airflow rate also affects NO_x formation and destruction rates. Increasing ignition rate with higher airflow rates in the regime-controlled by oxygen increases the amount of volatile material released in the reaction zone. Consequently, the level of NO_x precursor gases emitted from biomass, as NH_3, HCN and NO, rises. (Zhou et al., 2006). Since bed combustion in the two initial regimes is carried out under rich conditions, some combustible gases as CO use NO as oxidant according to equation 2.5 (Figure 2.14). However, further increasing in the airflow rate provokes more O_2 available to produce higher amounts of NO_x, principally NO (Houshfar et al., 2012; Rogaume et al., 2002; Olanders; Gunners, 1994), as shows 2.5.

Observing Figure 2.12 again, it is possible to realize the ignition rate in some fuels like wood pellets and high-temperature coke is stable within the reaction-limited regime and a part of the extinction regime. This behaviour contrasts with the straw ignition rate profile in Figure 2.12. Figure 2.15 plots critical data from the combustion of some fuels in experimentally fixed bed reactors along with their initial content of volatile material and fixed carbon ratio. This

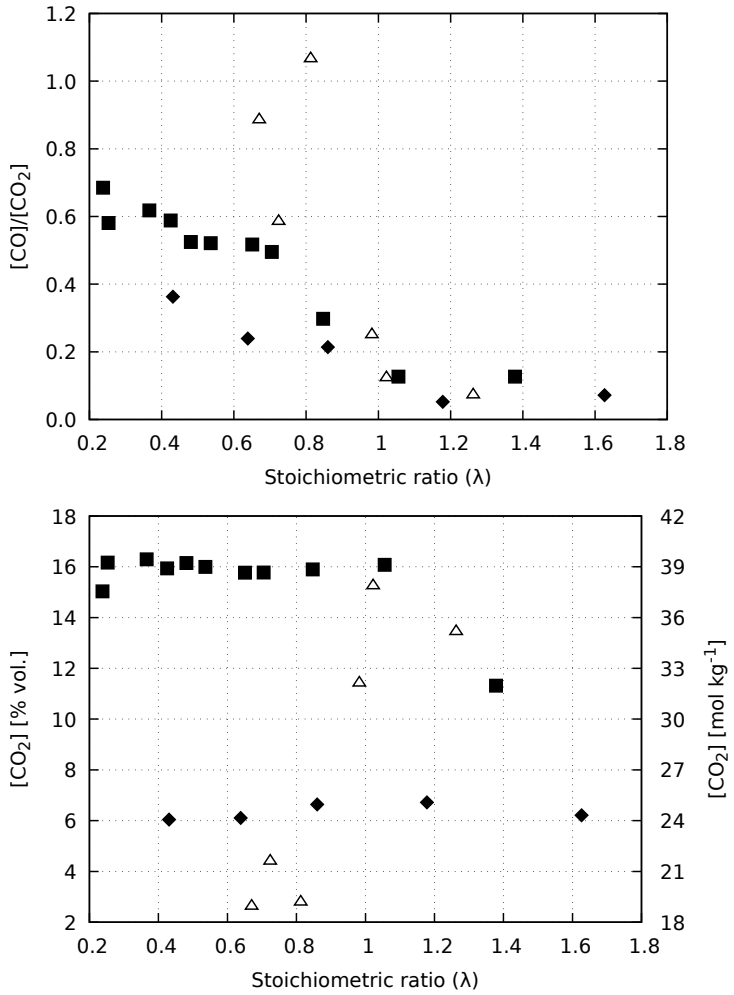

Figure 2.13 – Total CO_2 and CO levels variation with bed stoichiometry: ■ Straw (Zhou et al., 2005), △ Forestry residues (Olanders; Gunners, 1994), ♦ Hazardous wastes (Tao et al., 2010).

figure reveals a positive correlation between fuels' volatile material content and the maximum ignition rate. Further, there is a negative trend between this critical value and the corresponding stoichiometric ratio (critical stoichiometric ratio). On one side, fuels with higher volatile content are more reactive, expelling more energy in shorter times and with lower airflow rates than fuels with more fixed carbon (Granada et al., 2012). However, these fuels show flame instabilities during their combustion after reaching $\dot{m}''_{a,cr}$. In contrast, as the content in fixed carbon increases, it is necessary to augment airflow rates in order to reach the maximum ignition rate (Figure 2.15), and there is high stability between reaction-limited and extinction regimes.

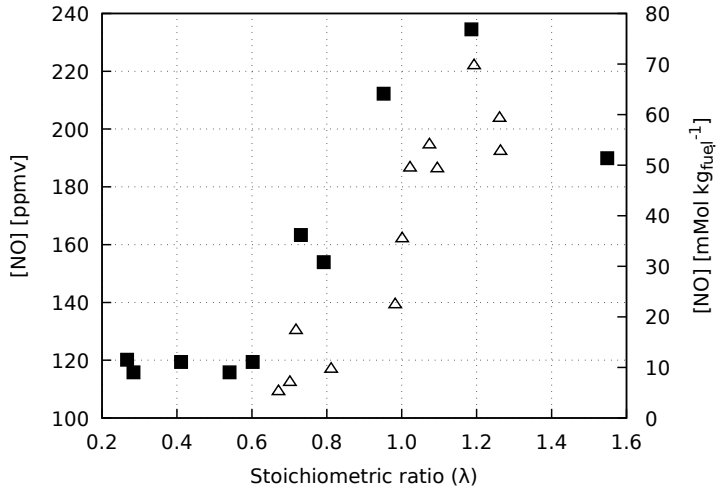

Figure 2.14 – Variation in total NO production with bed stoichiometry: ■ straw (left axis) (Zhou et al., 2006), and △ Forestry residues (right axis) (Olanders; Gunners, 1994).

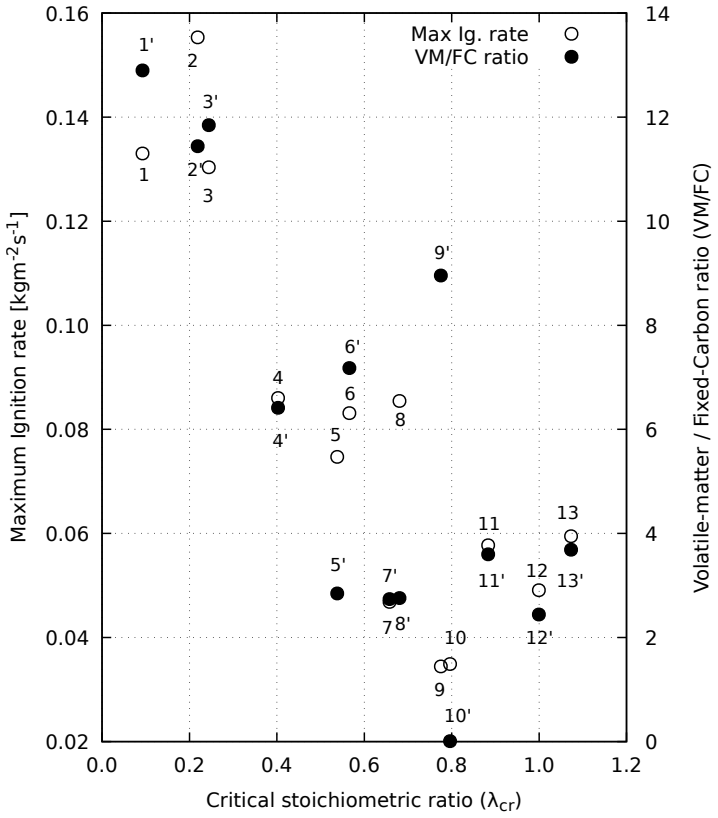

Figure 2.15 – Maximum ignition rate, volatile-fixed carbon content ratio versus critic stoichiometric ratio: 1. Textile residues (Ryu et al., 2007b), 2. Switchgrass (Khor et al., 2007), 3. Straw (Khor et al., 2007), 4. Cane leaves (Stubington; Fenton, 1984), 5. Wood (Porteiro et al., 2010), 6. Cardboard (Ryu et al., 2007b), 7. Almond shells (Porteiro et al., 2010), 8. Pine (Porteiro et al., 2010), 9. RDF (Porteiro et al., 2010), 10. High temperature coke (Nicholls, 1934), 11. Poplar (Porteiro et al., 2010), 12. Olive stone (Porteiro et al., 2010) and 13. Brassica (Porteiro et al., 2010).

In practice, it is desired to work with fuels with a stable reaction rate near its maximum value. The combustion of these fuels offers resilience to fluctuations inherent to boiler operation, for instance, variations in airflow and fuel feed rates (Porteiro et al., 2010). Fuels with very variable $\dot{m}''_{ig}$ and $\dot{m}''_{bur}$, as agricultural residues including straw and pine pellets in Figure 2.12, might need robust control in the primary air supply under the grate. Therefore, co-combustion with solid fuels with higher fixed carbon content is recommended for the proper integration of agricultural residues in thermal energy generation systems. In this way, may be reduced problems associated with flame instabilities.

Nevertheless, burning agricultural residues around $\dot{m}''_{a,cr}$ presents many challenges because of the higher temperatures. This condition increases the risk of presenting issues related to the deposition of inorganic material on burner heat transfer surfaces because of the high concentration of alkalis and chlorine in this type of biomass (Buchmayr et al., 2015; Wiinikka; Gebart, 2004). Additionally, given the increased oxygen availability as a consequence of high airflow rates, when biomass combustion occurs between the regimes controlled by reaction and extinction, the production of NO and the amount of entrained particles out of the bed increase (Royo et al., 2019; Regueiro et al., 2017).

2.6.1.2 Staged air combustion

Some works studied the effect of air flow rate on fixed bed combustion with staged air and continuous fuel feeding (Nussbaumer, 2003). These studies experimentally demonstrated the existence of a combination of primary and secondary air flows that enhances biomass combustion behaviour. The combination maintains substoichiometric conditions in the bed region and supplies enough secondary air to burn the fuel gases that escape from the bed. Fixing the stoichiometric conditions in the bed region and increasing the total airflow rate by supplying more secondary air allow rising the burning rate in the bed (Regueiro et al., 2016). As discussed previously, when a fixed bed burns with only primary air, the air streaming dissipation effect limits ignition and burning rates. On the other side, during bed combustion with staged air, the secondary combustion region has high oxygen availability to burn the excess volatile material and reduce soot production Girgis e Hallett (2010). The heat released during gas combustion offsets the heat dissipated from the bed by primary airflow. The exceeding heat gained in the bed increases ignition and burning rates in the bed's reaction zone. However, as Junejo et al. (2022) found out, the secondary air inlet port position plays an essential role in taking advantage of the

positive effects of staged air. There is a maximum distance between bed level and secondary air inlet beyond which burning rate, ignition front velocity, and bed temperature reduce.

Houshfar and collaborators observed that fuel-N conversion to NO is reduced under substoichiometric conditions in the bed region and over stoichiometric conditions in the secondary air zone. This effect is due to the low stoichiometry in the bed and the high residence time of gases evolving from the bed to the secondary zone, as previously explained (Houshfar et al., 2011; Houshfar et al., 2012; Houshfar et al., 2012b). Further, lower combustion temperatures in the bed within the regime limited by oxygen diminish the formation of inorganic vapors and the amount of entrained char and ash particles (Oman et al., 1999; Royo et al., 2019; Regueiro et al., 2017; Wiinikka; Gebart, 2004). However, for a given fuel or a fuel mixture, in order to optimize operational behaviour of fixed bed combustion it is necessary to investigate more about combustion gases variation in function on primary and secondary air rate combinations.

2.6.1.3 Air preheating temperature

Oxidant medium preheating allows for increasing the released net energy from the fuel. This effect occurs because of the reduction of the sensible energy load of the oxidant medium, which is required to lead the fuel-oxygen mixture to its ignition temperature. Therefore, the reactions are intensified together with $\dot{m}''_{ig}$, $\dot{m}''_{bur}$, and reaction zone temperature during fixed-bed combustion (Zhou et al., 1995; Zhao et al., 2008b).

Studies about preheating of air as the oxidant medium show the existence of two combustion behaviours that depend on the fuel pyrolysis temperature (Blijderveen et al., 2010). In the first case, the air is preheated to temperatures very lower than the fuel pyrolysis temperature. When air enters the bed, it transfers heat to the fuel layers closest to the grate, drying fuel particles. This effect propagates upward along the bed as a drying front. Nevertheless, the air current temperature drops, and its moisture arise due to heat and mass transfer with fuel particles (Kessel et al., 2004). The bed combustion performance may be negatively affected by preheating temperature, fuel moisture content, and bed height. Kessel et al. (2004) observed that when highly moist fuels burn in a moving grate reactor, a part of the moisture transported by air may condensate in intermediate bed layers, delaying ignition front propagation. The negative impact of preheating presents only before the drying and ignition fronts intercept during their propagation. This phenomenon was also reported by Vorotinskienė et al. (2020), who simulated

the drying process during biomass packing bed combustion experiments at different air flow preheating temperatures. After that, there is a sharp increase in ignition rate, and the previously dried fuel layers ignite rapidly. Kessel et al. (2004) defined this effect as total combustion.

The second situation happens when air preheating temperature is close to fuel pyrolysis temperature, around 230 and 250 °C (Blijderveen et al., 2010). As in the first case, a drying front propagates upwards. The air current continues to heat the particles left behind the drying front until they reach pyrolysis temperature. After that, an upward traveling devolatilization front appears. The layers on the grate ignite, and an ignition front propagates upwards. Some authors defined this type of fixed bed combustion as upward combustion (Markovic et al., 2014; Mahmoudi et al., 2015). Among the advantages of upward combustion, we have the following:

1. Drying and pyrolysis phase separation from bed combustion. This effect causes that reaction zone propagation along the bed to be less dependent on the heterogeneity of particles (Markovic et al., 2014; Mahmoudi et al., 2015). The volatile gases that escape from the bed may be burned by adding secondary air.

2. Because of the fuel layers over the reaction zone, there is more resistance to the combustion gases flowing through the bed; therefore, reducing the emission of entrained particles, as reported by Markovic et al. (2014)

.

Despite fixed bed upwards combustion advantages, this type of combustion tends to be uncontrollable when air is used as an oxidant because of high levels of volatile gases produced (Markovic et al., 2014). To avoid this effect, Markovic et al. (2014) recommended using a mixture of air and recirculated flue gases. However, as there are few works in the literature about this phenomenon, it is necessary to carry out more studies to implement this technique in biomass combustion in fixed bed reactors.

2.6.1.4 Oxidant medium composition

There are few works in the literature about the effect of oxidant medium composition over biomass combustion in fixed bed laboratory-scale reactors. Nonetheless, these studies address their aim into two main themes: NO_x reduction (Zhou et al., 2006; Houshfar et al., 2012a) and combustion behaviour. In this section, we discuss the latter topic.

The combustion behaviour of the fuel bed is principally sensitive to oxygen concentration and thermal properties of the gases that compose the oxidant medium. Meng et al. (2012) carried out combustion experiments of poplar sawdust in a fixed bed reactor using different oxygen-nitrogen mixtures as oxidant medium. They observed that both reaction zone temperature and combustion efficiency increase with the oxygen level in the oxidant medium. Tanui et al. (2018) evaluated the effect of atmospheres composed of CO_2 and O_2 mixtures over the propagation of the reaction zone during wood combustion. The measured reaction zone temperatures and the estimated ignition rates were smaller than those observed when air was used as the oxidant medium. This effect is due to the specific heat of inert gases in the oxidant medium (CO_2 has higher C_p than N_2 at temperatures over 600 K). It is necessary to explore this phenomenon deeper, especially with residual biomass because of its highly heterogeneous properties and its relevant role in future as a fuel source for power generation.

2.6.2 Effects of particle size and bed physical properties

A single particle's combustion depends on its characteristics as size, density, shape and physical properties. Conversely, when a group of particles burns together, as in packed bed combustion, the extent of the particles' arrangement in the bed also governs the combustion behaviour. This influence overlaps with a single particle's properties effects. Consequently, difficulties arise in distinguishing the impact of individual and packing properties on the combustion of beds composed of particles with different geometric characteristics.

Despite the limitation caused by the strong relationships between individual particle dimensions and packed bed properties, various authors achieved significant results on the effect of particle geometry variation over fixed bed combustion behaviour. In this section, initially, we present the effects of fuel particle size distribution. Then, the effect of packing parameters as porosity and bulk density are discussed.

2.6.2.1 Bed's particle size distribution effect

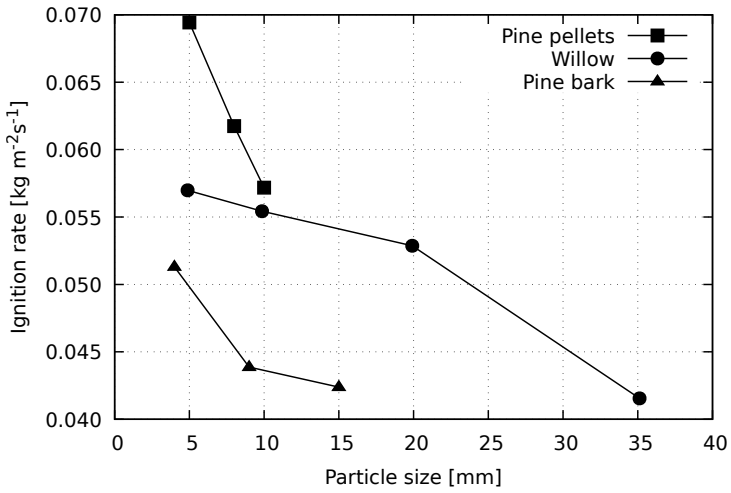

Figure 2.16 – Ignition rate variation with particle size for different biomas samples: Pine pellets (Horttanainen et al., 2002) ($\dot{m}''_a = 0.56\ kg/m^2s$), pine bark (Pérez et al., 2012) ($\dot{m}''_a = 0.15\ kg/m^2s$), and willow (Yang et al., 2005) ($\dot{m}''_a = 0.10\ kg/m^2s$).

.

One of the main effects of fuel particle size increasing over fixed bed combustion behaviour is the reduction of $\dot{m}''_{ig}$ and $\dot{m}''_{bur}$, as Figure 2.16 shows. For a given airflow rate, in beds composed of larger particles, because of the internal temperature gradients, each fresh fuel particle in layers near the reaction zone increases its temperature slower than in beds of small particles; consequently, the particles go through drying and pyrolysis phases at low rates. As bed particles' size augments, the availability of oxygen supplied in the air increases. This reduces the amounts of combustible gases emitted out of bed (Stubington; Fenton, 1984; Li et al., 2008; Tao et al., 2011; Yang et al., 2005), (Figure 2.17), and the levels of entrained bed particles, but this condition promotes the reaction zone temperature reduction (Saastamoinen et al., 2000). Thereby, the ignition rate is reduced.

While the ignition front propagates along the bed, an internal reaction front forms inside each particle. Since $\dot{m}''_{bur}$ is lower than $\dot{m}''_{ig}$, during bed combustion the reaction zone thickness increases along with residual char particles until the end of the process (Sun et al., 2016b). Additionally, because oxygen availability increases with particle size, there are more fuel-N converted to NO (Li et al., 2008). In some cases, when the bed is composed of large particles, the whole fixed bed combustion process is fragmented to isolated combustion of each particle (Stubington; Fenton, 1984).

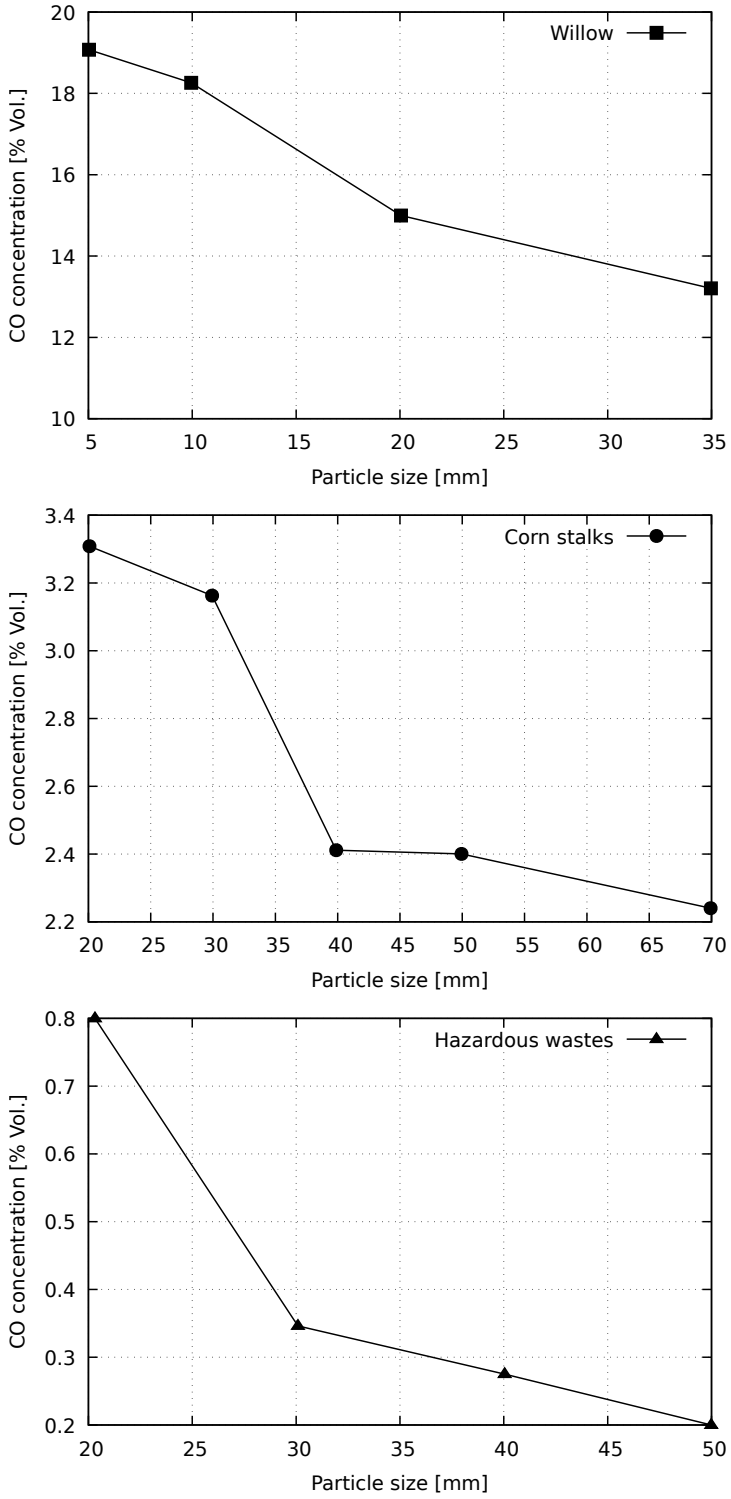

Figure 2.17 – Effect of particle size over CO emission during fixed bed combustion of willow (Yang et al., 2005) ($\dot{m}''_a = 0.10\ kg/m^2s$), corn stalks (Li et al., 2008) ($\dot{m}''_a = 0.053\ kg/m^2s$) and Hazardous wastes (Tao et al., 2011) (right y-axis).

2.6.2.2 Bed's packing properties effect

During fixed bed combustion of uniformly packed particles with the same density (ρ_p), the heat released from the reaction zone attains fresh particles by radiation. In beds with high porosities, the radiated heat may travel long distances, so the reaction zone thickness is wider than the observed in low porosity beds (Varunkumar et al., 2011). Under these conditions, the intensity of the heat received by every particle in close layers reduces. Thus, ignition and burning rates are slower in bulky beds than in more compact beds (Saastamoinen et al., 2000; Saastamoinen et al., 2001; Meng et al., 2017), as Figure 2.18-(a) shows.

Bed porosity also affects the fixed bed combustion range of usable airflow rates – the range of airflow rate values within which combustion takes place – (Figure 2.18-(a)). In beds of small particles, since combustion reactions are more intense because of the higher surface area and lower porosity, during combustion, large amounts of volatiles are released in a short time Figure 2.17. Hence, for a fixed airflow rate value, the reaction zone stoichiometry is lower than the observed in beds of larger particles due to the higher porosity (Horttanainen et al., 2002). This effect reduces the airflow rate required to quench the bed (Figure 2.18-(a)).

A different behaviour takes place during fixed-bed combustion experiments of thin-light particles such as straws, leaves, and grasses (Stubington; Fenton, 1984; Zhou et al., 2005). As Figure 2.18-(b) and (c) show, ignition rate is higher in beds with lower ρ_b (higher porosity) at a fixed airflow rate. Some authors attributed this effect to channelling. Channelling is the consequence of an uneven distribution of particle size that forms interconnected spots of low local porosity (Hallett et al., 2013), principally near reactor walls (Girgis; Hallett, 2010), which serve as shortcuts for air and gas flow. Since the airflow rate is higher at these locations, combustion reactions are more intense, and temperature variation along the bed cross-section is considerable. This increases ignition front speed, that rapidly reaches the grate even when there are particles under ignition process (Yang et al., 2003; Ryu et al., 2006; Khor et al., 2007). However, the burning rate has shown to be unaffected by the abrupt increase in $\dot{m}''_{ig}$, as Khor et al. (2007) pointed out. Beds composed of untreated fuel particles exhibit the above effects. For instance, Zhou et al. (2005) (Figure 2.18-(c)), Milijković (2015) and (Khor et al., 2007) (don't show) used long straw fibers in their experiments. The wide heterogeneity among bed particles established a non-uniform packing, which enables channelling appearing (Khor et al., 2007).

Tanui et al. (2020) observed a similar effect of bed porosity over ignition front in beds composed of fine wood particles (wood and sawdust). These results are interesting since

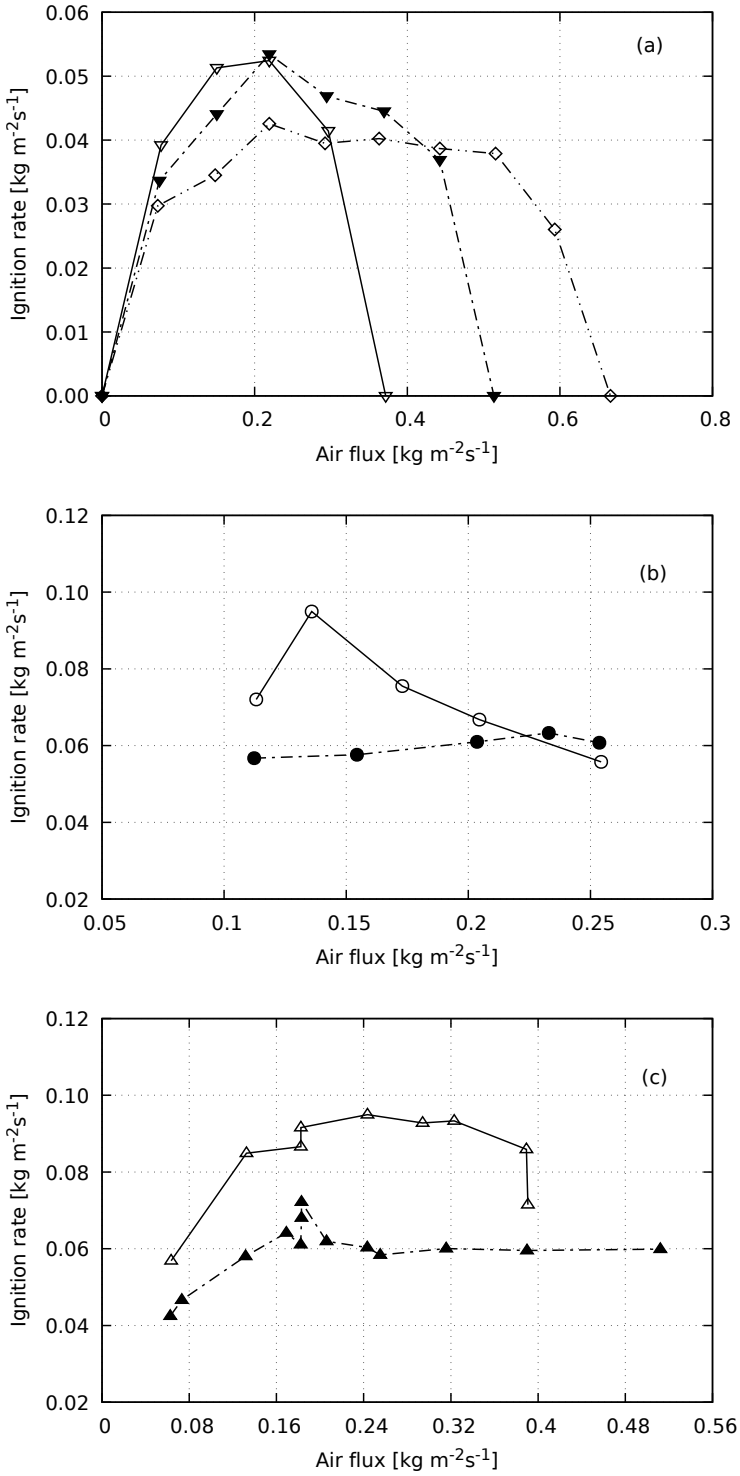

Figure 2.18 – Ignition rate variation with bulk density during fixed bed combustion of different biomass. (a) pine bark: ▽ 2–6 mm ($\rho_b = 189.6 kg/m^3$), ▼ 6–9 mm ($\rho_b = 171.5 kg/m^3$), ◊ 9-12 mm ($\rho_b = 165.7 kg/m^3$) (Pérez et al., 2012); (b) ○ Loose cane fibers ($\rho_b = 46.4 kg/m^3$), • Dense cane fibers ($\rho_b = 77.4 kg/m^3$) (Stubington; Fenton, 1984); (c) ▲ Cut straw ($\rho_b = 85.0 kg/m^3$), △ Whole straw ($\rho_b = 50.0 kg/m^3$) (Zhou et al., 2005).

the beds studied by Tanui and collaborators possessed higher bulk densities values – between 390 - 597 kg/m^3, than the biomasses discussed in the above paragraph (see Figure 2.18). Such increase on $\dot{m}''_{ig}$ reached a maximum value for a defined critical bed porosity. Beyond this critical bed porosity, the ignition rate dropped (Tanui et al., 2020) because of the increment in the convective dissipative effect. Nevertheless, it would be necessary to undertake more studies to have a complete insight into the bed porosity effect on fixed-bed performance.

Figure 2.18-(b) and (c) also show that although $\dot{m}''_{ig}$ drops by increasing ρ_b, the combustion is more stable in comparison with untreated biomass particles. When the biomass particle size is homogenized by size reduction processing, the odds for channelling formation drop. Also, a uniform particle size allows a better distribution of the airflow in the bed. In this way, the ignition front stably propagates along the bed. However, the type of solid fuels, as shown in Figure 2.18-(b) and (c) is characterized by possessing low density (ρ_p). Therefore, the positive effects of particle size reduction are considerable above some limit size of the particle. Below this dimension, losses by particle entrainment may be significant enough to affect fixed bed combustion efficiency.

In general, as Figure 2.18 points out, bed porosity (or bulk density) may affect fixed bed combustion in two ways, each that depending on the configuration and density of fuel particles: (1) thin-light and (2) coarse particles. The first group includes most agricultural residues like straws, leaves, and grasses; the latter consists of particles with either cubic, cylindrical or semi-spherical shapes such as coal and wood particles. In beds composed of particles of both groups, it is possible to obtain a stable and resilient combustion (Horttanainen et al., 2002; Zhao et al., 2008a). From a bed properties perspective, to harness the high availability and energetic potential of agricultural residues, co-combustion with biomass of the second group may represent a promising option.

2.6.3 Moisture content effect

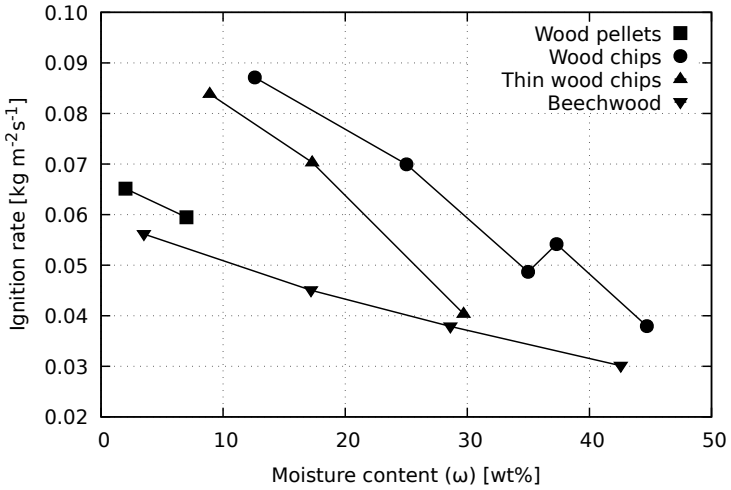

Figure 2.19 – Fuel particle moisture level influence over ignition rate for different biomass: Wood chips (Kolb et al., 2008) ($\dot{m}'_{air} = 0.15kg/m^2s$), Wood pellets (Porteiro et al., 2010), Thin wood chips (Saastamoinen et al., 2001) ($\dot{m}'_{air} = 0.11kg/m^2s$), and Beechwood chips(Mätzing et al., 2012) ($\dot{m}'_{air} = 0.014kg/m^2s$).

As Figures 2.19 and 2.20 show, for a fixed airflow rate, the increasing of fuel moisture level slows down both $\dot{m}''_{ig}$ and $\dot{m}''_{bur}$, what enlarges the combustion time. This effect is because the energy required to dry each particle in bed reaction zone increases, what reduces its heating rate to reach ignition temperature (Yang et al., 2003; Yang et al., 2004).

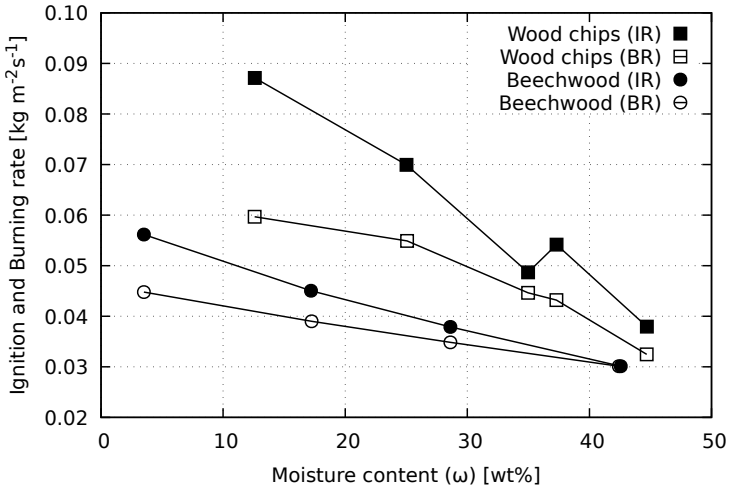

Figure 2.20 – Comparison between ignition and burning rate with moisture level: Wood chips ($\dot{m}'_{air} = 0.15kg/m^2s$) (Kolb et al., 2008) and Beechwood ($\dot{m}'_{air} = 0.014kg/m^2s$) (Mätzing et al., 2012).

Moisture level effect is more intense in $\dot{m}''_{ig}$ than $\dot{m}''_{bur}$, as Figure 2.20 shows. This

effect on both parameters suggest that the reaction zone thickness become narrower as fuel particles moisture level increases. Hence moisture increase promotes char consumption rate during the reaction zone stable propagation phase (Zhao et al., 2008b; Kolb et al., 2008; Yang et al., 2003). This effect is explained as follows: The particle heating rate influences its pyrolysis rate. Pyrolysis rate affects both $\dot{m}''_{ig}$ and $\dot{m}''_{bur}$; however the prior is more sensitive to this parameter variation (Saastamoinen et al., 2000; Yang et al., 2003). Then, at a fixed airflow rate, lower amounts of volatile gases increase oxygen availability to consume the char formed during the reaction zone stable propagation phase, as Figure 2.21 illustrates. As the moisture level of fuel particles increases, the reaction zone becomes thinner, and there is less residual char in the last fixed bed combustion phase (Yang et al., 2003). Consequently, the reaction zone propagates along the bed more stably, and the amount of non-burned gases evolving out of the bed reduces.

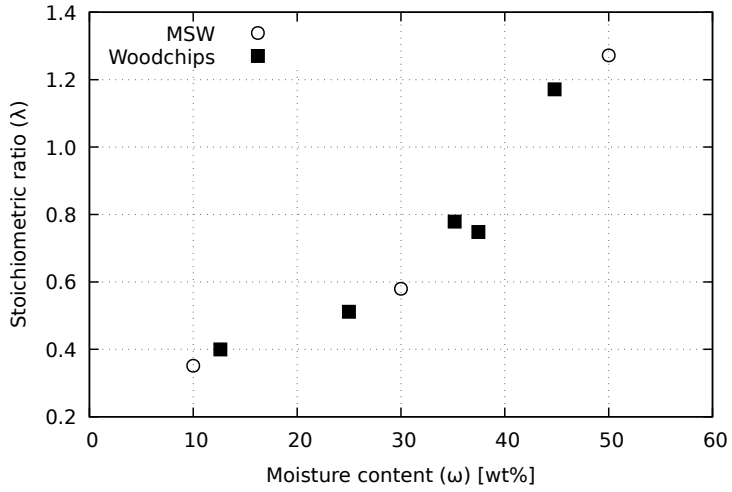

Figure 2.21 – Influence of moisture level on bed combustion stoichiometry: Municipal solid wastes (Yang et al., 2004), Wood chips (Kolb et al., 2008).

The reduction in pyrolysis rate with moisture level also affects the combustion regime region of the bed. As reported both in experimental (Porteiro et al., 2010) and numerical results (Yang et al., 2004), the critic air flow rate for drier fuels is higher than the observed in wetter fuels. Also, the usable air flow rate range is reduced as ω increases. Then a wetter fuel reaches the extinction at lower $\dot{m}'_{air}$.

Fuel moisture level reduces the reaction zone temperature because it is required a higher thermal load to evaporate the water and heat the steam released (Kolb et al., 2008). Nevertheless, as Figure 2.22 illustrates, the maximum combustion temperature (T_{max})is unaltered at low moisture levels, when ω variation is under 20% – 30% (Porteiro et al., 2010; Yang et

al., 2003; Saastamoinen et al., 2000). At a higher moisture level, the maximum combustion temperature in reaction zone drops until the humidity reach certain level. From that level, T_{max} remains unaltered up to a humidity level so high that combustion is unsustainable. Since char and volatiles react in a more narrow region, those combustion reactions counterbalance the heat consumed by the moisture, maintaining combustion temperature roughly constant.

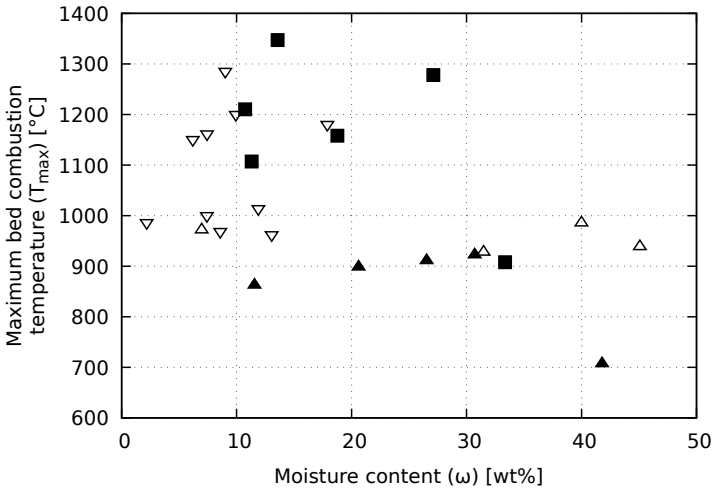

Figure 2.22 – Max bed combustion temperature variation with fuel moisture level: ■ wood-chips (Saastamoinen et al., 2000), ▽ wood pellets (Porteiro et al., 2010), △ municipal solid wastes (Yang et al., 2003), and ▲ corn straw (Zhao et al., 2008b).

Fuel moisture limits the combustion performance because it increases water's latent and sensible energy demands and extends the total combustion time. However, the experimental evidence demonstrates that fixed bed combustion of highly wet fuels happens under stable conditions of temperature and reaction front propagation. This effect can be beneficial for combusting highly humid fuel such as agricultural residues and MSW in fixed-bed combustion reactors. Such types of fuels are continuously produced over the year at low costs. Their availability may offset any moisture-related energy loss to produce cheap and environmentally friendly thermal energy.

3 MATERIALS AND METHODS

3.1 Experimental set-up

Figure 3.1 is a schematic representation of the laboratory-scale fixed-bed reactor employed in this work.

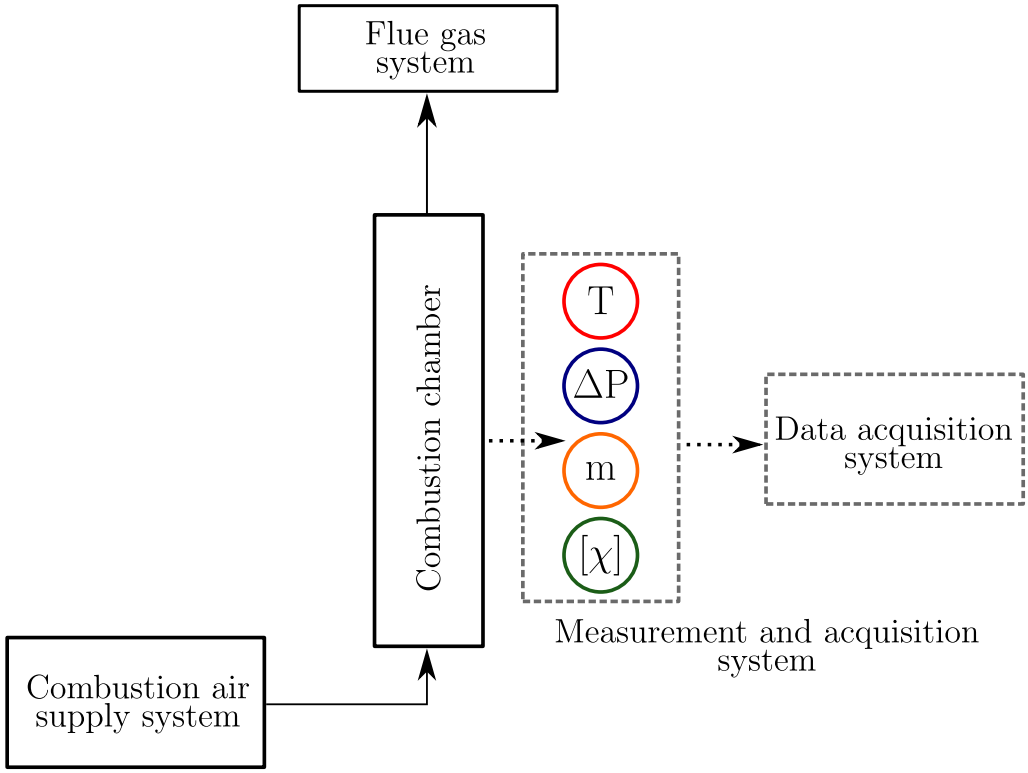

Figure 3.1 – Simplified schematic representation of experimental setup.

The experimental set-up consists of subsystems, each with an essential function for the equipment operation: Combustion chamber, combustion air supply system, measurement and acquisition system, and flue gas systems. Each subsystem is described below.

3.1.1 Combustion chamber

Figure 3.2 shows the main features of the experimental reactor. The combustion chamber and plenum compose the reactor. The former is a stainless steel cylindrical vessel, a thickness of 5 mm, an external diameter of 229 mm, and a height of 1300 mm. Along the body of the combustion chamber there are 22 drilled holes with a diameter of 1/8 inches each for local temperature and pressure measurement (T_1 to T_{18} and P_1 to P_4 in Figure 3.2). Near the reactor's

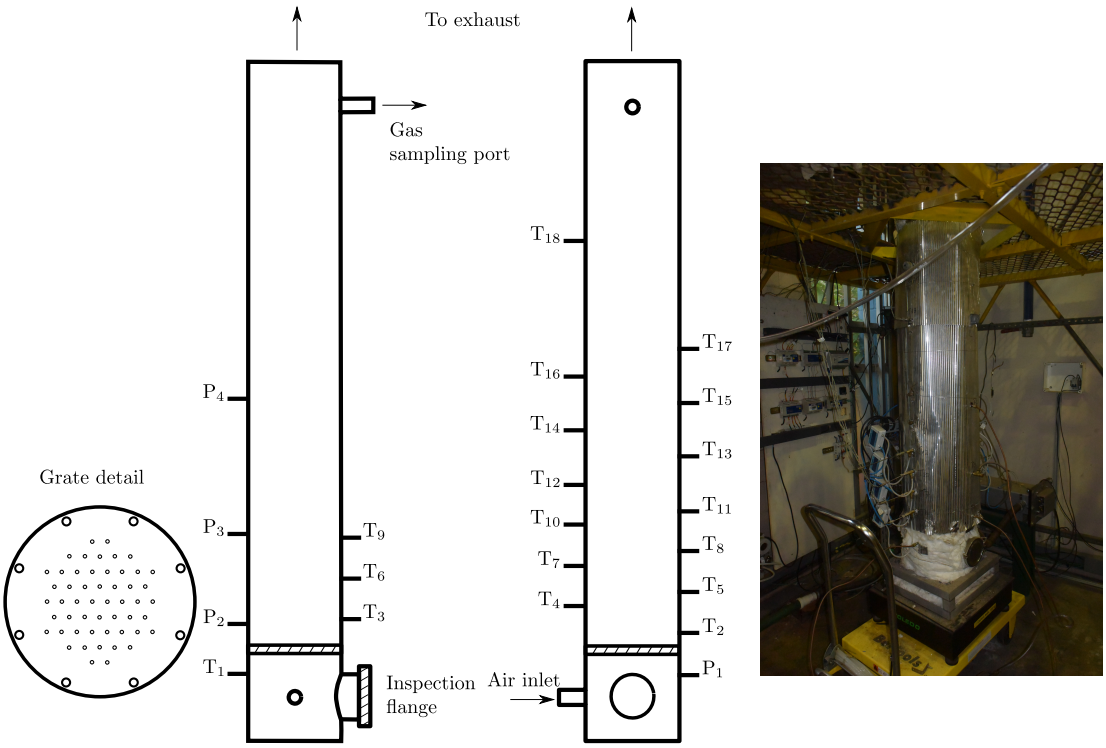

Figure 3.2 – Combustion chamber.

exit there is an additional 3/4 inches (BSP) sampling port for collecting combustion gases. A ceramic insulation blanket with a thickness of 50.8 mm wraps around the combustion chamber to reduce heat losses and achieve a uniform temperature distribution during the experiments. The entire system is mounted capacity of 300 kg. This platform allows for the approximation of the combustion chamber to the flue gas system during the experiments and refilling the reactor. For detailed design aspects of the combustion chambers, refer to the thesis by Castro (2018).

3.1.2 Combustion air supply system

Oxidant air flow is the more influential factor in fixed-bed combustion performance. In this work, atmospheric air was used under room conditions. Figure 3.3 presents a simplified scheme of the air supply system with its main components. A centrifugal fan forces the air to flow along the supply system. The fan, manufactured by *Delta*, is driven by a motor with a power rating of 4 Hp and a maximum rotation speed of 3465 RPM at 60 Hz frequency. A frequency inverter connected to the fan's motor controls the air flowing in the feeding duct. The estimation of airflow value involved measuring the pressure drop accross an orifice plate and appliying correlation from the ASME MFC-14M-2003 standard [1].

[1] Measurement of fluid flow using small bore precision orifice meters

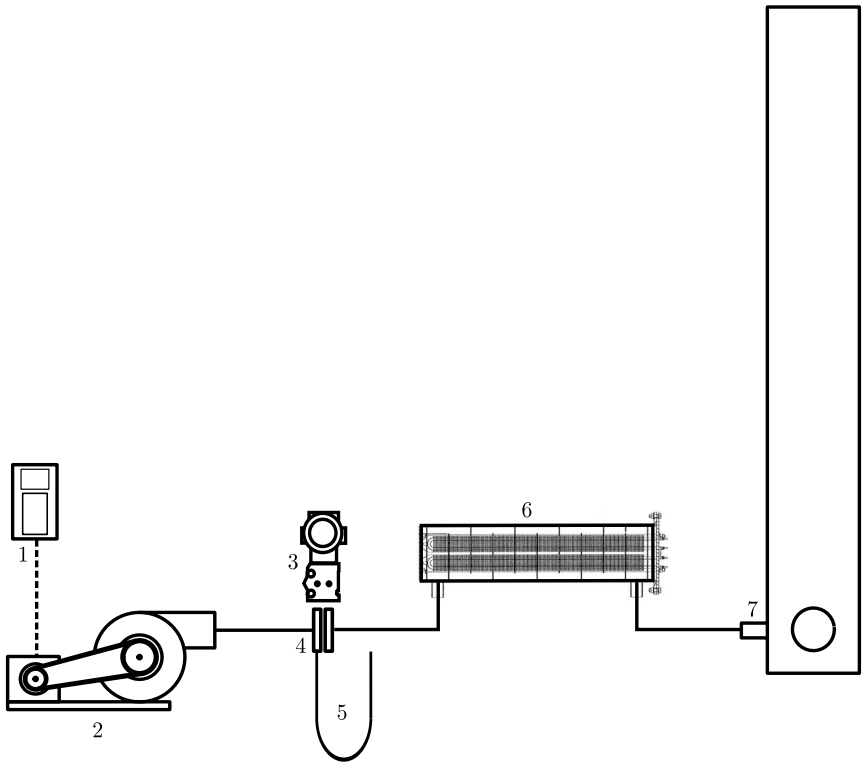

Figure 3.3 – Air feeding system: 1, Frequency inverter; 2, Fan; 3, Differential pressure transmitter; 4, Perforated plate; 5 water column manometer; 6, air preheater; and 7, reactor plenum.

The air supply system includes a preheating stage to regulate air temperature. The electric heater can increase the temperature up to 150 °C. In this work, the air injected into the combustion chamber was kept at room condition.

Finally, after the preheating stage, the oxidant flow enters the plenum, where the grate evenly distributes it before entering to the combustion chamber. Both the combustion chamber, the plenum and the grate are stainless steel.

3.1.3 Data acquisition system

3.1.3.1 Local bed temperature and pressure

Table 3.1 presents the position and function of each sampling port along the reactor body. K-type thermocouples were inserted into the corresponding sampling ports for temperature measurement in both bed and flame regions, ensuring that their tips reached the center of the reactor. The maximum temperature that thermocouples materials can withstand is 1150 °C; therefore, temperature values were watched during each experiment. If the temperature reached the thermocouple maximum permissible limit, the instrument would be removed from the sam-

Table 3.1 – Description of the ports along the combustion chamber.

Port	Position from the grate [mm]	Function
T1	-40	T
T2	30	T, ΔP
T3	60	T, ΔP
T4	90	T, ΔP
T5	120	T, ΔP
T6	150	T, ΔP
T7	180	T, ΔP
T8	210	T, ΔP
T9	240	T, ΔP
T10	270	T, ΔP
T11	300	T, ΔP
T12	360	T, ΔP
T13	420	T, ΔP
T14-T15	480 and 540	Blocked
T16	600	$[\chi]$
T17	660	Blocked
T18	900	T
P1	-50	Blocked
P2	50	Blocked
P3	250	ΔP
P4	550	Blocked
GS	1200	Blocked

T: Temperature
ΔP: Pressure drop
$[\chi]$: Flue gas composition

pling port. However, as shown in the results and discussion chapter, it was unnecessary to take this action.

An innovative aspect of this work is the real-time bed pressure drop monitoring during the tests. For this purpose, along the reactor, from the T_2 port, 11 pressure transmitters *Rüken* were installed with measurement span from 0 to 300 Pa. Figure 3.4 provides detailed information on the insertion of a thermocouple with a pressure transmitter in the same sampling port. The installation of the pressure gauges was such that the readings did not overpass the instrument capacity.

3.1.3.2 Mass loss measurements

The combustion chamber, the plenum, and the measurement instrumentation attached to the reactor body rest upon an electronic weight scale *Toledo* with 100 kg capacity and

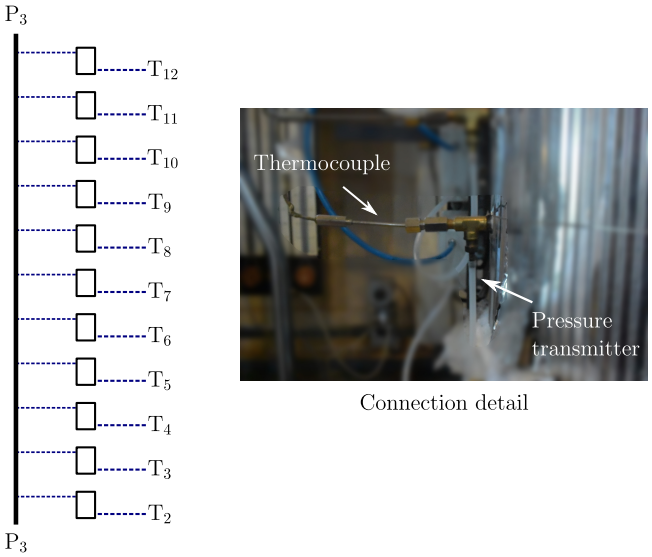

Figure 3.4 – Simplified diagram of pressure transmitter position along the combustion chamber and connecting detail of the instruments.

Figure 3.5 – Electronic weight scale.

0.01 kg resolution (see Fig 3.5). The weight scale allows for the transmission of the measurements via analogue signal for storage in a computer.

3.1.3.3 Flue gas composition

A suction probe inserted in port T_{16} continuously sampled a gas fraction and transported it to the FT-IR *Antaris IGS* manufactured by *Thermo Scientific*. This equipment measured the volumetric composition of CO_2, CO, C_2H_2, C_2H_4, CH_4, NO, and NH_3 in the combustion gases. A paramagnetic oxygen sensor *Parbox 1200* measures O_2 level. The following

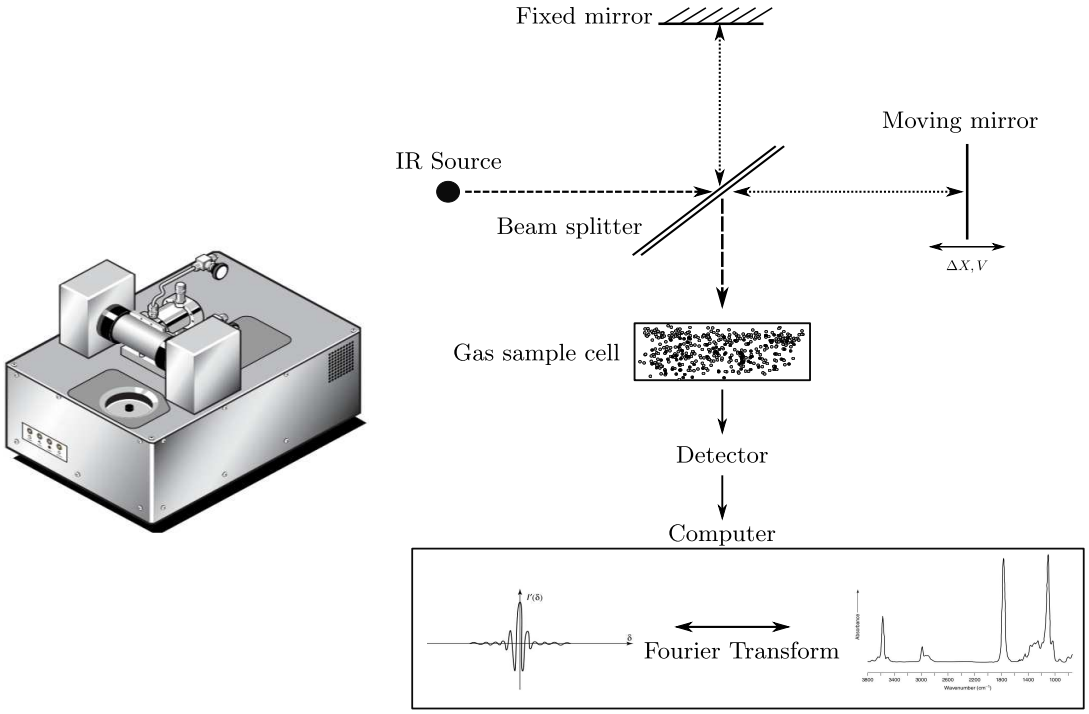

Figure 3.6 – FT-IR operation.

paragraphs briefly describe each instrument and the gas sample preparation process along the suction probe.

3.1.3.3.1 FT-IR

FT-IR (*Fourier Transform Infrared Spectroscopy*) is a technique that exposes a gas mixture to an infrared radiation source. Gas molecules selectively absorb incident radiation at specific frequencies, causing them to become excited into higher energy vibrational states (Stuart, 2004). A detector collects the signal containing information about the spectral fraction absorbed by the gas. This information is then processed and sent to a computer for analysis. Furthermore, the FT-IR continually measures the flue gas composition at a temperature up to 170 °C.

Figure 3.6 depicts FT-IR basic operation principle. The core of the instrument is an interferometer that quantifies the wavelength of the infrared radiation irradiating the gas sample. Initially, the IR radiation from the source reaches a beam splitter. This device disperses the beam in two rays, directing them towards two mirrors perpendicularly positioned. One mirror remains fixed, while the other is mobile. The distance between the beam splitter and the mobile mirror is controlled. The mirrors reflect the rays, causing them to return to the beam splitter,

Model	Parox 1200
Power supply	12 - 28 [V] (DC)
Output signal	0 - 20 [mA]
Measuring range	0-25 [vol.%]
Max. gas flow	300 [ml/min]
Operation Temp.	60 [°C]

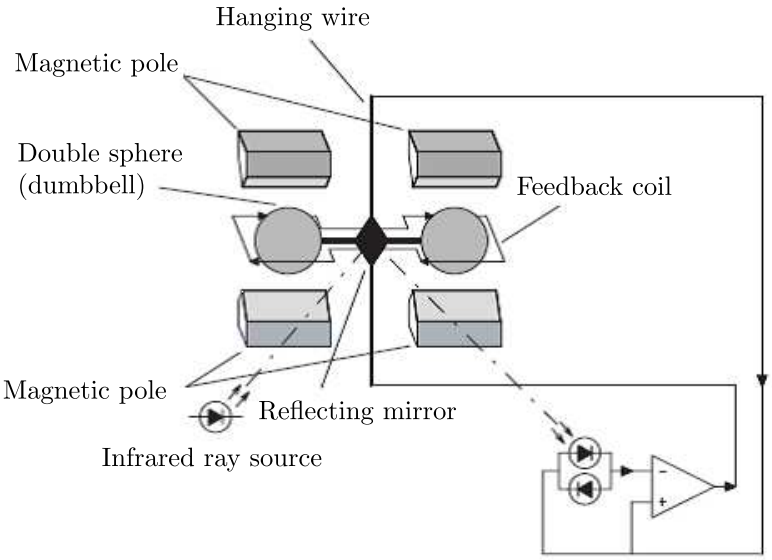

Figure 3.7 – Paramagnetic O_2 sensor operation data.

where they overlap. The resulting radiation is then directed toward the gas chamber, where it interacts with the sample. A detector captures the signal and generates an interferogram, which plots radiation intensity versus the distance between the mobile mirror and the beam splitter. Through Fourier Transformation, an algorithm converts the signal initially expressed in the distance domain to the electromagnetic wave frequency domain. In this way, the sample absorption spectre is obtained. To ensure the absence of compounds that might interfere with the sample signal, an additional test is carried out with the gas chamber empty.

Each substance has a characteristic absorption spectrum whose amplitude is proportional to the compound's concentration in the gas sample. Therefore, it was necessary to calibrate the equipment for each gas molecule that would be quantified during the experiments. A detailed description of the calibration process can be found in the work by Simões (2022).

3.1.3.3.2 Paramagnetic oxygen sensor

Homonuclear diatomic molecules such as O_2 are invisible to infrared radiation. Therefore, in order to obtain the unreacted oxygen level in flue gases, an oxygen sensor was employed. This instrument seizes O_2 paramagnetic characteristics to reads oxygen concentration in a gas current.

Inside the sensor, there are two glass spheres containing N_2. The spheres are connected through a metallic structure, which is suspended upon an axis that allows the system rotation (see Figure 3.7). The metal structure is exposed to a strong permanent magnetic field. An electric current flowing through the structure generates a force that compensates for the rotation induced by the magnetic field. When gas goes through the sensor, the magnetic field attracts the oxygen molecules deviating the gas flow direction and rotating the metallic structure. The electric current required to keep the structure static is proportional to the O_2 level in the gas. Figure 3.7 shows the main operative specifications of the device.

3.1.3.3.3 Gas sampling probe

The state in which the flue gas is collected from the combustion chamber are very different from the conditions required for the FT-IR and oxygen sensor. On one side, the FT-IR operates at temperatures below 150 °C, while the oxygen sensor works at 60 °C. Conversely, both instruments are susceptible to solid and liquid particles, which can damage their internal components. In the probe inlet, the gas temperature can overpass 900 °C and contain a significative presence of particles. Therefore, the gas sample must undergo a conditioning process for its subsequent compositional analysis. Figure 3.8 shows the conditioning gas line designed and implemented in the experimental set-up.

The gas sampling probe consists of a 6 mm diameter stainless steel line. The first duct's section is insulated by a ceramic blanket with the same characteristics as the one that wraps the combustion chamber. This section conducts the gases to a high-temperature condenser, which retains most of the condensable matter in the gases. In the condenser, the gas flows along a serpentine coil submerged in a Therminol oil bath kept at 150 °C by two controlled 500 W electric resistances. A stirrer maintains uniform the oil temperature. At the exit of the condenser, an auxiliary expansion condenser allows for catching the residual tar parti-

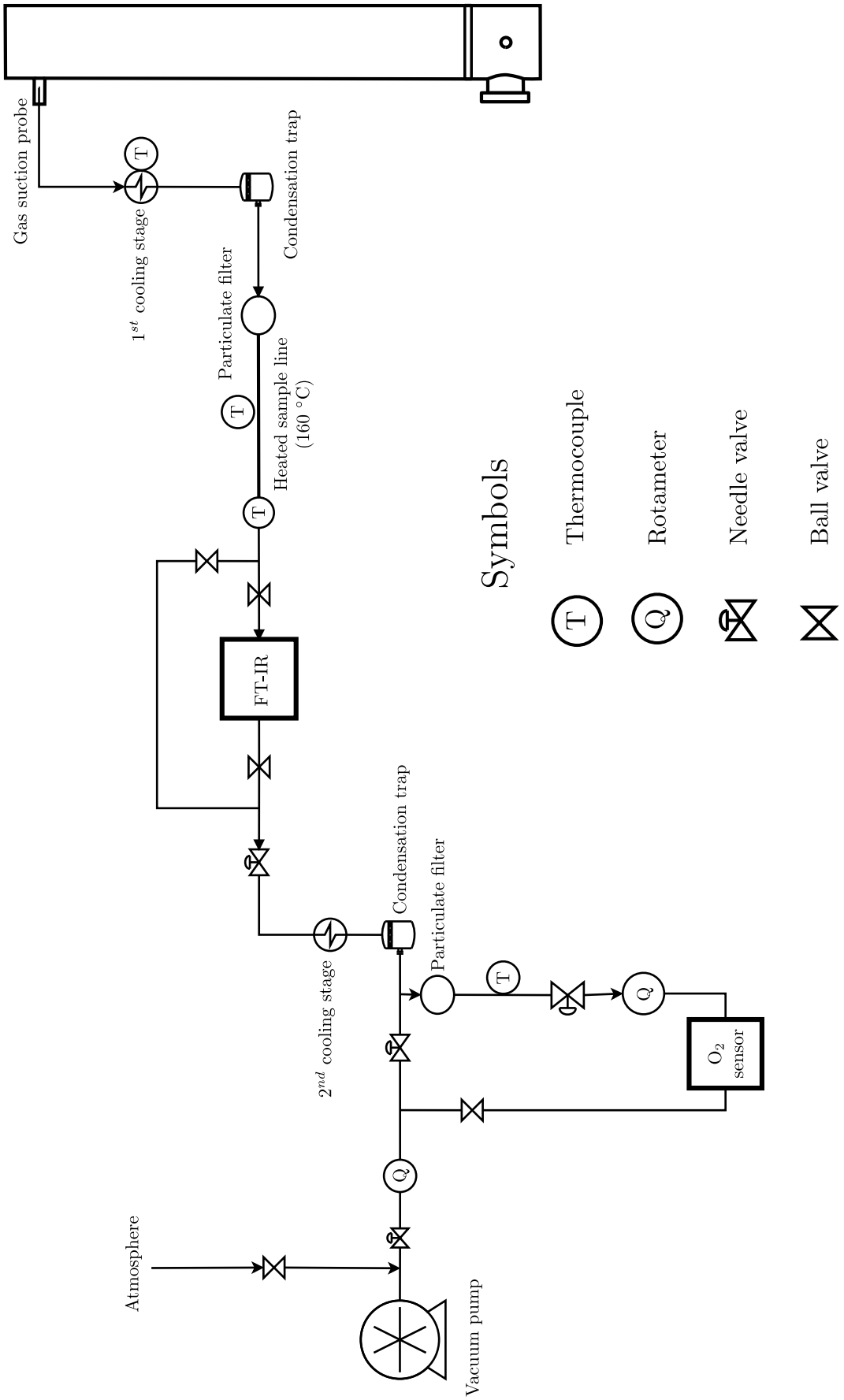

Figure 3.8 – Diagram of suction and conditioning gas sampling system.

cles that escape from the oil condenser. Furthermore, a particle filter removes most particles entrained with the gases.

Between the exit of the particles filter and the FT-IR entrance, the treated gases temperature keeps at 160 °C by a 2 m heated hose. After the FIT-IR, a second water-filled cooler vessel similar to the one used as a condenser in the first section reduces the gas temperature to room conditions. After the water cooler, some gas is led to the oxygen sensor.

A vacuum pump installed at the end of the gas sample path forces the gases to flow along the conditioning line. The pump's suction flow is around 100 L/min.

During the preliminary experimental set-up tests and throughout the experimental campaign, it was observed that the O_2 level readings by the oxygen sensor exhibited deviations from 2 to 5 % vol. in conditions where oxygen was absent. The vacuum pump induced this error in the measures. Despite this error, the O_2 level measurements can be used for qualitative analysis.

A gas element travelling along the sampling line takes around 6.5 seconds from the probe inlet to the oxygen sensor (Simões, 2022).

3.1.3.4 Acquisition system

All the measurement signals from the instruments are sent to field loggers *Novus*. This system receives and transforms digital analogue inputs before sending them to a computer. In the case of FT-IR, this device has an embedded computational terminal that stores the gas compositional signals for later processing. Therefore, all the collected parameters during the experiments were synchronized.

3.1.4 Flue gas system

The combustion gases are addressed through a duct from the combustion chamber exit to the chimney by a 4 Hp centrifugal fan *ventbras* (see Figure 3.9). A frequency inverter regulates the electric fan motor rotation.

3.1.5 Bottom and fly ash composition

Besides the real-time variation of fixed-bed combustion properties, the composition of bottom and fly ashes was analysed. So, after the experiment finishes and the reactor cools

Figure 3.9 – Flue gas extraction system.

down, particles left on the grate are collected and packed in individual labelled zipper bags. In the case of fly ashes, the filter papers inside the particulate filter are removed for their analysis.

The collected ash samples composition was measured through scanning electronic microscopy (SEM) in the *Laboratório de Recursos Analíticos e de Calibração* (LRAC) at *UNICAMP*. The bottom ashes were spread on carbon adhesive tape. On the other hand, since fly ash particles were embedded in the filter paper, it was necessary to cut the latter into 5 x 5 mm pieces for their fixing on the carbon tape. The prepared samples were inserted inside the equipment.

3.2 Sugarcane residues

The sugarcane bagasse and leaves feedstock were collected from the sugar mill *Usina La Pedra*, in Serrana – São Paulo, where leaves and stalks are separated during harvesting by mechanical techniques. Before the leaves integrate the cogeneration process with the bagasse, they pass through rinse and grinding stages to wash out every dirt and reduce particle size. The sugarcane leaves and the bagasse samples were directly taken from the conveyor just before their injection inside the boiler.

The samples contained higher amounts of water – around 50 % in mass. The biomasses were spread on the ground to dry the moisture excess and avoid feedstock decomposition. This process took three weeks until the moisture level equilibrated with the room

Table 3.2 – Physical-chemical properties of sugarcane residues (Jacome, 2018).

Analysis type	Bagasse	Leaves
Proximate analysis [wt.[a]%]		
Moisture[b]	3.27 ± 0.19	6.14 ± 0.17
Ash	2.57 ± 0.22	4.35 ± 0.24
Volatile material	85.1 ± 0.62	81.01 ± 0.70
Fixed carbon	12.42 ± 0.66	14.64 ± 0.74
HHV [kJ/kg][a]	18229 ± 163	18732 ± 76
Elemental analysis [wt.[a]%]		
C	40.55 ± 1.67	40.03 ± 0.64
H	6.55 ± 0.12	6.61 ± 0.02
N	0.31 ± 0.02	0.36 ± 0.14
S	0.30 ± 0.12	0.23 ± 0.01
Cl	0.018 ± 0.002	0.18 ± 0.04
O	49.72 ± 1.69	48.29 ± 0.62
Ash composition [wt.[a,c]%]		
SiO_2	41.34 ± 2.23	24.61 ± 1.42
Fe_2O_3	11.91 ± 1.20	8.05 ± 0.46
Al_2O_3	13.66 ± 1.25	9.82 ± 0.64
TiO_2	1.76 ± 0.23	0.87 ± 0.13
CaO	6.43 ± 0.03	16.87 ± 0.48
MgO	4.75 ± 0.06	5.68 ± 0.46
MnO_2	0.00 ± 0.00	0.00 ± 0.00
K_2O	13.19 ± 0.33	21.76 ± 0.95
P_2O_5	4.68 ± 0.39	4.05 ± 0.28
SO_3	3.28 ± 0.31	6.24 ± 0.35
Cl^-	0.00 ± 0.00	2.23 ± 0.33
Na_2O	0.00 ± 0.00	0.00 ± 0.00

[a] *dry basis*
[b] *dried by air*
[c] *prepared at 450 °C*

conditions. Regarding the samples' morphological properties, the feedstock particles did not undergo some size reduction process for the experimental campaign.

It must be pointed out that previous works in the laboratory used this feedstock from the same source (Jacome, 2018; Ramirez-Quintero, 2019). Those works measure the physicochemical characteristics of the biomasses. Tables 3.2 and 3.3 display such properties.

As Table 3.2 shows, the biomasses have similar characteristics respecting heating value, elementary composition, moisture, volatile material, and fixed carbon contents. However,

the leaves possess more ashes, which, in turn, contain higher presence of elements precursors of deposits formation on internal furnace surfaces such as K, Cl, and S. In general, leaves have more presence of these elements than stalks as consequence of the nutrient's transportation process from the roots (Jones et al., 2007).

The data in Table 3.3 originated from a segregation process that used different air velocities to drag the particles rather than the traditionally sieving techniques (Ramirez-Quintero, 2019). Figures A.1 and A.2 show the shape of the groups of particles of sugarcane bagasse and leaves after separation by elutriation, respectively. In concordance with their nature, the bagasse particles' shape resembles truncated cylinders, while the leaves are flat and thin. Consistently, the density of the bagasse particles is significantly higher than the bagasse.

The limited amount of feedstock imposes challenges in this work. Indeed, results could be affected if the number of available experiments is insufficient by either incorrect experimental planning, defective tests, or inadequate selection of factors' levels. Therefore, this work implemented a factorial experimental design. The section below describes the experiments contemplated during the experimental campaign.

3.3 Experimental campaign

This work's main objective was to evaluate the fixed-bed combustion behaviour of sugarcane bagasse and leaves mixtures and determine the primary air flow effect. Ideally, aimed to attain this purpose statistically supported, a complete factorial design is contemplated. Different sugarcane residues mixtures in this approach should be burnt at distinct air flow rates. Those experiments would include at least one replicate for estimating the experiment's standard error. However, the feedstock was insufficient for distribution in several experiments that covered all the desired combinations between sample mixture composition and air flow rate. For example, dividing each factor into five levels requires 50 experiments (see Figure 3.10). Additionally, the outbreak of the SARS-CoV-2 virus between 2020 and 2021 compelled governments to impose lockdowns to reduce the virus spreading. This conjuncture obligated us to use the biomass available in the laboratory.

Considering the limitations above, an experimental design was adopted based on a central composite rotatable approach. With this methodology, a lower number of tests than the required for a complete factorial scheme allows covering all the experimental factors domain without sacrificing statistic information (Rodrigues; Iemma, 2014). Therefore, the tests were

Table 3.3 – Distribution of particles' morphology of sugarcane residues (Ramirez-Quintero, 2019).

Separation velocity [m/s]	Mass fraction [w.t.%]		Volume [$m^3 \times 10^{-9}$]		Density [kg/m^3]	
	Bagasse	Leaves	Bagasse	Leaves	Bagasse	Leaves
0.6	13.56 ± 1.37	1.65 ± 0.67	5.7 ± 9.5	0.1 ± 0.2	908.2	675.8
0.9	9.50 ± 1.10	3.48 ± 0.59	9.1 ± 16.0	0.2 ± 0.3	809.3	662.4
1.3	14.03 ± 1.89	15.22 ± 1.00	9.3 ± 18.1	20.7 ± 5.9	764.1	437.3
1.7	11.32 ± 1.43	17.57 ± 1.69	24.5 ± 47.7	40.8 ± 11.5	651.1	355.0
2.1	8.96 ± 1.57	14.08 ± 0.54	23.4 ± 44.3	76.3 ± 18.1	577.6	298.0
2.6	11.32 ± 0.39	20.72 ± 2.41	48.8 ± 96.6	161.9 ± 48.1	487.2	267.8
3.0	9.22 ± 0.50	11.22 ± 0.75	92.4 ± 74.0	95.8 ± 54.4	569.3	239.4
3.6	7.51 ± 0.96	7.72 ± 2.29	122.5 ± 111.3	189.5 ± 93.5	538.3	261.4
4.0	5.40 ± 2.87	3.34 ± 0.89	116.5 ± 121.1	125.2 ± 156.3	532.7	236.3
5.0	5.51 ± 0.31	2.89 ± 1.11	426.2 ± 282.6	308.4 ± 185.3	555.8	211.5
6.2	3.68 ± 1.79	3.17 ± 0.52	153.7 ± 241.5	217.0 ± 257.4	558.7	270.5

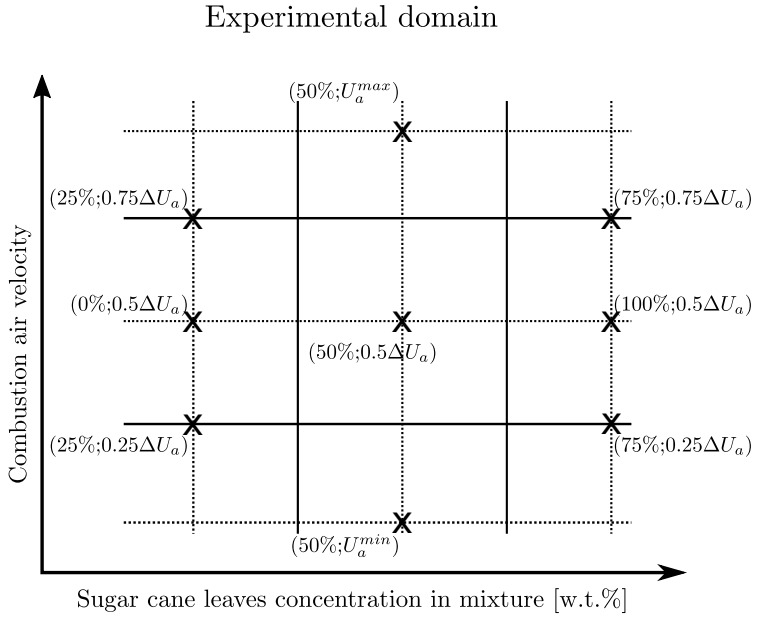

Figure 3.10 – Experimental design.

reduced to 11, distributed in this way:

- Four experiments at 25 and 75 of each factor range:
  {25%Y_p,25%$\dot{m}''_a$}, {25%Y_p,75%$\dot{m}''_a$}, {75%Y_p,25%$\dot{m}''_a$}, and {75%Y_p,75%$\dot{m}''_a$}

- Four experiments by permuting 50, 0, and 100 factors level:
  {0%Y_p,50%$\dot{m}''_a$}, {100%Y_p,50%$\dot{m}''_a$}, {50%Y_p,$\dot{m}''_{a,min}$}, and {50%Y_p,$\dot{m}''_{a,max}$}

- Three experiments in the central point of factors domain:
  {50%Y_p,50%$\dot{m}''_a$}

where Y_p is the sugarcane mass fraction in samples and $\dot{m}''_a$ the airflow rate.

In the case of airflow rate minimum and maximum values ($\dot{m}''_{a,min}$, and $\dot{m}''_{a,max}$, respectively), the air supply fan velocity was set following an empirical criterium based on stability of the fixed-bed combustion. The oxygen supply was insufficient to support the bed combustion at a meagre airflow rate. Conversely, at a very high airflow rate, the reaction zone in the bed intermittently extinguished and intensified during the test. The chosen values were 0.150 and 0.465 kg/sm^2 for $\dot{m}''_{a,min}$, and $\dot{m}''_{a,max}$, respectively.

Table 3.4 outlines the conditions of each of the 11 combustion tests in this work.

Table 3.4 – Sugarcane residues co-combustion experiments.

Experiment	$\dot{m}''_a$ [kg/sm^2]	Y_p [%mass]	Sample ID
1	0.230	25	025P0230U1
2	0.385	25	025P0385U1
3	0.230	75	075P0230U1
4	0.385	75	075P0385U1
5	0.150	50	050P0150U1
6	0.465	50	050P0465U1
7	0.310	0	000P0310U1
8	0.310	100	100P0310U1
9	0.310	50	050P0310U1
10	0.310	50	050P0310U2
11	0.310	50	050P0310U3

3.4 Experimental procedure

3.4.1 Fixed-bed combustion experiments

Initially, the gas suction system is adjusted to the desired gas sample conditions before accessing the FT-IR. For this purpose, the temperature in the high-temperature condenser is established to 150 °C, while the heated hose and the FT-IR gas chamber temperatures are set to 170 °C. At the other end of the sampling line, the valves near the vacuum pump (see Figure 3.8) are set to allow a gas flow in the sampling line between 5 and 10 L/min. Simultaneously, the centrifugal fan in the air supply system is adjusted to the required airflow.

After preparing the gas sampling probe system, the measurement devices, and the acquisition system, the combustion chamber is filled with the biomass sample so that the bed level is at least 5 cm above port T13. Next, the 13 thermocouples and the pressure transmitters are inserted in their corresponding sampling port. Finally, with a paper towel damped with alcohol and a lighter, the sample's upper surface is ignited.

The bed properties measured during the experiment are processed to estimate the parameters that describe the fixed-bed combustion performance. The next chapter explains data analysis in detail.

4 RESULTS AND DISCUSSION

This chapter presents the results obtained after the experimental campaign and discusses the main findings based on statistical analysis. To facilitate the narrative leading to the conclusions of this research, the chapter is divided into two parts. The first section explores the fixed-bed combustion properties measurements during the experiments. Traditional parameters used for describing experimental fixed-bed combustion behaviour are also defined. The second part contrasts the overall results by evaluating their dependency on the variation of the factors. This section discusses the advantages and drawbacks of sugarcane residues co-combustion.

4.1 Results description for one sample

This section describes the parameters derived from the measures taken during the experimental campaign using the data from sample *025P0230U1*. The description of such outcomes may apply to the other samples evaluated in this work. The Appendix B at the end of the document attach the graphs for all samples analysed.

4.1.1 Mass loss history

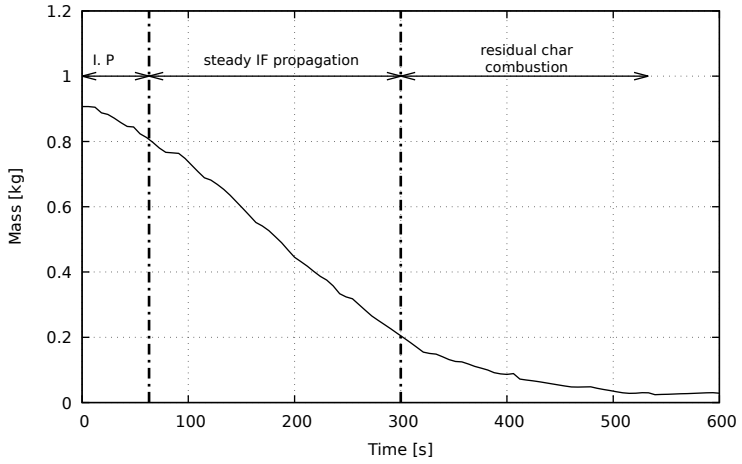

Figure 4.1 – Mass loss variation during fixed-bed combustion experiment of sample *025P0230U1*.

Since sample mass variation during the experiment is measured outside the reactor, the readings are unaffected by packing effects as channelling. This is an attribute that allows having a full insight into the whole process, as shown in Figure 4.1.

From the mass variation profile, it is possible to identify three characteristic stages of bed sample combustion. These stages correspond to variations in the slope of the curve, which itself is equivalent to the rate of the mass expelled along bed combustion (dm/dt):

1. In the first stage, from t = 0, the mass loss rate gradually increases, which is caused by transitory effects of the ignition at the top sample surface – ignition phase (IP in Figure 4.1.

2. When this initial effect stabilizes, the slope keeps roughly uniform as the bed continues burning. A constant mass loss rate suggests the reaction zone is moving downward at steady velocity – steady state phase.

3. Finally, the mass loss rate slowly reduces whilst the sample mass signal approaches zero. The reduction in mass loss rate from a constant value is related to the ignition front arrival to the grate. The residual mass left behind is mainly composed of char and ashes. Char particles continue burning out until all combustible material depletes – residual char combustion phase.

Despite the sample combustion starting when the top of the bed ignited, the initial transitory effects introduce a potential bias that could impact the information gathered from experiments. On the contrary, from the stable portion of Figure 4.1, the readings taken by the acquisition system are more reliable for analysis. Hence, the data measured during the first phase were discarded. All the information collected inside the stable phase was the subject of study in this work. The relevant parameters characterising the fixed-bed combustion were estimated from this discrimination in the experiment's temporal domain.

The criteria chosen to define the start of the experiment involved identifying the onset of the temperature increase at T_{13} from room temperature. The next section provides a detailed explanation of the procedure used to determine this initial time. Additionally, the time interval during which bed combustion reaches the steady state phase may be settled from temperature history and the position of the ignition front.

In the case of the end of the last fixed-bed combustion phase, challenges arise for identifying this instant. Firstly, a significant portion of the bed consists of light and thin particles with low bulk density values. During the drying and devolatilization steps, particles bulk density greatly reduces, while at the char combustion step, particle size gradually shrinks as the carbonaceous material is consumed. Under the char consumption phase, it is more likely that

the combustion air drags those particles whose terminal velocity is lower or equal to air velocity (see Figure 4.2). This effect introduces bias, which becomes more pronounced when the ignition front approaches the grate, making it difficult to estimate the endpoint of the last fixed-bed combustion phase. Further discussion on this topic continues in the section concerning the composition of combustion gases.

Figure 4.2 – Images from the reactor top during experiments of sugar cane leaves and bagasse mixture. The left and right photographs were taken along the sample's combustion steady state phase and residual char combustion phases, respectively.

4.1.2 Temperature history

Figure 4.3 depicts the temperature variation as measured by the thermocouples inserted at fixed positions along the reactor. The local temperature profile exhibit distinct features that coincide with the combustion stages of fuel bed particles surrounding the thermocouple.

Initially, the recorded temperature is the same as the air injected. This state holds until the ignition front reaches the thermocouple. At that moment, there is a sharp temperature increase. This increase results from heat transferred from the particles undergoing combustion

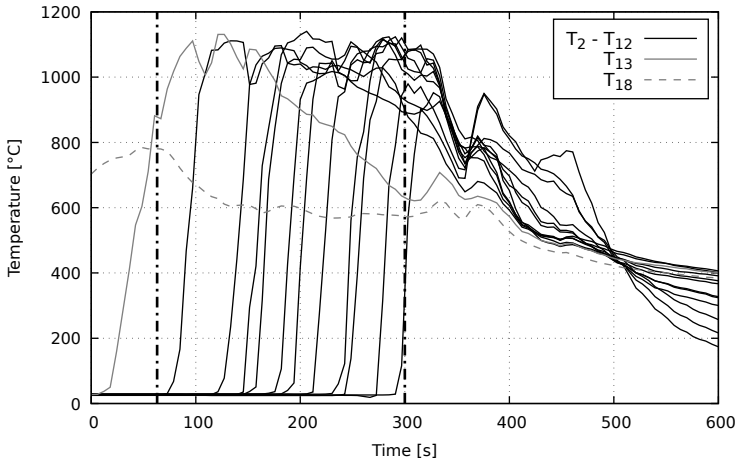

Figure 4.3 – Temperature history for sample *025P0230U1*.

in layers above the thermocouple and the ignition of the sample particles at the thermocouple level. The mean heating rate ($[dT/dt]_{ig}$) during ignition for sample *025P0230U1* was estimated as 1558 °C/min.

After the local temperature attains a first peak, its magnitude undergoes reductions and increases because of the propagation of the ignition front reaching the thermocouples in lower positions. This tendency continues as the fuel material is consumed. During this period, which coincides with the steady state phase, the combustion temperature reaches its maximum value. For sample *025P0230U1*, the maximum temperature of the experiment was 1141.4 °C.

When the ignition front reaches the particles above the grate, the temperature measured at all positions drops and peaks again for the last time before being reduced by the air-cooling effect (at around 370 sec in 4.3). Yang et al. (2003) suggested that this second temperature peak is a consequence of the combustion-gasification of fuel particles left behind after the ignition front reaches the grate. These particles, of char, burn intensely because of the higher oxygen availability, which provokes the observed sudden increase in temperature.

From temperature history, it is calculated the ignition front propagation velocity (v_{ig}), two approaches are commonly used to determine v_{ig} from temperature history:

1. Recording the time when a selected reference temperature in the ignition region is reached
2. Identifying the time when the sudden increase in local temperature happens (ignition phase onset – IPO).

In both cases, the recorded times in each position are plotted on a graph, as shown in Figure 4.4. The least-squares regression line models the position of the ignition front, and the absolute

value of the obtained slope represents v_{ig}.

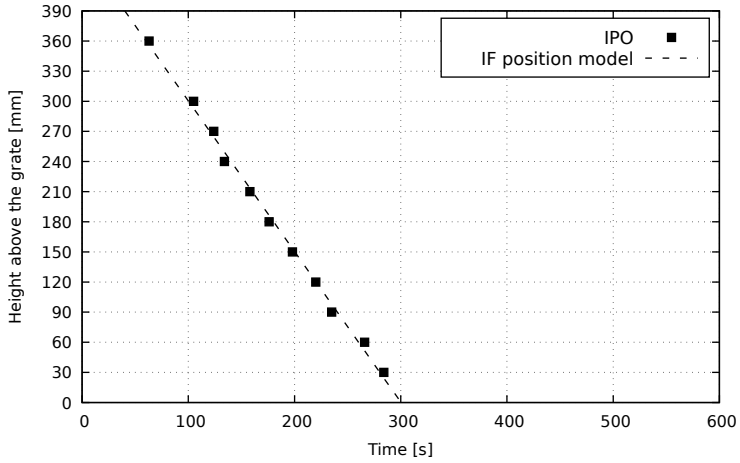

Figure 4.4 – Ignition front position for sample *025P0230U1*.

Statistically, either of the two methodologies produces similar results, as demonstrated in Appendix A. However, IPO's approach is more closely aligned to the physical meaning of the ignition front, which represents the moving boundary of the reaction zone. Therefore, v_{ig} was estimated using this method. In the case of sample *025P0230U1*, the linear model has an R-squared value of 0.9941. The absolute value of the least-square regression line slope in millimetres per second was determined to be 1.565. This value, in combination with the sample's bulk density, allows for the calculation of the ignition rate ($\dot{m}''_{ig}$) by using equation 2.2. However, the traditional method of estimation introduces uncertainty because of the variation in bulk density. The discussion about ignition rate estimation will be explored in subsequent sections.

Regarding the beginning of the steady phase, the IPO for T_{12} was supposed as a criterion to establish this time. For sample *025P0230U1*, the stable phase started at 63 seconds. This phase's end was estimated using the ignition front position least-square model. The criterion for identifying the end of the steady was the moment when the ignition front reaches the grate position(height = 0). This indicates that, at this point, almost all or entirely all volatile material had been depleted from the remaining particles. For sample *025P0230U1*, the steady-state phase ended 300 seconds after the experiment starts. Figures 4.1, 4.3, and plots in figures along this chapter depict both time limits as dashed vertical lines. Table 4.1 presents the beginning and ending times ($t_{i,SP}$ and $t_{f,SP}$, respectively) of the steady state phase for all the mixtures evaluated in this work.

Table 4.1 – Results for heating rate and maximum temperature for all samples.

Sample ID	$t_{i,SP}$ [seg]	$t_{f,SP}$ [seg]
025P0230U1	63	300
025P0385U1	70	333
075P0230U1	74	329
075P0385U1	83	292
050P0150U1	9	293
050P0465U1	100	402
000P0310U1	70	369
100P0310U1	68	396
050P0310U1	51	312
050P0310U2	78	285
050P0310U3	88	342

4.1.3 Mass loss rate and residual char after steady state phase

As the time that the reaction zone spends propagating steadily along the bed is known, it is possible to estimate the burning rate ($\dot{m}''_{bur}$) during this stage. For sample *025P0230U1*, $\dot{m}''_{bur}$ was initially calculated by taking the slope of least-squares linear model of the mass variation data inside the steady phase ($[dm/dt]_{sp}$). Finally, this value was divided by the reactor cross-section surface as described by equation 2.3 resulting in a $\dot{m}''_{bur}$ of 0.0709 $kgs^{-1}m^{-2}$.

The amount of residual mass left after the ignition front reaches the grate at the end of the steady-state phase is another parameter that can define the length of the effective[1] last section of a grate in travelling burners for a specific fuel. For example, for sample *025P0230U1*, this value expressed as a percentage of the mass at the experiment beginning was 25.33%. This analysis may be also adapted in the fuel bed displacement in "pinhole" grate-fired systems.

4.1.4 Pressure loss along the bed

The Figure 4.5 sketches the local pressure variation as measured by each of the pressure transducer in positions T_2 to T_{12}.

Before the steady phase onset, all the pressure signals simultaneously decreased (Figure 4.5). The tendency remains until the pressure difference reached a value of zero. This phenomenon results from the combustion of the sample. As the bed top surface advances towards the grate, the column of particles above the pressure transducer gradually diminishes. When the bed surface and pressure transducer are at the same level, the pressure difference

[1] The word "effective" applied to the length of the last section of the grate means the grate extension where the residual char particles completely burnoff.

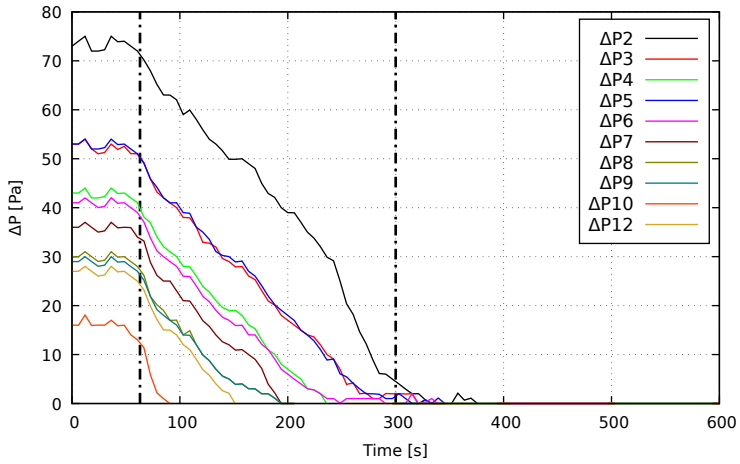

Figure 4.5 – Pressure drop variation for sample *025P0230U1*.

attains a zero value.

Figure 4.5 exhibits that some curves overlap, implying the formation of preferential channels for air passing (channelling). The higher heterogeneity in the sample's particle size distribution hinders the reactor's uniform packing. This effect increases the incidence of channelling, which influences the pressure distribution along the bed to a greater extent than the temperature history.

4.1.5 Bed level position

This section establishes a criterion for predicting the instant position of the bed level by analyzing data obtained from pressure loss variation and temperature history during the combustion test.

Regarding pressure loss, bed level position is estimated when the pressure transducers measure a difference equal to zero ($t(\Delta P = 0)$). On the other hand, there are indications that bed level is closely associated with the time at which the first local temperature peak reached at the end of the ignition phase ($t(T_{ig,max})$). Generally, reaching its initial maximum value, the temperature measured in a fixed position tends to decrease. This behaviour is characteristic of temperature history, as may be seen in several works in literature (Fatehi; Kaviany, 1994; Rogaume et al., 2002; Yang et al., 2003). Some authors have suggested that this reduction in temperature is because the thermocouple emerges from inside the bed (Zhou et al., 1995; Kuo et al., 1997; Lans et al., 2000; Varunkumar et al., 2011). Since the temperature in the freeboard is lower than inside the reaction zone, the thermocouple signal falls.

A straightforward method to verify if both $t(\Delta P = 0)$ and $t(T_{ig,max})$ effectively

predict the bed level position is by plotting each data set at different coordinate axes and assess whether the regression line has a slope around 1 and an intercept of 0. This evaluation was conducted using two statistical tests on the linear model:

$$t(T_{ig,max}) = b_0 + b_1 t(\Delta P = 0) \tag{4.1}$$

These tests check the validity of the null hypotheses: ($H_{0,1}$) the model's intercept is zero, and ($H_{0,2}$) the slope of the least-squares linear model is approximately equal to 1. The procedure was carried out using R software, and the summary of the linear model is as follows:

```
Residuals:
    Min      1Q  Median      3Q     Max
-67.164 -17.860   8.175  12.073  66.621

Coefficients:
             Estimate Std. Error t value Pr(>|t|)
(Intercept)   81.2057   40.2567   2.017  0.07446
t_dP0          0.6686    0.1716   3.895  0.00365 **
---
Signif. codes: 0 '***' 0.001 '**' 0.01 '*' 0.05 '.' 0.1 ' ' 1

Residual standard error: 40.71 on 9 degrees of freedom
Multiple R-squared: 0.6277,Adjusted R-squared: 0.5863
F-statistic: 15.17 on 1 and 9 DF, p-value: 0.003646
```

In the section "Coefficients" of the summary provided above, the p-value corresponding to the test over $H_{0,1}$ exceeds 0.05. Therefore, for a significance level of 5% there is insufficient evidence to reject the null hypothesis, and it is reasonable to assume that the least-squares line begins at the origin. Regarding the slope of the linear model between $t(T_{ig,max})$ and $t(\Delta P = 0)$, the null hypothesis has been evaluated using a Student's t-test (Navidi, 2010). For sample *025P0230U1*, the p-value obtained was roughly 0.09 (p-val($b_1 = 1$) in Table 4.2). Therefore, it is possible to consider that the slope is approximately unitary. These results demonstrate that statistically, the least-squares line of the model exhibits the same behaviour

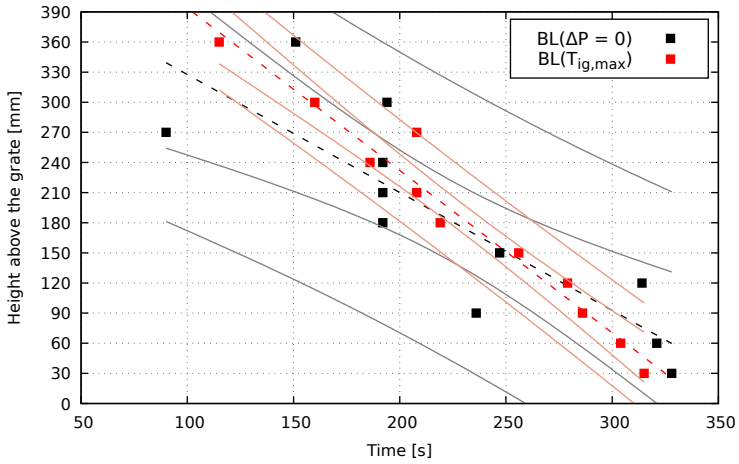

Figure 4.6 – Comparison between the linear models for sample *025P0230U1* bed level (BL) position prediction. The dashed lines represent the least-squares regression line. The continuous lines are the confident and prediction bands of each regression model.

as a line that starts at the origin with a unitary slope. Consequently, both pressure drop and temperature history can be used to estimate the bed level.

A question arises: which of the two models provides more accurate results? Figure 4.6 presents a height-versus-time diagram plotting the set of points corresponding to $t(\Delta P = 0)$ and $t(T_{ig,max})$. This figure visually displays each data point, its regression line, as well as the confidence and prediction bands to predict the bed level position. It is evident the significative dispersion in the data from pressure drop. Furthermore, it is possible to point out the appearance of channelling by observing that pressure drop in ports T_{11}, T_9, T8, and T7 become zero simultaneously. On the contrary, the data set for $T_{ig,max}$ exhibits less spreading and narrower confidence and prediction bands. Although channelling also affects the temperature readings, as Yang et al. (2003) reported, its effects are more prominent in pressure distribution along the bed. Therefore, in the case of sample *025P0230U1*, the bed level position is better predicted by using the maximum temperature at the end of the ignition phase. This conclusion is drawn from all the samples of this work (Table 4.2).

4.1.6 Ignition rate, bulk density variation, reaction zone thickness and reaction zone mass variation

In literature, the challenge of determining the bed level location has been tackled by using invasive techniques, as discussed in the literature review chapter. However, in the last section, criteria were established based on the use of traditional laboratory-scale fixed-

Table 4.2 – Results of the statistical evaluation of the least-squares model relating $t(\Delta P = 0)$ and $t(T_{ig.max})$ for all samples.

Sample	Model $h(\Delta P = 0)$		Model $h(T_{ig,max})$		Model $t(T_{ig,max}) = b_0 + b_1 \times t(\Delta P = 0)$				
	n	Std.Err.	n	Std.Err.	Std.Err.	b_0	p-val ($b_0 = 0$)	b_1	p-val ($b_1 = 1$)
025P0230U1	11	58.89	11	21.20	40.71	81.21	0.07	0.67	0.09
025P0385U1	11	52.08	11	10.29	38.61	49.80	0.23	0.87	0.50
075P0230U1	9	39.04	11	23.09	23.44	36.42	0.31	0.93	0.59
075P0385U1	10	52.75	11	13.49	23.53	67.05	0.07	0.78	0.14
050P0150U1	11	57.11	11	47.09	60.24	57.04	0.33	0.73	0.29
050P0310U1	9	32.16	11	13.05	24.03	28.34	0.39	0.95	0.74
050P0310U2	9	39.08	11	18.84	26.61	14.94	0.70	0.94	0.72
050P0310U3	10	38.67	11	24.20	25.44	-43.56	0.27	1.10	0.43
050P0465U1	10	44.35	11	10.0	31.36	73.35	0.05	0.85	0.23
000P0310U1	10	44.35	11	24.56	39.85	16.49	0.74	0.91	0.56
100P0310U1	9	33.34	11	32.70	40.79	63.43	0.22	0.92	0.63

bed combustion techniques. From this information, it becomes feasible to estimate various properties dependent on bed level position, such as reaction zone thickness δ and char burning rate at the top of the bed $\dot{m}''_{char}$. Additionally, it enables exploring the ignition rate variation during the experiment. This last parameter has been considered constant by authors of papers in the literature. The following paragraphs present a discussion around these fixed-bed combustion parameters.

4.1.6.1 Bulk density variation

Figure 4.7 shows the evolution of bulk density along the bed as a function of time for sample *025P0230U1*. This data was calculated by following the expression:

$$\rho_b(t) = \frac{m(t)}{A_r h_{BL}(t)} \tag{4.2}$$

where $m(t)$, A_r, and $h_{BL}(t)$ represent the mass over the grate at time t, the reactor cross-section surface, and the instant bed level, respectively.

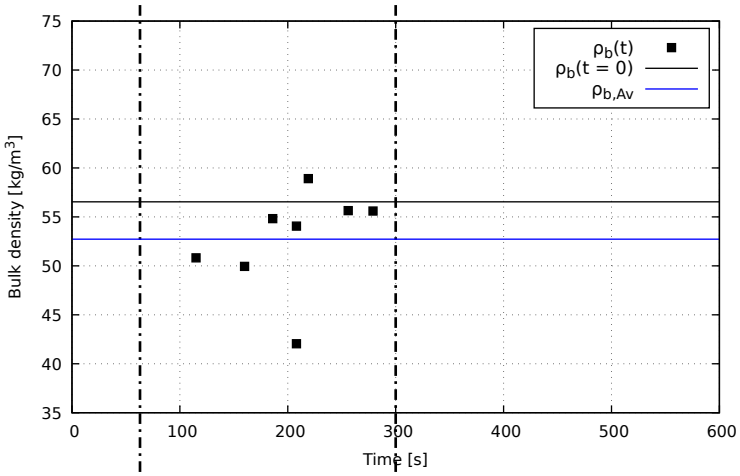

Figure 4.7 – Bulk density variation for sample *025P0230U1*. The black horizontal line represents the bulk density of the bed before sample ignition, whilst the blue horizontal line is the average bulk density during the steady-state phase.

Figure 4.7 also includes a horizontal line whose value is the same as the bulk density calculated before the experiment ($\rho_b(t = 0)$). During the steady phase, certain values of $\rho_b(t)$ were lower than $\rho_b(t = 0)$. Indeed, the average value of bulk density variation during the steady phase ($\rho_{b,Av}$) is lower than the initially calculated (4.7). The reduction in bulk density may be attributed to the high proportion of fine particles in the biomass samples (see Table 3.3). The rate at which the drying and pyrolysis phases progress depends on the surface area of the fuel

particle. Finer particles within the reaction zone will pass through these stages more rapidly, consequently losing mass quickly in conjunction with a reduction in their terminal velocity. At certain point, the air stream flowing across the bed can surpass fine particle's terminal velocity. As a result, a substantial number of particles that are still undergoing combustion will be expelled from the bed, impacting the measurement of the bulk bed density.

At the end part of the steady phase, the bed bulk density undergoes a sharp increase as the ignition front attains the grate (see bulk density longitudinal profiles in Appendix B). When the ignition front ends its travel along the bed, the mass left behind consists of burning char particles. In general, it is considered that a solid fuel particle reduces its size mainly during the char-burning phase. As explained further, the char consumption rate is proportional to bed level lowering speed. Therefore, the bulk density behaviour shown in Figure 4.7 points out that amid the last part of the experiment, the bed level changes faster than mass loss, confirming that only char is burning inside the bed.

The tendency in Figure 4.7 presents in almost all the samples except for samples *100P0310U1* and *050P0310U3* (see Figures C.54 and C.75 in Appendix B). For those samples, the bulk density has an opposed effect during the last phase of the experiment. In such cases, ρ_b is reduced, indicating that the mass loss rate overcomes the bed level reduction velocity. This behaviour indicates a high quantity of fuel particles being dragged out of bed by air flow.

Turning to the differences between $\rho_b(t = 0)$ and $\rho_{b,Av}$, Table 4.3 shows the outcomes of a statistical test of similarity carried out over all the samples. The results reveal that, in almost all samples, there exist evidence that bulk density variates during experiments in comparison to the initially estimated value. Additionally, it's observed that average bulk density reduces as airflow rate increases, supporting the hypothesis of a bias generated by primary air stream.

4.1.6.2 Ignition rate

The ignition rate is defined as the mass swept by the ignition front during its propagation along the bed per unit of time and surface (Ryu et al., 2006). This parameter is calculated as the product of bulk density and the ignition front propagation velocity. Traditionally, literature has assumed that $\dot{m}''_{ig}$ remains constant throughout the combustion of the bed in a laboratory-scale fixed bed reactor. This assumption held true when the sample bulk density was kept constant during the experiment. However, in the case of the samples analyzed in this

Table 4.3 – Initial and mean bulk density comparison.

Sample ID	$\rho_{b,0}$ [kg/m^3]	$\rho_{b,Av}$ [kg/m^3]	s_{ρ_b} [kg/m^3]	p-val ($\rho_{b,0}/\rho_{b,m}$)
025P0230U1	56.54	52.73	5.16	0.02
025P0385U1	63.08	55.89	4.09	<0.001
075P0230U1	52.92	51.65	4.15	0.18
075P0385U1	53.01	36.80	2.31	<0.001
050P0150U1	52.92	63.65	18.34	0.05
050P0465U1	61.59	45.17	3.61	<0.001
000P0310U1	69.52	55.63	7.85	<0.001
100P0310U1	56.64	43.15	7.80	<0.001
050P0310U1	55.01	44.91	2.29	<0.001
050P0310U2	67.87	61.26	5.53	<0.01
050P0310U3	60.06	47.49	3.08	<0.001

work, it was demonstrated that the bulk density might differ from the one measured before the experiment due to effects such as particle elutriation. Therefore, variations in the ignition front can be expected when calculated based on the initial bulk density.

The ignition front, calculated based on the instant bulk density over the steady state phase, exhibit a similar profile as ρ_b (see Fig. 4.7). Therefore as illustrated in Figure 4.7 it is evident that for sample *025P0230U1* there are significant differences between the ignition rate calculated by using initial bulk density and the average value of bulk density variation. Specifically, the ignition rate calculated using the constant and variable bulk density model were 0.1033 and 0.079 kg/sm^2, respectively. Therefore, in this work the average ignition rate is used.

4.1.6.3 Reaction zone thickness

In the literature review chapter it was introduced the concept of reaction zone as that region where all combustion reactions proceed in the bed. Ignition front and top bed surface mark the lower and upper boundaries of the reaction zone, respectively; therefore:

$$\delta(t) = h_{BL}(t) - h_{IF}(t) \qquad t_{SP,i} \leq t \leq t_{SP,f} \tag{4.3}$$

where $h_{IF}(t)$ represents the ignition front position in function of the time. This relationship is only defined amid the steady phase of bed combustion. The Figure 4.8 shows the variation of reaction zone thickness during the combustion test of sample *025P0230U1*.

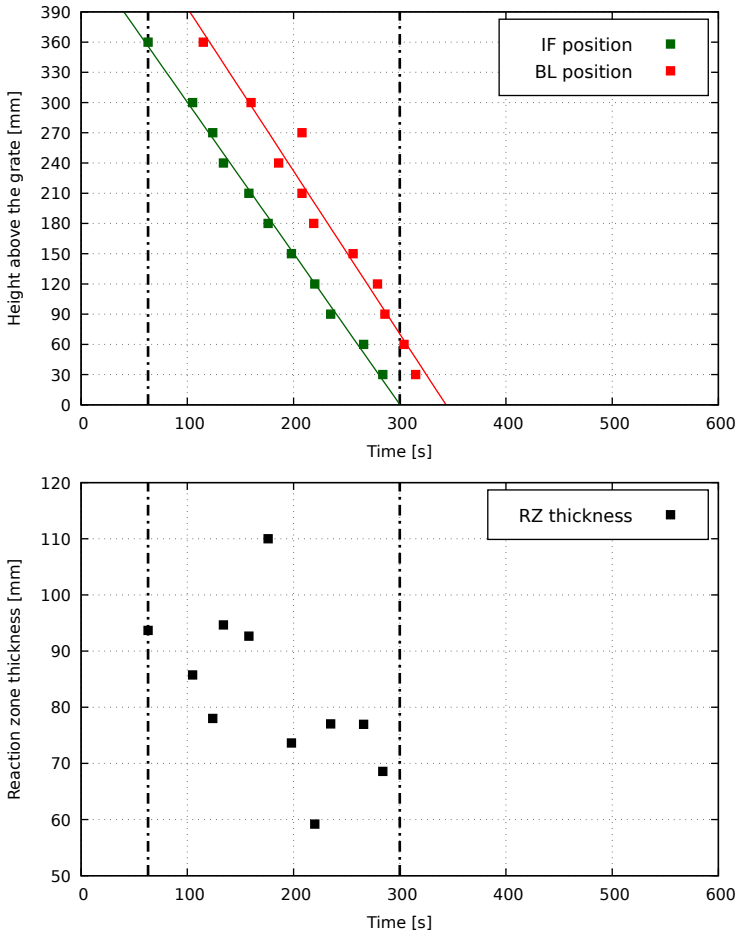

Figure 4.8 – Reaction zone thickness variation for sample *025P0230U1*. IF: Ignition front, BL: Bed level, RZ: Reaction zone.

The reaction zone thickness shows independence on time and high variability. Indeed, a test of hypothesis for the regression model between δ and time confirms this characteristic. Table 4.4 displays results obtained for all samples.

4.1.6.4 Char mass loss rate during steady phase

A generally accepted assumption taken in numerical studies of solid fuel combustion establishes that fuel particle reduces its size at the char combustion stage (Dernbecher et al., 2019). On the contrary, during the drying and devolatilization stages, the size of a solid particle remains relatively constant as it loses mass. In the fixed-bed combustion context, the volume occupied by a column of packed particles keeps uniform while the particles lose their volatile material. Since moisture and volatile material content are an essential portion of the particle mass, drying and devolatilization directly affect particle density and bulk density. In contrast, when the carbonaceous part of the solid matrix is exposed to the oxidant, the fuel particle size

Table 4.4 – Mean reaction zone thickness for mixtures of sugarcane leaves and bagase.

Muestra	δ_{RZ} [mm]	SD [mm]	p-val ($b_1 = 0$)
025P0230U1	78.12	21.45	0.30
025P0385U1	64.53	9.83	0.73
075P0230U1	81.86	21.91	0.95
075P0385U1	85.18	16.89	0.03
050P0150U1	76.49	45.69	0.54
050P0465U1	49.30	9.91	0.39
000P0310U1	83.02	23.44	0.75
100P0310U1	65.60	31.24	0.73
050P0310U1	59.57	14.10	0.14
050P0310U2	53.61	18.39	0.49
050P0310U3	63.50	25.05	0.22

reduces or shrinks as heterogeneous gasification and combustion reactions progress. Therefore, in a bed of packed fuel particles under combustion, the bed height reduces by the action of char consumption as the reaction zone advances.

Based on the considerations above, the char mass loss rate of fuel particles in the bed ($\dot{m}''_{char}$) is proportional to bed level lowering velocity. In this work, the following expression was used for $\dot{m}''_{char}$ estimation during the steady state phase:

$$\dot{m}''_{char} = \rho_{char} v_{BL} \tag{4.4}$$

where v_{BL} is the lowering bed level speed and ρ_{char} is the density of char particles based on proximate analysis and sugarcane leaves and bagasse concentration in the mixture. For sample *025P0230U1*, v_{BL} was 1.617 mm/sec while char consumption rate was equal to 0.007 kg/sm^2.

4.1.7 Composition of combustion gases

Figure 4.9 depicts the evolution of gaseous species released during sample *025P0230U1* combustion test. Along the steady phase, both the combustible species (CO, C_2H_2, C_2H_4, and CH_4) and CO_2 show a roughly uniform composition. The presence of those hydrocarbon gases and the shallow level of oxygen point out that the combustion undertook under substoichiometric conditions.

At the end of the steady phase, when the ignition front reaches the grate, the concentration of combustible gases species plummets simultaneously as oxygen availability increases. This drop is because the volatile content depleting from the remaining fuel particles in the bed.

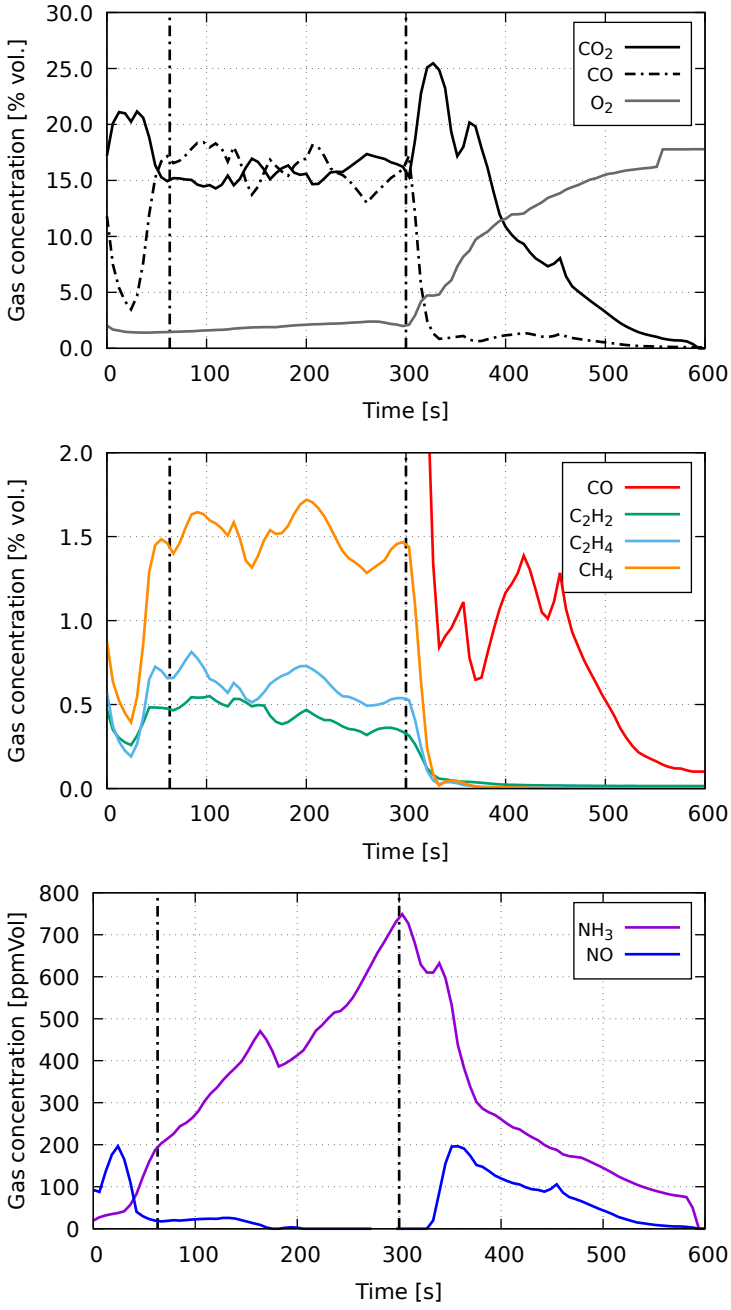

Figure 4.9 – Combustion gases composition for sample *025P0230U1*.

The high oxygen accessibility causes gasification reactions which consume the char particles and produce CO_2 and CO(see 4.9) (Smoot; Smith, 1985; Basu, 2013):

$$C_{(s)} + O_2 \rightarrow CO_2 \tag{4.5}$$

$$C_{(s)} + \frac{1}{2}O_2 \rightarrow CO \tag{4.6}$$

This reaction is exothermic, leading to local temperature rises. Most CO released from char gasification oxidizes to produce CO_2 increasing CO_2 levels until a peak value. The excess thermal energy released allows the temperature to rise to a second maximum, as Figure 4.3 shows.

Regarding the time behaviour of NO_x precursors, NO and NH_3, Figure 4.9 shows that the latter was the dominant specie released during the experiment. Throughout the steady phase, NH_3 content in combustion gases increased as the reaction zone propagated through the bed. This NH_3 variation contrasts with NO, whose emission levels were almost zero between the steady phase. This behaviour is consistent with experimental observations reported from biomass fixed-bed experimental works (Stubenberger et al., 2008). Reaction zone stoichiometry influences to a great extent the yield of N-containing species from biomass particles' pyrolysis stage. Rich combustion conditions promote NO reduction because at lower oxygen levels, combustible gases in volatiles react with NO by following the reactions:

$$NO + CO \rightarrow CO_2 + \frac{1}{2}N_2 \tag{4.7}$$

$$NO + CH4 \rightarrow CO + 2H_2 + \frac{1}{2}N_2 \tag{4.8}$$

In Figure 4.9, this negative relationship between CO and NO production is evident between 0 and 100 seconds. In this period, CO levels dropped momentarily whilst NO concentrations increased.

After the end of the steady phase, NO levels arose while NH_3 fell. Indeed, in char combustion, the nitrogen bound to char is mainly converted to NO because of the direct contact of oxygen with the carbonaceous residue (Glarborg et al., 2003; Williams et al., 2012; Karlström et al., 2017).

The following sections discuss the role of the experimental factors over the combustion parameters, including combustion gas emissions.

4.2 Results description for all samples

This study assessed the performance of the combustion of sugarcane residues by examining the variation of combustion parameters in function of the experimental factors, especifically the airflow rate ($\dot{m}''_a$) and the mass concentration of sugarcane leaves in mixtures with bagasse (Y_p). The preceding section defined the critical parameters characterizing reaction zone based on the experimental results in the laboratory-scale fixed-bed burner. Additionally, the discussion approached the temporal evolution fixed-bed combustion properties for a single experiment.

This section explores the overall impact of combustion parameters resulting from variations in the experimental factors selected in the experimental design. Using a least-squares linear regression model, the presence of any correlation between fixed-bed combustion performance parameters and the experimental factors is statistically assessed. In general, it was analyzed the following second-order model:

$$X = b_0 + b_{\dot{m}a}\dot{m}''_a + b_{Yp}Y_p + b_{\dot{m}aYp}(\dot{m}''_a \times Y_p) + b_{\dot{m}a2}\dot{m}''^2_a + b_{Yp2}Y_p^2 \tag{4.9}$$

where X represents the parameter under study and the b's are the regression coefficients associated to the terms $\dot{m}''_a$, Y_p, $(\dot{m}''_a \times Y_p)$, $\dot{m}''^2_a$, and Y_p^2. Regarding the results obtained in the midpoint (50% of sugarcane leaves at an airflowrate of 0.310 kg/m^{2}s the mean value of the three replicates is used. The results of the linear model statistical analysis for each parameter are summarize in the Appendix B. This statistical analysis will provide the experimental results with evidence to make inferences about the entire population of biomass from which the samples were obtained. In any case, the conclusions drawn from this work are based on the trends exhibited by each of the parameters evaluated.

4.2.1 Ignition rate and ignition rate velocity

Tables B.1 and B.2 summarize the hypothesis test results over the regression coefficients and the linear model proposed regarding ignition front properties. Graphically the increase in both air flow rate and the content of sugarcane leaves affects ignition rate and ignition front velocity. Nevertheless, the statistical evaluation of these factors indicated low influence, especially for ignition front velocity. These outcomes are a result of the heterogeneity in particles size distribution and void spaces in the bed, leading to significant variations for a single

test. This effect was further amplified by the limited number of experiments and replicates due to biomass availability constraints. Despite these outcomes, the conclusions drawn from the information collected can applied to the samples analyzed in this research and used for future works.

Figure 4.10 exhibits the variation in ignition rate as a function of airflow rate and the proportion of leaves in the samples. Due to changes in bulk density relative to its initial value during the experiments, which impact the calculated values of the ignition rate, $\dot{m}''_{ig}$ was calculated by using the average value of ρ_b during the steady-state phase. Literature reports that $\dot{m}''_{ig}$ vs $\dot{m}''_{a}$ flow rates profile exhibits a convex shape, allowing for the identification of well-known fixed-bed combustion regimes. Since bulk density reduces with air flow rate, likely due to the dragging of fine fuel particles, as discussed in section above, the ignition rate decreases as $\dot{m}''_{a}$ increases. For mixtures with 25% sugarcane leaves, the ignition rates appear to roughly maintain their value despite the increase in air flow rate. However, this effect may result from the absence of replicates for these samples and combustion experiments carried out at an intermediate air supply. A similar conclusion can be deduced for samples composed of 75% leaves.

Figure 4.10 includes a line representing the ignition rate required for stoichiometric combustion for a mixture of 50% leaves and 50% bagasse. The values at the left of the stoichiometric line characterize combustion under rich conditions ($\lambda < 1$). Values on the right side correspond to lean conditions ($\lambda > 1$). It is observed that except for samples *075P0385U1*, *050P0465U1*, and *100P0310U*, most of the combustion experiments proceeded under substoichiometric conditions. For samples with 50% of sugarcane leaves, although $\dot{m}''_{ig}$ reduced with air flow rate, in the $\lambda > 1$ region, the drop in ignition rate intensifies. The significant decrease in $\dot{m}''_{ig}$ within the fuel lean region can be attributed to the increase in the oxidant flow, which intensifies both the dissipative effect and the amount of unreacted and in-combustion fine particles expelled from the bed.

The upper plot in Figure 4.11 depicts the variation in ignition front propagation velocity with air flow rate. For samples composed of similar proportions of bagasse and leaves, the observed pattern resembles the profile of fixed-bed combustion regimes. At low air flow rates, limited oxygen availability results in combustion reactions with low release of thermal energy. This energy reaches unreacted particles in close layers beneath the ignition front, heating them slowly. As airflow increases, the thermochemical reactions are more intense, releasing

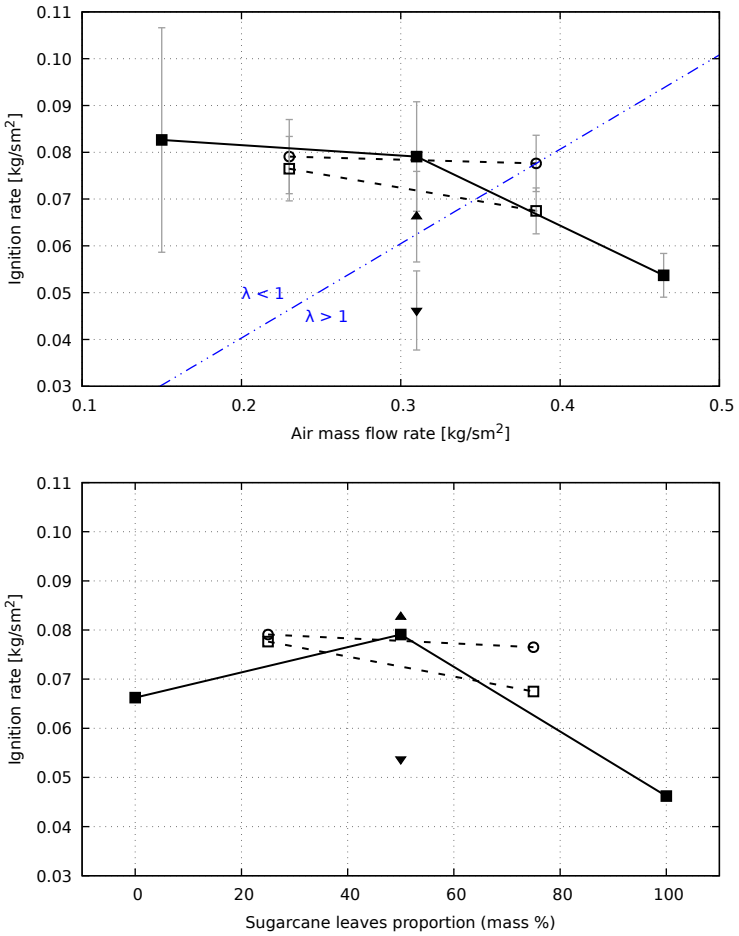

Figure 4.10 – $\dot{m}''_{ig}$ variation in function of airflow rate and sugarcane leaves content. Upper plot: 100% of bagasse (▲), 25% of leaves (○), 50% of leaves (■), 75% of leaves (□), and 100% of leaves (▼). Lower plot: $\dot{m}''_a = 0.150$ kg/sm^2 (▲), $\dot{m}''_a = 0.230$ kg/sm^2 (○), $\dot{m}''_a = 0.310$ kg/sm^2 (■), $\dot{m}''_a = 0.385$ kg/sm^2 (□), and $\dot{m}''_a = 0.465$ kg/sm^2 (▼).

more heat inside the reaction zone; therefore, the ignition front advances faster despite the drop in bulk density caused by . When the oxygen supply surpasses stoichiometric conditions, the counterbalance effect of airflow exceeds the reaction rate between oxygen and fuel particles. Therefore, the energy released in the reaction zone is dissipated, directly affecting ignition front velocity that slows down as the combustion cools.

The ignition rate establishes the fuel particles' mass getting into the reaction zone. This information is used for reaction zone stoichiometry estimation. However, the evidence collected in the experiments of this work indicates that this parameter is inappropriate for describing fixed-bed combustion performance at different primary air supply levels. On the other hand, the results for ignition front velocity exhibit characteristics that suggest its dependency on both thermochemical properties (fixed-bed combustion regimes discussed above) and geometry which contribute simultaneously (see Figures 4.10 and 4.11).

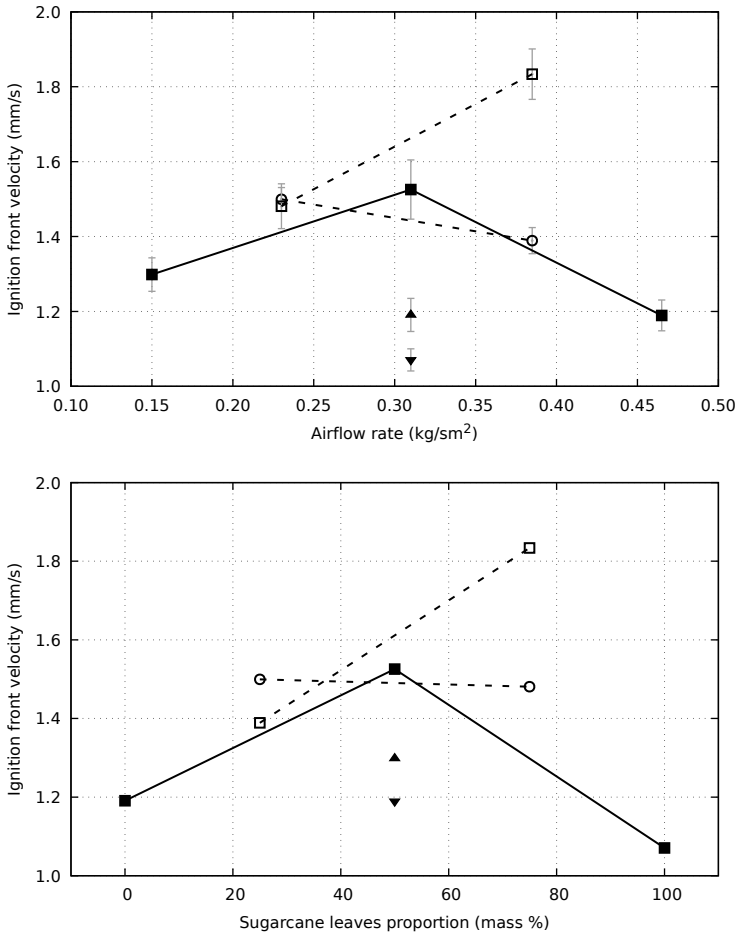

Figure 4.11 – v_{ig} variation in function of airflow rate and sugarcane leaves content. Upper plot: 100% of bagasse (▲), 25% of leaves (○), 50% of leaves (■), 75% of leaves (□), and 100% of leaves (▼). Lower plot: $\dot{m}''_a$ = 0.150 kg/sm^2 (▲), $\dot{m}''_a$ = 0.230 kg/sm^2 (○), $\dot{m}''_a$ = 0.310 kg/sm^2 (■), $\dot{m}''_a$ = 0.385 kg/sm^2 (□), and $\dot{m}''_a$ = 0.465 kg/sm^2 (▼)

The lower plots in Figures 4.10 and 4.11 show the effect of Y_p on ignition rate and ignition front velocity, respectively. The values of $\dot{m}''_{ig}$ for samples burned at a $\dot{m}''_a$ of 0.310 kg/sm^2 presents a bell-shaped trend suggesting it variates with sample composition. However, the tendency in $\dot{m}''_{ig}$ is a consequence of its dependency on ignition front velocity. The ignition rate definition, as the product of ρ_b and v_{ig}, explains this effect. When the influence of air flow rate on ignition rate is evaluated, the domain of $\dot{m}''_a$ on bulk density hinders the impact of ignition front velocity (see Figure Figure 4.10). The effect on bulk density is reduced when the proportion of the biomasses in the mixture is studied. Hence, $\dot{m}''_{ig}$ may be governed mainly by packing flow properties than over thermochemical variables.

Particle volume and density are incidental factors that depend on uncontrollable variables in experimental design, and they are related to sample composition. However, these factors significantly impact the kinematics of the reaction front. Table 4.5 shows the mean val-

Table 4.5 – Particle and packing properties. Source Ramirez-Quintero (2019).

Sample ID	Vol$_p$ [m^3 $\times$ 10^{-8}]	ρ_p [kg/m^3]	$\rho_{b,Av}$ [kg/m^3]
025P0230U1	7.50	578,0	52.73
025P0385U1	7.50	578,0	55.89
075P0230U1	9.17	412,8	51.65
075P0385U1	9.17	412,8	36.80
050P0150U1	8.33	495,4	63.65
050P0465U1	8.33	495,4	45.17
000P0310U1	6.66	660,6	55.63
100P0310U1	10.00	330,2	43.15
050P0310U1	8.33	495,4	44.91
050P0310U2	8.33	495,4	61.27
050P0310U3	8.33	495,4	47.49

ues of the particle volume (V_p), particle density (ρ_p) and bulk density of each sample. The data relating to V$_p$ and ρ_p were obtained from the thesis of Ramirez-Quintero (2019), who studied the effect of the granulometric separation by sieving and elutriation techniques on biomass particle aerodynamics. The propagation velocity of the reaction front inside a particle under combustion depends on its Biot's number (Bi) which links the particle's internal and external effects on heat transfer. Particles characterized as thermally thin have Bi less than one, usually associated with small size and lightweight particles such as leaves and straws. Conversely, thermally thick particles have Bi values greater than one (Mousavi et al., 2022) and include more volumetric sized particles as wood particles and municipal solid wastes. The combined effect of V_p, ρ_p (essentially representing mean particle mass), and ρ_b on ignition front velocity was quantified in the relation $(V_p\rho_p)/\rho_b$. The results are plotted in Figure 4.12. For a constant air flow rate, the reaction rates increase if the particle mass effect dominates over bulk density. When ρ_b rules, the porosity inside the reaction zone reduces the heat releasing intensity emitted from combustion reactions. This reduction in the rate of energy release impacts chemical reactions, causing a reduction on the velocity of the reaction. Although the experimental results show the influence of particle and packing physical properties on fixed-bed combustion, it is necessary to carry out more studies with other biomasses to confirm or reject the conclusions drawn in this work.

A further reason for the influence in Y$_p$ on ignition properties links the content of alkalis in the samples. As the proportion of sugarcane leaves increases in the mixtures, the share of alkalis grows proportionally in the samples. The presence of these elements have demonstrated to intensify the reaction rates during pyrolysis and char consumption phases (Fahmi

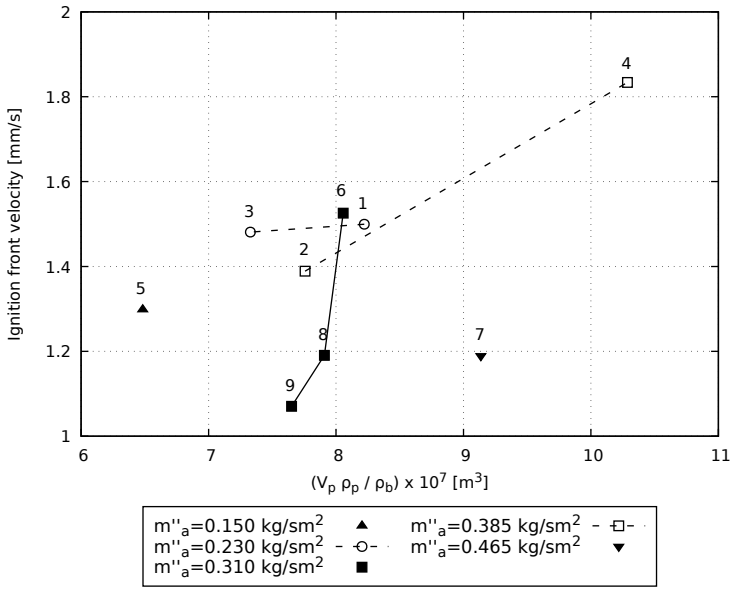

Figure 4.12 – Effect of particle and packed physical properties on ignition front velocity. 025P0230U1 (1), 025P0385U1 (2), 075P0230U1 (3), 075P0385U1 (4), 050P0150U1 (5), 050P0310U-mean (6), 050P0465U1 (7), 000P0310U1 (8), 100P0310U1 (9).

et al., 2007). The effect of alkalis on fixed-bed combustion performance will be discussed in conjunction with the results obtained for the other combustion parameters.

4.2.2 Mass loss rate and char mass loss rate

The regression coefficients obtained for burning rate and char mass loss rate in function of experimental factors are summarized in Tables B.3 and B.4, respectively. For $\dot{m}''_b$ the outcomes of the hypothesis test on the regression coefficients strongly support the influence of nearly all the terms in Equation (4.9). Indeed, the mass loss rate evolution for samples composed of 50% leaves in Figure 4.13 sustains these results. The mass loss rate for samples burned with Y_p equal 25 and 75% of sugarcane leaves may have a bell-shape trend similar to samples with 50% Y_p. However, further experiments conducted at different air flow rates within the range of 0.230 to 0.385 kg/sm^2 would be necessary to confirm this. The goodness-of-fit of the model for the burning rate is attributed to the absence of fluid-dynamics effects on the measurements of mass loss variation during experiments. This contrasts with thermocouple-based measurements parameters, such as ignition rate, which are subject to errors due to the interactions between air current and the bed. In fact, the uncertainties in burning rate estimates in this work were lower than 1.8×10^{-4}, whilst for $\dot{m}''_{ig}$, the errors were in the order of 1×10^{-1}. Therefore, owing to

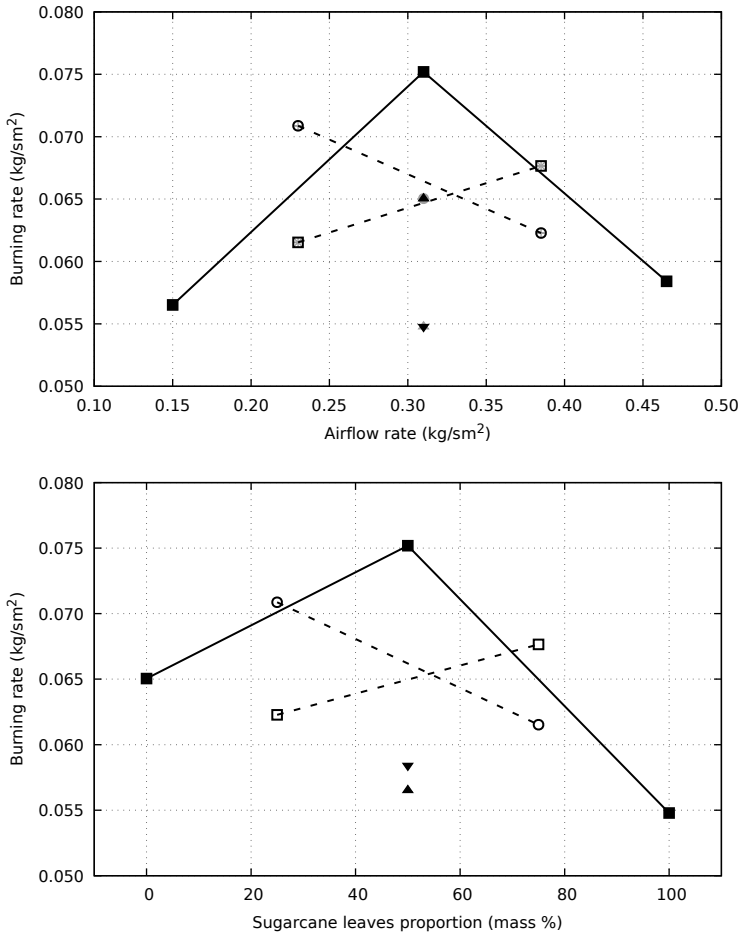

Figure 4.13 – $\dot{m}''_b$ variation in function of airflow rate and sugarcane leaves content. Upper plot: 100% of bagasse (▲), 25% of leaves (○), 50% of leaves (■), 75% of leaves (□), and 100% of leaves (▼). Lower plot: $\dot{m}''_a$ = 0.150 kg/sm^2 (▲), $\dot{m}''_a$ = 0.230 kg/sm^2 (○), $\dot{m}''_a$ = 0.310 kg/sm^2 (■), $\dot{m}''_a$ = 0.385 kg/sm^2 (□), and $\dot{m}''_a$ = 0.465 kg/sm^2 (▼).

its thermochemical nature, burning rate exhibits a behaviour that makes it a reliable parameter for fixed-bed combustion analysis.

Burning rate is associated with the kinetics of combustion reactions within the reaction zone. Under rich conditions, as air supply increases, if the combustion reactions rate exceeds the oxygen availability, energy release, temperature, mass loss rate, and reaction rate itself will increase. This reaction kinetics will reach its maximum value at a critical air flow rate. Beyond this point, with continued increases in air flow rate, the reaction rate becomes insufficient for capturing the provided oxygen. Thereby, the conditions in the reaction zone change from rich to lean. With further increases in the supply of oxidant , the reaction zone enters the extinction regime. In this regime, the air stream's dissipative effect leads to a slowdown of combustion reactions; subsequently, the mass loss rate drops.

Similar to v_{ig}, fuel bed composition also affects $\dot{m}''_b$ (see Fig. 4.13), pointing out the

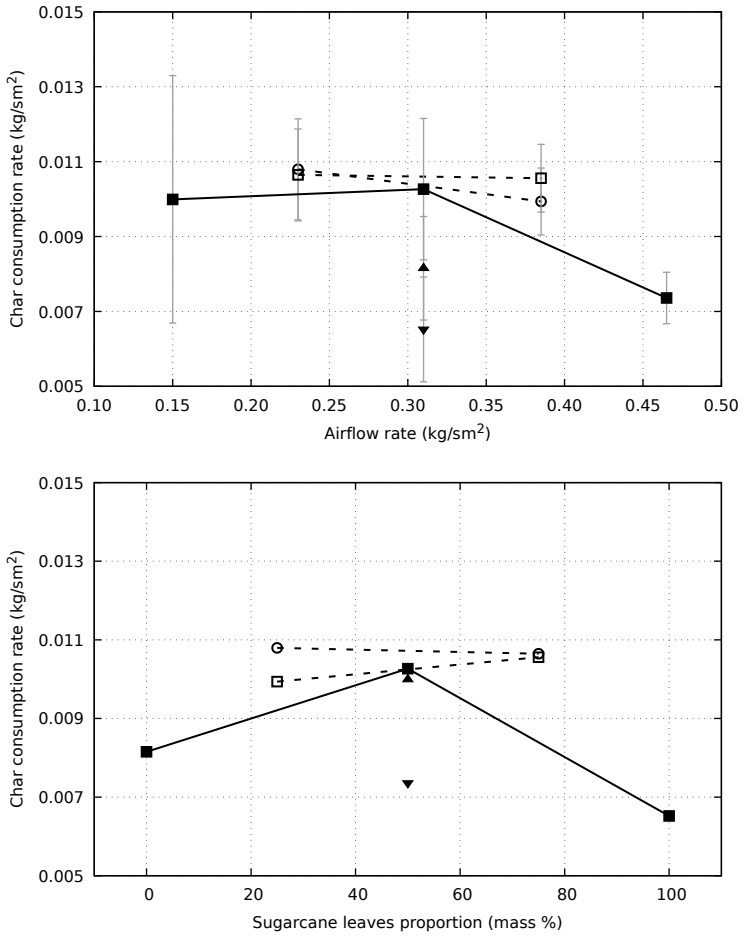

Figure 4.14 – $\dot{m}''_{char}$ variation in function of airflow rate and sugarcane leaves content. Upper plot: 100% of bagasse (▲), 25% of leaves (○), 50% of leaves (■), 75% of leaves (□), and 100% of leaves (▼). Lower plot: $\dot{m}''_a$ = 0.150 kg/sm^2 (▲), $\dot{m}''_a$ = 0.230 kg/sm^2 (○), $\dot{m}''_a$ = 0.310 kg/sm^2 (■), $\dot{m}''_a$ = 0.385 kg/sm^2 (□), and $\dot{m}''_a$ = 0.465 kg/sm^2 (▼).

significant role of the combined effect of particle and packing properties. Moreover, by comparing the results for v_{ig} and $\dot{m}''_b$ in bed samples undergoing combustion at $\dot{m}''_a$ of 0.310 kg/sm^2, it becomes evident that the parameter values for the mixtures are higher than the observed for individual biomass samples. This finding shows a synergy when sugarcane processing residues are co-combusted.

Although the Figure 4.14 shows that char burning rate is affected by air flow rate and the proportion of sugarcane leaves, the outcome of the regression model reveals low influence by the former (Table B.4). However, the limited amount of experiments gather enough statistical information to indicate the existence of an effect of the square of Y_p. Observing the lower plot in Figure 4.14, as the case of burning rate, it is evident a synergistic effect in char burning rate in mixtures of similar proportions sugarcane residues.

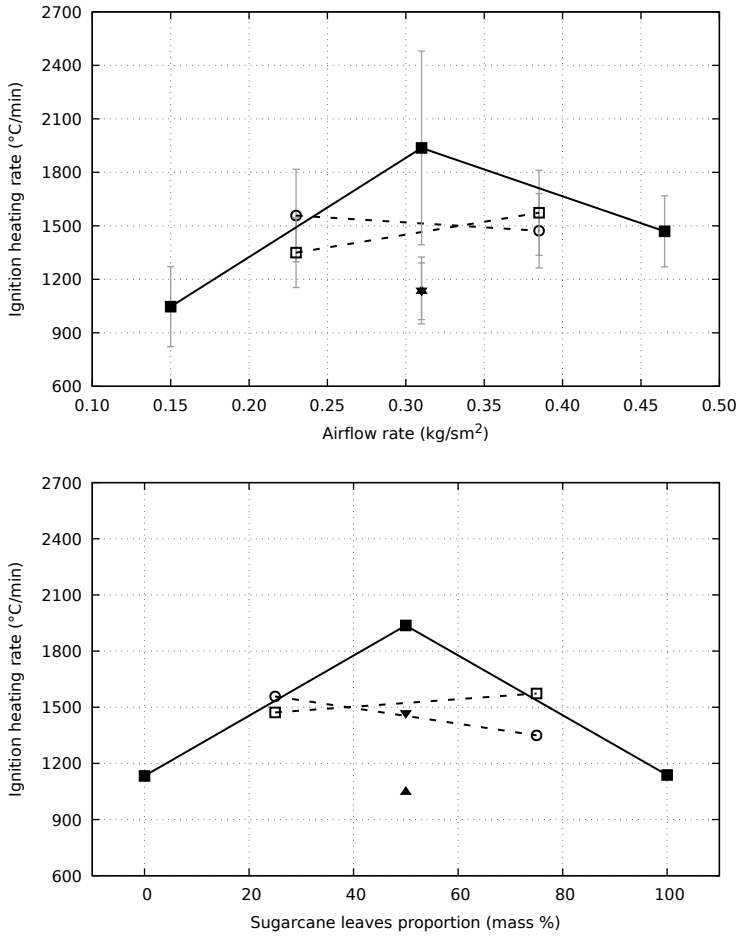

Figure 4.15 – dT/dt variation in function of airflow rate and sugarcane leaves content. Upper plot: 100% of bagasse (▲), 25% of leaves (○), 50% of leaves (■), 75% of leaves (□), and 100% of leaves (▼). Lower plot: $\dot{m}''_a$ = 0.150 kg/sm^2 (▲), $\dot{m}''_a$ = 0.230 kg/sm^2 (○), $\dot{m}''_a$ = 0.310 kg/sm^2 (■), $\dot{m}''_a$ = 0.385 kg/sm^2 (□), and $\dot{m}''_a$ = 0.465 kg/sm^2 (▼).

4.2.3 Heating rate and maximum combustion temperature

The sharp local temperature increase from room conditions is a clear physical indication of the ignition front's arrival. The results of the multilinear regression analysis for this parameter are presented in Table B.5. It is possible to observe that statistically, the heating rate is influenced by all the independent variables in Equation (4.9) except for the interaction between air flow rate and the composition of fuel feedstock term ($\dot{m}''_a \times \mathrm{Y}_p$). Figure 4.15 contains the dT/dt plots versus airflow rate, and sugarcane leaves concentration.

The heating rate inside the reaction zone is primarily associated with fuel reactivity, which, in combination with bed stoichiometry, controls the intensity of combustion reactions inside the reaction zone. The influence of the airflow factor becomes evident through the previously discussed combustion regimes. Additionally, although in this work Y_p effects upon

fixed-bed combustion have been attributed to the shift in particle and packing properties, elementary fuel composition also needs to be explored, especially its inorganic elements content.

The impact of biomass metal content on combustion have been widely studied. For instance, alkali species (potassium and sodium) in biomass can promote the formation of corrosive depositions on burner surfaces (Niu et al., 2016). Several studies have also highlighted the role of alkali species as catalyst of pyrolysis and char burnout phases (Fahmi et al., 2007; Jones et al., 2007; Saddawi et al., 2012). Specifically, the presence of potassium in biomass has been shown to lower the pyrolysis onset temperature, increase pyrolysis gas yield, and accelerates char consumption (Guo et al., 2020). As Table 3.2 shows, both ashes as alkali content in sugarcane leaves are greater than bagasse. This difference is expected since, during plant growth, the leaves accumulate alkali species after the water transpiration process (Jones et al., 2007). Therefore, samples with higher content of sugarcane leaves will have higher concentrations of ashes and alkali species. Observing the lower plot in Figure 4.15, by keeping the airflow rate and increasing Y_p initially, the heating rate raises until reaching a maximum value and further drops (likewise to ignition front velocity and mass loss rate). A critical alkali content may exist from which the catalytic effect on sugarcane processing residue combustion reaches a maximum. From this critical content, the combustion performance will be lower as potassium concentration increases.

Based on the results obtained from the experimental combustion tests, the impact of the proportion of sugarcane leaves on the combustion parameters might be associated with a combination of particles' morphology and the alkali species content of those residues. Sugarcane leaves increase the amount of thermally thin particles in the biomass mixture with bagasse in the samples. Such particles boost the reaction rates in the reaction zone. Moreover, these lighter particles contain significant amounts of alkali species bonded to their molecular structure. As a consequence, the reactivity of the bed increases due to the thermal and catalytic effects supplied by the leaves. However, it will be necessary to undertake additional studies to determine the effect of high alkali content in fixed-bed combustion.

Table B.6 exhibits the yield from the statistical analysis of the proposed multilinear model (Equation (4.9)) applied for T_{max}. Unfortunately, the model fails to correlate the parameter with experimental factors. After observing the shift in T_{max} with each experimental factor (Figure 4.16), a more straightforward linear model was used by just considering first-order terms – $T_{max} = b_0 + b_1\dot{m}''_a + b_2 Y_p$. The results for this second model are the following:

Table 4.6 – Simplified first order linear model for T_{max}.

Stat	Reg. coeff.	Std. error	t-value	p-value (b_i = 0)
b_0	1213.3809	35.9438	33.758	4.5×10^{-8}
$\dot{m}''_a$	-210.2142	100.5434	-2.091	0.0815
Y_p	-0.9410	0.3151	2.987	0.0244
Res. Std. Err.	27.29			
R^2	0.689			
ANOVA				
Source of Var.	SS	MSQ	F	p-value
Regression	9895.703	4947.851	6.646	0.03009
Error	4467.2	744.5		
Total	14362.86			

In this case, the simpler model showed better results than the second-order model, and Y_p was more significant than the airflow rate.

The weak effect of $\dot{m}''_a$ on T_{max} might be associated with the position of the flame respecting the reaction zone. This hypothesis is based on considering that the difference between flame position and bed level increases with airflow rate. The higher level in air current will drag the flame region farther from the reaction zone, consequently reducing the radiated heat intensity on bed level. However, assessing this hypothesis requires to carry out a numerical analysis for detecting the most likely position of the flame region.

In case of the effect of leaves proportion in the sample mixtures, the domain of this factor is related to the higher heat value (HHV) and the ash content of each sample (HHV/Ash). As Table 3.2 shows, both feedstocks possess roughly similar HHV. In contrast, sugarcane leaves have a higher content of ashes compared to bagasse. In Figure 4.17, the maximum combustion temperature of each experiment is paired with the HHV/Ash ratio. The graph reveals that T_{max} is proportional to HHV/Ash. During biomass combustion, those metals bonded to biomass organic structure react with oxygen and among themselves to form the different species that constitute ashes. Such compounds absorb and reflect the heat released by combustion chemical reactions (Varunkumar et al., 2013). The more ash content in fuel, the more combustion heat is absorbed, and the lower is the combustion temperature. This effect is shown in Figure 4.17. For a constant airflow supply, the maximum temperature in each experiment increases at higher values of HHV/Ash. In other words, the lower content in ashes enables the sample combustion to reach higher temperatures. This effect explains the negative trend in v_{ig}, $\dot{m}''_b$, $\dot{m}''_{char}$, and dT/dt observed in the region comprised by mixtures over 50% Y_p in Figures 4.11 and 4.13 to 4.15.

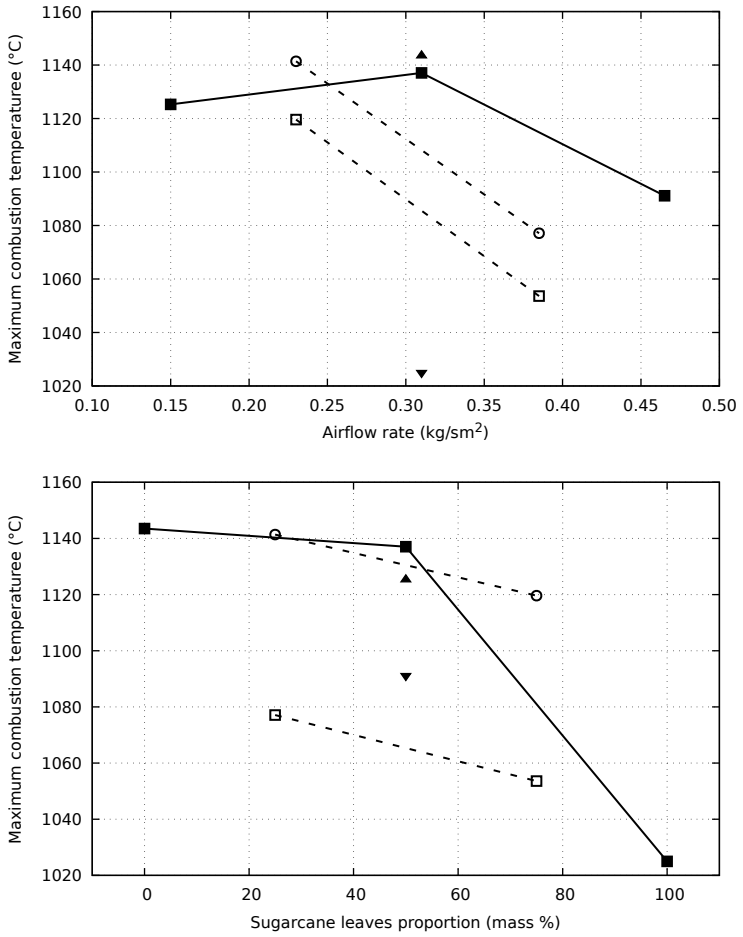

Figure 4.16 – T_{max} variation in function of airflow rate and sugarcane leaves content. Upper plot: 100% of bagasse (▲), 25% of leaves (○), 50% of leaves (■), 75% of leaves (□), and 100% of leaves (▼). Lower plot: $\dot{m}''_a$ = 0.150 kg/sm^2 (▲), $\dot{m}''_a$ = 0.230 kg/sm^2 (○), $\dot{m}''_a$ = 0.310 kg/sm^2 (■), $\dot{m}''_a$ = 0.385 kg/sm^2 (□), and $\dot{m}''_a$ = 0.465 kg/sm^2 (▼).

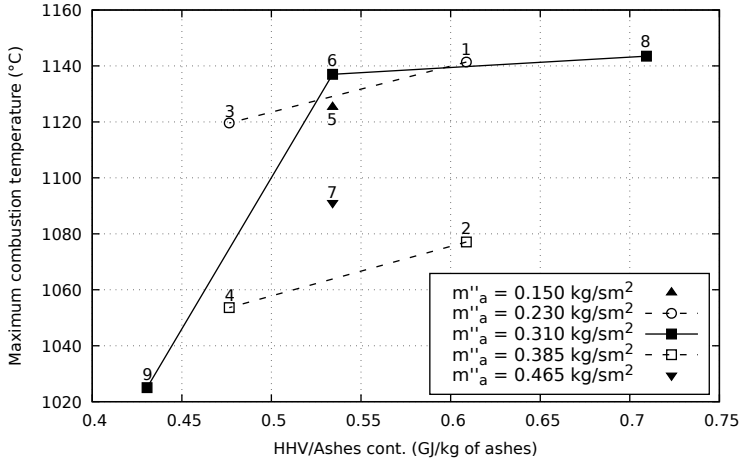

Figure 4.17 – Effect of HHV/ash content ratio on T_{max}. 025P0230U1 (1), 025P0385U1 (2), 075P0230U1 (3), 075P0385U1 (4), 050P0150U1 (5), 050P0310U-mean (6), 050P0465U1 (7), 000P0310U1 (8), 100P0310U1 (9).

4.2.4 Steady state duration and residual mass after steady state

The steady-state duration (t_{SP}) and the residual mass left behind this phase ($m_{r,SP}$) are two essential parameters that control the fixed-bed combustion efficiency. Throughout the elapsed time, when the reaction zone uniformly propagates along the bed until the ignition front reaches the grate, most of the chemical energy stored in the fuel is released. This results from biomass's high volatile matter content (Williams et al., 2012). In contrast, the residual mass remaining after the steady phase consists of a carbonaceous matrix with low or no volatile material, as well as ashes. Since char burns slowly, burning all combustible residual material in the bed will require more prolonged periods. In many cases, mismanagement of these parameters leads to considerable efficiency losses in the reactor due to unburned carbon.

Tables B.7 and B.8 display the analysis of regression coefficients of the multilinear model applied to t_{SP} and $m_{r,SP}$ (Equation (4.9)). Although the statistical yield indicates a lack of fit between the parameters and the factors in the model, Figure 4.18 points out that there exists a correlation consistent with the multilinear model proposed for t_{SP}. Additionally, as explained earlier, the limited availability of feedstock for creating multiple samples, combined with significant variability in the measurements, impacts the model's accuracy. In case of $m_{r,SP}$, a simplified first-order linear model was tested considering only the effect of airflow. This alternative model exhibits a possible better adjustment to the data collected as Table 4.7 shows. Despite this results, in Figure 4.18 is evident the influence of Y_p on this parameter.

Table 4.7 – Simplified first order linear model for $m_{r,SP}$.

Stat	Reg. coeff.	Std. error	t-value	p-value ($b_i = 0$)
b_0	34.185	7.133	4.792	0.00198
$\dot{m}''_a$	-48.261	22.169	-2.174	0.06623
Res. Std. Err.	6.025			
R^2	0.403			
ANOVA				
Source of Var.	SS	MSQ	F	p-value
Regression	171.540	171.540	4.726	0.0623
Error	254.04	36.296		
Total	425.6095			

Observing Figure 4.18 is evident that t_{SP} has an inverse tendency to the one for v_{ig} and m_b. Therefore, stoichiometry, flow dynamics, and the combination of particle and packing properties alter the steady-state duration. On the other hand, an increase in the air supply leads to a reduction in $m_{r,SP}$. This feature is mainly a consequence of two effects: (i) A signifi-

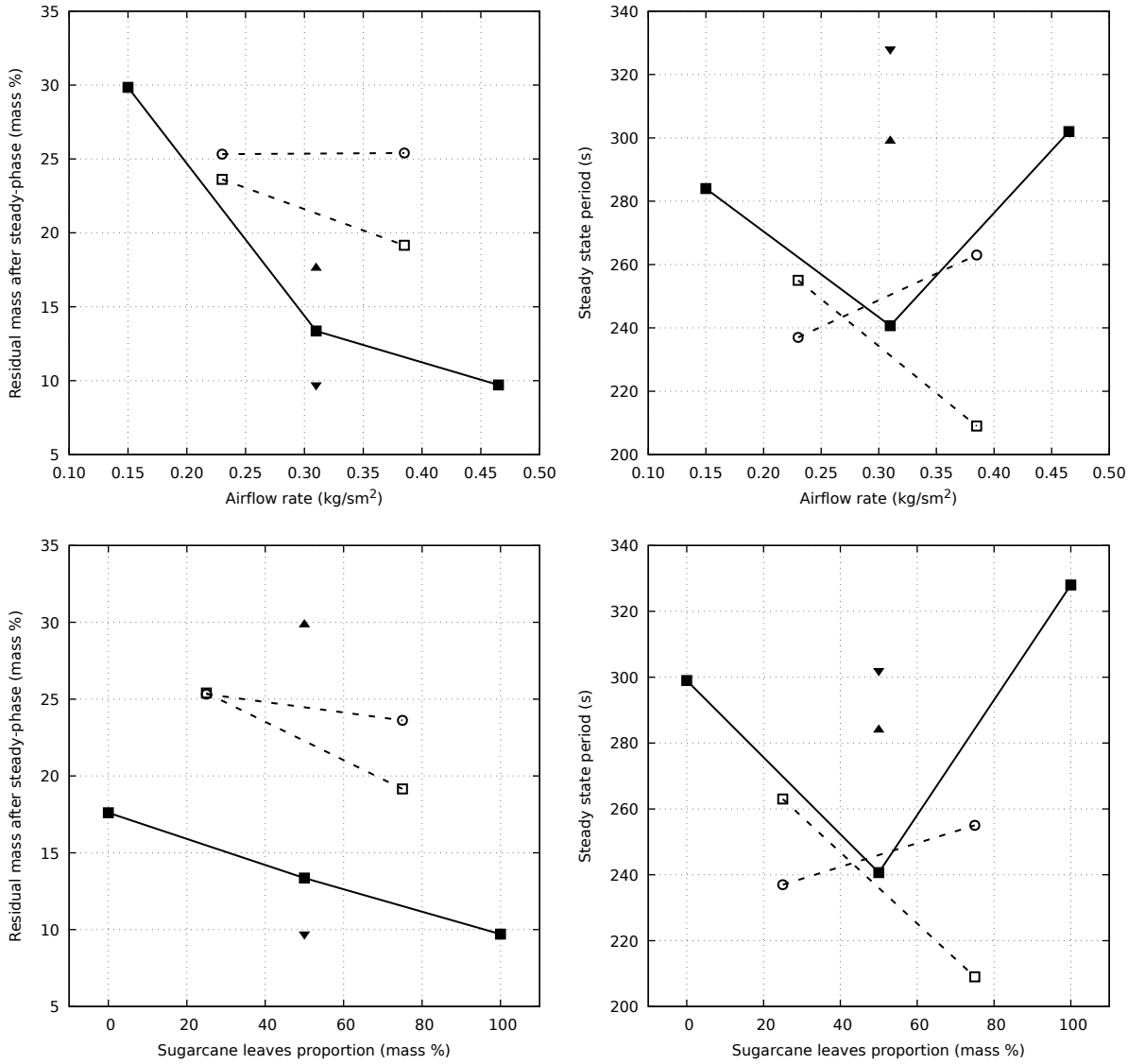

Figure 4.18 – Steady state duration and residual mass after steady state phase in function of airflow rate and sugarcane leaves content. Upper plot: 100% of bagasse (▲), 25% of leaves (○), 50% of leaves (■), 75% of leaves (□), and 100% of leaves (▼). Lower plot: $\dot{m}''_a$ = 0.150 kg/sm^2 (▲), $\dot{m}''_a$ = 0.230 kg/sm^2 (○), $\dot{m}''_a$ = 0.310 kg/sm^2 (■), $\dot{m}''_a$ = 0.385 kg/sm^2 (□), and $\dot{m}''_a$ = 0.465 kg/sm^2 (▼).

cant quantity of dragged particles out from the bed and (ii) the reduction in the reaction zone thickness (see Table 4.4).

Let a given bed with constant composition be exposed to different air flow rates. As the oxidant supply grows, reaction zone thickness narrows. In a thinner reaction zone, the fuel particles inside have more contact with oxygen. This results in combustion reactions consuming a greater amount of combustible material than in thicker reaction zones. However, the combustion is carried out more slowly as the airflow supply increases because of the convective

cooling effect. In this way, t_{SP} raises.

The plots in Figure 4.18 depict that adding more sugarcane leaves to the mixture leads to lower $m_{r.SP}$ values. This finding contrasts with the observations in Figure 4.12, which establish the reduction in ignition front velocity and consumption mass rate when the variable $V_p\rho_p/\rho_b$ is low. As previously discussed, the potassium content in biomass catalyzes char burnout. Hence, by increasing the potassium content in the fuel, char consumption is boosted until an apparent critical potassium content is reached. If this critical condition is exceeded by increasing the proportion of sugarcane leaves, the higher amount of ashes affect the net combustion heat transfer, hindering both pyrolysis and char consumption phases. This effect on char burnout rate counterbalances the ignition front velocity reduction caused by $V_p\rho_p/\rho_b$ decline. Consequently, the reaction zone holds its thickness as bed combustion proceeds. On the other hand, the increase in the concentration of light and fine particles with the increase in the proportion of sugarcane leaves leads to higher losses of combustible material that is carried out of the bed by the oxidant stream. Those effects combined with a longer steady period provokes that more fuel being consumed or dragged from the bed. As a result, there is a small amount of mass left at the end of the ignition front propagation.

4.2.5 Bottom and fly ashes composition

At this point, the variation in the composition of the ashes left on the reactor bottom is discussed after combustion experiments and the dragged particles captured by the filter in the gas sampling probe. Table 4.8 shows the composition of the material collected as measured by the EDS instrument.

In the case of fly ashes, it was impossible to separate the filters' collected particles or focus the electron beams in the SEM instrument on regions where the filter composition was undetectable. Therefore, the acquired spectra of the observed region had interference due to the overlap between fly ash compositions and the filter. To address this issue, elements shared by both ashes and filters were excluded from the results. Based on the data obtained, the elementary composition was recalculated. These results are shown in Table 4.8.

The composition of the bottom ashes may indicate the extent of retention of inorganic elements and provide insights into how much combustible material was consumed during combustion.

The results show that all particles had carbon content. Initially, carbon content in

Table 4.8 – Bottom and fly ashes elementary analysis for selected samples.

Bottom ashes elementary analysis [% mass (d.b.)]										
Sample ID	050P0150U1		050P0310U1		050P0465U1		000P0310U1		100P0310U1	
Element	Content	SD	Content	SD	Content	SD	Content	SD	Content	SD
C	5.314	2.146	6.214	1.350	5.104	1.096	4.916	5.275	3.808	1.056
Si	14.164	4.100	18.648	7.768	22.546	6.896	14.928	11.338	11.704	6.763
Fe	4.642	2.747	4.162	3.205	5.248	3.289	12.608	10.403	11.310	9.347
Al	3.908	0.482	4.754	2.972	4.232	2.722	2.230	2.083	3.918	1.746
Ti	0.614	0.493	0.587	0.337	0.828	0.559	0.585	0.629	0.690	0.432
Ca	8.028	3.670	2.622	3.384	3.645	3.318	2.850	2.801	7.762	1.849
Mg	1.664	0.624	1.036	0.786	1.110	0.743	0.700	0.534	2.092	0.283
K	14.288	3.280	11.382	3.609	7.642	6.513	2.846	3.964	12.560	3.150
P	0.832	0.337	0.558	0.410	0.668	0.308	0.218	0.245	1.002	0.458
S	0.380	0.186	0.210	0.164	0.178	0.092	0.170	0.161	0.470	0.456
Cl	0.402	0.191	0.354	0.467	0.240	0.014	0.065	0.049	0.756	0.709
Na	0.273	0.080	0.212	0.103	0.185	0.049	0.123	0.117	0.373	0.136
Fly ashes elementary analysis [% adjusted mass (d.b.)]										
Sample ID	050P0150U1		050P0310U1		050P0465U1		000P0310U1		100P0310U1	
Element	Content	SD	Content	SD	Content	SD	Content	SD	Content	SD
C	89.22	1.77	52.94	10.87	70.37	4.23	92.83	0.5	69.78	2.68
Ca	0.75	0.19	1.17	0.27	1.88	0.62	1.97	0.23	1.83	0.3
Mg	0.46	0.07	0.51	0.08	0.42	0.16	0.34	0.05	0.46	0.34
K	5.98	0.81	22.77	5.53	14.84	1.82	4.3	0.24	16.25	1.67
P	0.24	0.06	0.32	0.09	0.27	0.12	ND	ND	0.1	0.16
S	0.47	0.14	0.82	0.17	0.63	0.15	ND	ND	1.04	0.25
Cl	3.22	0.75	22.26	5.44	11.58	2.46	0.56	0.01	10.55	1.23

the bottom ashes increased from lower to mid-airflow rates, but decreased with higher airflow rates. Moreover, the carbon content in the bottom ashes of samples prepared with 50 % Y_p exceeded that retained in the ashes of sugarcane bagasse and leaves. This difference may be related to the duration of the char consumption phase, although analyzing this hypothesis was deemed impractical due to difficulties in estimating the time.

Regarding S, K, Na and Cl, the compositional analysis revealed that bottom ashes retained lower amounts of these elements as the airflow rate increased. Therefore, the volatility of these elements increased with air supply. Conversely, concentrations of P, Fe, Ca, Ti, and Mg initially decreased at airflow rates between 0.150 and 0.310 kg/sm^2 before increasing between 0.310 and 0.465 kg/sm^2. This behaviour contrasts with the observed Al, which presented a contrary trend. Finally, the content of Si in bottom ashes exhibited positive correlation with airflow rate.

Fly ash composition provides information about efficiency losses caused by unburned carbon bonded to particles ejected from the reactor. It also offers an overview of the proportion of dragged particles containing elements with lower vaporization temperatures, such as K, Na, Cl, S, and P, which are responsible for causing structural problems on internal burners surfaces.

The presence of unburned carbon in fly ashes inversely correlates with the mass loss rate. In other words, lower carbon content was detected in samples burned with $\dot{m}''_a$ equals 0.310 kg/sm^2. These results point out that in terms of combustion efficiency, the best experimental conditions were around the middle airflow level for samples with 50% sugarcane leaves. Furthermore, the unburned carbon bonded to dragged particles may be even more reduced by implementing staged air supply combustion.

Conversely, the change in the concentration of K, Na, Cl, S, and P with airflow was consistent with $\dot{m}''_b$ (Figure 4.13). This outcome is consequent to the fact that elevated values in mass loss rate are associated with higher amounts of particles expelled out of bed.

4.2.6 Combustion gas emissions

From the temporal evolution of each gaseous species emitted during fixed-bed combustion (as illustrated in Figure 4.9), the mean volume concentrations were calculated across all experiments. Such volume concentrations were numerically estimated by using equation 2.9. The results are summarized in Table 4.9.

Table 4.9 – Average gas species emission during all experiments.

Sample ID	CO_2 [% vol.]	CO [% vol.]	C_2H_2 [% vol.]	C_2H_4 [% vol.]	CH_4 [% vol.]	NO [ppmVol]	NH_3 [ppmVol]	O_2 [% vol.]
025P0230U1	10.12	6.43	0.19	0.25	0.58	37.57	245.75	9.39
025P0385U1	8.69	1.44	0.06	0.02	0.09	56.43	75.90	10.87
075P0230U1	7.57	4.65	0.12	0.18	0.38	28.84	230.83	11.11
075P0385U1	9.26	1.51	0.04	0.03	0.13	56.93	193.13	10.46
050P0150U1	6.34	2.61	0.07	0.15	0.22	26.65	30.29	13.94
050P0465U1	7.12	1.11	0.06	0.03	0.07	90.01	30.79	14.06
000P0310U1	8.05	4.57	0.15	0.18	0.30	19.93	182.07	10.45
100P0310U1	10.31	2.22	0.08	0.08	0.21	71.08	256.92	9.80
050P0310U1	13.87	2.54	0.12	0.05	0.19	110.06	147.73	9.07
050P0310U2	8.41	5.37	0.15	0.17	0.43	29.65	226.61	8.21
050P0310U3	10.45	3.90	0.14	0.11	0.30	56.31	182.82	11.65

Firstly, the variation of carbon dioxide mean concentration ([CO_2]) by airflow increasing exhibits a trend similar to the observed for mass loss rate and heating rate change (see Figures 4.13 and 4.15). Under substoichiometric conditions, [CO_2] rose proportionally with the airflow rate until it attained a maximum value around the middle air flow rate level. Further increments in air supply reduced CO_2 portion in combustion gases as the fixed-bed combustion proceeds through the extinction regime.

Unreacted combustible gas levels also experiment [CO_2] tendency (Table 4.9). In a fuel-rich environment, it is expected that combustible gas emissions from bed to reduce as oxygen availability increases (Yang et al., 2004; Čepić; Nakomčić-Smarahdakis, 2017; Tao et al., 2011), but the data obtained from the experimental campaign in this work disagrees with these observations. Particularly, at airflow levels below the critical point, volatile gas emissions align with mass loss rate, indicating increased pyrolysis gas yield. This suggests that, despite the increased oxygen supply, a portion of these gases and oxygen escapes from the reactor, possibly due to poor gas mixing in the freeboard.

One method to assess the extent of combustion reactions is by examining the relationship between the mean contents of volatile gases and CO_2. The value estimated from the experimental results reveal an inversely proportional correlation with air flow rate (Figure 4.19). Hence, although fuel gases and oxygen levels coexist in the freeboard region, inside the fixed-bed, the combustion reactions rate improves with the airflow rate increase. However, it's important to note that exceeding the critical airflow value can lead to adverse effects, such as an increase in the content of unreacted carbon in fly ashes (Table 4.8).

The results demonstrate that, regarding fuel content harnessing, fixed-bed combustion of the evaluated mixtures has the best performance around the critical air flow rate. Finally, to avoid the implications of burning the fuel in rich conditions, additional air feed stages may be employed along the freeboard.

In the case of NO_x precursor gases NO and NH_3, data in Table 4.9 reveals the predominant role of reaction zone stoichiometry upon forming these compounds. In rich conditions, both NO and NH_3 emissions increased with higher airflow supply. Since volatile gases also rise with air $\dot{m}''_a$, its presence hindered NO yield because of NO reduction through equations 4.7. As a result, NO levels were lower than NH3 at airflow rates below $\dot{m}''a.cr$. The convective effect negatively impacted fuel gas emissions when the air supply exceeded the critical air flow rate, and the reaction zone proceeded in a lean environment. However, the decay in volatile

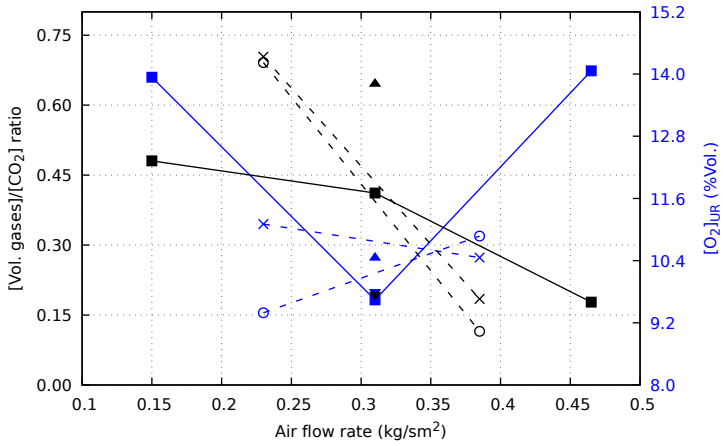

Figure 4.19 – Unreacted volatile gases - Carbon dioxide ratio and excess of oxygen concentration in function of air flow rate. 100% of bagasse (▼), 25% of leaves (×), 50% of leaves (■), 75% of leaves (∗), and 100% of leaves (▲).

gases and higher O_2 availability boosted NO production while NH_3 content in flue gases was reduced.

The proportion of sugarcane residues in the fuel feedstock also played a role in combustion gas emissions. On the one hand, volatile gases to CO_2 emission ratio reduced with the increment in Y_p (Figure 4.19). Besides, NO and NH_3 emissions significantly increase as sugarcane leaves proportion in the fixed-bed grow. This behaviour is expected since sugarcane leaves possess more potassium despite the relatively same nitrogen content in both biomasses. On the other hand, the increment of potassium in the fuel mixture leads to higher gas emissions because alkalis catalytic effect on the pyrolysis phase.

Regarding pollutant gas emissions, the better bed mixture conditions are around similar proportions between bagasse and leaves. Furthermore, to improve the combustion performance, the combustion of such fuel mixture should be carried out under substoichiometric conditions close to the critical air flow rate. Finally, additional air feed stages will warrant lower emissions of environmentally hazardous gases in the flame region over the bed.

5 CONCLUSIONS AND FINAL REMARKS

This work experimentally evaluated the effect of airflow rate and fuel feedstock proportions in fixed-bed combustion performance. For this purpose, a laboratory-scale fixed-bed reactor equipped with instruments for monitoring combustion properties was used. The first part of the thesis discussed the parameters usually employed to analyse the results obtained in this type of study. This analysis was based on a literature review that consolidated all the knowledge reported throughout history. The second part of the work embraced the analysis of the co-combustion of sugarcane byproducts mixtures. The following paragraphs summarize the main findings drawn from the experimental campaign.

Part I: Experimental fixed-bed combustion performance parameters

From the mass loss profile, it was identified three characteristic phases associated with mass loss rate variation: (i) Ignition phase, (ii) Steady-state phase, and (iii) Residual char consumption phase. During the second phase, the ignition front and the reaction zone progress uniformly along the fuel bed. In this period, the volatile content in the biomass is primarily released. Conversely, in the residual char consumption phase, every fuel material left after the end of ignition front propagation burns out. This last phase features a slow reduction in the bed mass due to the char combustion-gasification reactions.

The evolution of pressure drop of the gases flowing across the bed enables determining bed level position during the experiment. From this information, a straightforward criterion was defined to measure the reduction in the bed height by applying a set of statistical tests based on the hypothesis and findings reported in the literature over the local maximum temperature at the final ignition region. The statistical evaluation demonstrates that the maximum ignition temperature may be used as a signal for the bed's free surface arrival. Furthermore, the knowledge of the instantaneous bed level position leads to estimating other parameters to characterize fixed-bed combustion performance as bulk density variation, char consumption rate, and reaction zone thickness. This result represents an important contribution to the experimental study of fixed-bed combustion.

The ignition rate calculation was a topic of discussion in this work because of the ambiguity that emerges from its definition as the product of bed bulk density and ignition front

propagation velocity. The following points stand out after analyzing the results obtained in this work:

1. From bed level position, the bed bulk density variation during the experiment was calculated. It was observed that bulk density changes in comparison with the value estimated before the experiments. This effect could be associated with the morphology of the particles that make up the samples. These particles, being mostly lightweight and flat, behaved as thermally thin under the conditions inside the reaction zone. The higher reaction rates in these particles resulted in a reduction in their terminal velocity, causing a significant increase in particles carried by the oxidant stream. Consequently, the instant bulk density of the bed was reduced.

2. A test of hypothesis about the statistical similarity between the two methodologies used for calculating ignition front velocity yields no apparent difference between both approaches. This evidences that the ignition front velocity is a feature property of the temperature history with little dispersion during the experiment.

3. In comparison to the ignition front velocity, the ignition rate showed characteristics that limited its usefulness for describing fixed-bed combustion performance. First, the effects of airflow rate upon bulk density controls the ignition rate behaviour. Such ignition rate variation showed a different pattern from the commonly reported in the literature from which it is possible to identify the characteristics of three fixed-bed combustion regimes. This discrepancy evidenced the predominant role of packing characteristics over the physicochemical properties of the fuel particles that compose the bed. This finding suggests a bias in the ignition rate that causes the packing properties to prevail.

4. Conversely, the ignition front velocity can be applied as a reliable parameter for fixed-bed combustion analysis. This parameter depends on the airflow supply and the fuel particle properties. In the case of airflow rate, it was possible to distinguish the combustion regimes. At the same time, the bed feedstock composition analysis revealed the influence of the combination between particle and packing properties.

In general, the use of laboratory-scale reactors for fixed-bed combustion research is a valuable tool that, despite its age, might assume an essential role during this period of energy transition. Furthermore, the knowledge generated from experiments with various solid fuel sources offers valuable insights that can be applied at both domestic and industrial scales.

Part II: Co-combustion of sugarcane residues

The proportion of each feedstock composing the biomass mixture significantly influenced the performance of fixed-bed combustion. The combined contribution of sugarcane residues in fixed-bed combustion was closely related to the content of inorganic compounds, especially alkali elements. On one hand, the increase in the content of these elements when a higher proportion of sugarcane leaves was added had a notable impact on the heating rate inside the reaction zone. This effect was caused by the catalytic function of alkali elements on the rate of volatile material release during the pyrolysis stage. The existence of a maximum heating rate in a bed made of biomasses with essentially similar properties, except for ash content and composition, suggests the presence of a critical alkali content. Beyond this critical concentration, the catalytic effect diminishes as the content of alkali metals increases for a given air flow rate. On the other hand, the presence of ashes in the bed reduced the thermal energy released during combustion, likely due to the heat absorption by the ashes, which directly impacted the temperature in the flame region.

The co-combustion of sugarcane bagasse and leaves mixtures in a fixed-bed showed superior performance compared to the separate combustion of each byproduct. The ignition front velocity, mass loss rate, and heating rate exhibited higher values for beds composed of similar proportions of both biomasses burned around the middle airflow level, which roughly coincided with the critical air flow rate. Under these experimental conditions, the duration of the steady phase and the content of unreacted carbon in fly ashes were the lowest. Gas emissions were also affected by the influence of these factors. Thus, the experimental design in this work demonstrated a synergistic nature in the properties of both biomasses when directly burned in fixed-bed reactors.

To better incorporate these byproducts for thermal energy generation, implementing secondary air in the flame region while the bed zone burns with an airflow rate close to the critic airflow rate may prevent higher NO_x gases formation without sacrificing the improved effect of the biomasses co-combustion. In addition, this strategy, combined with control techniques upon the flow of primary air that enters the grate regions, would reduce efficiency losses for unburned carbon bound in bottom ashes.

5.1 Suggestions for future works

Fixed-bed combustion of sugarcane residues mixtures exhibited satisfactory behavior with air flows around 0.310 kg/m^{2}s. This assessment is based on values obtained for consumption rate, heating rate during the ignition phase, and ignition front propagation velocity. Additionally, the maximum combustion temperature was recorded around this air flow rate. However, given the nature of the studied biomasses, characterized by high contents of alkalis and chlorine, forming compounds with low vaporization points at temperatures lower than those observed during the experiments, and considering the elevated nitrogen oxide emissions due to increased oxygen availability under these air flow conditions, it is not recommended to use these biomasses with a single supply of primary air under the conditions observed in this study. Alternatively, it is suggested to extend the research initiated in this work by evaluating inorganic compound emissions under different primary air flows, aiming to determine an optimal primary air flow that, combined with a secondary air supply, reduces deposit formation inside the burner and nitrogen oxide emissions.

Two variables not considered in this study were the initial moisture level of the biomasses and the combustion air preheating temperature. Given that, in practice, sugarcane processing residues are injected into the boiler with a high moisture content, it is essential to complement the results obtained in this study with an analysis of the impact of these two factors under the optimal air flow conditions determined in this work.

Experimental results revealed that the reaction zone propagation is susceptible to the combined effect of biomass particle morphology, bed packing properties, combustion air flow dynamics, and alkali compound content in the fuel. These variables are strongly interconnected, making it impossible to conduct macroscopic experimental studies that unravel the role of each of these factors individually in the biomass fixed-bed combustion behavior. However, under appropriate considerations and based on experimental observations, a numerical approach to the fixed-bed combustion process would allow controlling the level of involvement of fuel physicochemical properties and oxidant flow. Thus, one of the main recommendations for future research focuses on the computational simulation of the combustion process, initially under conditions similar to those imposed by the experiments carried out in this study.

REFERENCES

‘Aliman, I.; Pasek, A. D. The evaluation of experimental and numerical study of combustion process on mini traveling chain grate furnace (incinerator) by computational fluid dynamics method. **AIP Conference Proceedings**, v. 1984, n. 1, p. 030005, jul. 2018.

Anca-Couce, A.; Sommersacher, P.; Evic, N.; Mehrabian, R.; Scharler, R. Experiments and modelling of NOx precursors release (NH3 and HCN) in fixed-bed biomass combustion conditions. **Fuel**, v. 222, p. 529–537, 2018.

Andrade, J. M.; Estévez-Pérez, M. G. Statistical comparison of the slopes of two regression lines: A tutorial. **Analytica Chimica Acta**, v. 838, p. 1–12, ago. 2014.

Barzegar, R.; Yozgatligil, A.; Olgun, H.; Atimtay, A. T. TGA and kinetic study of different torrefaction conditions of wood biomass under air and oxy-fuel combustion atmospheres. **Journal of the Energy Institute**, v. 93, n. 3, p. 889–898, jun. 2020.

Basu, P. **Biomass Gasification, Pyrolysis and Torrefaction**. Boston: Academic Press, 2013. ISBN 978-0-12-396488-5.

Biswas, A. K.; Umeki, K. Simplification of devolatilization models for thermally-thick particles: Differences between wood logs and pellets. **Chemical Engineering Journal**, v. 274, p. 181–191, ago. 2015.

Antonio Bizzo, W.; Lenço, P. C.; Carvalho, D. J.; Veiga, J. P. S. The generation of residual biomass during the production of bio-ethanol from sugarcane, its characterization and its use in energy production. **Renewable and Sustainable Energy Reviews**, v. 29, p. 589–603, jan. 2014.

Blijderveen, M. van; Gucho, E. M.; Bramer, E. A.; Brem, G. Spontaneous ignition of wood, char and RDF in a lab scale packed bed. **Fuel**, v. 89, n. 9, p. 2393–2404, 2010.

Buchmayr, M.; Gruber, J.; Hargassner, M.; Hochenauer, C. Experimental investigation of the primary combustion zone during staged combustion of wood-chips in a commercial small-scale boiler. **Biomass and Bioenergy**, v. 81, p. 356–363, 2015.

Carvalho, D. J. **Generation of bioelectricity in ethanol mill using bagasse sugarcane straw and sorgum**. Tese (Doutorado) — University of Campinas, 2017.

Castro, L. R. **Study of Combustion of Eucalyptus Biomass in a Fixed Bed Reactor**. Tese (Doutorado) — University of Campinas, 2018.

Centro de Tecnologia Canavieira. **Emissões atmosféricas caldeiras à bagaço de cana**. [S.l.], 2009.

Čepić, Z. M.; Nakomčić-Smarahdakis, B. B. Experimental analysis of the influence of air-flow rate on wheat straw combustion in a fixed bed. **Thermal Science**, v. 21, n. 3, 2017.

Dernbecher, A.; Dieguez-Alonso, A.; Ortwein, A.; Tabet, F. Review on modelling approaches based on computational fluid dynamics for biomass combustion systems: Focus on fixed bed and moving grate systems. **Biomass Conversion and Biorefinery**, v. 9, n. 1, p. 129–182, 2019.

Eapen, T.; Blackadar, R.; Essenhigh, R. H. Kinetics of gasification in a combustion pot: A comparison of theory and experiment. **Symposium (International) on Combustion**, v. 16, n. 1, p. 515–522, 1977.

El-Sayed, S. A.; Ismail, M. A.; Mostafa, M. E. Thermal decomposition and combustion characteristics of biomass materials using TG/DTG at different high heating rates and sizes in the air. **Environmental Progress & Sustainable Energy**, v. 38, n. 4, p. 13124, 2019.

Fahmi, R.; Bridgwater, A. V.; Darvell, L. I.; Jones, J. M.; Yates, N.; Thain, S.; Donnison, I. S. The effect of alkali metals on combustion and pyrolysis of Lolium and Festuca grasses, switchgrass and willow. **Fuel**, v. 86, n. 10, p. 1560–1569, jul. 2007.

Fatehi, M.; Kaviany, M. Adiabatic reverse combustion in a packed bed. **Combustion and Flame**, v. 99, n. 1, p. 1–17, 1994.

Febrero, L.; Granada, E.; Regueiro, A.; Míguez, J. L. Influence of Combustion Parameters on Fouling Composition after Wood Pellet Burning in a Lab-Scale Low-Power Boiler. **Energies**, v. 8, n. 9, p. 9794–9816, 2015.

Friberg, R.; Blasiak, W. Measurements of mass flux and stoichiometry of conversion gas from three different wood fuels as function of volume flux of primary air in packed-bed combustion. **Biomass and Bioenergy**, v. 23, n. 3, p. 189–208, 2002.

Gehrmann, H.-J.; Kolb, T.; Seifert, H.; Mark, F.; Frankenhaeuser, M.; Schanssema, A.; Wittstock, K.; Kolb, J. Synergies between biomass and solid recovered fuel in energy conversion processes. **Environmental Engineering Science**, v. 27, n. 7, p. 557–567, 2010.

Girgis, E.; Hallett, W. L. H. Wood Combustion in an Overfeed Packed Bed, Including Detailed Measurements within the Bed. **Energy & Fuels**, v. 24, n. 3, p. 1584–1591, 2010.

Glarborg, P.; Jensen, A. D.; Johnsson, J. E. Fuel nitrogen conversion in solid fuel fired systems. **Progress in Energy and Combustion Science**, v. 29, n. 2, p. 89–113, jan. 2003.

Granada, E.; Eguíia, P.; Antonio Comesaña, J.; Patiño, D.; Porteiro, J.; Saavedra, Á. Experimental analysis of several biomass fuels: The effect of the devolatilization rate on packed bed combustion. **Journal of Renewable and Sustainable Energy**, v. 4, n. 5, p. 053104, 2012.

Guo, Q.; Cheng, Z.; Chen, G.; Yan, B.; Hou, L.; Ronsse, F. Optimal strategy for clean and efficient biomass combustion based on ash deposition tendency and kinetic analysis. **Journal of Cleaner Production**, v. 271, p. 122529, out. 2020.

Hallett, W.; Green, B.; Machula, T.; Yang, Y. Packed bed combustion of non-uniformly sized char particles. **Chemical Engineering Science**, v. 96, p. 1–9, 2013.

Hobbs, M. L.; Radulovic, P. T.; Smoot, L. D. Combustion and gasification of coals in fixed-beds. **Progress in Energy and Combustion Science**, v. 19, n. 6, p. 505–586, 1993.

Horttanainen, M.; Saastamoinen, J.; Sarkomaa, P. Operational Limits of Ignition Front Propagation against Airflow in Packed Beds of Different Wood Fuels. **Energy & Fuels**, v. 16, n. 3, p. 676–686, 2002.

Houshfar, E.; Khalil, R. A.; Løvås, T.; Skreiberg, Ø. Enhanced NOx Reduction by Combined Staged Air and Flue Gas Recirculation in Biomass Grate Combustion. **Energy & Fuels**, v. 26, n. 5, p. 3003–3011, 2012.

Houshfar, E.; Løvås, T.; Skreiberg, Ø. Experimental Investigation on NOx Reduction by Primary Measures in Biomass Combustion: Straw, Peat, Sewage Sludge, Forest Residues and Wood Pellets. **Energies**, v. 5, n. 2, p. 270–290, 2012.

Houshfar, E.; Skreiberg, Ø.; Løvås, T.; Todorović, D.; Sørum, L. Effect of Excess Air Ratio and Temperature on NOx Emission from Grate Combustion of Biomass in the Staged Air Combustion Scenario. **Energy & Fuels**, v. 25, n. 10, p. 4643–4654, 2011.

Houshfar, E.; Skreiberg, ø.; Todorović, D.; Skreiberg, A.; Løvås, T.; Jovović, A.; Sørum, L. NOx emission reduction by staged combustion in grate combustion of biomass fuels and fuel mixtures. **Fuel**, v. 98, p. 29–40, 2012.

Hupa, M.; Karlström, O.; Vainio, E. Biomass combustion technology development – It is all about chemical details. **Proceedings of the Combustion Institute**, v. 36, n. 1, p. 113–134, 2017.

IEA – International Energy Agency. **World Energy Balances 2022 – Total Energy Supply by Source, World 1990-2020**. 2021. Https://www.iea.org/data-and-statistics/data-browser?country=WORLD&fuel=Energy%20supply&indicator=TESbySource.

Franco Jacome, D. L. Avaliação das características físico-químicas das cinzas de bagaço e palha de cana-de-açúcar. 2018.

Jones, J. M.; Darvell, L. I.; Bridgeman, T. G.; Pourkashanian, M.; Williams, A. An investigation of the thermal and catalytic behaviour of potassium in biomass combustion. **Proceedings of the Combustion Institute**, v. 31, n. 2, p. 1955–1963, 2007.

Junejo, A.; Al-Abdeli, Y. M.; Porteiro, J. Role of Primary Freeboard on Staged Combustion of Hardwood Pellets in a Fixed Bed Combustor. **BioEnergy Research**, ago. 2022.

Karlström, O.; Perander, M.; DeMartini, N.; Brink, A.; Hupa, M. Role of ash on the NO formation during char oxidation of biomass. **Fuel**, v. 190, p. 274–280, fev. 2017.

Kessel, L. B. M. van; Arendsen, A. R. J.; Boer-Meulman, P. D. M. de; Brem, G. The effect of air preheating on the combustion of solid fuels on a grate. **Fuel**, v. 83, n. 9, p. 1123–1131, 2004.

Khatami, R.; Stivers, C.; Joshi, K.; Levendis, Y. A.; Sarofim, A. F. Combustion behavior of single particles from three different coal ranks and from sugar cane bagasse in O2/N2 and O2/CO2 atmospheres. **Combustion and Flame**, v. 159, n. 3, p. 1253–1271, mar. 2012.

Khodaei, H.; Al-Abdeli, Y. M.; Guzzomi, F.; Yeoh, G. H. An overview of processes and considerations in the modelling of fixed-bed biomass combustion. **Energy**, v. 88, p. 946–972, 2015.

Khodaei, H.; Guzzomi, F.; Yeoh, G. H.; Regueiro, A.; Patiño, D. An experimental study into the effect of air staging distribution and position on emissions in a laboratory scale biomass combustor. **Energy**, v. 118, p. 1243–1255, 2017.

Khor, A.; Ryu, C.; Yang, Y.-b.; Sharifi, V. N.; Swithenbank, J. Straw combustion in a fixed bed combustor. **Fuel**, v. 86, n. 1, p. 152–160, 2007.

Kluska, J.; Ochnio, M.; Kazimierski, P.; Kardaś, D. Comparison of downdraft and updraft gasification of biomass in a fixed bed reactor. **Archives of Thermodynamics**, v. 39, n. 4, p. 59–69, 2018.

Kolb, T.; Bleckwehl, S.; Gehrmann, H.-J.; Seifert, H. Characterisation of combustion behaviour of refuse derived fuel. **Journal of the Energy Institute**, v. 81, n. 1, p. 1–6, 2008.

Koppejan, J.; Van Loo, S. **The Handbook of Biomass Combustion and Co-Firing**. [S.l.]: Routledge, 2012.

Kuo, J. T.; Hsu, W.-S.; Yo, T.-C. Effect of air distribution on solid fuel bed combustion. **Journal of energy resources technology**, v. 119, n. 2, p. 120–128, 1997.

Van Der Lans, R. P.; Pedersen, LT.; Jensen, A.; Glarborg, P.; Dam-Johansen, K. Modelling and experiments of straw combustion in a grate furnace. **Biomass and Bioenergy**, v. 19, n. 3, p. 199–208, 2000.

Lenis, Y. A.; Agudelo, A. F.; Pérez, J. F. Analysis of statistical repeatability of a fixed bed downdraft biomass gasification facility. **Applied Thermal Engineering**, v. 51, n. 1, p. 1006–1016, 2013.

Levendis, Y. A.; Joshi, K.; Khatami, R.; Sarofim, A. F. Combustion behavior in air of single particles from three different coal ranks and from sugarcane bagasse. **Combustion and Flame**, v. 158, n. 3, p. 452–465, 2011.

Li, Z.; Zhao, W.; Zhao, G.; Zhang, F.; Zhu, Q. Effect of Corn Stalk Length on Combustion Characteristics in a Fixed Bed. **Energy & Fuels**, v. 22, n. 3, p. 2009–2014, 2008.

Liang, L.; Sun, R.; Fei, J.; Wu, S.; Liu, X.; Dai, K.; Yao, N. Experimental study on effects of moisture content on combustion characteristics of simulated municipal solid wastes in a fixed bed. **Bioresource technology**, v. 99, n. 15, p. 7238–7246, 2008.

Magdziarz, A.; Wilk, M. Thermogravimetric study of biomass, sewage sludge and coal combustion. **Energy Conversion and Management**, v. 75, p. 425–430, nov. 2013.

Mahapatra, S.; Dasappa, S. Experiments and analysis of propagation front under gasification regimes in a packed bed. **Fuel Processing Technology**, v. 121, p. 83–90, 2014.

Mahmoudi, A. H.; Markovic, M.; Peters, B.; Brem, G. An experimental and numerical study of wood combustion in a fixed bed using Euler–Lagrange approach (XDEM). **Fuel**, v. 150, p. 573–582, 2015.

Mantananont, N.; Patumsawad, S. Particulate matter and gaseous emission rate from combustion of Thai lignite and agricultural residues in a fixed-bed combustor. **Energy Sources, Part A: Recovery, Utilization, and Environmental Effects**, v. 38, n. 4, p. 478–484, 2016.

Markovic, M.; Bramer, E. A.; Brem, G. Experimental investigation of wood combustion in a fixed bed with hot air. **Waste Management**, v. 34, n. 1, p. 49–62, 2014.

Mason, P. E.; Darvell, L. I.; Jones, J. M.; Pourkashanian, M.; Williams, A. Single particle flame-combustion studies on solid biomass fuels. **Fuel**, v. 151, p. 21–30, 2015.

Mätzing, H.; Gehrmann, H.-J.; Kolb, T.; Seifert, H. Experimental and Numerical Investigation of Wood Particle Combustion in Fixed Bed Reactors. **Environmental Engineering Science**, v. 29, n. 10, p. 907–914, 2012.

Maxwell, D.; Gudka, B. A.; Jones, J. M.; Williams, A. Emissions from the combustion of torrefied and raw biomass fuels in a domestic heating stove. **Fuel Processing Technology**, v. 199, p. 106266, mar. 2020.

Mehrabian, R.; Shiehnejadhesar, A.; Scharler, R.; Obernberger, I. Multi-physics modelling of packed bed biomass combustion. **Fuel**, v. 122, p. 164–178, 2014.

Mehrabian, R.; Zahirovic, S.; Scharler, R.; Obernberger, I.; Kleditzsch, S.; Wirtz, S.; Scherer, V.; Lu, H.; Baxter, L. L. A CFD model for thermal conversion of thermally thick biomass particles. **Fuel Processing Technology**, v. 95, p. 96–108, mar. 2012.

Meng, Q.; Chen, X.; Bu, C.; Ma, J. Experimental study on the controlled air oxidation of sawdust in a packed-bed reactor. **Korean Journal of Chemical Engineering**, v. 29, n. 4, p. 534–539, 2012.

Meng, X.; Sun, R.; Ismail, T. M.; Zhou, W.; Ren, X.; Zhang, R. Parametric studies on corn combustion characteristics in a fixed bed: Primary air flow rate and different corn lengths. **Applied Thermal Engineering**, v. 126, p. 702–716, 2017.

Meng, X.; Sun, R.; Ismail, T. M.; Zhou, W.; Ren, X.; Zhang, R. Parametric studies on corn straw combustion characteristics in a fixed bed: Ash and moisture content. **Energy**, v. 158, p. 192–203, 2018.

Meng, X.; Sun, R.; Liu, X.; Ismail, T. M.; Zhou, W.; El-Salam, M. A.; Ren, X. Assessment of Chopped Corn Straw Lengths for Combustion in a Fixed Bed Using a Numerical Model. **Energy & Fuels**, v. 32, n. 4, p. 5187–5198, 2018.

Milijković, B. M. Experimental Facility for analysis of biomass combustion characteristics. **Thermal Science**, v. 19, n. 1, 2015.

Ministerio de Minas e Energia. Resenha Energética Brasileira 2020. **MME. Brasília**, p. 31, 2021.

Mitchell, E. J. S.; Lea-Langton, A. R.; Jones, J. M.; Williams, A.; Layden, P.; Johnson, R. The impact of fuel properties on the emissions from the combustion of biomass and other solid fuels in a fixed bed domestic stove. **Fuel Processing Technology**, v. 142, p. 115–123, fev. 2016.

Mock, C.; Lee, H.; Choi, S.; Manovic, V. Combustion Behavior of Relatively Large Pulverized Biomass Particles at Rapid Heating Rates. **Energy & Fuels**, v. 30, n. 12, p. 10809–10822, 2016.

Mousavi, S. M.; Fatehi, H.; Bai, X.-S. Multi-region modeling of conversion of a thick biomass particle and the surrounding gas phase reactions. **Combustion and Flame**, v. 237, p. 111725, mar. 2022.

Navidi, W. **Statistics for Engineers and Scientists**. [S.l.]: Mc Graw Hill, 2010.

Nicholls, P. **Underfeed Combustion, Effect of Preheat, and Distribution of Ash in Fuel Beds**. [S.l.]: USGPO, 1934. v. 370.

Niu, Y.; Tan, H.; Hui, S. Ash-related issues during biomass combustion: Alkali-induced slagging, silicate melt-induced slagging (ash fusion), agglomeration, corrosion, ash utilization, and related countermeasures. **Progress in Energy and Combustion Science**, v. 52, p. 1–61, 2016.

Nowakowski, D. J.; Jones, J. M.; Brydson, R. M. D.; Ross, A. B. Potassium catalysis in the pyrolysis behaviour of short rotation willow coppice. **Fuel**, v. 86, n. 15, p. 2389–2402, out. 2007.

Nussbaumer, T. Primary and Secondary Measures for the Reduction of Nitric Oxide Emissions from Biomass Combustion. In: Bridgwater, A. V.; Boocock, D. G. B. (Ed.). **Developments in Thermochemical Biomass Conversion: Volume 1 / Volume 2**. Dordrecht: Springer Netherlands, 1997. p. 1447–1461. ISBN 978-94-009-1559-6.

Nussbaumer, T. Combustion and Co-combustion of Biomass: Fundamentals, Technologies, and Primary Measures for Emission Reduction. **Energy & Fuels**, v. 17, n. 6, p. 1510–1521, nov. 2003.

Olanders, B.; Gunners, N.-E. Some aspects of the formation of nitric oxide during the combustion of biomass fuels in a laboratory furnace. **Biomass and Bioenergy**, v. 6, n. 6, p. 443–451, 1994.

Oman, J.; Tacer, M.; Tuma, M. Overfeed fixed-bed combustion of wood. **Bioresource technology**, v. 67, n. 2, p. 139–147, 1999.

Panahi, A.; Levendis, Y. A.; Vorobiev, N.; Schiemann, M. Direct observations on the combustion characteristics of Miscanthus and Beechwood biomass including fusion and spherodization. **Fuel Processing Technology**, v. 166, p. 41–49, 2017.

Pérez, J. F.; Melgar, A.; Benjumea, P. N. Effect of operating and design parameters on the gasification/combustion process of waste biomass in fixed bed downdraft reactors: An experimental study. **Fuel**, v. 96, p. 487–496, 2012.

Pettersson, E.; Lindmark, F.; Ohman, M.; Nordin, A.; Westerholm, R.; Boman, C. Design changes in a fixed-Bed pellet combustion device: Effects of temperature and residence time on emission performance. **Energy & Fuels**, v. 24, n. 2, p. 1333–1340, 2010.

Polesek-Karczewska, S.; Turzyński, T.; Kardaś, D.; Heda, L. Front velocity in the combustion of blends of poultry litter with straw. **Fuel Processing Technology**, v. 176, p. 307–315, 2018.

Porteiro, J.; Patino, D.; Collazo, J.; Granada, E.; Moran, J.; Miguez, JL. Experimental analysis of the ignition front propagation of several biomass fuels in a fixed-bed combustor. **Fuel**, v. 89, n. 1, p. 26–35, 2010.

Porteiro, J.; Patiño, D.; Miguez, J. L.; Granada, E.; Moran, J.; Collazo, J. Study of the reaction front thickness in a counter-current fixed-bed combustor of a pelletised biomass. **Combustion and Flame**, v. 159, n. 3, p. 1296–1302, 2012.

Porteiro, J.; Patiño, D.; Moran, J.; Granada, E. Study of a fixed-bed biomass combustor: Influential parameters on ignition front propagation using parametric analysis. **Energy & Fuels**, v. 24, n. 7, p. 3890–3897, 2010.

Price-Allison, A.; Lea-Langton, A. R.; Mitchell, E. J. S.; Gudka, B.; Jones, J. M.; Mason, P. E.; Williams, A. Emissions performance of high moisture wood fuels burned in a residential stove. **Fuel**, v. 239, p. 1038–1045, mar. 2019.

Ramirez-Quintero, D. A. Caracterização física de partículas de biomassa separadas por elutriação e peneiramento. 2019.

Rashidian, B.; Al-Abdeli, Y. M.; Patiño, D.; Guzzomi, F. G.; Yeoh, G. H. Effect of freeboard deflectors in the fixed bed combustion of biomass. **Applied Thermal Engineering**, v. 103, p. 543–552, 2016.

Rashidian, B.; Al-Abdeli, Y. M.; Yeoh, G. H.; Patiño, D.; Guzzomi, F. Methodologies for Processing Fixed Bed Combustor Data. **Combustion Science and Technology**, v. 189, n. 1, p. 79–102, 2017.

Rayaprolu, K. **Boilers for Power and Process**. [S.l.]: CRC press, 2009.

Razuan, R.; Chen, Q.; Zhang, X.; Sharifi, V.; Swithenbank, J. Pyrolysis and combustion of oil palm stone and palm kernel cake in fixed-bed reactors. **Bioresource Technology**, v. 101, n. 12, p. 4622–4629, 2010.

Recman, M.; Hájek, J. Experimental reactor for analysing biomass combustion properties. **Chemical Engineering Transactions**, v. 18, p. 977–982, 2009.

Regueiro, A.; Patiño, D.; Granada, E.; Porteiro, J. Experimental study on the fouling behaviour of an underfeed fixed-bed biomass combustor. **Applied Thermal Engineering**, v. 112, p. 523–533, 2017.

Regueiro, A.; Patiño, D.; Porteiro, J.; Granada, E.; Míguez, J. L. Effect of Air Staging Ratios on the Burning Rate and Emissions in an Underfeed Fixed-Bed Biomass Combustor. **Energies**, v. 9, n. 11, 2016.

Rhodes, M. Particle Size Analysis. In: **Introduction to Particle Technology**. [S.l.]: John Wiley & Sons, Ltd, 2008. cap. 1, p. 1–28. ISBN 978-0-470-72710-2.

Riaza, J.; Gibbins, J.; Chalmers, H. Ignition and combustion of single particles of coal and biomass. **Fuel**, v. 202, p. 650–655, 2017.

Rico, J. J.; Pérez-Orozco, R.; Patiño Vilas, D.; Porteiro, J. TG/DSC and kinetic parametrization of the combustion of agricultural and forestry residues. **Biomass and Bioenergy**, v. 162, p. 106485, jul. 2022.

Rodrigues, M. I.; Iemma, A. F. **Experimental Design and Process Optimization**. Boca Raton: CRC Press, 2014. ISBN 978-0-429-16186-5.

Rogaume, T.; Auzanneau, M.; Jabouille, F.; Goudeau, J. C.; Torero, J. L. The effects of different airflows on the formation of pollutants during waste incineration. **Fuel**, v. 81, n. 17, p. 2277–2288, 2002.

Rönnbäck, M.; Axell, M.; Gustavsson, L.; Thunman, H.; Lecher, B. Combustion Processes in a Biomass Fuel Bed-Experimental Results. In: **Progress in Thermochemical Biomass Conversion**. [S.l.]: John Wiley & Sons, Ltd, 2008. cap. 59, p. 743–757. ISBN 978-0-470-69495-4.

Royo, J.; Canalís, P.; Quintana, D.; Díaz-Ramírez, M.; Sin, A.; Rezeau, A. Experimental study on the ash behaviour in combustion of pelletized residual agricultural biomass. **Fuel**, v. 239, p. 991–1000, 2019.

Ryan, J. S.; Hallett, W. L. H. Packed bed combustion of char particles: Experiments and an ash model. **Chemical Engineering Science**, v. 57, n. 18, p. 3873–3882, 2002.

Ryu, C.; Phan, A. N.; Sharifi, V. N.; Swithenbank, J. Co-combustion of textile residues with cardboard and waste wood in a packed bed. **Experimental Thermal and Fluid Science**, v. 32, n. 2, p. 450–458, 2007.

Ryu, C.; Phan, A. N.; Sharifi, V. N.; Swithenbank, J. Combustion of textile residues in a packed bed. **Experimental Thermal and Fluid Science**, v. 31, n. 8, p. 887–895, 2007.

Ryu, C.; Phan, A. N.; Yang, Y.-b.; Sharifi, V. N.; Swithenbank, J. Ignition and burning rates of segregated waste combustion in packed beds. **Waste Management**, v. 27, n. 6, p. 802–810, 2007.

Ryu, C.; Yang, Y. B.; Khor, A.; Yates, N. E.; Sharifi, V. N.; Swithenbank, J. Effect of fuel properties on biomass combustion: Part I. Experiments-fuel type, equivalence ratio and particle size. **Fuel**, v. 85, n. 7-8, p. 1039–1046, 2006.

Saastamoinen, J. J.; Aho, M. J.; Linna, V. L. Simultaneous pyrolysis and char combustion. **Fuel**, v. 72, n. 5, p. 599–609, 1993.

Saastamoinen, J. J.; Horttanainen, M.; Sarkomaa, P. Ignition Wave Propagation and Release of Volatiles in Beds of Wood Particles. **Combustion Science and Technology**, v. 165, n. 1, p. 41–60, 2001.

Saastamoinen, J. J.; Taipale, R.; Horttanainen, M.; Sarkomaa, P. Propagation of the ignition front in beds of wood particles. **Combustion and Flame**, v. 123, n. 1, p. 214–226, 2000.

Saddawi, A.; Jones, J. M.; Williams, A. Influence of alkali metals on the kinetics of the thermal decomposition of biomass. **Fuel Processing Technology**, v. 104, p. 189–197, 2012.

Saeed, M. A.; Andrews, G. E.; Phylaktou, H. N.; Gibbs, B. M. Global kinetics of the rate of volatile release from biomasses in comparison to coal. **Fuel**, v. 181, p. 347–357, out. 2016.

Sakthivadivel, D.; Iniyan, S. Combustion characteristics of biomass fuels in a fixed bed micro-gasifier cook stove. **Journal of Mechanical Science and Technology**, v. 31, n. 2, p. 995–1002, fev. 2017.

Shan, L.; Kong, M.; Bennet, T. D.; Sarroza, A. C.; Eastwick, C.; Sun, D.; Lu, G.; Yan, Y.; Liu, H. Studies on combustion behaviours of single biomass particles using a visualization method. **Biomass and Bioenergy**, v. 109, p. 54–60, 2018.

Shin, D.; Choi, S. The combustion of simulated waste particles in a fixed bed. **Combustion and Flame**, v. 121, n. 1, p. 167–180, 2000.

Simões, V. C. **NOx formation in the combustion of cassava residues, eucalyptus, sugarcane bagasse and straw**. Tese (Doutorado) — University of Campinas, 2022.

Smoot, L. D.; Smith, P. J. **Coal Combustion and Gasification**. Boston, MA: Springer US, 1985. ISBN 978-1-4757-9723-7 978-1-4757-9721-3.

Sommersacher, P.; Brunner, T.; Obernberger, I. Fuel indexes: A novel method for the evaluation of relevant combustion properties of new biomass fuels. **Energy and Fuels**, v. 26, n. 1, p. 380–390, 2012.

Sommersacher, P.; Brunner, T.; Obernberger, I.; Kienzl, N.; Kanzian, W. Combustion related characterisation of Miscanthus peat blends applying novel fuel characterisation tools. **Fuel**, v. 158, p. 253–262, 2015.

Stuart, B. H. **Infrared Spectroscopy: Fundamentals and Applications**. Chichester, West Sussex, England ; Hoboken, NJ: [s.n.], 2004. ISBN 978-0-470-85428-0.

Stubenberger, G.; Scharler, R.; Zahirović, S.; Obernberger, I. Experimental investigation of nitrogen species release from different solid biomass fuels as a basis for release models. **Fuel**, v. 87, n. 6, p. 793–806, 2008.

Stubington, JF.; Fenton, H. Combustion characteristics of dried and pelletized bagasse. **Combustion Science and Technology**, v. 37, n. 5-6, p. 285–299, 1984.

Sugarcane Renewable Energy. **Cartilha – Processamento e queima de palha de cana-de-açúcar**. [S.l.], 2019.

Sun, R.; Ismail, T. M.; Ren, X.; El-Salam, M. A. Effect of ash content on the combustion process of simulated MSW in the fixed bed. **Waste Management**, v. 48, p. 236–249, 2016.

Sun, R.; Ismail, T. M.; Ren, X.; El-Salam, M. A. Influence of simulated MSW sizes on the combustion process in a fixed bed: CFD and experimental approaches. **Waste Management**, v. 49, p. 272–286, 2016.

Tanui, J. K.; Kioni, P. N.; Mirre, T.; Nowitzki, M. The effect of carbon dioxide on flame propagation speed of wood combustion in a fixed bed under oxy-fuel conditions. **Fuel Processing Technology**, v. 179, p. 285–295, 2018.

Tanui, J. K.; Kioni, P. N.; Mirre, T.; Nowitzki, M.; Karuri, N. W. The influence of particle packing density on wood combustion in a fixed bed under oxy-fuel conditions. **Energy**, v. 194, p. 116863, mar. 2020.

Tao, L.; Zhao, G.; Sun, R. Combustion gas and NO emission characteristics of hazardous waste mixture particles in a fixed bed. **Korean Journal of Chemical Engineering**, v. 28, n. 3, p. 778–787, 2011.

Tao, L.; Zhao, G.; Sun, R.; Wang, Q. Combustion characteristics of particles of hazardous solid waste mixtures in a fixed bed. **Journal of Hazardous Materials**, v. 181, n. 1, p. 305–314, 2010.

Thunman, H.; Leckner, B. Ignition and propagation of a reaction front in cross-current bed combustion of wet biofuels. **Fuel**, v. 80, n. 4, p. 473–481, 2001.

Tripathi, P.; Rao, L. Single particle and packed bed combustion characteristics of high ash and high plastic content refuse derived fuel. **Fuel**, v. 308, p. 121983, jan. 2022.

Trudel, É.; Hallett, W. L. H.; Wiens, E.; O'Neil, J. D.; Busigin, M. K.; Berdusco, D. Fuel particle shape effects in the packed bed combustion of wood. **Combustion and Flame**, v. 198, p. 100–111, 2018.

Turns, S. **An Introduction to Combustion Third Edition**. [S.l.]: McGraw-Hill Education, 2011.

Vakkilainen, E. K. **Steam Generation from Biomass: Construction and Design of Large Boilers**. [S.l.]: Butterworth-Heinemann, 2016.

Varunkumar, S.; Rajan, N. K. S.; Mukunda, H. S. Single Particle and Packed Bed Combustion in Modern Gasifier Stoves—Density Effects. **Combustion Science and Technology**, v. 183, n. 11, p. 1147–1163, 2011.

Varunkumar, S.; Rajan, N. K. S.; Mukunda, H. S. Universal Flame Propagation Behavior in Packed Bed of Biomass. **Combustion Science and Technology**, v. 185, n. 8, p. 1241–1260, 2013.

Vorotinskienė, L.; Paulauskas, R.; Zakarauskas, K.; Navakas, R.; Skvorčinskienė, R.; Striūgas, N. Parameters influencing wet biofuel drying during combustion in grate furnaces. **Fuel**, v. 265, p. 117013, abr. 2020.

Wiinikka, H.; Gebart, R. Critical Parameters for Particle Emissions in Small-Scale Fixed-Bed Combustion of Wood Pellets. **Energy & Fuels**, v. 18, n. 4, p. 897–907, 2004.

Wiinikka, H.; Gebart, R. The influence of fuel type on particle emissions in combustion of biomass pellets. **Combustion Science and Technology**, v. 177, n. 4, p. 741–763, 2005.

Wiinikka, H.; Gebart, R.; Boman, C.; Bostrom, D.; Nordin, A.; Ohman, M. High-temperature aerosol formation in wood pellets flames: Spatially resolved measurements. **Combustion and Flame**, v. 147, n. 4, p. 278–293, 2006.

Wiinikka, H.; Gebart, R.; Boman, C.; Boström, D.; Öhman, M. Influence of fuel ash composition on high temperature aerosol formation in fixed bed combustion of woody biomass pellets. **Fuel**, v. 86, n. 1, p. 181–193, 2007.

Williams, A.; Jones, J. M.; Ma, L.; Pourkashanian, M. Pollutants from the combustion of solid biomass fuels. **Progress in Energy and Combustion Science**, v. 38, n. 2, p. 113–137, 2012.

Williams, F. A. **Combustion Theory**. [S.l.]: CRC Press, 2018.

Woodruff, E. B.; Lammers, H. B.; Lammers, T. F. **Steam Plant Operation, 10th Edition**. [S.l.]: McGraw-Hill Education, 2017. ISBN 978-1-259-64133-6.

Yang, Y. B.; Nasserzadeh, V.; Goodfellow, J.; Swithenbank, J. Simulation of Channel Growth in a Burning Bed of Solids. **Chemical Engineering Research and Design**, v. 81, n. 2, p. 221–232, 2003.

Yang, Y. B.; Ryu, C.; Khor, A.; Sharifi, V. N.; Swithenbank, J. Fuel size effect on pinewood combustion in a packed bed. **Fuel**, v. 84, n. 16, p. 2026–2038, 2005.

Yang, Y. B.; Sharifi, V. N.; Swithenbank, J. Effect of air flow rate and fuel moisture on the burning behaviours of biomass and simulated municipal solid wastes in packed beds. **Fuel**, v. 83, n. 11, p. 1553–1562, 2004.

Yang, Y. B.; Sharifi, V. N.; Swithenbank, J. Numerical Simulation of the Burning Characteristics of Thermally-Thick Biomass Fuels in Packed-Beds. **Process Safety and Environmental Protection**, v. 83, n. 6, p. 549–558, 2005.

Yang, Y. B.; Yamauchi, H.; Nasserzadeh, V.; Swithenbank, J. Effects of fuel devolatilisation on the combustion of wood chips and incineration of simulated municipal solid wastes in a packed bed. **Fuel**, v. 82, n. 18, p. 2205–2221, 2003.

Yin, C.; Rosendahl, L. A.; Kær, S. K. Grate-firing of biomass for heat and power production. **Progress in Energy and Combustion Science**, v. 34, n. 6, p. 725–754, 2008.

Zhao, W.; Li, Z.; Wang, D.; Zhu, Q.; Sun, R.; Meng, B.; Zhao, G. Combustion characteristics of different parts of corn straw and NO formation in a fixed bed. **Bioresource Technology**, v. 99, n. 8, p. 2956–2963, 2008.

Zhao, W.; Li, Z.; Zhao, G.; Zhang, F.; Zhu, Q. Effect of air preheating and fuel moisture on combustion characteristics of corn straw in a fixed bed. **Energy Conversion and Management**, v. 49, n. 12, p. 3560–3565, 2008.

Zhou, C.; Liu, G.; Cheng, S.; Fang, T.; Lam, P. K. S. Thermochemical and trace element behavior of coal gangue, agricultural biomass and their blends during co-combustion. **Bioresource Technology**, v. 166, p. 243–251, ago. 2014.

Zhou, H.; Jensen, A. D.; Glarborg, P.; Jensen, P. A.; Kavaliauskas, A. Numerical modeling of straw combustion in a fixed bed. **Fuel**, v. 84, n. 4, p. 389–403, 2005.

Zhou, H.; Jensen, A. D.; Glarborg, P.; Kavaliauskas, A. Formation and reduction of nitric oxide in fixed-bed combustion of straw. **Fuel**, v. 85, n. 5, p. 705–716, 2006.

Zhou, X.; Torero, J. L.; Goudeau, J. C.; Bregeon, B. On the Propagation of a Reaction Front Through a Porous Fuel in the Presence of an Opposed Forced Flow: Application to Mixtures Characteristic of Municipal Waste. **Combustion Science and Technology**, v. 110–111, n. 1, p. 123–146, 1995.

APPENDIX A – EVALUATION OF METHODOLOGIES FOR IGNITION FRONT PROPAGATION VELOCITY ESTIMATION

Ignition rate is a key parameter for the evaluation of fixed bed combustion performance. It represents the mass flow which the ignition front advances along the bed and it is equal to the product between the bed bulk density (ρ_b) and the ignition front propagation velocity (v_{ig}):

$$\dot{m}''_{ig} = \rho_b v_{ig} \tag{A.1}$$

Bulk density is straightforwardly determined from the mass of the bed and its volume including void spaces. On the other hand, the propagation velocity may be calculated from two approaches, each one requiring to define a reference time (t_{ref}) from temperature history:

(i) By choosing a fixed temperature inside the ignition phase and taking the time when such temperature is registered at each thermocouple along the bed.

(ii) By taking the time at which each thermocouple measures the surge in temperature just at ignition phase onset (IPO).

In any case, v_{ig} is estimated by taking the slope obtained from the least-squares regression equation of the line that relates the position of the thermocouples and t_{ref}. Nevertheless, confusion may arise because the existence of two methodologies. In literature authors have used any of both approaches without a support for explain their choice.

In this section it is verified if there are considerable discrepancies for the calculation of v_{ig} by using the above approaches. For this purpose, a series of statistic hypothesis tests are carried out over the slopes obtained from the linear models considered. Initially, it is evaluated if v_{ig} is affected by the reference temperature chosen in the method (i). Afterwards, the ignition fronts propagation velocities calculated from approaches (i) and (ii) are statistically compared. In the both cases, the analysis are applied to the data obtained during the experimental campaign in this thesis.

Effect of the reference chosen temperature

The Figure A.1 shows the temperature historic obtained during fixed-bed combustion of the sample *025P0230U1*. Considering the first approach, there were chosen the following temperatures inside the ignition phase: 100, 200, 400, 600 and 800 °C. Figure A.1 also plots the position and time when the thermocouples record these temperatures. In addition, the Table A.1 contains the data plotted in the position vs time graph for each reference temperature.

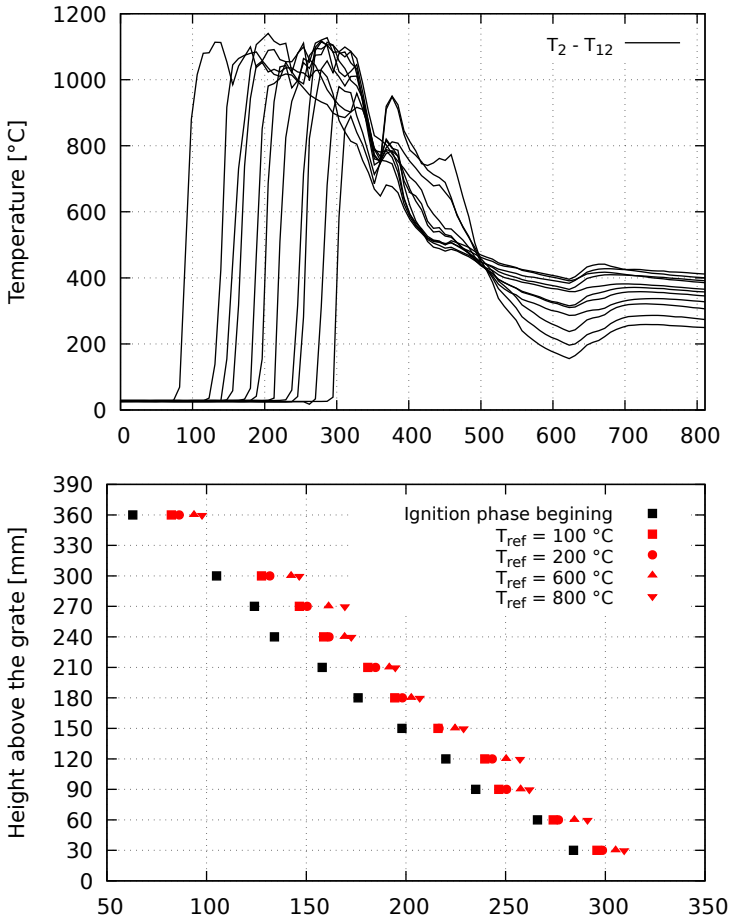

Figure A.1 – Temperature history and isotemperatures field for *025P0230U1*.

In order to evaluate if in the approach (i) the selected temperature affects the model that allows to predict the ignition front position along the bed it is considered a multilinear model. This model relates position as dependent variable with time and temperature as independent variables by following the linear expression:

$$H = b_0 + b_1 T_{ref} + b_2 t_{ref} + b_3 (T_{ref} \times t_{ref}) \tag{A.2}$$

Table A.1 – Data used in Figure A.1.

Thermocouple	Reference time [s]					
position [mm]	100	200	400	600	800	IPO
30	296	299	302	305	309	272
60	274	276	280	285	291	279
90	247	250	255	258	262	216
120	240	243	246	250	257	220
150	216	217	221	225	229	213
180	194	198	199	203	207	187
210	181	185	188	192	195	165
240	159	161	165	169	173	132
270	147	150	155	161	169	128
300	128	132	139	142	147	110
360	82	86	90	94	98	70

where b_i with $i = 0, 1, 2, 3$ represents the coefficients determined by the least-squares regression and T_{ref} the reference temperature. Observe that an interaction variable between t_{ref} and T_{ref} is considered in the model. Through the R statistical package this model was fitted by least-squares regression. However, it was necessary to adjust the data in Table A.1 so that all the times associated to each T_{ref} share the same initial point at t = 0. After this modification and define the linear model, the results generated by R are the following:

```
Call:
lm(formula = Height ~ Temp + Time + Temp*Time, data = datostTL)

Residuals:
   Min      1Q  Median      3Q     Max
-12.311  -5.439   1.273   6.343  13.347

Coefficients:
             Estimate Std. Error t value Pr(>|t|)
(Intercept)  3.644e+02  4.643e+00  78.483   <2e-16 ***
Temp         4.685e-03  1.235e-02   0.379    0.706
Time        -1.594e+00  3.579e-02 -44.531   <2e-16 ***
Temp:Time   -4.532e-05  9.533e-05  -0.475    0.637
---
Signif. codes: 0 '***' 0.001 '**' 0.01 '*' 0.05 '.' 0.1 ' ' 1
```

```
Residual standard error: 7.481 on 40 degrees of freedom
Multiple R-squared: 0.9949,Adjusted R-squared: 0.9945
F-statistic: 2579 on 3 and 40 DF, p-value: < 2.2e-16
```

The summary above presents the main parameters associated with the adjusted linear model. The coefficient of determination (`Multiple R-squared`) quantifies the strength of the linear relationship (Navidi, 2010). A R-square close to 1 indicates a strong linear association among the independent and dependent variables. For the sample *025P0230U1*, the R-squared is equal to 0.9934; therefore the linear model may be considered an adequate representation of the relationship between ignition front position, time and the reference temperature.

The values of the b's coefficients are also presented. In this case, `(Intercept)`, `Temp`, `Time`, and `Temp:Time` corresponds to the coefficients b_0, b_1, b_2, and b_3, respectively. Each one of the least-squares coefficients are submit at a statistical test that evaluates the null hypothesis that affirms the coefficient itself has a value zero. If there are enough statistical evidence to demonstrate that the null hypothesis is true, the coefficient may be considered to have little influence over the dependent variable. All the tests are carried out at a significant level of 5% and are assessed through the p-value. If the p-value obtained is less than 0.05 (5%), the null hypothesis may be discarded. Conversely, if the p-value is greater than 0.05, the null hypothesis may be not discarded. In the summary of the model above, the p-value for the test is given by the column labeled `Pr(>|t|)`.

Observing the results, both reference temperature and the interaction factor between time and reference temperature have little influence on the model. However, the time variable reveals to have an important role in the linear model. Therefore, for the sample *025P0230U1* it is possible to conclude that the model that describes the ignition front position (and implicitly the intercept and slope) is independent of the reference temperature selected. The Table A.2 presents the results of the previous analysis performed over all the samples employed in this work. As can be seen, the conclusion drawn from the sample *025P0230U1* may be generalized over other types of fixed bed of particles, with the exception of the samples *025P0385Un1* and *050P0465U1*. However, in those samples the coefficients b_1 and b_3 have values close to zero, allowing to consider that their influence over their respective models is almost neglected.

Table A.2 – Results obtained from test of hypothesis.

Sample ID	R^2	b_0	b_0 p-val	b_1	b_1 p-val	b_2	b_2 p-val	b_3	b_3 p-val
025P0230U1	0.9949	364.4	1.966×10^{-45}	4.658×10^{-3}	0.706	-1.594	1.056×10^{-35}	-4.532×10^{-5}	0.637
025P0385U1	0.7285	429.5	5.98×10^{-16}	-3.198×10^{-1}	1.840×10^{-4}	-1.807	4.22×10^{-10}	2.184×10^{-3}	2.20×10^{-4}
075P0230U1	0.992	369.4	1.657×10^{-41}	5.581×10^{-3}	0.725	-1.499	3.63×10^{-32}	4.680×10^{-5}	0.671
075P0385U1	0.9889	381.5	1.858×10^{-38}	-3.488×10^{-3}	0.857	-1.873	2.590×10^{-29}	3.471×10^{-5}	0.831
050P0150U1	0.9885	367.2	1.584×10^{-38}	-4.431×10^{-3}	0.812	-1.307	7.106×10^{-29}	-3.403×10^{-5}	0.773
050P0465U1	0.7253	418.1	4.57×10^{-16}	-0.309	1.850×10^{-4}	-1.502	4.53×10^{-10}	1.839×10^{-3}	1.920×10^{-4}
000P0310U1	0.9934	373.1	3.975×10^{-43}	2.405×10^{-3}	0.868	-1.241	1.033×10^{-33}	$3.737 \times 10^{-}6$	0.964
100P0310U1	0.995	349.8	4.266×10^{-46}	4.248×10^{-3}	0.712	-1.069	4.834×10^{-36}	-2.315×10^{-5}	0.714
050P0310U1	0.9961	364.6	8.074×10^{-48}	4.625×10^{-4}	0.966	-1.410	2.857×10^{-38}	5.977×10^{-5}	0.409
050P0310U2	0.9946	359.8	3.127×10^{-45}	-7.452×10^{-3}	0.545	-1.756	2.581×10^{-35}	-4.810×10^{-6}	0.964
050P0310U3	0.9908	372.6	3.197×10^{-40}	2.382×10^{-3}	0.890	-1.474	7.460×10^{-31}	2.197×10^{-5}	0.851

Comparison of both methodologies for v_{ig} estimation

In previous section it was demonstrated that linear model describing the ignition front position is independent on the reference temperature by using the approach (i). Therefore, in general the model that better predicts the ignition front position takes the form:

$$Height = b_0 + b_1 t_{ref} \tag{A.3}$$

where b_0 is the intercept of the line with the y-axis and b_1 the slope, which is directly associated with v_{ig}.

The next task was to verify if there is some difference from the results yield by employing either approach (i) or (ii) in the determination of v_{ig}. Aiming to carry out this comparison, it was applied a statistical test of hypotheses that evaluated the equality between the slopes obtained from the linear models defined by the approaches.

The procedure effectuated was a Student's t-test based in a pooled variance made up of the variances of each of the regression models as suggested by Andrade e Estévez-Pérez (2014). The data used as example were taken from the experimental results for sample *050P0465U1* showed in Table A.1. For the approach based in a reference temperature, it was used the data registered for 200 °C. In the column labeled IPB are presented those time when ignition phase began in every thermocouple position along the fixed-bed (approach ii).

Initially it was necessary to carry out an statistical test over the null hypothesis claiming the squared errors of the regression models ($s^2_{(y/x)_i}$) were taken from a normal distribution possessing the same variance (homoscedasticity). This is:

$$s^2_{(y/x)_1} / s^2_{(y/x)_2} = 1 \tag{A.4}$$

The previous relationship between regression model variances has a Fisher-Snedecor's F distribution (Andrade; Estévez-Pérez, 2014) with $n_1 - 1$ and $n_2 - 1$ degrees of freedom. n_1 and n_2 represent the pairs of x and y in each set of data in the evaluated models. This test is evaluated with a significant level of 1%. If the null hypothesis of homoscedasticity cannot be

rejected, it is possible to apply the t-test over the slopes of both regression models. This test follows the expression:

$$t_{exp} = \frac{(b_1 - b_2)}{\sqrt{s^2_{(y/x),pool}[1/\sum(x_{i,1} - \bar{x}_1)^2 + 1/\sum(x_{i,2} - \bar{x}_2)^2]}} \tag{A.5}$$

where the pooled variance $s^2_{(y/x),pool}$ is calculated from the variances of each linear model:

$$s^2_{(y/x),pool} = \frac{(n_1 - 2)s^2_{(y/x)_1} + (n_1 - 2)s^2_{(y/x)_1}}{n_1 + n_2 - 4} \tag{A.6}$$

From this part, the subindex 1 and 2 correspond to the parameters obtained by approaches (i) and (ii), respectively. The t-Student test is carried out at a 5% of significant level. The values for the main parameters of the test are the following:

$$b_1 = -1.606 \tag{A.7}$$

$$s_{(y/x)_1} = 50.673 \tag{A.8}$$

$$b_2 = -1.500 \tag{A.9}$$

$$s_{(y/x)_2} = 46.545 \tag{A.10}$$

$$p - value(s_{(y/x)_1}/s_{(y/x)_2}) = 0.451 \tag{A.11}$$

$$p - value(b_1 - b_2) = 0.0352 \tag{A.12}$$

The results show that, on the case of sample *025P0230U1* there are sufficient statistical evidence to reject the null hypothesis. Therefore, it is possible to affirm that the ignition front propagation velocity estimated by approach (i) and (ii) are different.

The Table A.3 presents the results obtained after perform the statistical test on all the samples analyzed in this work. As can be seen, in most of the samples there are similarity in the slopes of the linear models based on approaches (i) and (ii).

Although statistically the estimation of v_{ig} is independent of the reference employed, it is necessary to point out that ignition front represents the boundary of the reaction zone. The combustion of the particles in a fixed bed is a process made up of sequential phases that begins when the particle temperature increases from room conditions. Since each one of the

Table A.3 – Results from statistical t-test for slopes similarity.

Sample	b_1	$s_{(y/x)_1}$	b_2	$s_{(y/x)_2}$	p-value$(s_{(y/x)_1}/s_{(y/x)_2})$	p-value$(b_1 - b_2)$
025P0230U1	-1.606	50.673	-1.500	46.545	0.451	0.035
025P0385U1	-1.391	77.560	-1.540	361.870	0.016	0.131
075P0230U1	-1.485	85.638	-1.460	171.193	0.158	0.732
075P0385U1	-1.865	123.638	-1.866	267.711	0.133	0.991
050P0150U1	-1.314	130.861	-1.324	128.91	0.488	0.887
050P0465U1	-1.146	85.656	-1.215	180.633	0.141	0.256
000P0310U1	-1.243	68.512	-1.193	138.368	0.155	0.357
100P0310U1	-1.072	47.759	-1.079	108.421	0.119	0.869
050P0310U1	-1.396	48.757	-1.396	78.538	0.244	0.996
050P0310U2	-1.764	70.980	-1.684	162.629	0.116	0.328
050P0310U3	-1.464	118.324	-1.463	307.727	0.085	0.995

phases develop inside the reaction zone, it is more convenient in physical terms considering as reference time for v_{ig} estimation the moment when the particles temperature increases quickly. Therefore, it is recommended to use the second approach.

APPENDIX B – STATISTICAL ANALYSIS OF MODEL 4.9 APPLIED OVER REACTION ZONE BEHAVIOUR PARAMETERS

Table B.1 – Statistical evaluation of linear model 4.9 for $\dot{m}''_{ig}$

Stat	Reg. coeff.	Std. error	t-value	p-value (b_i = 0)
b_0	1.974×10^{-2}	3.411×10^{-2}	0.579	0.603
$b_{\dot{m}a}$	3.245×10^{-1}	1.728×10^{-1}	1.878	0.157
b_{Yp}	1.163×10^{-3}	5.193×10^{-4}	2.239	0.111
$b_{\dot{m}a2}$	-5.654×10^{-1}	2.528×10^{-1}	-2.236	0.111
b_{Yp2}	-1.031×10^{-5}	2.514×10^{-6}	-4.10	0.026
$b_{\dot{m}a \times Yp}$	-9.971×10^{-4}	1.455×10^{-3}	-0.685	0.542
Res. Std. Err.	0.005639			
R^2	0.9253			
ANOVA				
Source of Var.	SS	MSQ	F	p-value
Regression	0.001182	0.000236	7.433	0.0647
Error	0.000095	0.000032		
Total	0.001277			

Table B.2 – Statistical evaluation of linear model 4.9 for v_{ig}

Stat	Reg. coeff.	Std. error	t-value	p-value (b_i = 0)
b_0	1.652×10^{-2}	1.297	0.359	0.744
$b_{\dot{m}a}$	7.332	6.572	1.116	0.346
b_{Yp}	3.595×10^{-3}	1.975×10^{-2}	0.182	0.867
$b_{\dot{m}a2}$	-1.663	9.614	-1.730	0.182
b_{Yp2}	-2.098×10^{-4}	9.558×10^{-5}	-2.195	0.116
$b_{\dot{m}a \times Yp}$	5.822×10^{-2}	5.531×10^{-2}	1.053	0.370
Res. Std. Err.	0.2144			
R^2	0.6761			
ANOVA				
Source of Var.	SS	MSQ	F	p-value
Regression	0.425823	0.057580	1.252	0.4545
Error	0.137925	0.045975		
Total	0.425823			

Table B.3 – Statistical evaluation of linear model 4.9 for $\dot{m}''_b$

Stat	Reg. coeff.	Std. error	t-value	p-value ($b_i = 0$)
b_0	2.857×10^{-2}	1.34×10^{-2}	2.132	0.123
$b_{\dot{m}a}$	3.217×10^{-1}	6.791×10^{-2}	4.737	0.018
b_{Yp}	-9.207×10^{-5}	2.040×10^{-4}	-0.451	0.682
$b_{\dot{m}a2}$	-6.735×10^{-1}	9.934×10^{-2}	-6.780	0.007
b_{Yp2}	-5.708×10^{-6}	9.876×10^{-7}	-5.780	0.010
$b_{\dot{m}a \times Yp}$	1.880×10^{-3}	5.716×10^{-4}	3.289	0.046
Res. Std. Err.	0.002216			
R^2	0.9598			
ANOVA				
Source of Var.	SS	MSQ	F	p-value
Regression	0.000352	7.0372×10^{-5}	14.34	0.02636
Error	1.4726×10^{-5}	4.9090×10^{-6}		
Total	0.000367			

Table B.4 – Statistical evaluation of linear model 4.9 for $\dot{m}''_{char}$

Stat	Reg. coeff.	Std. error	t-value	p-value ($b_i = 0$)
b_0	2.056×10^{-3}	7.231×10^{-3}	0.284	0.7947
$b_{\dot{m}a}$	5.080×10^{-2}	3.664×10^{-2}	1.386	0.2597
b_{Yp}	1.14×10^{-4}	1.101×10^{-4}	1.040	0.3747
$b_{\dot{m}a2}$	-1.011×10^{-1}	5.360×10^{-2}	-1.886	0.1558
b_{Yp2}	-1.528×10^{-6}	5.329×10^{-7}	-2.867	0.0642
$b_{\dot{m}a \times Yp}$	9.358×10^{-5}	3084×10^{-4}	0.303	0.7814
Res. Std. Err.	0.001195			
R^2	0.788			
ANOVA				
Source of Var.	SS	MSQ	F	p-value
Regression	1.593793e-5	$3.187\,586 \times 10^{-6}$	2.231	0.2706
Error	4.2871×10^{-6}	1.4290×10^{-6}		
Total	$2.022\,50 \times 10^{-5}$			

Table B.5 – Statistical evaluation of linear model 4.9 for dT/dt

Stat	Reg. coeff.	Std. error	t-value	p-value ($b_i = 0$)
b_0	-9.380×10^2	5.692×10^2	-1.648	0.197
$b_{\dot{m}a}$	1.444×10^4	2.884×10^3	5.005	0.0154
b_{Yp}	1.711×10^1	8.666	1.975	0.1428
$b_{\dot{m}a2}$	-2.503×10^4	4.218×10^3	-5.932	0.010
b_{Yp2}	-2.985×10^{-1}	4.194×10^{-2}	-7.116	0.006
$b_{\dot{m}a \times Yp}$	4.014×10^1	2.427×10^1	1.654	0.1968
Res. Std. Err.	94.09			
R^2	0.9572			
ANOVA				
Source of Var.	SS	MSQ	F	p-value
Regression	593344.3	118 668.9	13.4	0.02896
Error	26 560	8853		
Total	619904.3			

Table B.6 – Statistical evaluation of linear model 4.9 for T_{max}

Stat	Reg. coeff.	Std. error	t-value	p-value ($b_i = 0$)
b_0	1123.693 82	195.132 72	5.759	0.0104
$b_{\dot{m}a}$	213.331 44	988.754 83	0.216	0.8430
b_{Yp}	0.779 90	2.970 79	0.263	0.8099
$b_{\dot{m}a2}$	−653.058 08	1446.361 04	-0.452	0.6823
b_{Yp2}	−0.015 90	0.014 38	-1.106	0.3495
$b_{\dot{m}a \times Yp}$	−0.422 18	8.321 61	-0.051	0.9627
Res. Std. Err.	32.26			
R^2	0.7827			
ANOVA				
Source of Var.	SS	MSQ	F	p-value
Regression	11241.23	2248.247	2.161	0.2794
Error	3121.6	1040.5		
Total	14362.86			

Table B.7 – Statistical evaluation of linear model 4.9 for t_{SP}

Stat	Reg. coeff.	Std. error	t-value	p-value ($b_i = 0$)
b_0	4.354×10^2	1.791×10^2	2.431	0.0933
$b_{\dot{m}a}$	-1.340×10^3	9.077×10^2	-1.476	0.2364
b_{Yp}	-8.473×10^{-1}	2.727	-0.311	0.7764
$b_{\dot{m}a2}$	2.949×10^3	1.328×10^3	2.221	0.1129
b_{Yp2}	3.735×10^{-2}	1.320×10^{-2}	2.830	0.0662
$b_{\dot{m}a \times Yp}$	-9.104	7.639	-1.192	0.3191
Res. Std. Err.	29.61			
R^2	0.7683			
ANOVA				
Source of Var.	SS	MSQ	F	p-value
Regression	8721.994	1744.399	1.989	0.3031
Error	2630.5	876.8		
Total	1132.54			

Table B.8 – Statistical evaluation of linear model 4.9 for $m_{r,SP}$

Stat	Reg. coeff.	Std. error	t-value	p-value ($b_i = 0$)
b_0	27.774 225	44.353 608	0.626	0.576
$b_{\dot{m}a}$	$-34.902\,071$	224.743 677	-0.155	0.886
b_{Yp}	0.313 221	0.675 259	0.464	0.674
$b_{\dot{m}a2}$	26.140 717	328.757 429	0.080	0.942
b_{Yp2}	$-0.002\,116$	0.003 268	-0.647	0.563
$b_{\dot{m}a \times Yp}$	$-0.584\,681$	1.891 499	-0.309	0.777
Res. Std. Err.	7.332			
R^2	0.6211			
ANOVA				
Source of Var.	SS	MSQ	F	p-value
Regression	264.3304	52.866 08	0.9834	0.5412
Error	161.279	53.760		
Total	425.6095			

APPENDIX C – EXPERIMENTAL CAMPAIGN RESULTS FOR ALL SAMPĹES

Sample 025P0230U1

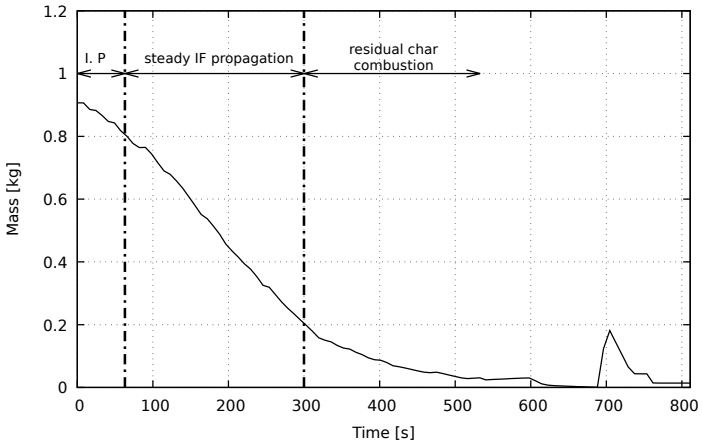

Figure C.1 – Mass loss variation during fixed-bed combustion experiment of sample *025P0230U1*

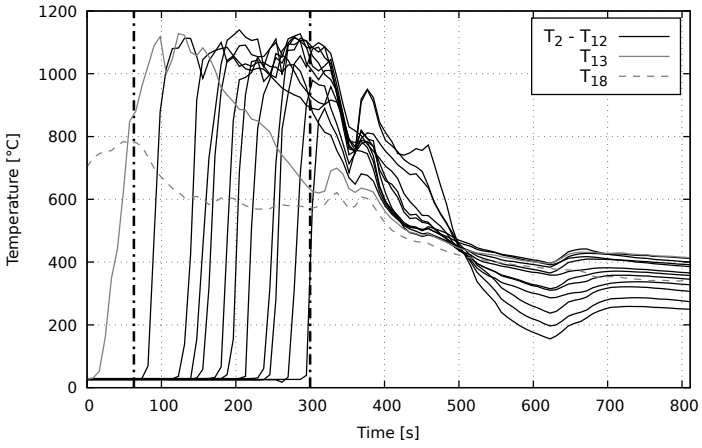

Figure C.2 – Temperature history for *025P0230U1*

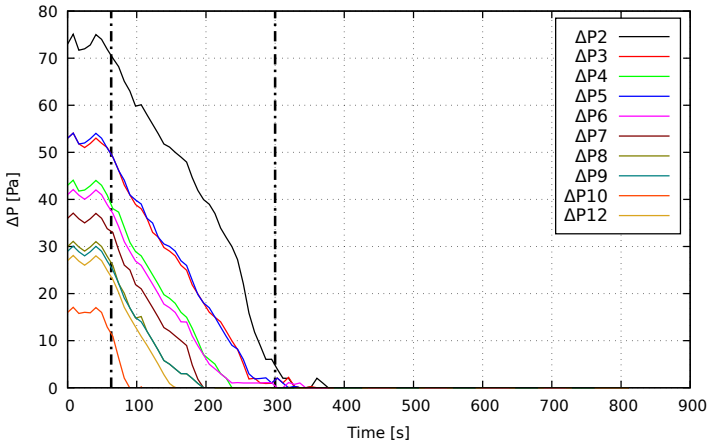

Figure C.3 – Pressure drop variation for sample *025P0230U1*

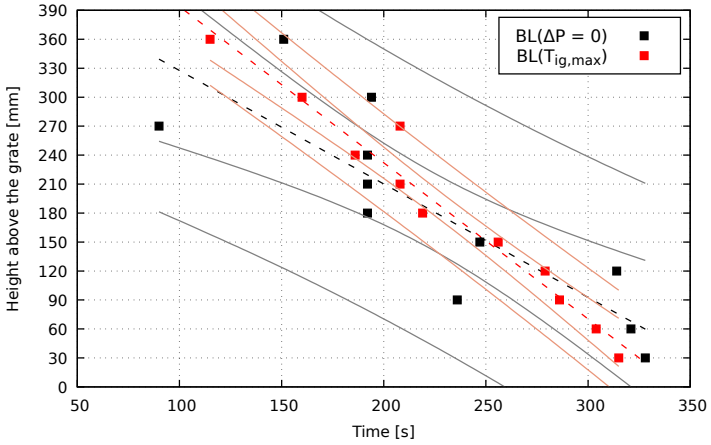

Figure C.4 – Comparison between the linear models for sample *025P0230U1* bed level position prediction.

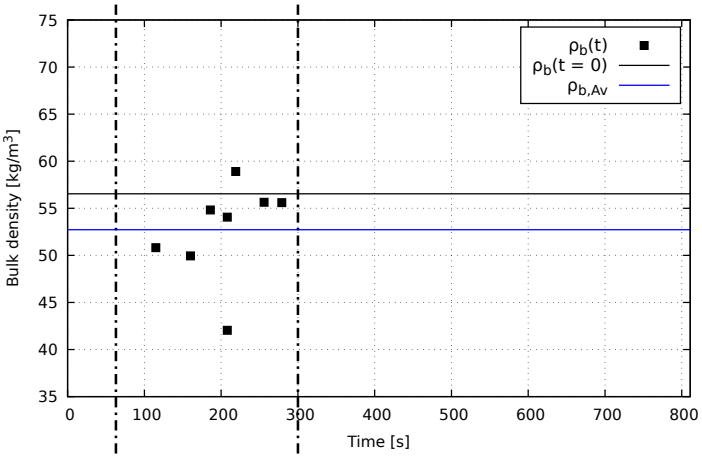

Figure C.5 – Bulk density variation for sample *025P0230U1*.

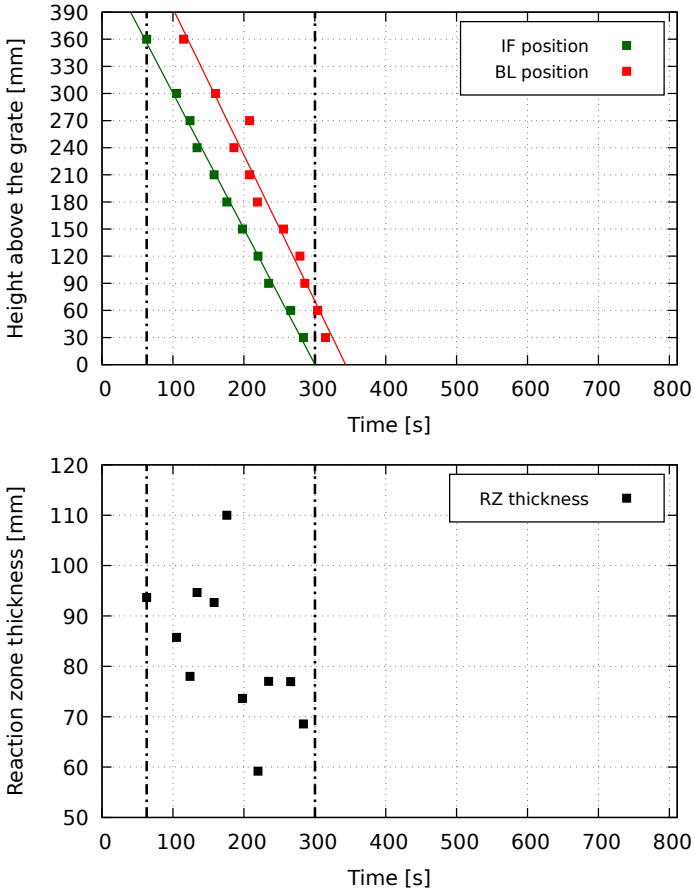

Figure C.6 – Reaction zone thickness variation for sample *025P0230U1*

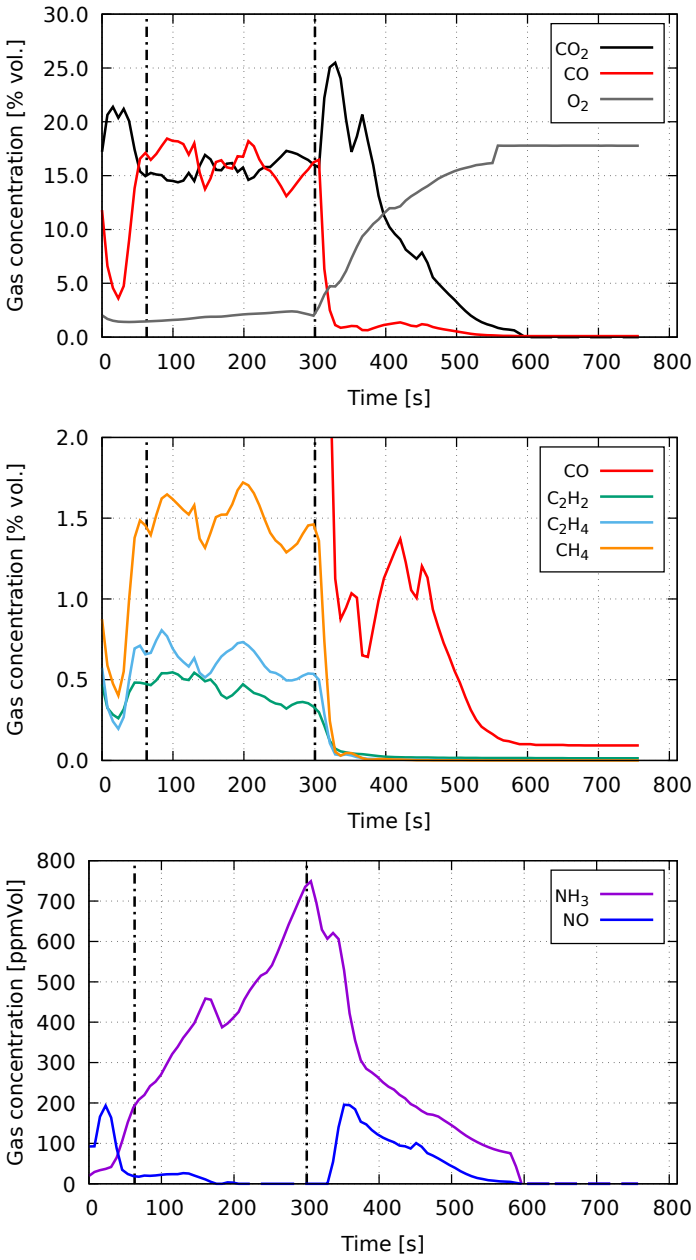

Figure C.7 – Combustion gases composition for sample *025P0230U1*

Sample 025P0385U1

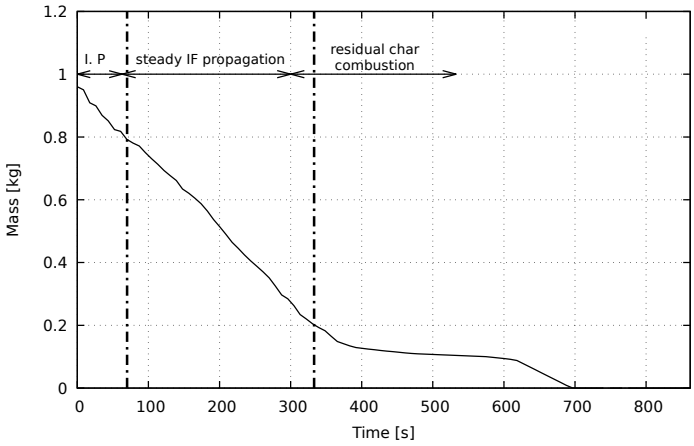

Figure C.8 – Mass loss variation during fixed-bed combustion experiment of sample *025P0385U1*

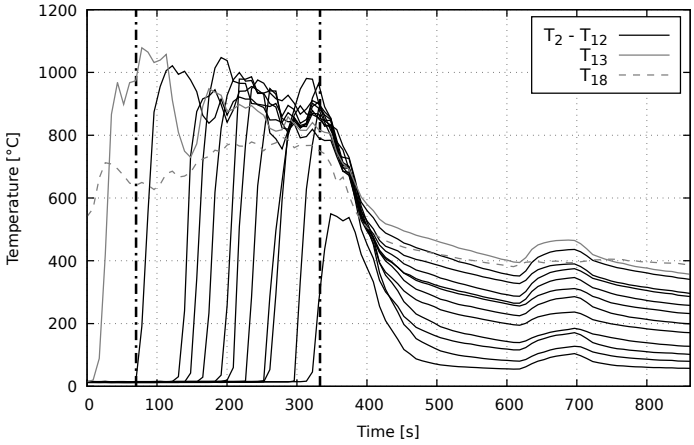

Figure C.9 – Temperature history for *025P0385U1*

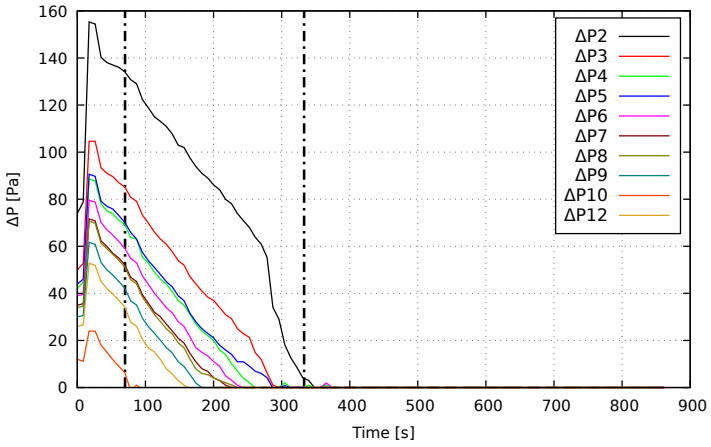

Figure C.10 – Pressure drop variation for sample *025P0385U1*

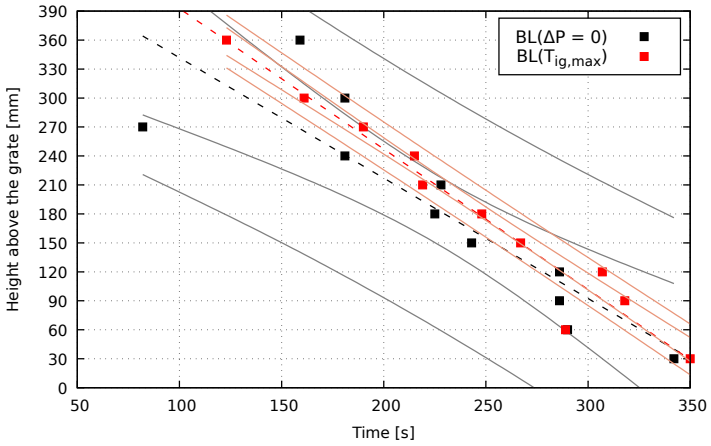

Figure C.11 – Comparison between the linear models for sample *025P0385U1* bed level position prediction.

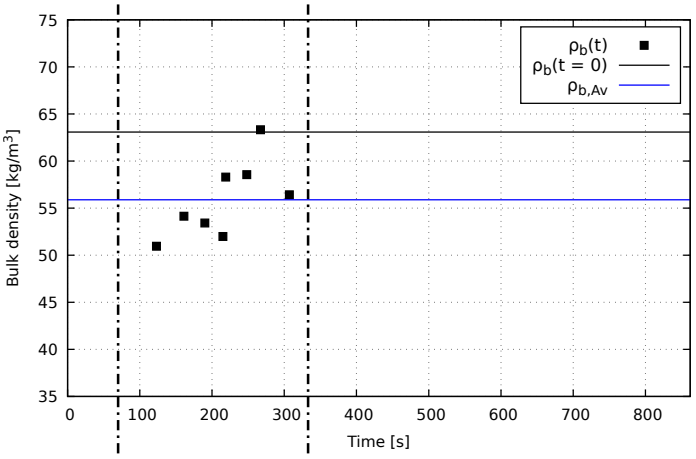

Figure C.12 – Bulk density variation for sample *025P0385U1*.

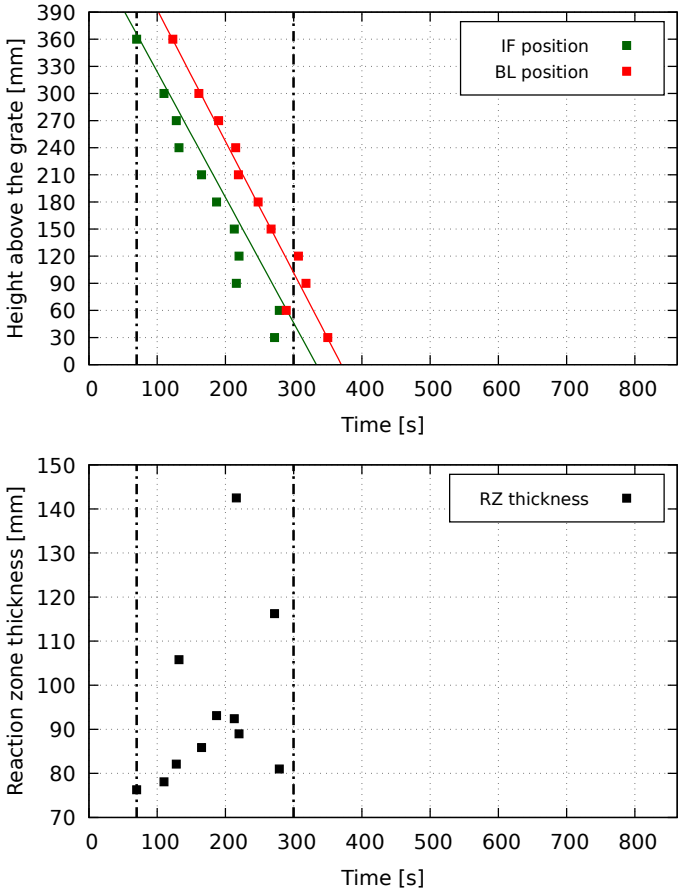

Figure C.13 – Reaction zone thickness variation for sample *025P0385U1*

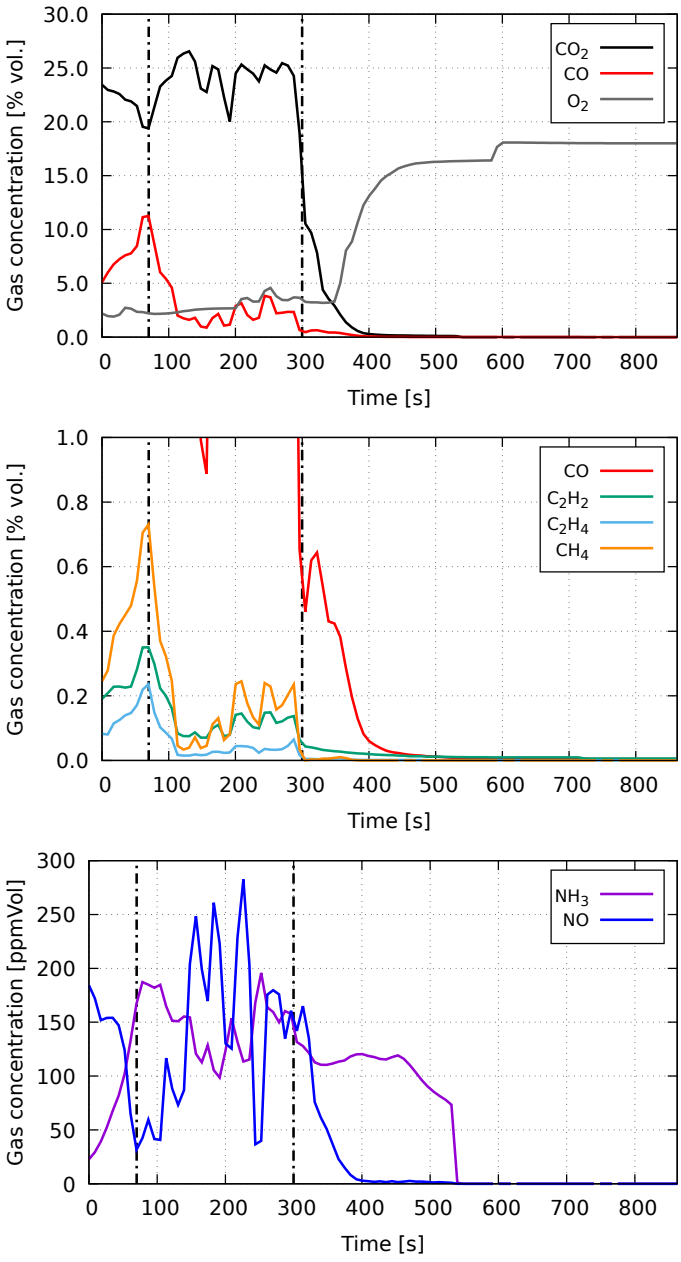

Figure C.14 – Combustion gases composition for sample *025P0385U1*

Sample 075P0230U1

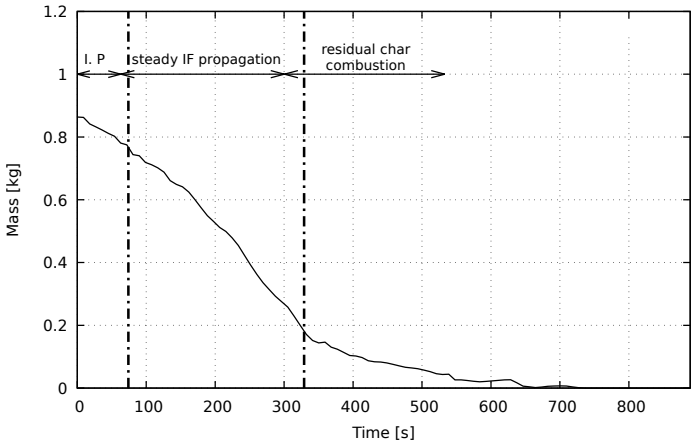

Figure C.15 – Mass loss variation during fixed-bed combustion experiment of sample *075P0230U1*

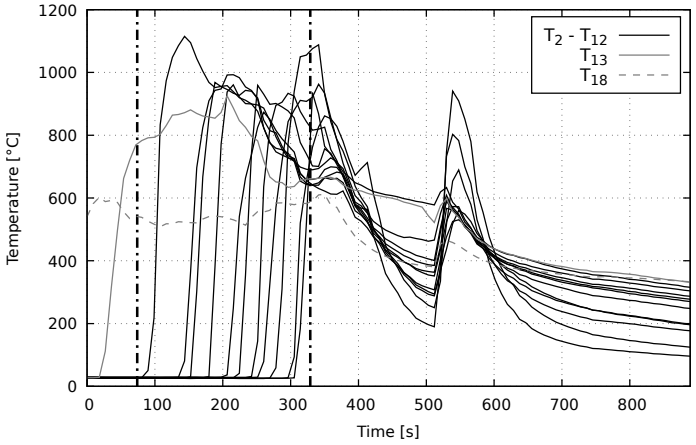

Figure C.16 – Temperature history for *075P0230U1*

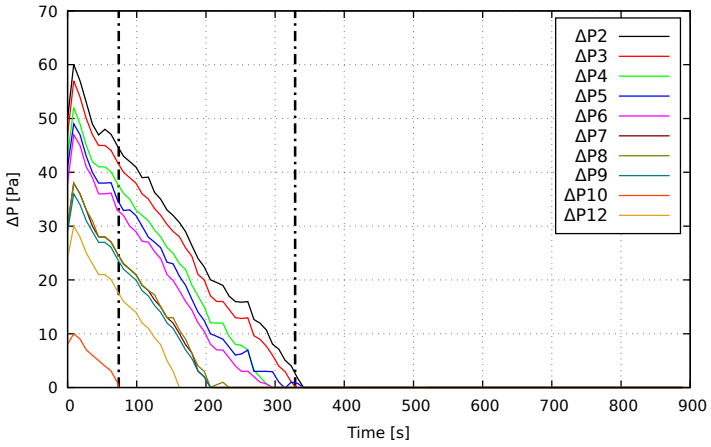

Figure C.17 – Pressure drop variation for sample *075P0230U1*

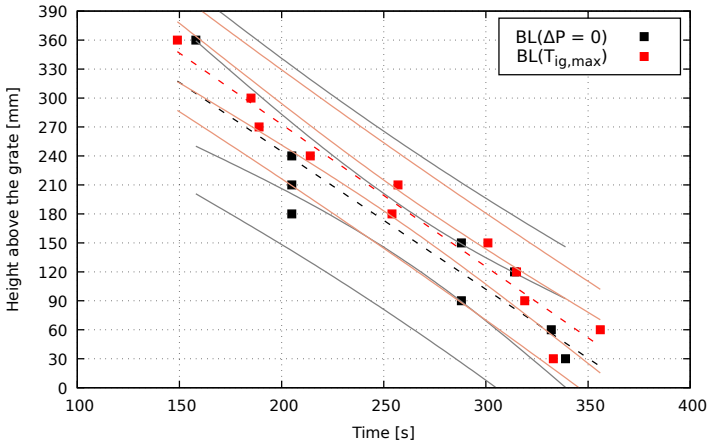

Figure C.18 – Comparison between the linear models for sample *075P0230U1* bed level position prediction.

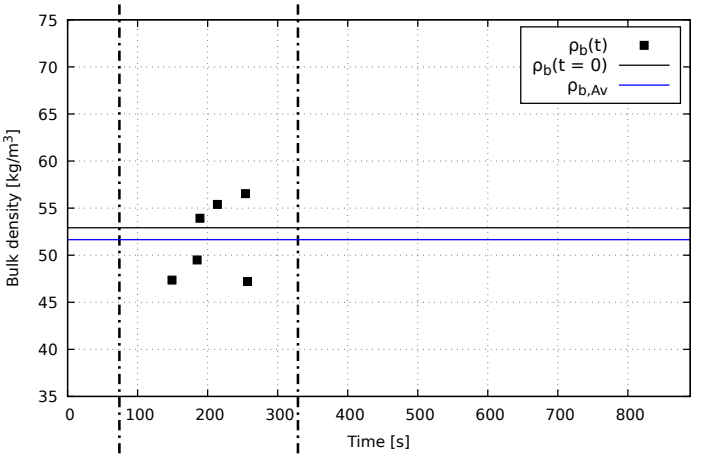

Figure C.19 – Bulk density variation for sample *075P0230U1*.

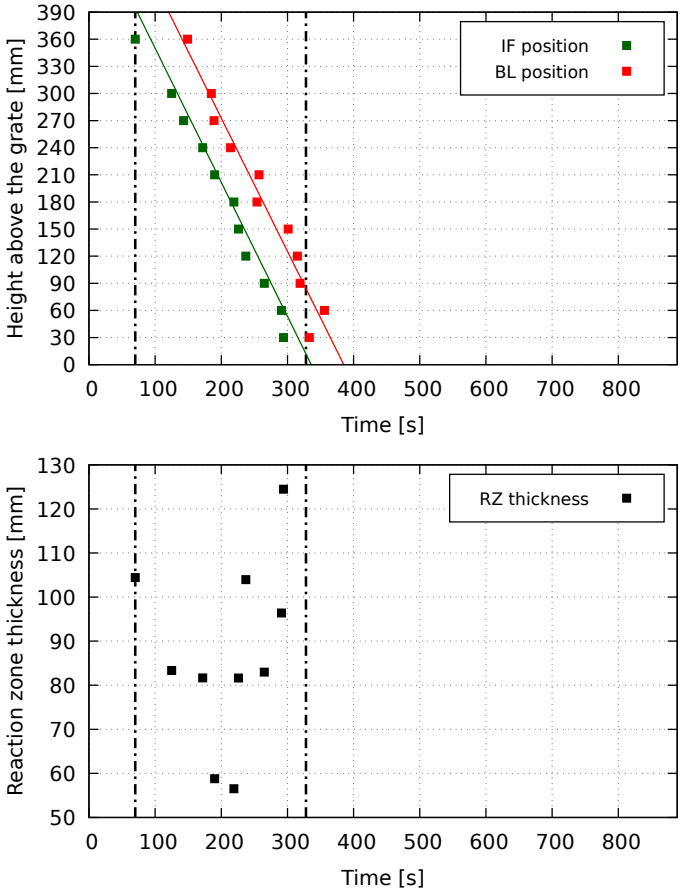

Figure C.20 – Reaction zone thickness variation for sample *075P0230U1*

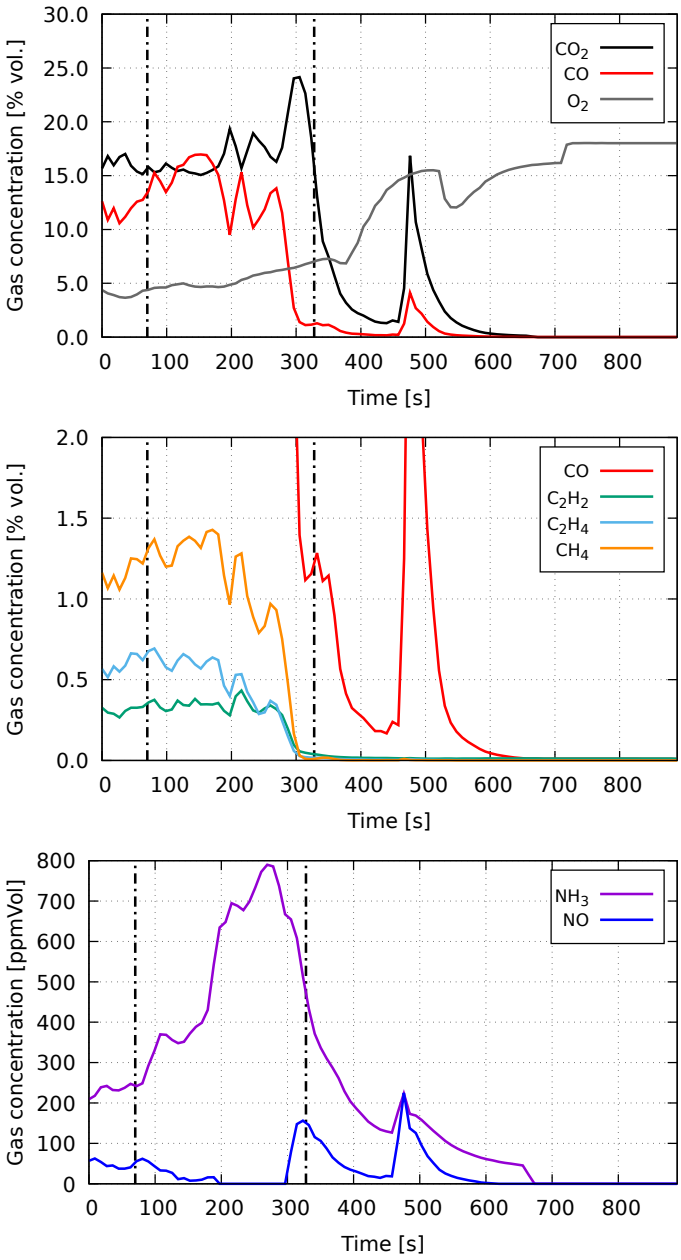

Figure C.21 – Combustion gases composition for sample *075P0230U1*

Sample 075P0385U1

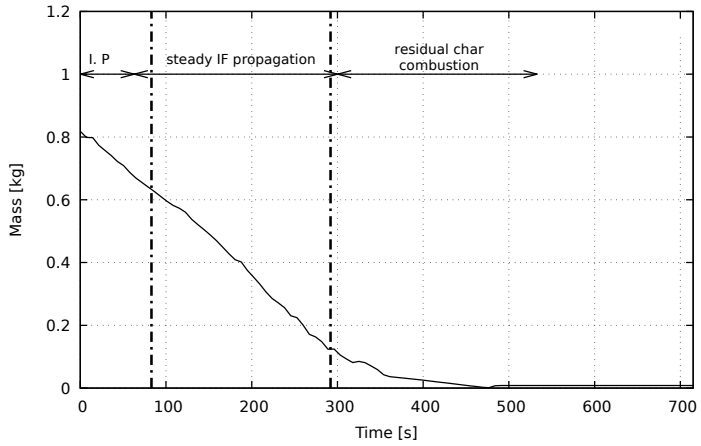

h

Figure C.22 – Mass loss variation during fixed-bed combustion experiment of sample *075P0385U1*

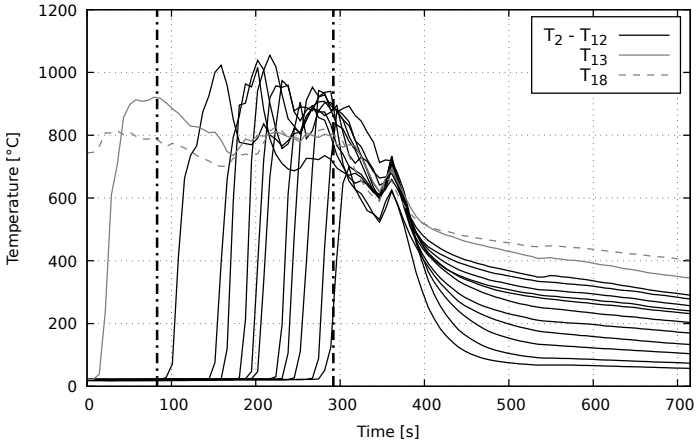

Figure C.23 – Temperature history for *075P0385U1*

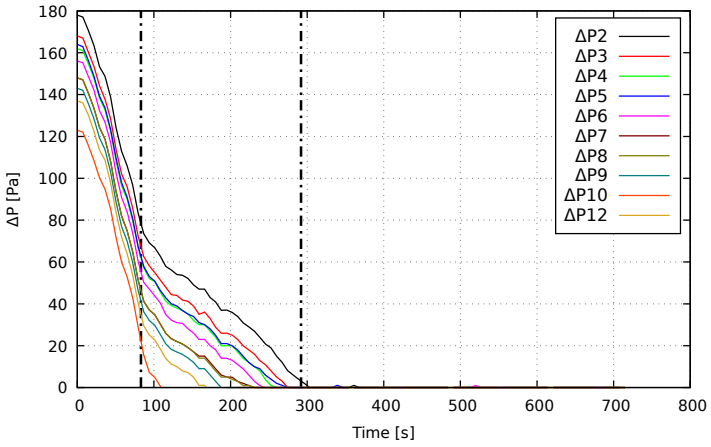

Figure C.24 – Pressure drop variation for sample *075P0385U1*

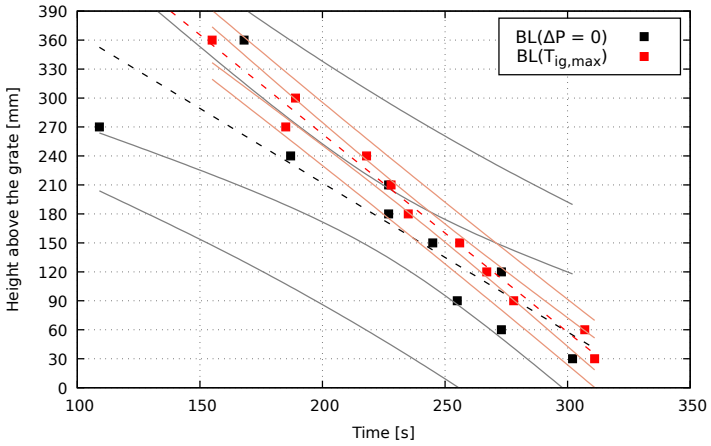

Figure C.25 – Comparison between the linear models for sample *075P0385U1* bed level position prediction.

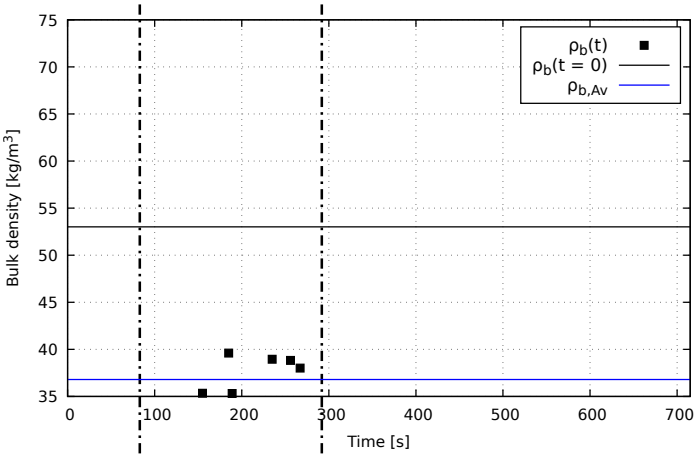

Figure C.26 – Bulk density variation for sample *075P0385U1*.

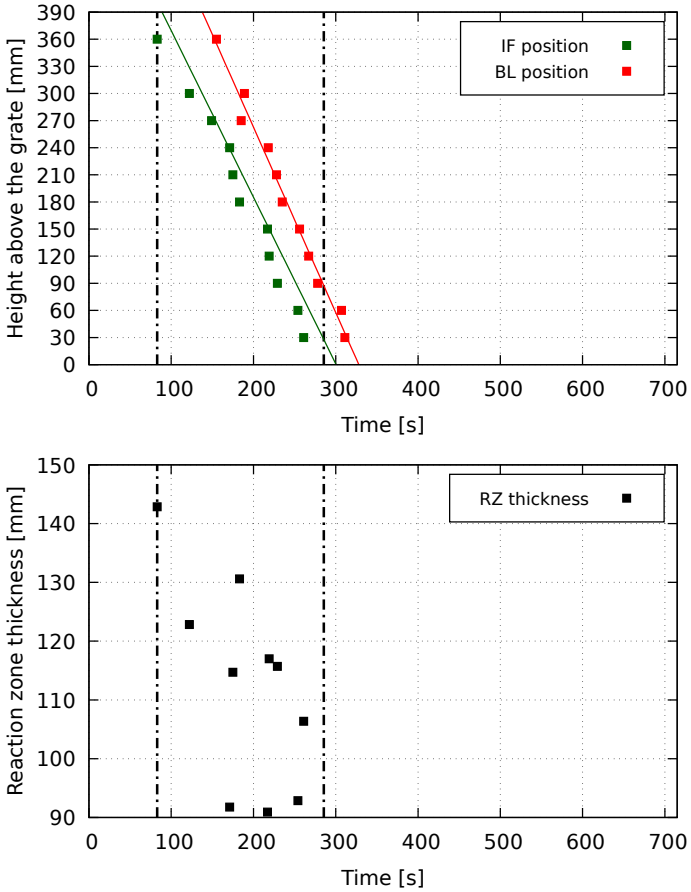

Figure C.27 – Reaction zone thickness variation for sample *075P0385U1*

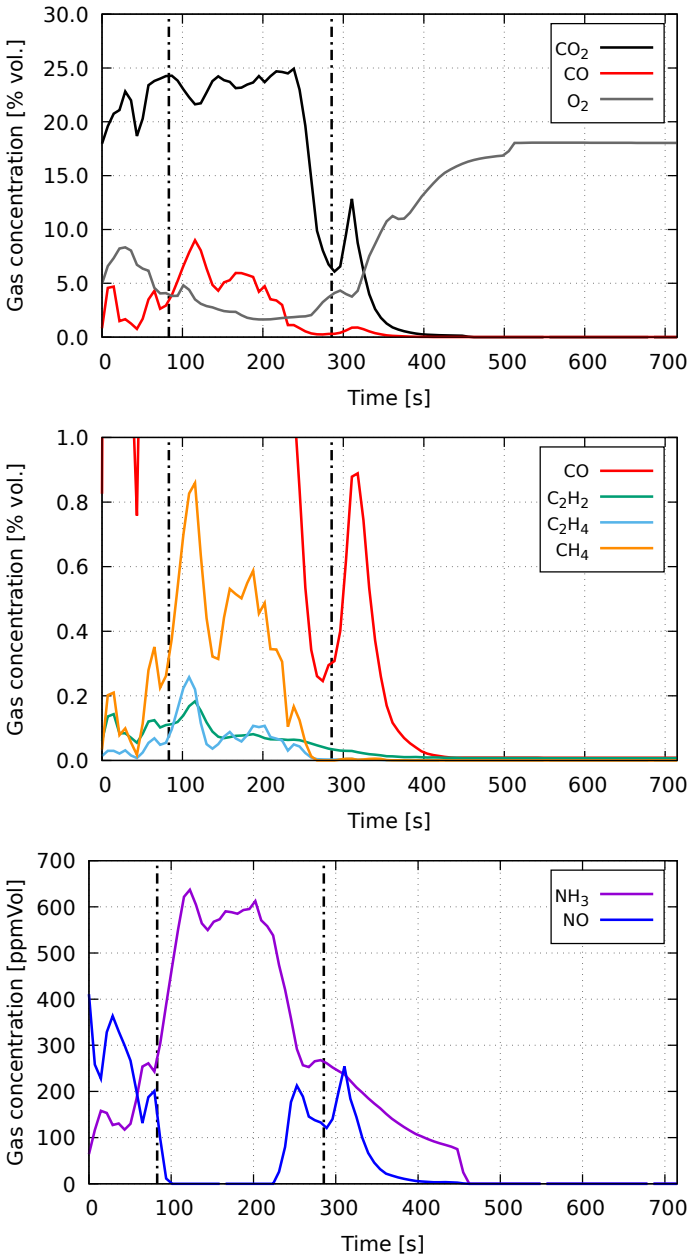

Figure C.28 – Combustion gases composition for sample *075P0230U1*

Sample 050P0150U1

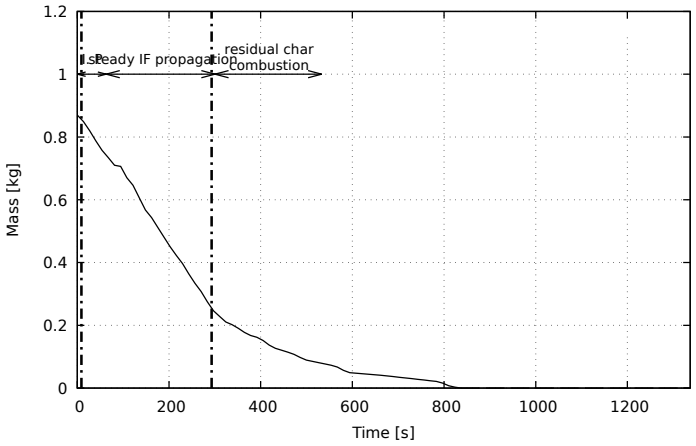

Figure C.29 – Mass loss variation during fixed-bed combustion experiment of sample *050P0150U1*

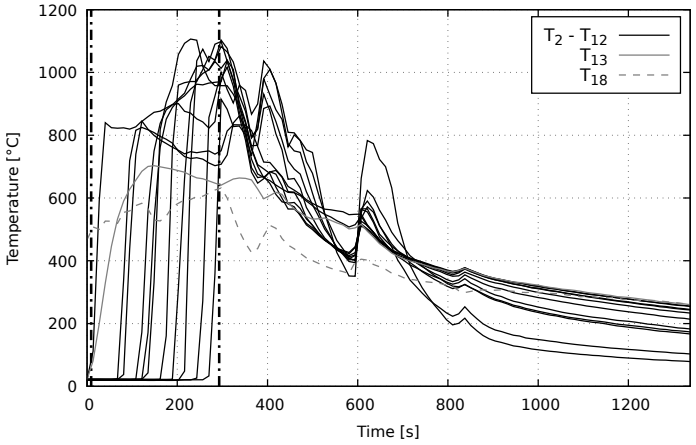

Figure C.30 – Temperature history for *050P0150U1*

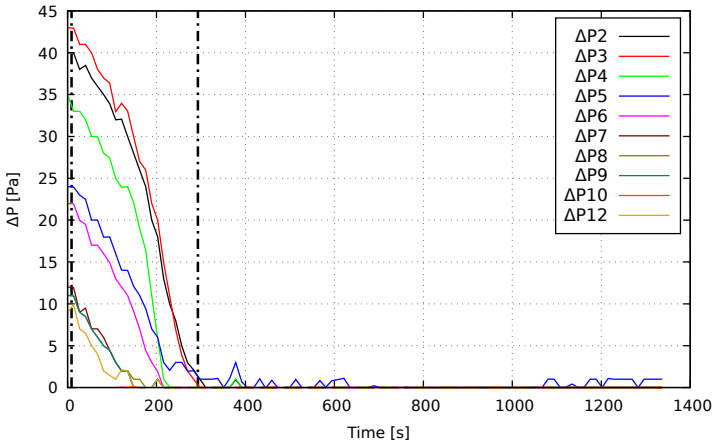

Figure C.31 – Pressure drop variation for sample *050P0150U1*

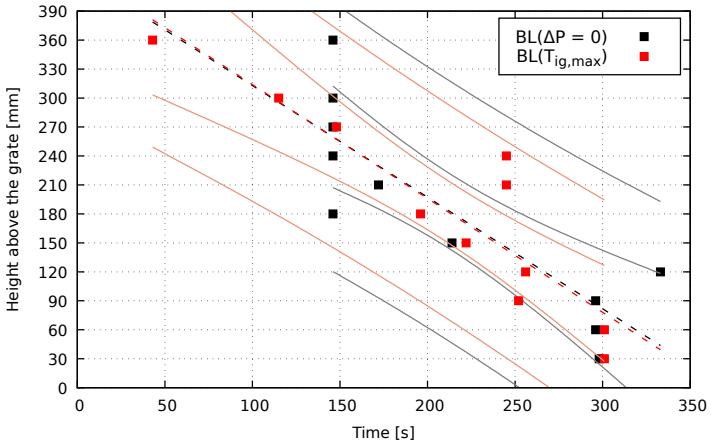

Figure C.32 – Comparison between the linear models for sample *050P0150U1* bed level position prediction.

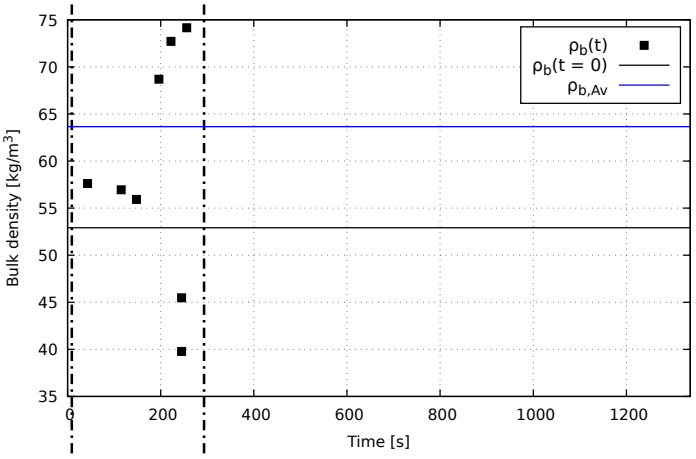

Figure C.33 – Bulk density variation for sample *050P0150U1*.

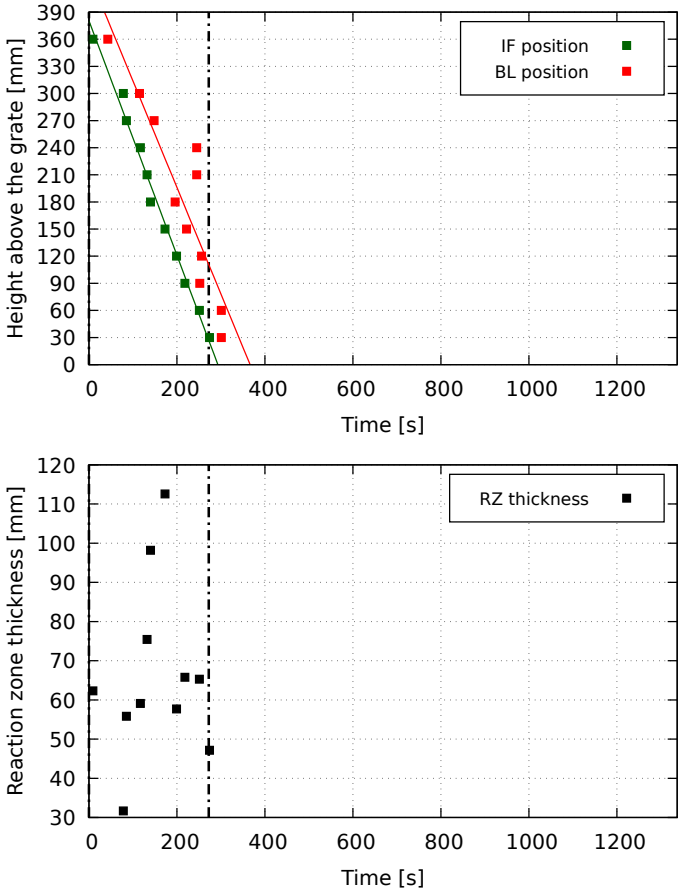

Figure C.34 – Reaction zone thickness variation for sample *050P0150U1*

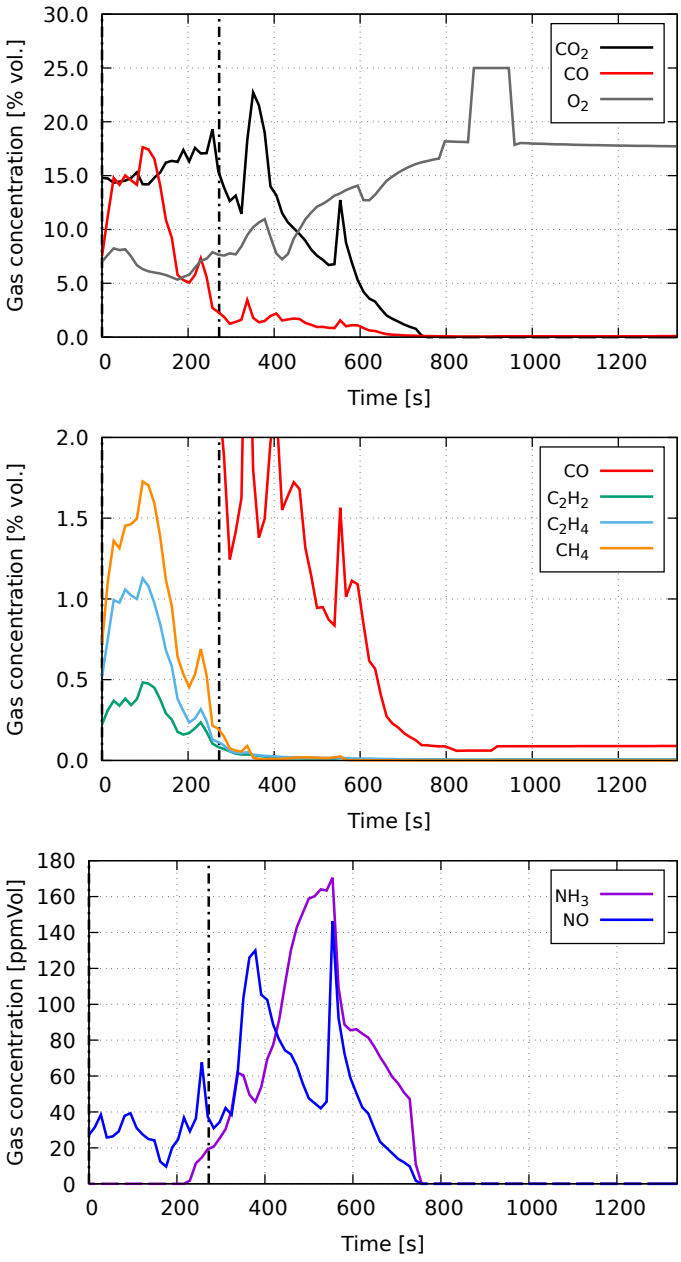

Figure C.35 – Combustion gases composition for sample *050P0150U1*

Sample 050P0465U1

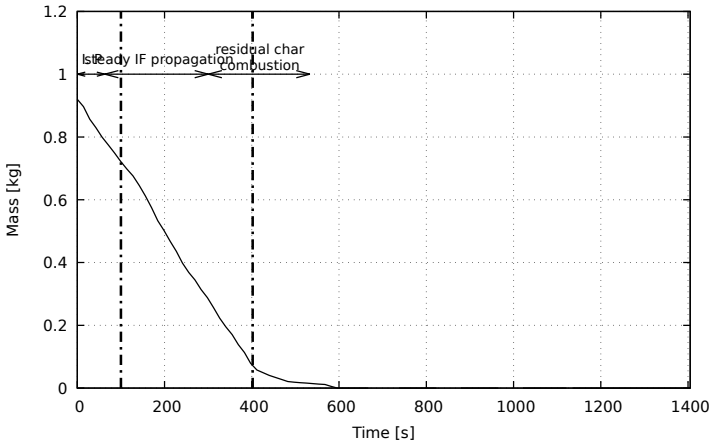

Figure C.36 – Mass loss variation during fixed-bed combustion experiment of sample *050P0465U1*

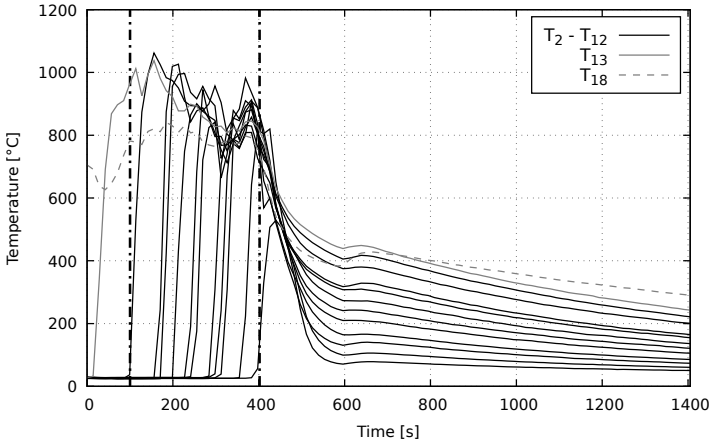

Figure C.37 – Temperature history for *050P0465U1*

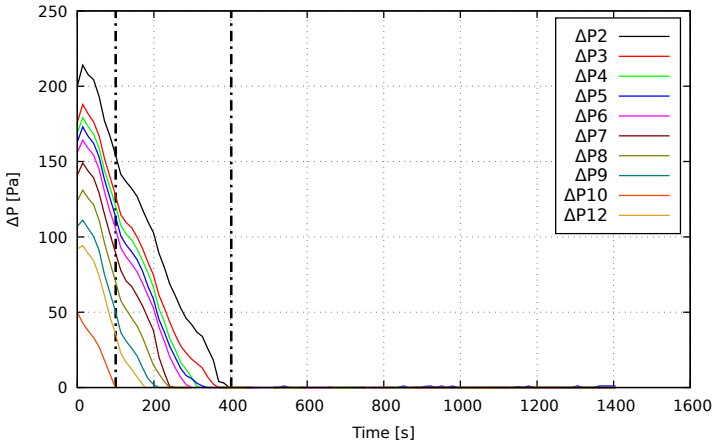

Figure C.38 – Pressure drop variation for sample *050P0465U1*

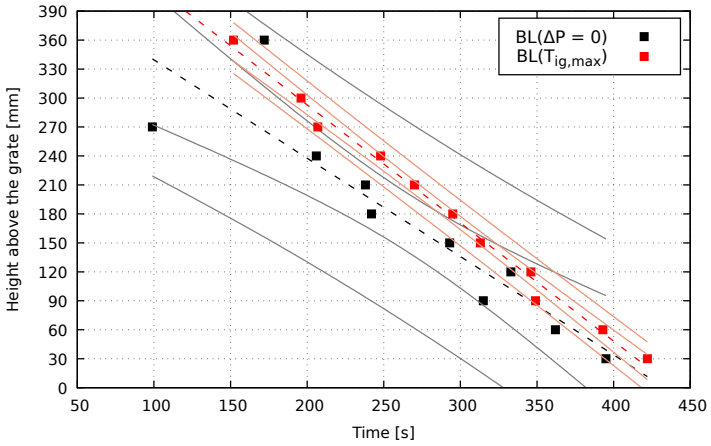

Figure C.39 – Comparison between the linear models for sample *050P0465U1* bed level position prediction.

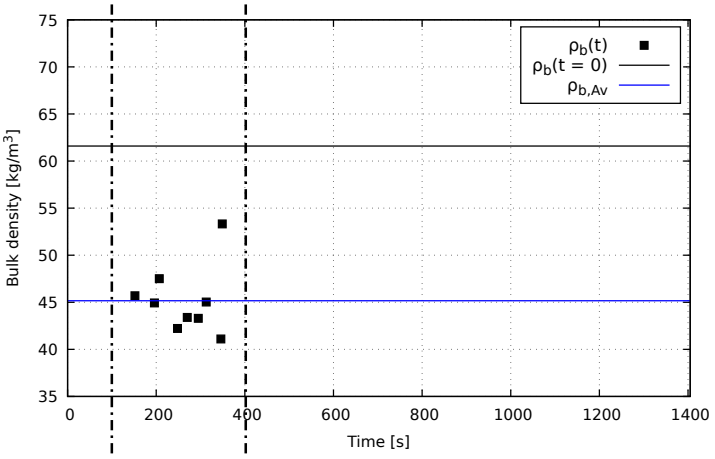

Figure C.40 – Bulk density variation for sample *050P0465U1*.

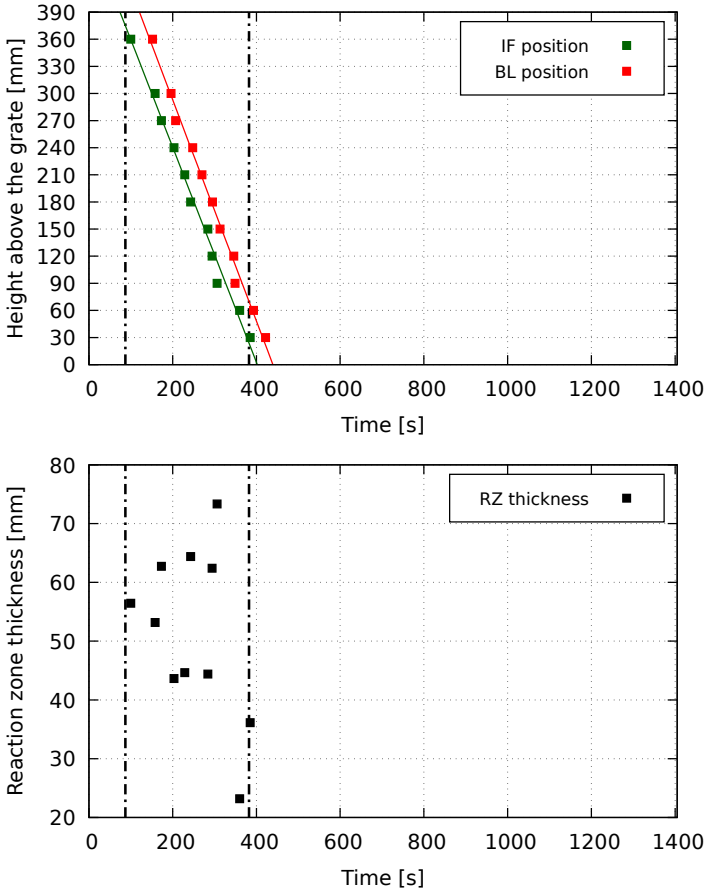

Figure C.41 – Reaction zone thickness variation for sample *050P0465U1*

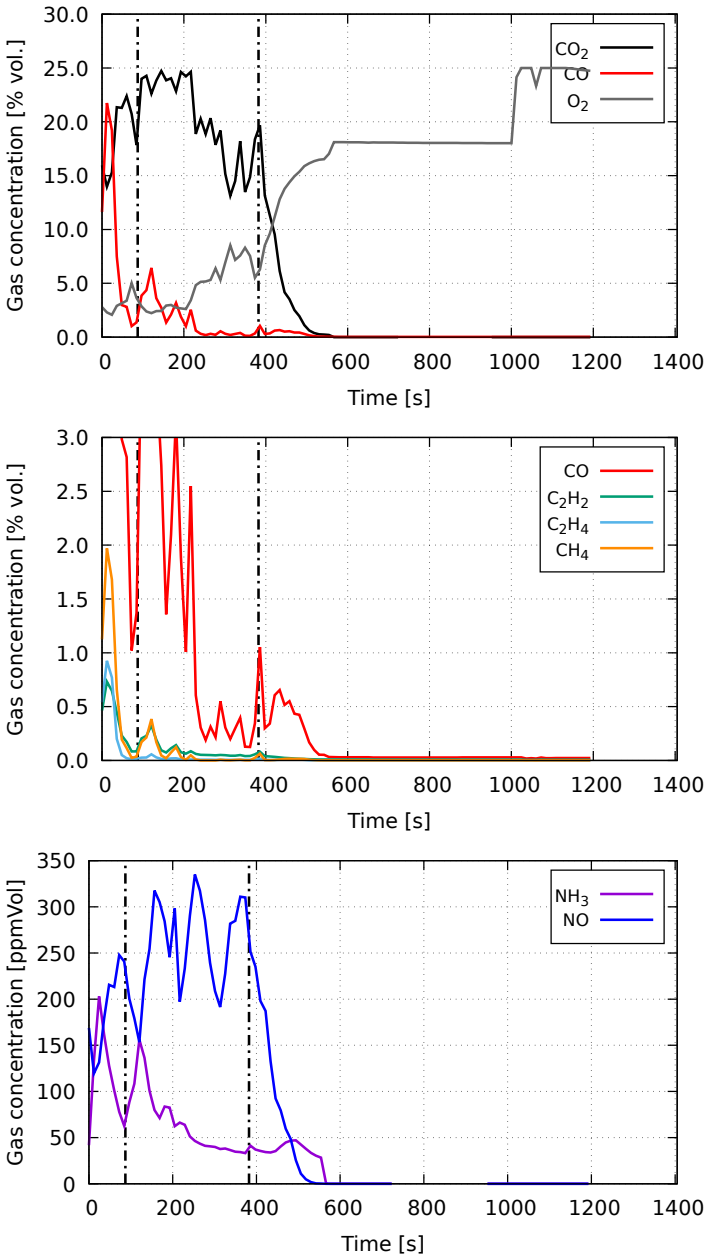

Figure C.42 – Combustion gases composition for sample *050P0465U1*

Sample 000P0310U1

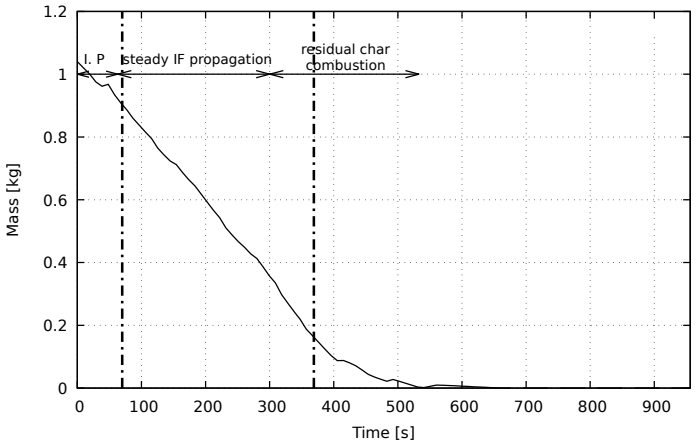

Figure C.43 – Mass loss variation during fixed-bed combustion experiment of sample *000P0310U1*

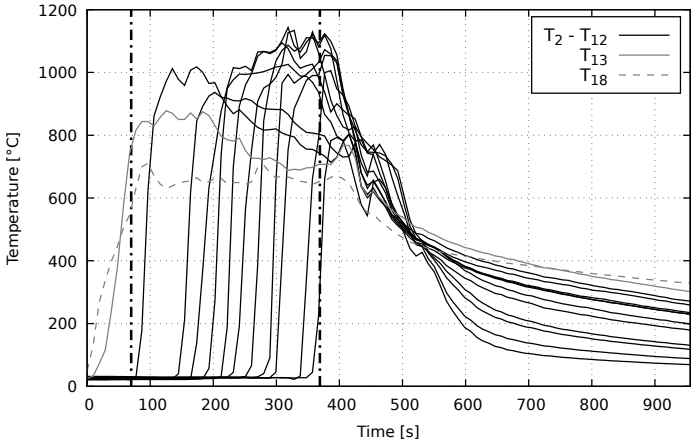

Figure C.44 – Temperature history for *000P0310U1*

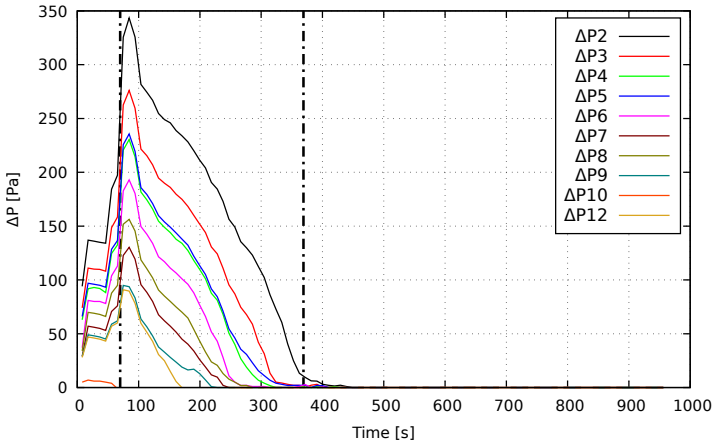

Figure C.45 – Pressure drop variation for sample *000PU0310U1*

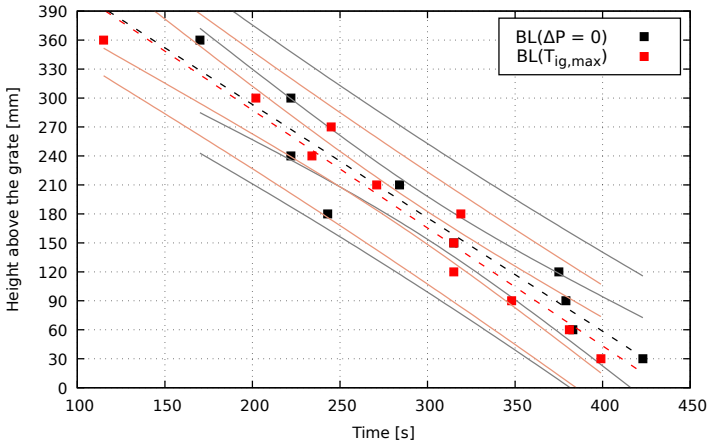

Figure C.46 – Comparison between the linear models for sample *000P0310U1* bed level position prediction.

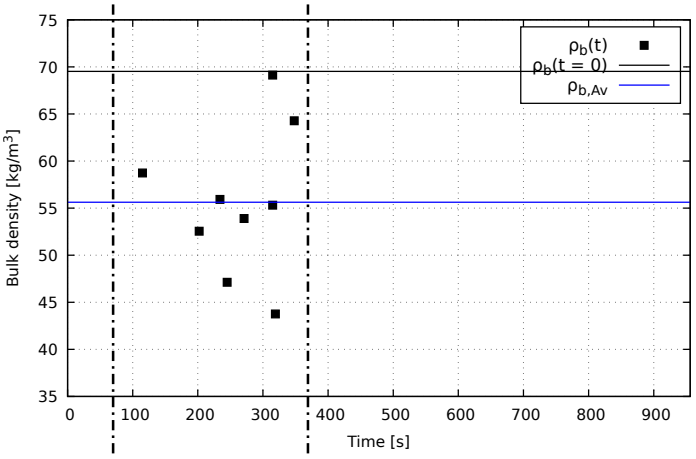

Figure C.47 – Bulk density variation for sample *000P0310U1*.

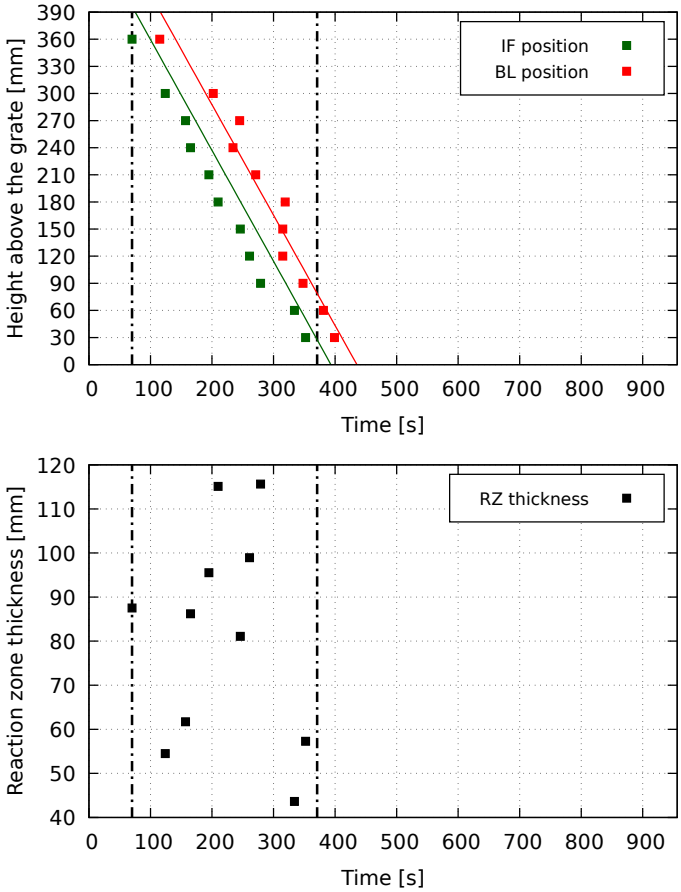

Figure C.48 – Reaction zone thickness variation for sample *000P0310U1*

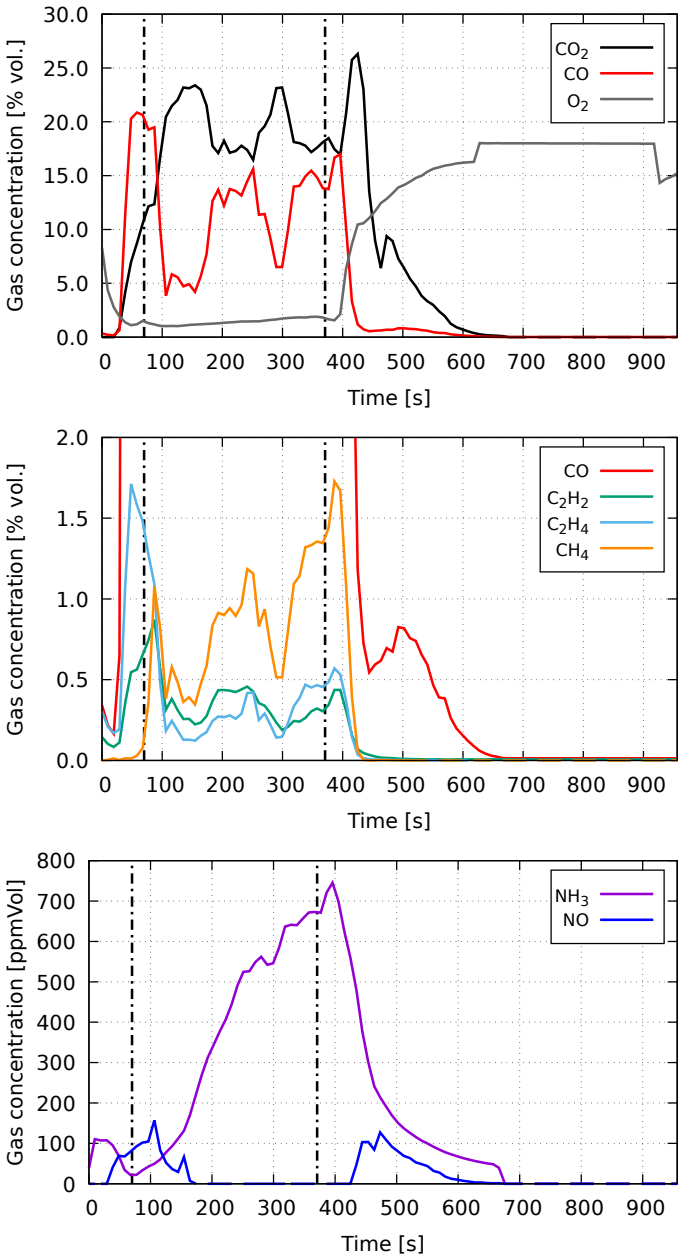

Figure C.49 – Combustion gases composition for sample *000P0310U1*

Sample 100P0310U1

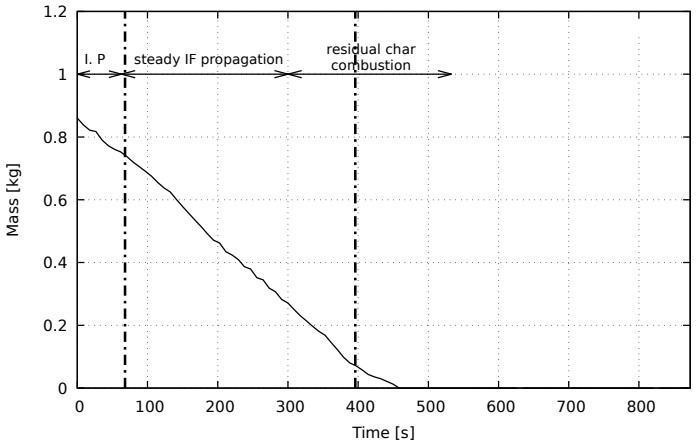

Figure C.50 – Mass loss variation during fixed-bed combustion experiment of sample *100P0310U1*

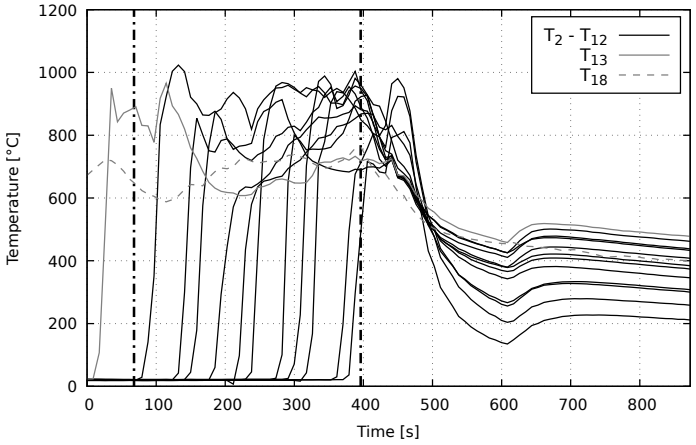

Figure C.51 – Temperature history for *100P0310U1*

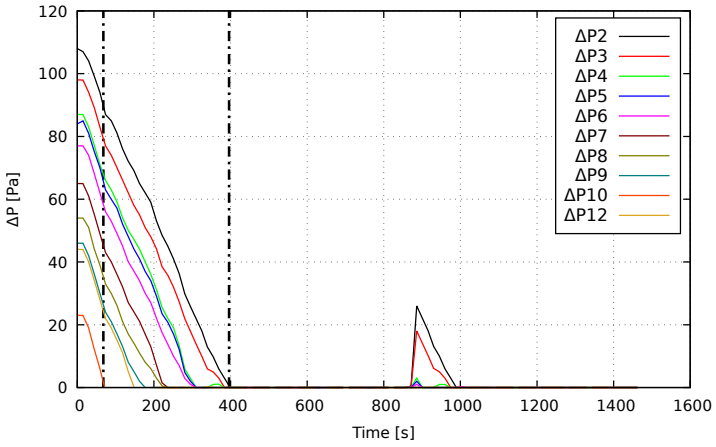

Figure C.52 – Pressure drop variation for sample *100P0310U1*

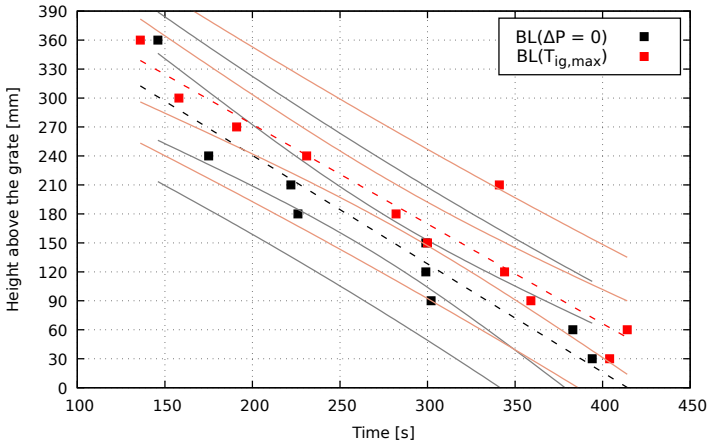

Figure C.53 – Comparison between the linear models for sample *100P0310U1* bed level position prediction.

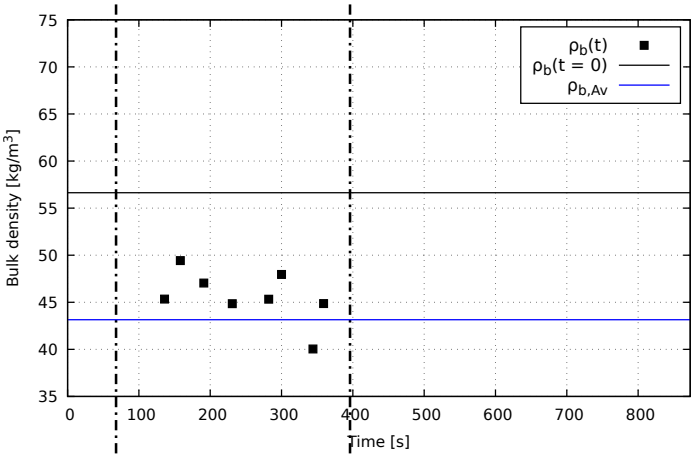

Figure C.54 – Bulk density variation for sample *100P0310U1*.

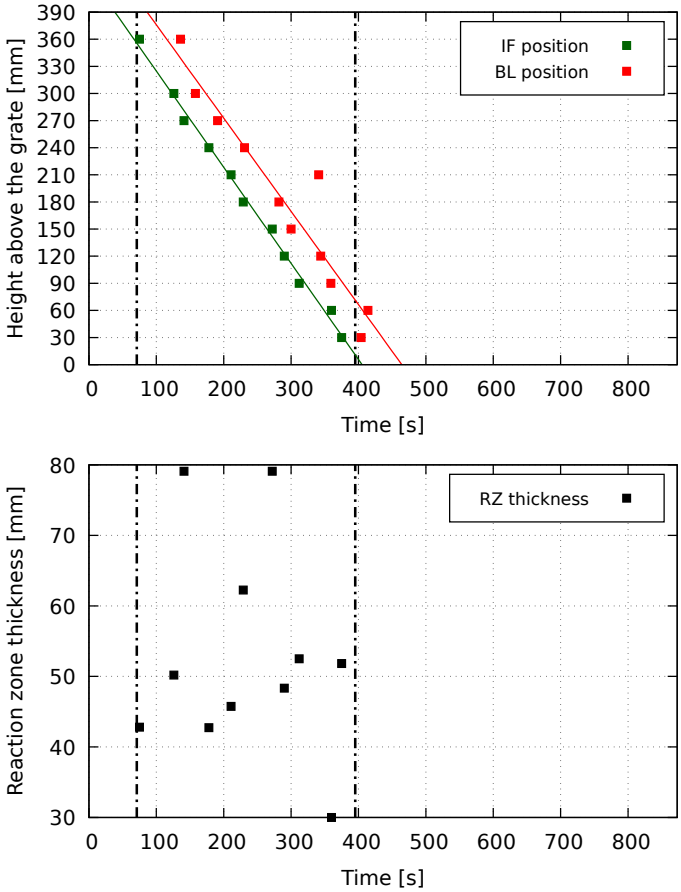

Figure C.55 – Reaction zone thickness variation for sample *100P0310U1*

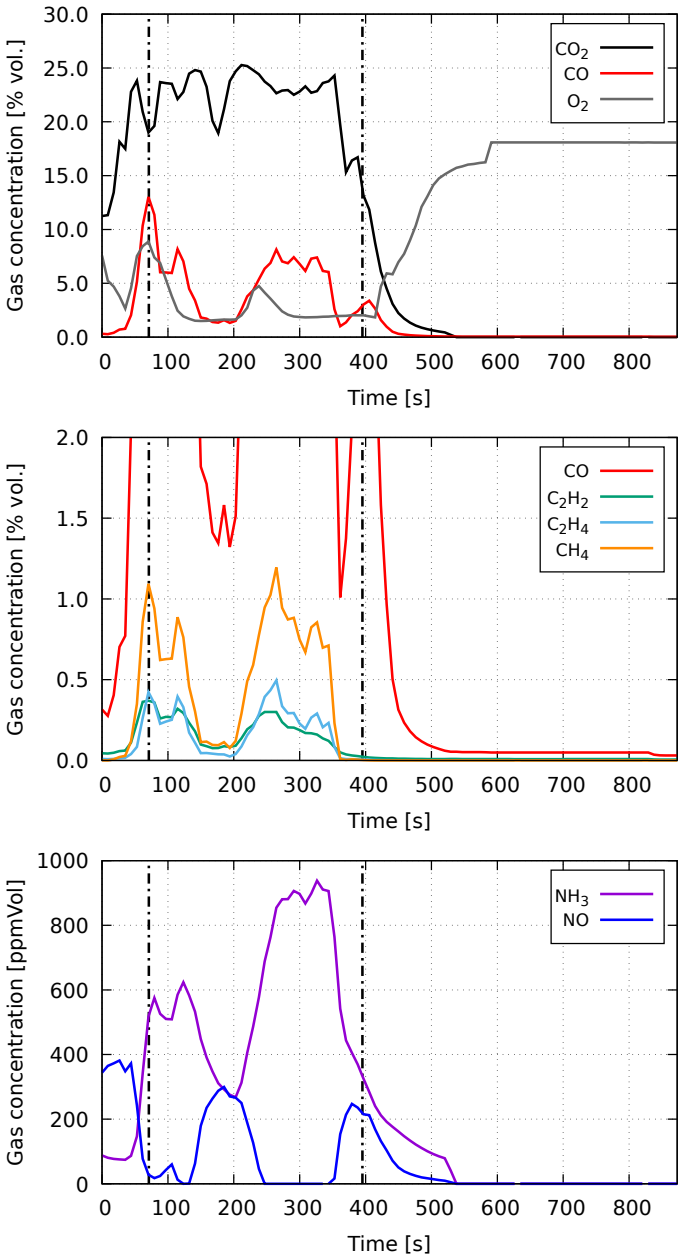

Figure C.56 – Combustion gases composition for sample *100P0310U1*

Sample 050P0310U1

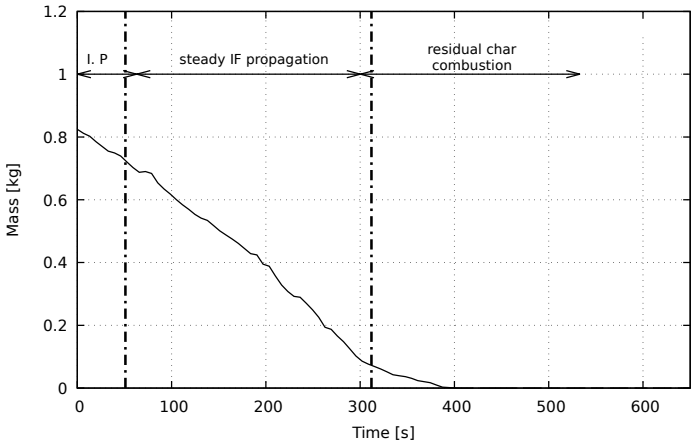

Figure C.57 – Mass loss variation during fixed-bed combustion experiment of sample *050P0310U1*

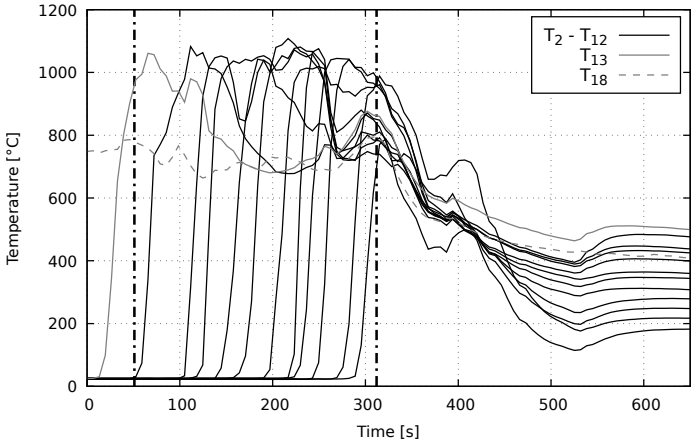

Figure C.58 – Temperature history for *050P0310U1*

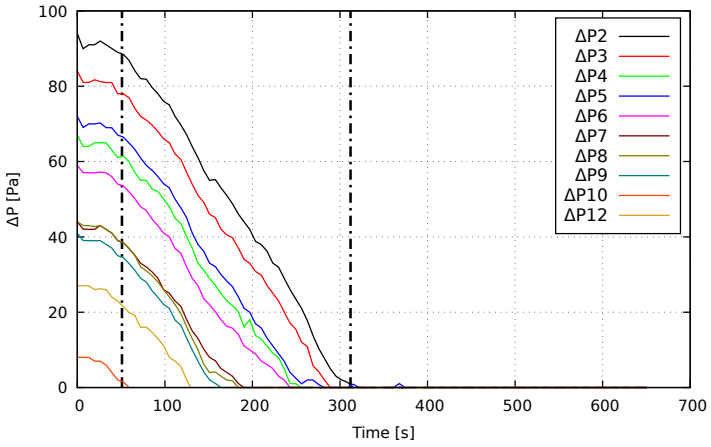

Figure C.59 – Pressure drop variation for sample *050P0310U1*

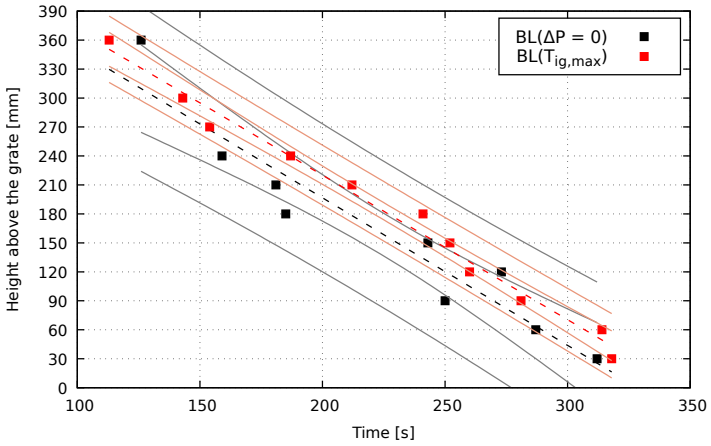

Figure C.60 – Comparison between the linear models for sample *050P0310U1* bed level position prediction.

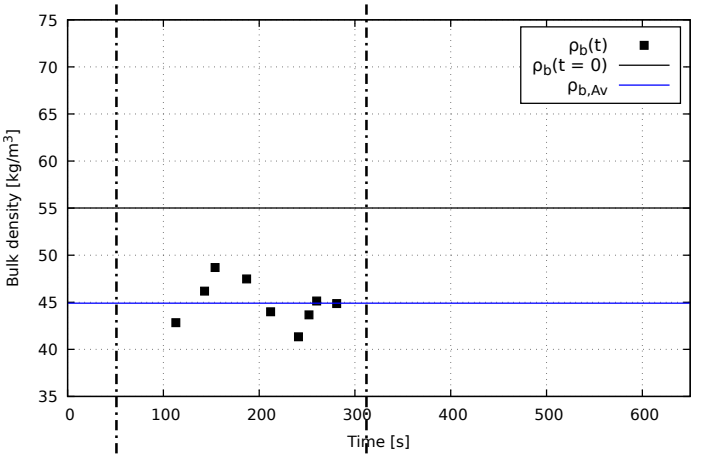

Figure C.61 – Bulk density variation for sample *050P0310U1*.

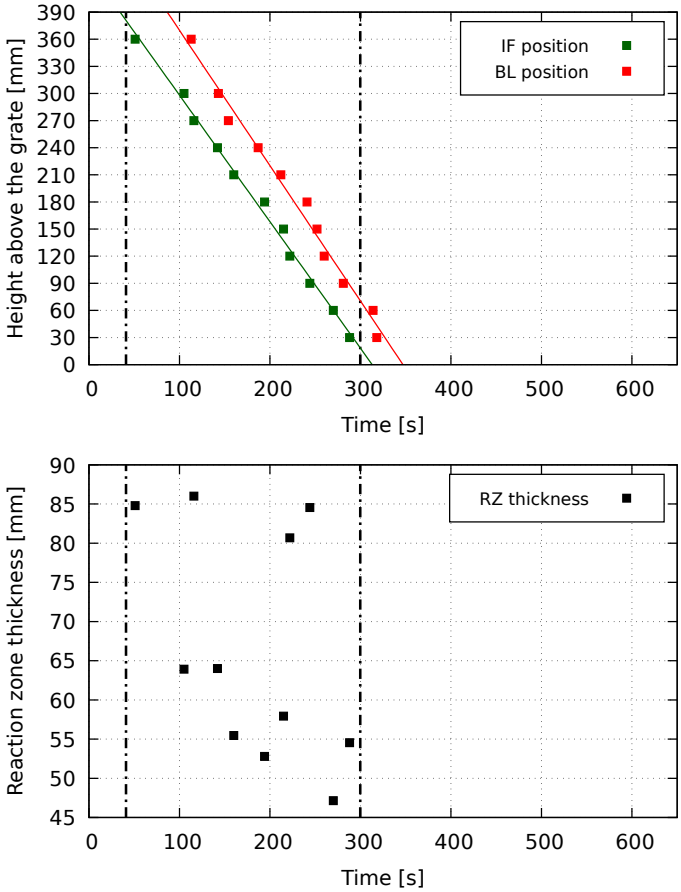

Figure C.62 – Reaction zone thickness variation for sample *050P0310U1*

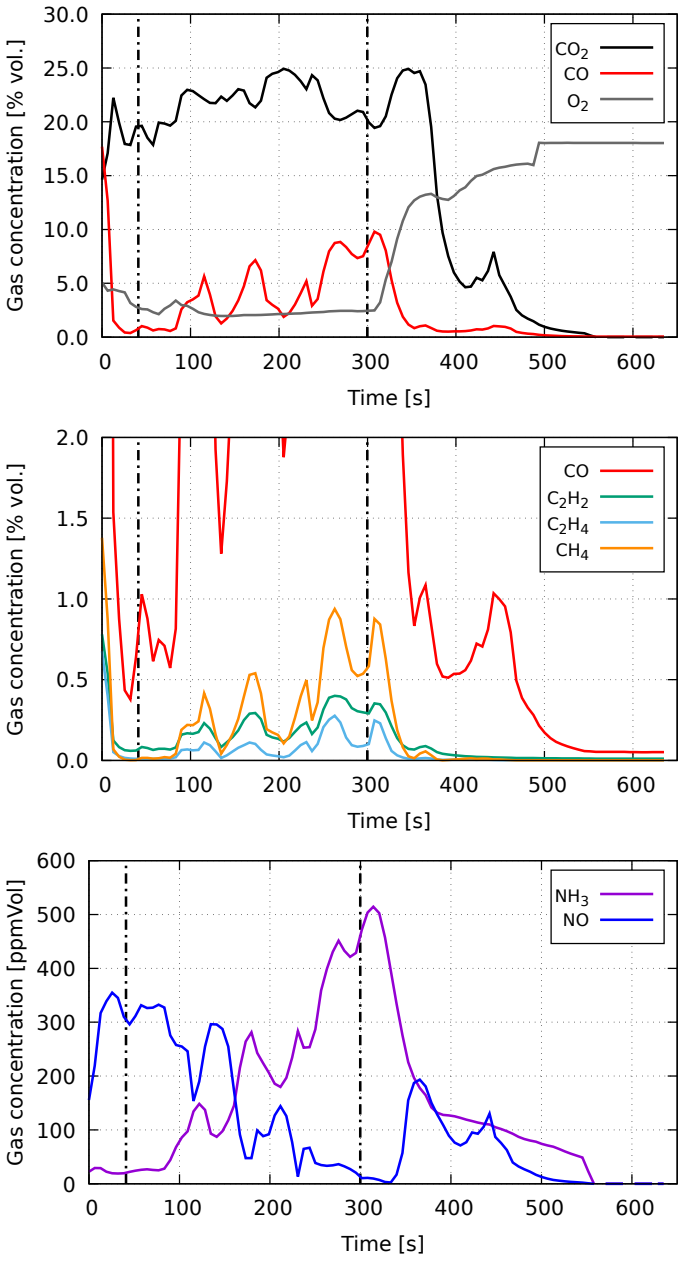

Figure C.63 – Combustion gases composition for sample *050P0310U1*

Sample 050P0310U2

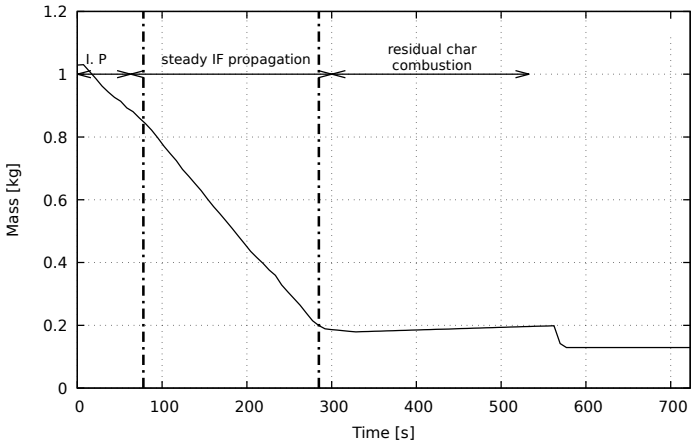

Figure C.64 – Mass loss variation during fixed-bed combustion experiment of sample *050P0310U2*

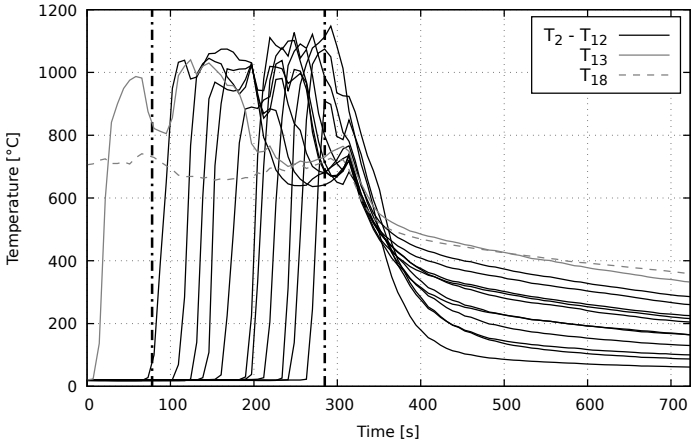

Figure C.65 – Temperature history for *050P0310U2*

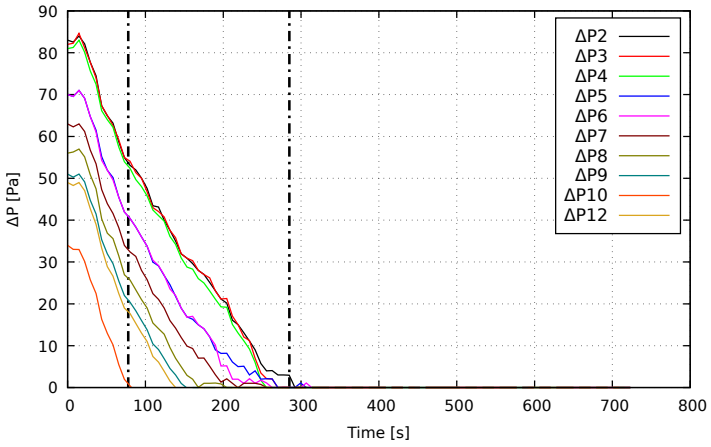

Figure C.66 – Pressure drop variation for sample *050P0310U2*

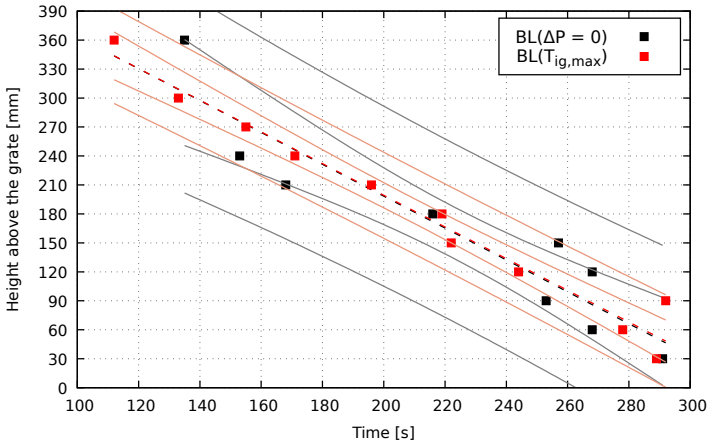

Figure C.67 – Comparison between the linear models for sample *050P0310U2* bed level position prediction.

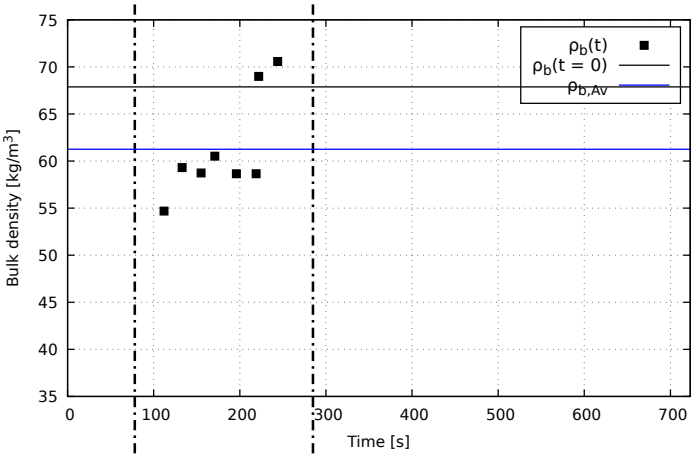

Figure C.68 – Bulk density variation for sample *050P0310U2*.

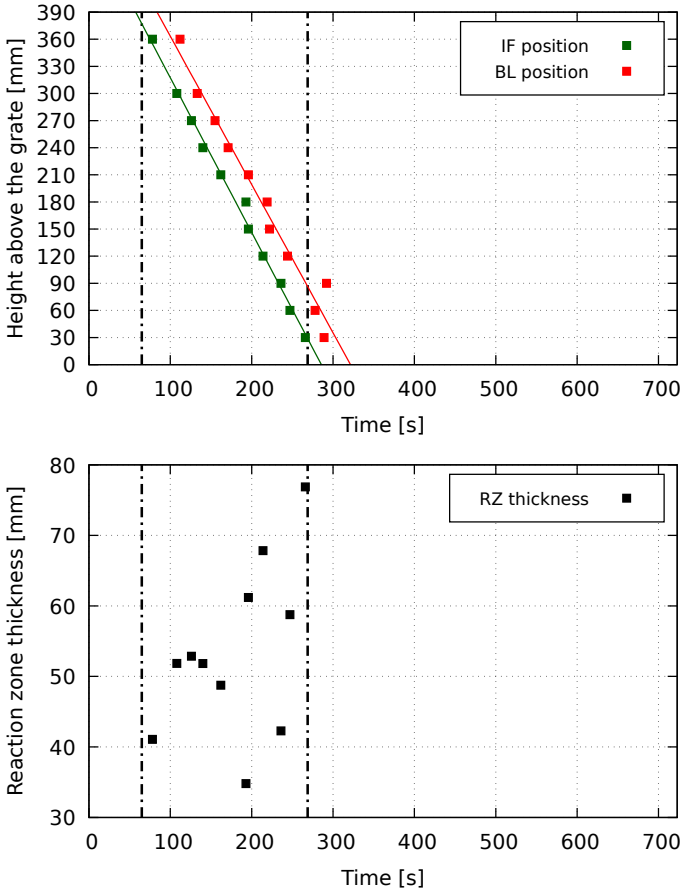

Figure C.69 – Reaction zone thickness variation for sample *050P0310U2*

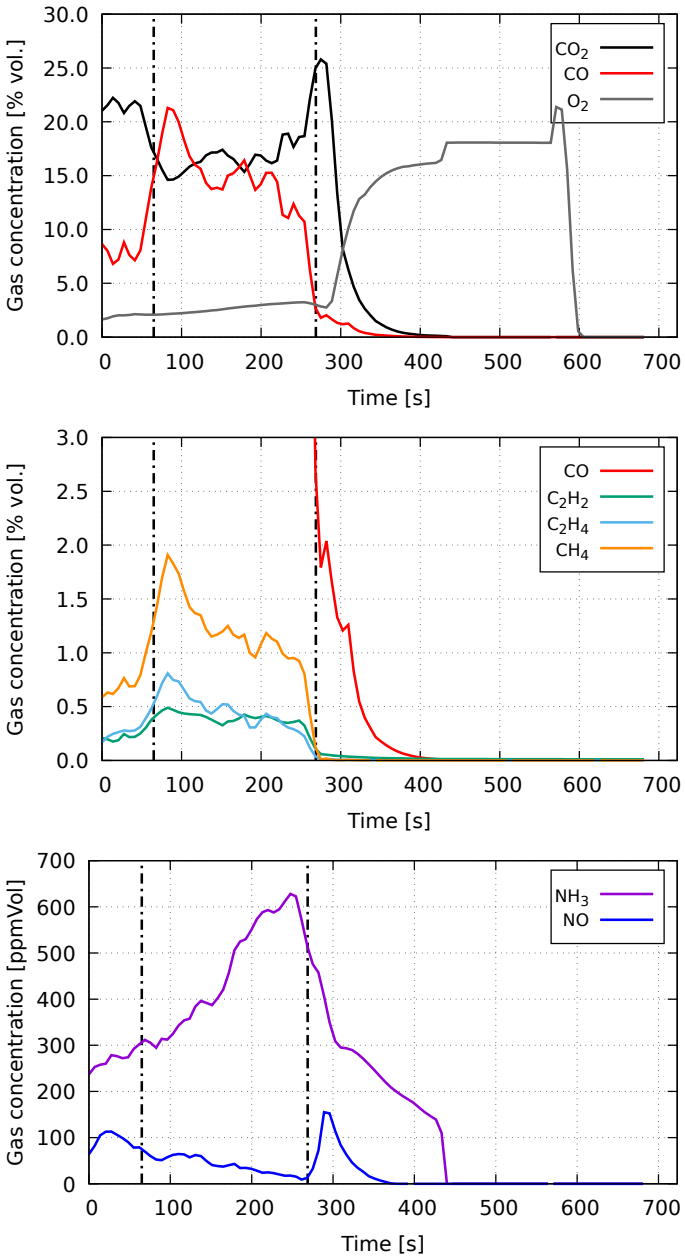

Figure C.70 – Combustion gases composition for sample *050P0310U2*

Sample 050P0310U3

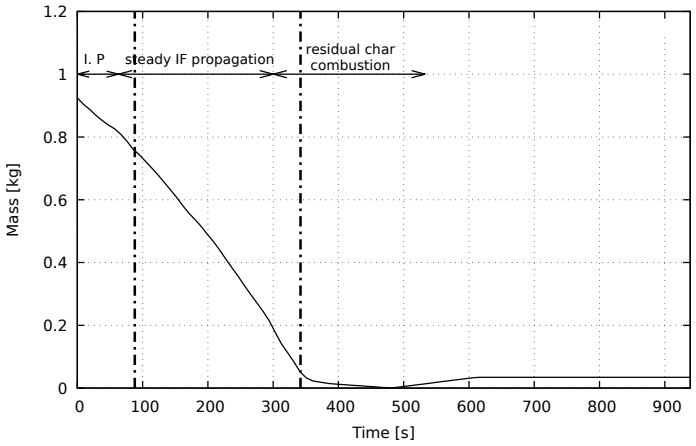

Figure C.71 – Mass loss variation during fixed-bed combustion experiment of sample *050P0310U3*

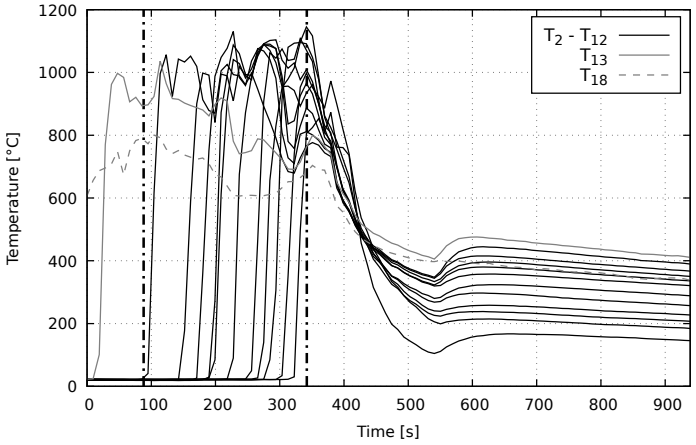

Figure C.72 – Temperature history for *050P0310U3*

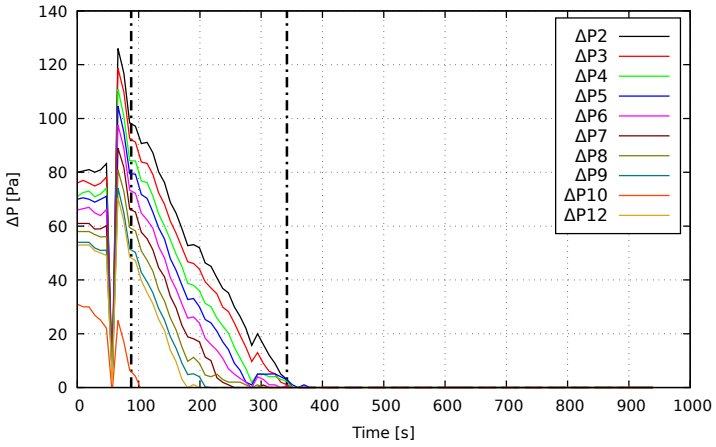

Figure C.73 – Pressure drop variation for sample *050P0310U3*

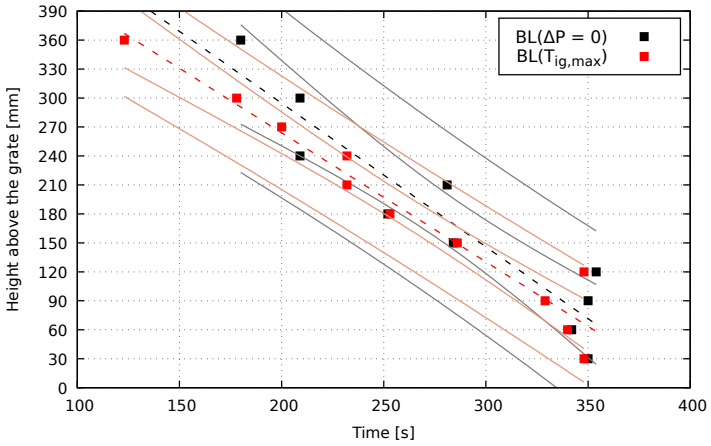

Figure C.74 – Comparison between the linear models for sample *050P0310U3* bed level position prediction.

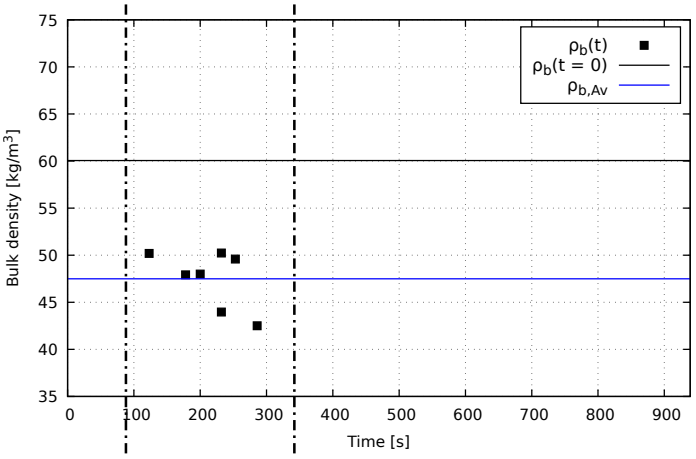

Figure C.75 – Bulk density variation for sample *050P0310U3*.

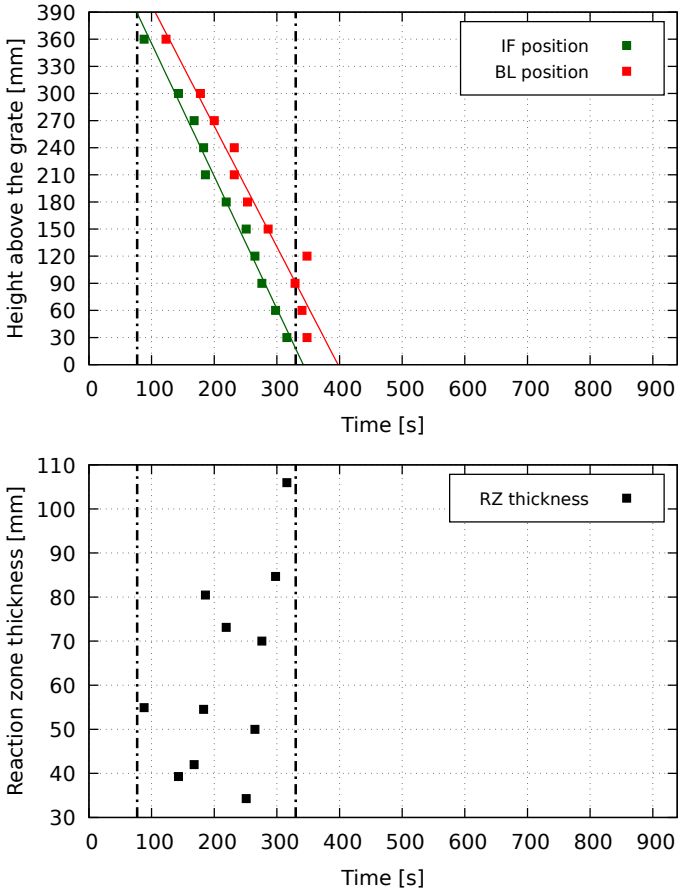

Figure C.76 – Reaction zone thickness variation for sample *050P0310U3*

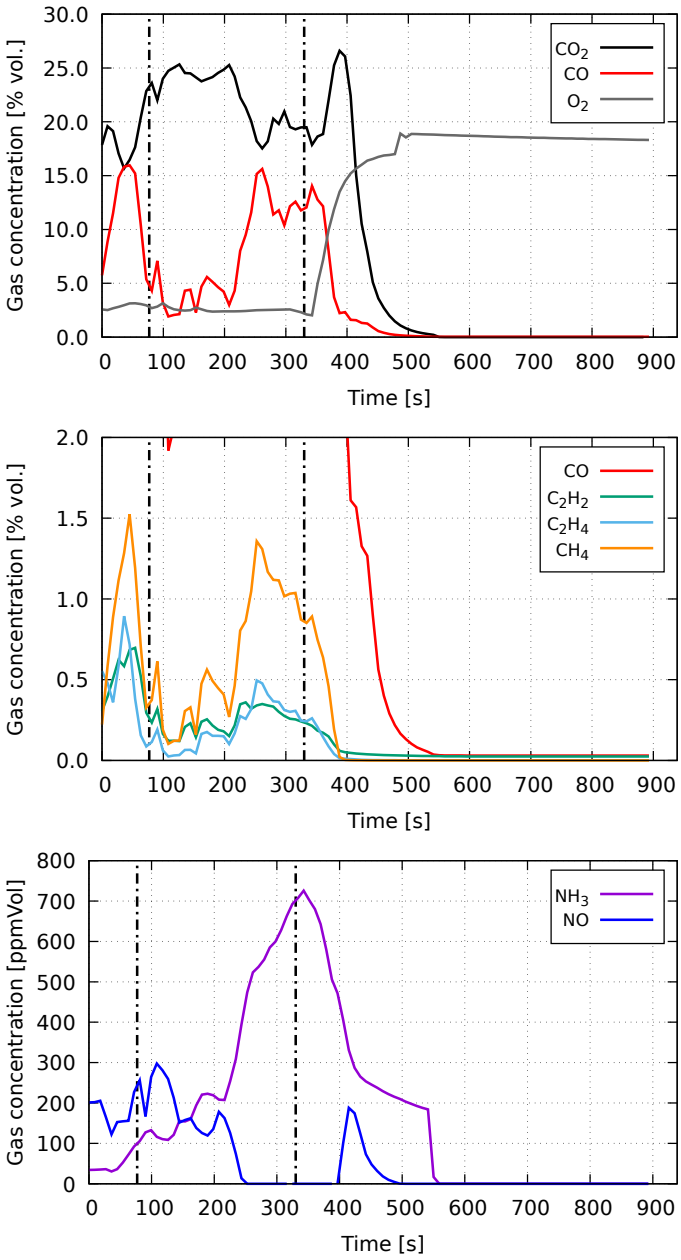

Figure C.77 – Combustion gases composition for sample *050P0310U3*

ANNEX A – FEEDSTOCK PARTICLES MORPHOLOGY DISTRIBUTION

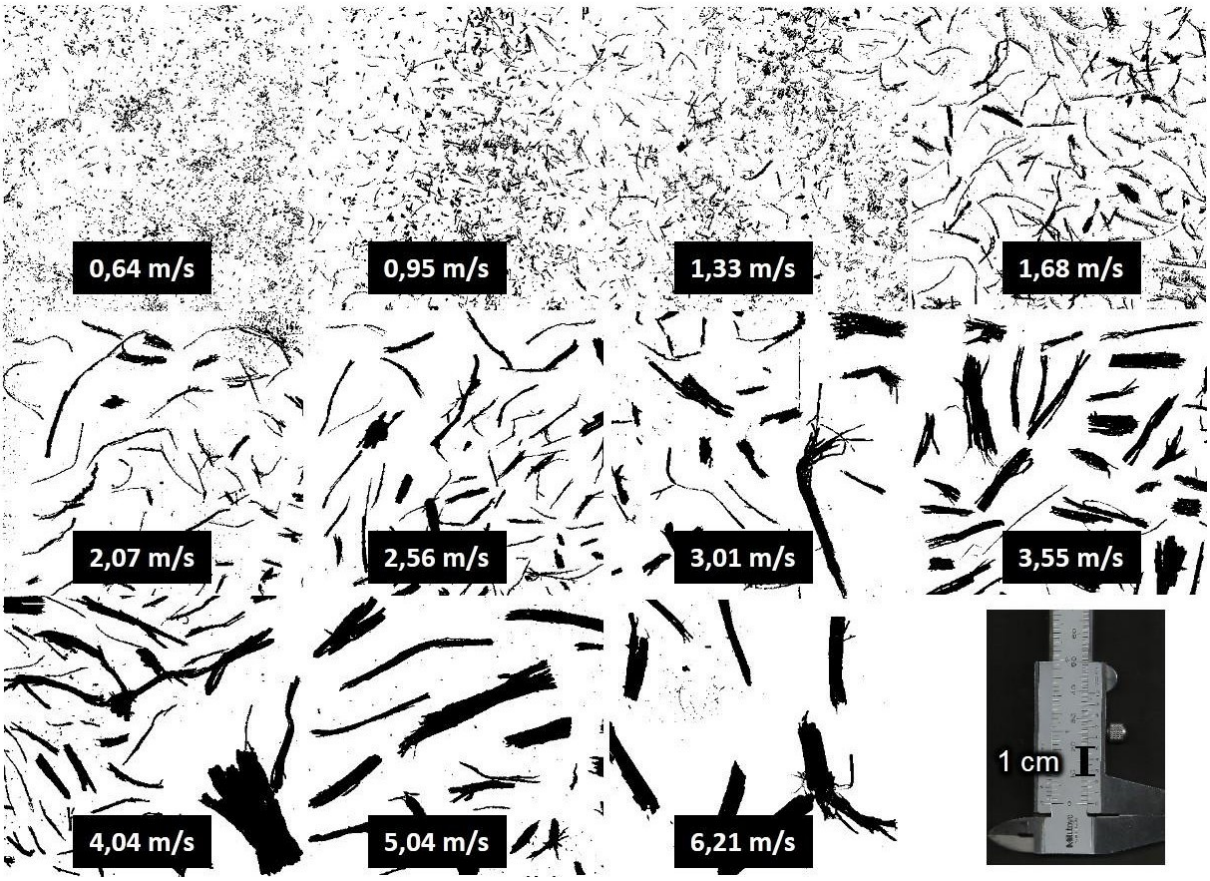

Figure A.1 – Detail of bagasse particles' morphology. Source: Ramirez-Quintero (2019)

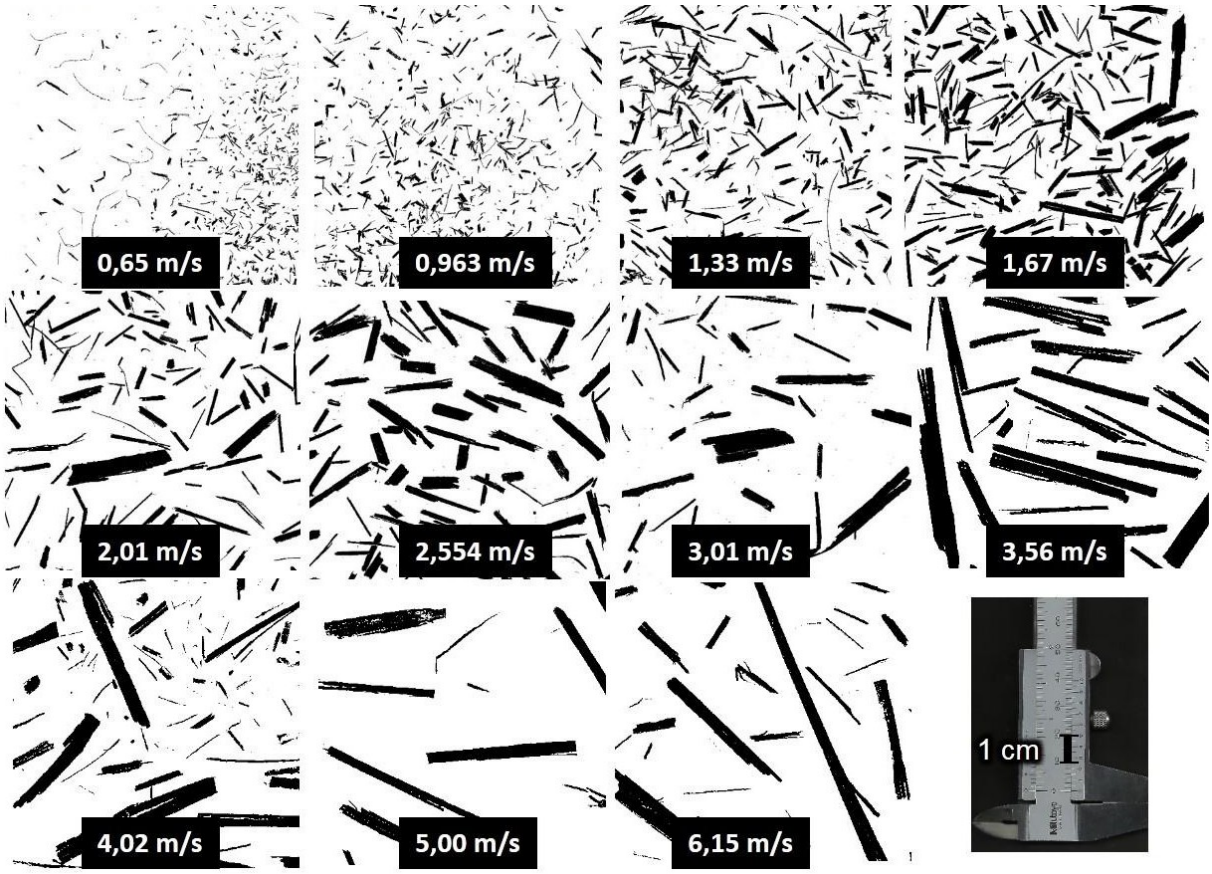

Figure A.2 – Detail of leaves particles' morphology. Source: Ramirez-Quintero (2019)